Experimental study of boiling : characterization of near-wall phenomena and bubble dynamics

Cassiano Tecchio

université
PARIS-SACLAY

Experimental study of boiling: characterization of near-wall phenomena and bubble dynamics

Etude expérimentale de l'ébullition : caractérisation des phénomènes en proche paroi et de la dynamique d'une bulle

Thèse de doctorat de l'université Paris-Saclay

Ecole doctorale n° 564, Physique en Ile-de-France (EDPIF)
Spécialité de doctorat: Physique
Graduate School: Physique. Référent: Faculté des Sciences d'Orsay

Thèse préparée dans les unités de recherche **Service de Physique de l'Etat Condensé** (**Université Paris-Saclay, CEA, CNRS**) et le **Service de Thermo-hydraulique et de Mécanique des Fluides** (**Université Paris-Saclay, CEA**) sous la direction de **Vadim NIKOLAYEV**, directeur de recherche, le co-encadrement de **Benjamin CARITEAU**, ingénieur-chercheur

Thèse soutenue à Paris-Saclay, le 30 Septembre 2022 par

Cassiano TECCHIO

Composition du jury

Membres du jury avec voix délibérative

M. Jocelyn BONJOUR Professeur, INSA Lyon et CETHIL/CNRS	Président
Mme Catherine COLIN Professeure, INP/ENSEEIHT et IMFT/CNRS	Rapportrice & Examinatrice
M. Paolo DI MARCO Professeur, Université de Pise, Italie	Rapporteur & Examinateur
M. Matteo BUCCI Professeur adjoint, MIT, Cambridge, USA	Examinateur
M. Fabrice CHARRA Directeur de recherche, SPEC/CEA Paris-Saclay	Examinateur
M. Pere ROCA i CABARROCAS Professeur, LPICM/Ecole Polytechnique	Examinateur

Membres du jury sans voix délibérative

M. Vadim NIKOLAYEV Directeur de recherche, SPEC/CEA Paris-Saclay	Directeur de thèse
M. Benjamin CARITEAU Ingénieur-chercheur, STMF/CEA Paris-Saclay	Co-encadrant

THESE DE DOCTORAT
NNT : 2022UPASP095

ÉCOLE DOCTORALE
Physique en île-de-France (EDPIF)

Titre: Etude expérimentale de l'ébullition: caractérisation des phénomènes en proche paroi et de la dynamique d'une bulle

Mots clés: ébullition, bulles, microcouche, interférométrie, thermographie infrarouge, expérience

Résumé: Ce travail consiste en une étude expérimentale des phénomènes physiques à micro-échelle se produisant lors de la croissance d'une seule bulle attachée à la paroi chauffante en régime d'ébullition nucléée. L'expérience est réalisée avec de l'eau à pression atmosphérique en utilisant des diagnostics optiques rapides (4000 images par seconde) et à l'échelle microscopique. La surface d'ébullition est constituée d'un film d'oxyde d'indium et d'étain (ITO) déposé sur une fenêtre transparente en MgF_2. La bulle est déclenchée par un chauffage local avec un laser infrarouge (IR). Nous étudions la dynamique et le transfert de chaleur d'une microcouche liquide qui peut se former entre la paroi et la bulle. Des mesures simultanées et synchronisées du profil de la microcouche, de la forme macroscopique de la bulle et de la température de la paroi sont obtenues respectivement par interférométrie en lumière blanche, par ombroscopie latérale et par thermographie IR. Le flux de chaleur de la paroi est reconstruit en utilisant la distribution de la température de la paroi. Une nouvelle caractéristique de la forme de la microcouche a été détectée : une bosse dans le profil de la microcouche qui apparaît au stade initial de la croissance de la bulle. Une théorie simple qui nous permet d'expliquer cette bosse est présentée. La bosse est expliquée par la croissance rapide des bulles et par l'interaction des forces visqueuses et capillaires agissant dans la microcouche pendant sa formation. Nous décrivons également une simulation numérique 2D de la dynamique de la microcouche qui montre un bourrelet de démouillage mis en évidence dans les simulations numériques précédentes près de la ligne de contact et une bosse plus éloignée. Un bon accord est trouvé entre les profils de microcouche simulés et expérimentaux dans la région de la bosse. Nous montrons que le démouillage est accéléré par l'évaporation, ce qui entraîne la formation d'un large bourrelet aux premiers stades de la croissance des bulles. Nos résultats montrent que l'amincissement de la microcouche dans le temps est dû à son évaporation. La résistance thermique mesurée à l'interface liquide-vapeur est plusieurs fois plus grande que sa valeur théorique et semble grossir dans le temps, ce qui est expliqué par une faible contamination de l'eau.

Title: Experimental study of boiling: characterization of near-wall phenomena and bubble dynamics

Keywords: boiling, bubble, microlayer, interferometry, infrared thermography, experiments

Abstract: This work consists of an experimental study of the microscale physical phenomena occurring during the growth of a single bubble attached to the heater at nucleate boiling. The experiment is performed with water at normal conditions by using the state-of-the-art high-speed (4000 frames per second) and microscopic-scale optical diagnostics. The boiling surface consists of an indium-tin oxide (ITO) film deposited on the transparent MgF_2 porthole. The ITO heating is performed locally with an infrared (IR) laser directed from below. We study the liquid microlayer that can form between the heater and the bubble. Simultaneous and synchronous measurements of the microlayer profile, macroscopic bubble shape and wall temperature are obtained by the white-light interferometry, sidewise shadowgraphy and IR thermography, respectively. The wall heat flux is reconstructed using the wall temperature distribution. A new feature in the microlayer shape has been detected: a bump in the microlayer profile that appears at the initial stage of the bubble growth. A simple theory that allows us to explain the bump is presented. The bump is explained by the fast bubble growth accompanied by the bubble edge deceleration and as an interplay of viscous and capillary forces acting in the microlayer during its formation. We also describe a 2D numerical simulation of microlayer dynamics that shows both a dewetting ridge evidenced in earlier numerical simulations near the contact line and a bump farther away. A good agreement is found between the simulated and experimental microlayer profiles in the bump region. We show that the dewetting is accelerated by evaporation, which leads to the formation of a large dewetting ridge at the initial stages of bubble growth. Our results also show that the microlayer thinning in time is due to its evaporation. The measured thermal resistance at the liquid-vapor interface is a few times larger than its theoretical value and seems to grow in time, which suggests the water weak contamination as its cause.

To my parents, Alcibides and Nelci Tecchio

To everyone who contributed to this work

To my grandparents, João Tecchio, Candida Tecchio and Nilo Zanetti
in memorium

Acknowledgements

First of all, I would like to express my gratitude to my parents, Alcibides Tecchio and Nelci Tecchio, who have taught me the value of life and supported me throughout all these years to pursue my studies and dreams abroad even 10k Km apart from each other. I am also grateful to may grandmother, Elsa Guollo, who always took care of me and helped our family with her hard work. To my aunt Edineia Zanetti and her husband Leonardo Iarcheski also thank you for supporting me on this journey abroad.

To my beloved girlfriend, Seoyun Sohn, who has supported me since the first day we met. Thanks for being in my side and giving me your thrust and love.

I will be forever in debt to my thesis director, Vadim Nikolayev, and my thesis supervisor Benjamin Cariteau, who gave me the opportunity and believed in me to perform this challenging work. I appreciate very much your patience and wiliness to discuss countless times. I admire your enthusiasm with our work throughout these years (even during difficult times) and I am extremely grateful for your excellent mentorship and guidance during this journey. Thank you, Vadim and Benjamin, for understanding my limitations and providing such a nice environment to work. I certainly finish this chapter of my life with a better view of research and science for the upcoming projects. I have to acknowledge the support you gave me all the time, specially during the uncertain times that we have faced during this work: COVID pandemic, the requests to extend the contract, the bureaucracy to get the IR camera and the many others technical challenges that, for many times, put a question mark on our goals but you never gave up. BIG thanks for that! Also, I am extremely grateful to Gilbert Zalczer (SPEC), whose contribution to this work was also noteworthy and taught me many things in optics. Thanks to your helpful advises on the optical installation, we were able to measure what we needed. You were the "eyes" of this thesis. You three have inspired me so much that i will be forever grateful for this experience. I have learned plenty of new things from you that have helped me to grow not only in technical knowledge but also personally. Hopefully, we can make more bubbles and this "Dynabulle" installation will give many more interesting results. Without any doubt, this challenging work was only possible thanks to you.

I acknowledge with gratitude the contribution of Guillaume Bois, Elie Saikali (STMF) and Xiaolong Zhang (SPEC) for their numerical simulations, Iouri Moukharski and Vincent Padilla (SPEC) for the help on the micro and macro fabrication, Simon Vassant (SPEC) for the FTIR measurements and Cindy Rountree (SPEC) for the ITO surface characterization with AFM.

This work would not be possible without the friendly assistance of my colleagues from LPICM (Ecole Polytechnique), who were willing to collaborate with us to solve the major technical challenge we have faced. Special thanks go to Jérôme Charliac, Pere Roca i Cabarrocas and Pavel Bulkin for solving the issue of deposition of the ITO on such a "difficult" substrate as MgF_2. You are the real magicians for me.

During this thesis I had a pleasure to advise and learn from Guillaume Laruelle, Loïc Loigerot and Corentin Le Houedec during their internships. The contribution of every one of you was noteworthy and helped to increase the quality of this work. I wish you all the best in your future careers.

I am truly thankful to my colleagues, friends and members of LIEFT and LATF laboratories at STMF, who helped me since my first day to understand and overcome technical and bureaucratic

challenges of the research environment and also contributed to make this work possible. Special thanks to Etienne, Sergey, Ludivine, Hervé, Constantin, Lucia, Danielle, Eric, Philippe, Clément, Céline, Frederic, Pierre-Louis, Gilles Bernard-Michel, Véronique, Marie-Claude, Olivier, Jean-Luc. I have to particularly highlight the help of Etienne, with whom I had really nice discussions that helped me with technical issues. I have also to acknowledge the help of Romain Abadie (DPC) for providing us with the extra-pure water for our experiments.

I have to express my gratitude to my friends and colleagues I met in France. Thanks Diana, Riccardo (thanks for all the pizzas you have prepared for us), Arthur (courage pour la fin de thèse), Awa, Rofeida, and Vincent(courage aussi pour ta thèse!) for all the discussions, conversations, coffee breaks and the lunch time in the cantine, most of them in French, which really helped me to overcome the language and cultural barriers. Merci beaucoup. Special thanks also to Vinod and Mampi with whom I shared nice moments. Thanks Diego for being the coolest flatmate I possibly could have and for providing such a nice and organized place to live.

My special thanks to my friends from Brazil (from UFSC Joinville and UFSC Mechanical Engineering Department-Labtucal laboratoty in Florianópolis) and also from Netherlands TU/e. Thanks for supporting me all the time, Cesar, Bruno, Hermann, Cristina, Mécia, Rodrigo Barros, Carina, Guilherme, Luis, Vishak, Igor, Milena, Dunja, Thales, Leonardo, Felipe Mineiro, Marta, Rodrigo, Felipe Costa, Ashish, Ahmet; Also, thanks to the kindest French teacher in the world, Alessandra Toscano, for you patience and time with me learning French. I hope we can meet in person soon.

I have to say thanks to my friends from the table tennis section at CEA. I have spent such nice moments with you guys. I hope the club will grow more and more. Special thanks to my friends Micka and Nicolas.

I also appreciate the financial support given for this work by DM2S/STMF and CEA/CFR sponsorship. I particularly acknowledge Pierre Gavoille, Gilles Rampal, Marion Le Flem from STMF and Sylvie Naury and Sebastien Carassou from DM2S.

"The mind that opens to a new idea, never comes back to its original size"
Albert Einstein

"Never agree to crawl if you want to soar"
Helen Keller

"A life without challenges is not worth living"
Socrates

Contents

Contents **ix**

Nomenclature **xxi**

1 INTRODUCTION **1**
1.1 Boiling: General overview 1
1.2 Near-wall features 3
1.3 Motivation, scope and objectives 4
1.4 Thesis structure 4

2 BOILING AT THE MICROSCALE: STATE OF THE ART **7**
2.1 Relevant physical phenomena 7
2.1.1 Contact line phenomena 7
2.1.2 Contact angle hysteresis 8
2.1.3 Kelvin effect 9
2.1.4 Interface slope variation in microregion 9
2.1.5 Interfacial thermal resistance 10
2.1.6 Vapor recoil 11
2.1.7 Hydrodynamic slip 11
2.1.8 Intermediate region and dewetting ridge 12
2.2 Microlayer 13
2.2.1 Physics of microlayer formation 15
2.2.2 Description of the flow in the microlayer 16
2.3 Bubble growth regimes: microlayer and contact line 16
2.4 Near-wall heat transfer 17
2.4.1 Determination of the heat flux toward the liquid 17
2.4.2 Heat transfer in the microlayer 19
2.4.3 Heat transfer in porthole 19
2.5 Experimental issues 20
2.5.1 Multiple bubbles versus single bubble 20
2.5.2 Choice of the boiling surface 21
2.6 Experimental techniques 21
2.6.1 Microlayer thickness measurement 21
2.6.2 Dry and wet areas 23
2.6.3 Wall temperature and heat flux 24
2.7 Summary and concluding remarks 24

3 EXPERIMENTAL APPARATUS **27**
3.1 Introduction . . . 27
3.2 The boiling cell . . . 27
3.2.1 Boiling surface: Practical issues and solutions . . . 28
3.3 ITO surface state . . . 31
3.4 Optical apparatus arrangement . . . 31
3.4.1 Visible-IR light beam splitter . . . 32
3.5 Characterization of the IR laser heating . . . 34
3.5.1 Source heat flux . . . 35
3.5.2 Measurement of ITO absorption . . . 36
3.5.3 Measurement of the angle of incidence of IR laser . . . 37
3.5.4 Measurement of angle β . . . 39
3.5.5 Measurement of heat source profile . . . 39
3.6 Microlayer heating estimation . . . 39
3.7 Experimental protocol . . . 40
3.8 Summary and concluding remarks . . . 41

4 OPTICS STUDY **43**
4.1 Interferometry . . . 43
4.1.1 Introduction . . . 43
4.1.2 Scalar beam interference theory . . . 45
4.1.3 Reflectance, transmittance and absorbance . . . 48
4.1.4 Intensity of the fringe map . . . 50
4.1.5 Comparison with the electromagnetic theory . . . 51
4.1.6 Spectral and spatial calibration of the setup . . . 52
4.1.7 Fringe geometry as a function of the thickness profile . . . 53
4.1.8 Image processing: Map compensation and symmetry analysis . . . 55
4.1.9 Image processing: Determination of the microlayer thickness $\delta(x)$ in validation 60
4.1.10 Image processing: Determination of microlayer thickness $\delta(x)$ in boiling . . . 62
4.1.11 Validation: air layer thickness without spacer layer . . . 64
4.1.12 Validation: air microlayer thickness with spacer layer . . . 67
4.1.13 Thickness resolution of measurements . . . 68
4.1.14 Fringe quality . . . 70
4.1.15 Microlayer maximum slope limit . . . 71
4.2 Infrared thermography . . . 73
4.2.1 Theory . . . 73
4.2.2 Sources of IR radiation . . . 75
4.2.3 Calibration . . . 77
4.3 Sidewise shadowgraphy . . . 79
4.3.1 Image post-processing . . . 80
4.4 Summary and concluding remarks . . . 81

5 NEAR-WALL PHENOMENA IN NUCLEATE BOILING **83**
5.1 Generalities . . . 83
5.2 Bubble nucleation, growth and departure . . . 84
5.3 Bubble, dry spot and microlayer radii . . . 85
5.4 Microlayer dynamics . . . 85
5.4.1 Simple bump model . . . 87
5.4.2 Numerical simulation of the microlayer dynamics . . . 88
5.5 Wall temperature . . . 89

5.6 Wall heat flux . . . 92
5.6.1 Heat transfer in ITO . . . 92
5.6.2 Heat transfer in MgF_2 . . . 93
5.6.3 Heat flux reconstruction and interfacial resistance . . . 94
5.7 Microlayer evaporation contribution to bubble growth . . . 97
5.8 Dewetting dynamics . . . 98
5.9 Discussion . . . 99
5.9.1 Microlayer and contact line evaporation regimes . . . 99
5.9.2 Homogeneous versus local heating: effect on contact line dynamics . . . 100
5.9.3 Effects of enlarged heating spot . . . 102
5.10 Summary and concluding remarks . . . 102

6 CONCLUSIONS and PERSPECTIVES **105**

Bibliography **106**

APPENDICES **121**

A Electromagnetic theory of interference **123**

B Spectral and spatial calibrations **127**
B.1 Spectral calibration . . . 127
B.2 Spatial calibration . . . 128
B.3 Optical magnification . . . 129

C Physical properties **131**
C.1 Optical properties . . . 131
C.2 Thermophysical properties . . . 132
C.3 Mechanical properties . . . 133

D Film thickness determination: alternative formulas **135**
D.1 Wavelength and fringe order difference of maxima . . . 135
D.2 Wavelength difference of maxima . . . 135
D.3 Film thickness difference . . . 136

E Uncertainty and error analysis **139**
E.1 Uncertainty in the linear regression for λ and x determination . . . 139
E.2 Uncertainty on measurements . . . 139
E.3 Error on formulas to compute film thickness . . . 140
E.4 RTD Temperature verification . . . 141

F WLI setup: optical alignment **143**

G Scanning line positioning **145**
G.1 Positioning protocol . . . 145
G.2 Positioning verification . . . 145

H Temperature spatial extrapolation and smoothing **147**
H.1 Temperature extrapolation . . . 147
H.2 Temperature smoothing . . . 148
H.2.1 Savitzky-Golay filter . . . 149

Abstract in French (Résumé substantiel) **151**

List of Figures

1.1 Schematics of Nukiyama's experiment. . . . 2
1.2 Pool boiling curve. Temperature controlled experiment: Path A-B-C-D-E-F. Heat flux controlled experiments: Path B-C-D-F during heating and F-E-B during cooling. B-B' represents the onset of boiling. . . . 2
1.3 Bubble macroscopic and near-wall regions in a single bubble. . . . 4

2.1 Contact angles in boiling. . . . 8
2.2 Advancing (θ_{adv}) and receding (θ_{rec}) contact angles. . . . 8
2.3 Formation of a thin liquid film by receding liquid surface. . . . 15
2.4 Two kinds of interface shapes near the foot of growing bubble in nucleate boiling. . . . 17
2.5 Schematics of the heat transfer at the boiling surface. . . . 18
2.6 Light interference. a) fringe pattern in LI [162] and b) WLI. . . . 22

3.1 Schematics of the boiling cell and optical measurement apparatus. . . . 28
3.2 Initial design of ITO deposited on a porthole. Ag busbars provide electrical contact between the ITO and the wires for Joule heating. . . . 29
3.3 ITO before and after the boiling test with Joule heating. . . . 30
3.4 ITO surface imaged by atomic force microscopy with the help of Cindy Rountree at SPEC/CEA Paris-Saclay. . . . 32
3.5 Design of visible-IR beam splitter (hot mirror). . . . 33
3.6 Transmittance and reflectance of the IR-visible beam splitter at an incident angle of 45°. 34
3.7 Signal to noise ratio(SNR) of the IR camera for a fixed pixel. . . . 34
3.8 The IR laser beam power $q_{i,IR}$ as a function of the laser current as given by the manufacturer. . . . 35
3.9 Schematics of the heat source created on ITO by the IR laser. . . . 35
3.10 Illustration of the optical installation to determine $\mathcal{A}_w$. . . . 37
3.11 ITO absorbance determined by IR power meter and FTIR measurements. . . . 38
3.12 Distribution of $\hat{T}_w^0(x,y)$. Its value is shown with a color scale. The ellipse is the $\hat{T}_w^0(x,y) = 0.3$ isoline fit. . . . 38
3.13 Ellipticity f as a function of $\hat{T}_w^0(x,y)$ and $\hat{q}_0''(x,y)$. . . . 39
3.14 Schematics of the optical installation to determine laser beam profile. . . . 40
3.15 Heat source profile. The ellipses correspond to the value of flux that is a half of the maximum. . . . 40

4.1 Schematics of the interferometry part of the experimental setup fully represented in Fig. 3.1. . . . 44
4.2 Fringe maps obtained in interferometry. . . . 45
4.3 Schematic of the light path in the porthole, spacer layer and microlayer. The y-axis is perpendicular to the paper plane. . . . 46

4.4 Positions of interference maxima calculated for $\delta^{min} = 0.5\,\text{nm}$. The symbols correspond to h in nm. The shaded interval of λ indicates the spectrometer bandwidth. 48
4.5 Theoretical I_{13} and I_{23} for two different values of δ. 52
4.6 Normalized by I_s intensity for the microlayer case calculated for $h = 850\,\text{nm}$ and $\delta = 1.5\mu\text{m}$. 52
4.7 Plano-convex lens with on a flat optical porthole for validation and comparison of WLI and LI. 55
4.8 WLI fringe maps for the lens. 56
4.9 LI fringe maps for the lens. 57
4.10 WLI and LI fringe maps for wedge films. 58
4.11 WLI fringe maps for spacer layer and lens. 59
4.12 Fringe symmetry analysis. 60
4.13 Normalized distribution of midpoints with respect to x'. 60
4.14 Flowchart to compute $\delta(x)$ from the maxima of $I(x)$ for the case without spacer layer. The steps inside the yellow rectangle are repeated for all maxima. 61
4.15 $I(x)$ profile by WLI at $\lambda = 573.49\,\text{nm}$. 62
4.16 Flowchart to compute $\delta(x)$ using $I(\lambda)$ profiles for the validation case without spacer layer. The steps inside the yellow rectangle are repeated for all x. 63
4.17 $I(\lambda)$ profiles for two points over x. 64
4.18 Flowchart to determine $\delta(x,t)$ in the case of ITO, spacer layer and bubble. 65
4.19 Fringe profile and thickness of ITO film used for the boiling case at $t = 0$ just before the bubble nucleation ($\delta = 0$). 66
4.20 Fit of theoretical $I(\lambda)$ profiles to the experiment. 66
4.21 Film thickness obtained by WLI from $I(x)$ profiles and its relative experimental error. 67
4.22 Film thickness by LI and its relative error. 67
4.23 Film thickness by WLI and its relative error by $I(\lambda)$ profiles. 68
4.24 Comparison between theoretical lens shape and WLI for $\delta < 100\,\text{nm}$. 69
4.25 Measurements of neighboring thicknesses in the lens case without spacer layer by LI and WLI by $I(\lambda)$. The theoretical lens shape has been corrected to take into account the lens displacement in the experiment due to the Hertz contact as discussed in subsection 4.1.7.2. 69
4.26 $I(x')$ profiles and fringe sharpness for different slit widths. The exposure time is 0.25 ms. 70
4.27 Mean visibility as a function of exposure time and slit width. The different symbols indicate different exposure times in ms. 71
4.28 Schematics of maximum slope limit θ_{lim}. 72
4.29 Theoretical θ_{lim} as a function of λ for layers of air and water. 73
4.30 Fringe map showing visible and invisible fringe regions. 73
4.31 Experimental WLI maximum slope limit of measurements at $\lambda = 463.04\,\text{nm}$. At this λ, $\theta_{lim} = 0.451°$. 74
4.32 Theoretical and experimental x_{lim} in the $x - \lambda$ map. 74
4.33 Schematics of the infrared radiation sources. The hot mirror is at 45° with regards to the optical axis of the IR camera. 76
4.34 Spectral transmittance of the IR camera's objective and sensibility of the IR camera detector. Data provided by FLIR. 78
4.35 IR thermometry calibration fits. 79
4.36 IR image of the hole into which the MgF_2 porthole is installed. 79
4.37 Illustration of the sidewise shadowgraphy observation. 80
4.38 Image post-processing for sidewise shadowgraphy. 80
4.39 $I(x')$ profile across the bubble. 81

5.1 Schematics of the microlayer underneath a single bubble. 84
5.2 Wall superheating evolution at the center of the bubble. The shaded zone indicates the bubble growth period. 85
5.3 Typical WLI fringe maps observed throughout the microlayer existence. 86
5.4 Experimental time evolution $r_{b,eq}$, microlayer radius r_m and dry spot (contact line) radius r_{cl} with laser heating. 86
5.5 Experimental data of Jung and Kim [12] for the time evolution of $r_{b,eq}$, r_m and r_{cl} with Joule heating. 86
5.6 Experimental microlayer profiles obtained by WLI for different growth times in ms indicated as curve parameters. 87
5.7 Theoretical microlayer profiles. 88
5.8 Superheating ΔT distribution on the wall. The color bar represents ΔT in K. 90
5.9 Spatial distributions $\Delta T(x)$ (blue dotted lines) for different t during the microlayer formation as compared to $\Delta T(x, t = 0)$ (black lines). The shaded areas at the center and in the sides represent the extent of dry spot (in red) and microlayer (in blue). . . 91
5.10 Spatial distributions $\Delta T(x)$ for different t after the microlayer development as compared to $\Delta T(x, t = 0)$. The shaded areas at the center and in the sides represent the extent of dry spot (in red) and microlayer (in blue). 92
5.11 Comparison of ΔT at $x = 1.6\,\mathrm{mm}$ obtained from the IR thermography with the theory (2.34) using δ from WLI. 93
5.12 Schematics of the boundary conditions for the porthole heat transfer calculations. . . . 94
5.13 Reconstructed heat flux spatial distribution $q''_l(x, y)$ at $t = 6.25\,\mathrm{ms}$ corresponding to Fig. 5.8b. The color bar represents the heat flux value in $\mathrm{MW/m^2}$. 95
5.14 Heat flux contributions as a function of time at $x = 1.1\,\mathrm{mm}$ and $y = 0$. 95
5.15 Spatio-temporal evolution of q''_l. 95
5.16 R^i and its effect on ΔT at $x = 1.60\,\mathrm{mm}$. 96
5.17 Time evolution of q''_l and ΔT at the contact line. 97
5.18 Microlayer evaporation contribution to the overall bubble growth. 98
5.19 Ca_{cl} and ΔT_{cl} at the contact line during its receding. 99
5.20 First nucleated bubble on a uniform heater without defects. Bubble macroscopic shape and wall phase distribution. The image corresponds to its receding moment 0.5 ms after bubble nucleation. 100
5.21 Bubble macroscopic shape and wall phase distribution near boiling crisis at single bubble growth. 101
5.22 Fringe of interference by laser interferometry. 102
5.23 WLI fringe with enlarged IR laser beam. a) Linear and parabolic fringe b) two parabolic fringe and c) an illustrative description of microlayer profile. 103

B.1 Spectra of the optical filters with known central wavelengths indicated in nm. The wavelength increases downwards. 127
B.2 Calibration of the wavelength axis in WLI. 128
B.3 Calibration of the x axis for WLI and LI. 128

C.1 ITO index of refraction n (blue rectangles) and extinction coefficient, κ (red circles). . 132

D.1 Schematics of constructive fringes with order N and $N + 1$ in a $x - \lambda$ fringe maps. . . 136

F.1 Optical path during fine alignment. The M_4 reference mirror replaces the MgF_2 porthole. 144
F.2 Position of λ' along x' for the bandpass filter at $\lambda = 532\,\mathrm{nm}$. 144

G.1 Comparison between WLI and IR thermography for r_{cl} and r_m radii. 146

H.1 T_w distribution on the ITO before bubble nucleation for different Θ. 148
H.2 T_w profile with extrapolation for $\Theta = 0$. 148
H.3 Raw and smoothed $T_w(x)$ at $y = 0$ for $t = 0.5\,\text{ms}$ and $0.75\,\text{ms}$. 149
H.4 Spatial and temporal derivatives from the smoothed temperature distribution. 149

List of Tables

4.1 Phase shifts at reflections and range of N values. 48
4.2 $\mathcal{R}$ values for the case with lens and without spacer layer (Fig. 4.7). 49
4.3 $\mathcal{R}$ values for the case with ITO spacer layer (Fig.4.3b). 50

C.1 Refraction indexes for $\lambda = 550\,\mathrm{nm}$. 131
C.2 Coefficients for the dispersion formula in Eq. (C.1). 131
C.3 Physical properties of ITO, liquid water and MgF_2. 132
C.4 Mechanical properties of several optical material. 133

E.1 Uncertainties on measurements. 140
E.2 Temperatures measured at steady-state conditions. 142

Nomenclature

$\mathcal{A}$	Absorbance
a	Spectral resolution [m/px] or minor half-axis of an ellipse [m]
b	Major half-axis of an ellipse [m]
Ca	Capillary number $= \mu U/\sigma$
c	Specific heat capacity at constant pressure [J/(kg K)]
D	Thermal diffusivity [m^2/s]
E	Electric field [V/m]
$\mathtt{E}$	Young modulus [Pa]
$\hat{\mathtt{E}}$	Young modulus normalized by the Poisson coefficient [Pa]
e	Thermal effusivity [$W\,s^{1/2}/(m^2\,K)$] or Euler number $\simeq 2.71$
F	Force [N]
$\mathcal{F}$	Accommodation coefficient
f	ellipticity
g	Gravitational acceleration [m/s^2]
H	Magnetic field [A/m] or thickness of the porthole [m]
h	thickness of ITO film [m]
I	Intensity of light
$\mathcal{I}$	Dimensionless light intensity
i	Imaginary unit
J	Volumetric heat source [W/m^3]
$\mathcal{J}$	Mass evaporation flux [$kg/(m^2\,s)$]
Ja	Jakob number $= c\,(T_w - T_{sat})\,/\mathcal{L}$
K	curvature [m^{-1}]
K	spatial resolution [m]
$\mathcal{K}$	Scaling factor
k	Thermal conductivity [W/(m K)]
$\mathcal{L}$	Latent heat of vaporization [J/kg]
l	Characteristic length [m]
$\mathcal{M}$	Number of maxima
$\mathbb{M}$	Molar mass [g/mol]
$\mathbf{M}$	Characteristic matrix
m	Mass [kg]
N	Fringe sequential order number
$\mathcal{N}$	Complex index of refraction $= n - i\kappa$
$\mathcal{N}$	Number of minima
n	Index of refraction
$\mathcal{P}$	Optical path difference [m]
p	Pressure [Pa]
Q	Maximum heat flux [W/m^2]

q	Power [W]
q''	Heat flux [W/m^2]
R	Thermal resistance [K m^2/W] or ray
$\mathbb{R}$	Universal gas constant [J/(mol K)]
$\mathtt{R}$	Lens radius of curvature [m]
$\mathcal{R}$	Reflectance
r	Radius [m]
Re	Reynolds number $= \rho u l/\mu$
S	Fringe sharpness [px^{-1}]
$\mathcal{S}$	Spectral sensibility
T	Temperature [K]
$\mathcal{T}$	Transmittance
t	Time [s]
U	Velocity [m/s]
V	Fringe visibility or volume[m^3]
$\mathcal{V}$	Volume [m^3]
W	Spectral power density [W/(m^3)]
$\mathcal{W}$	Emitted heat flux [W/m^2]
x	Abscissa [m]
x'	Horizontal axis in the fringe map [px]
y	Ordinate [m]
y'	Vertical axis in the LI fringe map [px]
z	Applicate [m]

Abbreviations

CHF	Critical heat flux
FTIR	Fourier transform infrared spectroscopy
IR	Infrared
ITO	Indium-tin oxide
LI	Laser interferometry
LPICM	Laboratory of physics of interface and thin films
RTD	Resistance thermal detector
SNR	Signal to noise ratio
SWS	Sidewise shadowgraphy
WLI	White light interferometry

Greek symbols

α	Angle of inclination of a flat plate [rad] or microlayer evaporation contribution to bubble growth[-]
β	Angle between horizontal axis of the image and major axis of an ellipse [rad]
γ	ratio of radii
Δ	Net path difference [m]
ΔT	Wall superheating [K]
δ	microlayer thickness [m]
η	optical admittance
ϵ	relative error
ε	emissivity
ε_0	permittivity of free space [F/m]
θ	angle of incidence or slope of the vapor-liquid interface [rad]
κ	extinction coefficient
λ	wavelength [m]

λ'	vertical axis in the WLI fringe map [px]
μ	shear viscosity [Pa s]
μ_0	permeability of free space [H/m]
ν	kinematic viscosity [m^2/s]
ξ	full width at half maximum of amplitude [px]
ϖ	absorption coefficient [m^{-1}]
ρ	density [kg/m^3]
σ	surface tension [N/m] or standard deviation
$\boldsymbol{\sigma}$	Stefan constant [$W/(m^2\,K^4)$]
ϕ	dimensionless phase shift
φ	phase shift at reflection [rad]
χ	thickness resolution of measurements [m^{-1}]
Ω	optical phase shift

Superscripts

0	initial
b	black body
i	interface

Subscripts

0	heating source
app	apparent
atm	atmosphere
b	bubble
c	curvature or compensated
cl	contact line
exp	experimental
hm	hot mirror
i	incident
l	liquid
lim	limit
m	microlayer
max	maximum
min	minimum
$micro$	microscopic
obj	objective
p	porthole
r	reflected
s	source
sat	saturation
t	transmitted
th	threshold
$theo$	theoretical
tot	total
V	Voinov
v	vapor
w	wall

Chapter 1

Introduction

1.1 Boiling: General overview 1
1.2 Near-wall features 3
1.3 Motivation, scope and objectives 4
1.4 Thesis structure 4

1.1 Boiling: General overview

The heat and mass transfer via boiling is involved in a wide range of scientific and industrial applications nowadays, such as cooling of electronic equipment by two-phase heat transfer exchangers, steam generation in chemical plants and in nuclear power stations. Worldwide, most of the electric energy is generated by steam-power plants. High amounts of energy can be transported by means of phase change without the need of large areas or temperature gradients, making boiling-based equipment compact, cheaper and highly efficient. However, the overall efficiency and safety of such equipment relies on the fundamental understanding of the physical aspects governing the phase change process to generate the steam. Boiling is considered a complex multi-scale phenomenon where several bubbles nucleate, grow and can interact with each other in a multitude of modes very fast [1]. This imposes numerous difficulties to observe and understand the physics of the process. Better design specifications and safeguards are then still missing.

In terms of safety, one particular phenomenon in the boiling process is the great concern: the boiling crisis. It is a transition between the regimes of nucleate and film boiling. In the second regime the heater is entirely covered by a film of vapor. Unlike liquid water, water vapor is an excellent insulator. Film boiling is then characterized by a very low heat-exchange rate between heater and bulk fluid. The associated heat flux when the transition has been initiated is known as critical heat flux, q''_{CHF}. The temperature of the heater surface increases sharply and, if the heating supply is not cut-off, it will lead to the complete burnout of the heater material. The consequences of such an event can be multiple, dangerous and irreparable. For instance, in nuclear power plants the leakage of radioactive material to the environment, rupture of fuel rods and explosions of containment vessels can cause a severe nuclear accident [2–4].

Over more than eight decades several researchers worldwide have devoted their studies on the understanding of the physical phenomena associated to boiling. Nukiyama [5] was the pioneer in the study of pool boiling. The term "pool" designates that there is no external fluid flow acting on the boiling dynamics. Therefore, the fluid flow is caused only by the motion of the vapor bubbles through the liquid and the natural convection. A schematics of the Nukiyama's experiment is shown in Fig. 1.1.

In his experiment, Nukiyama [5] used a heat flux-controlled setup to study the boiling of water at normal conditions. The heat flux dissipated over a thin wire made of nickel-chromium was determined

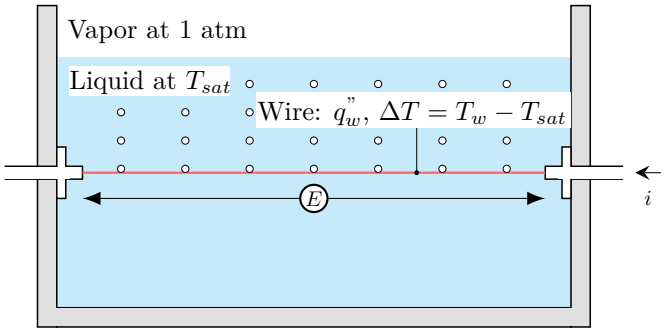

Figure 1.1: Schematics of Nukiyama's experiment.

by measuring the electrical potential E and the current i. The bulk liquid is consider to be at saturated temperature, T_{sat}. The wall superheating temperature is defined as $\Delta T = T_w - T_{sat}$, where T_w stands for the wall (wire) temperature. Nukiyama was able to observe the main flow characteristics of the boiling process according to the imposed wall heat flux q''_w, in W/m^2. The boiling is then described by a plot of ΔT against q''_w. Different regimes are distinguished according to the boiling features. Fig. 1.2 presents the boiling curve for temperature controlled and heating controlled experiments. The following regimes describe the boiling characteristics:

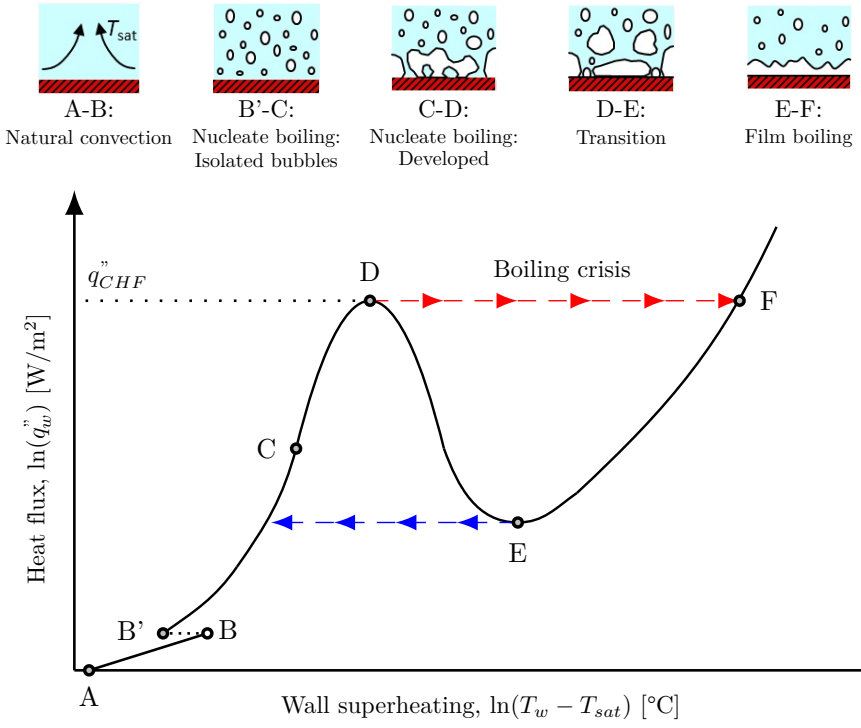

Figure 1.2: Pool boiling curve. Temperature controlled experiment: Path A-B-C-D-E-F. Heat flux controlled experiments: Path B-C-D-F during heating and F-E-B during cooling. B-B' represents the onset of boiling.

- **Regime A-B: Natural convection.** In this regime the heat supplied is low and not enough to promote boiling. The heat is transferred from the heater to the liquid mostly by natural convection. A low heat transfer coefficient is associated to this regime.

- **Regime B'-C: Nucleate boiling - Isolated bubbles.** Onset of boiling is usually followed by a wall superheating excursion (B-B' in Fig. 1.2), which is caused by the nucleation energy barrier in the heater cavities [6]. Once the boiling starts, isolated bubbles appear. The number of active nucleation sites and the bubble frequency increase with increasing wall superheating from B' to C. Heat is transported by phase change and also due to the strong fluid flow close to the heating surface carrying away the superheated liquid from it.

- **Regime C-D: Developed nucleate boiling.** A further increase in the heat flux promotes a large number of active nucleation sites and high frequency of bubbles. The bubbles start to coalesce close to heating surface. The rewetting of liquid at the heating surface is no longer efficient as in the regime (B'-C). The heat transfer coefficient starts to decrease but the increase in the wall superheating is still high enough to maintain the heat flux increasing up to the critical heat flux (CHF).

- **Regime D-E: Transition.** After CHF has been reached, the fluid flow from the bulk liquid to rewet the heating surface is significantly blocked by the bubble coalescence. This regime is characterized by the partial blanketing of the heating surface by vapor patches. This promotes unstable boiling and fluctuations on the surface temperature due to dry regions. The covering area of the vapor patches increases with increasing the wall superheating from D to E. The heat transfer coefficient and the heat flux decrease due to the low conductivity of the vapor.

- **Regime E-F: Film boiling.** In this regime, the vapor blanket covers the entire heating surface and there is no longer contact between the liquid phase and the wall. The radiation through the vapor film becomes an important heat transfer mechanism, increasing the heat transfer coefficient and the heat flux monotonically.

1.2 Near-wall features

Boiling is a multiscale phenomenon. The macroscopic bubble that can be seen by a human naked eye in daily life applications of boiling (heating up water for cooking pasta or tea, for instance) is shown in the schematics of Fig. 1.3a. The characteristic length scale, l, is the bubble radius r_b (which goes up to a few mm). Within this region, capillary forces at the liquid-vapor interface are balanced out by liquid inertia, gravity and viscous shear stresses created due to convection. However, near the wall a microlayer that can not be seen by naked eyes, located between the solid surface and the liquid-vapor interface of the bubble as shown in Fig. 1.3b, can be formed during the bubble growth. The microlayer has a thickness profile $\delta(x)$ that can be as the one illustrated in Fig. 1.3b. δ is up to a few μm and the microlayer extents over a few mm on the solid surface. The conditions in which the microlayer exists are still under research [7–9]. Convection, inertial effects and gravity are unimportant whereas surface tension and viscous forces are predominant in the microlayer.

In this work, we refer to the thermal and hydrodynamic processes taking place in the microlayer, contact line and in the dry spot as near-wall phenomena. The contact line is a line on the solid surface where the three phases (liquid, vapor and solid) meet. The length scale of the dry spot diameter is of a few mm on the wall and it defines a surface on the solid where the liquid is not in contact with wall. It if formed due to the high evaporation rates at the contact line.

The physical phenomena driving the microlayer dynamics are of a great importance to the overall bubble growth. The geometry of the microlayer and the contact line dynamics have an impact on the heat transfer from the wall to the liquid-vapor interface and on the liquid fluid flow characteristics in the microlayer. The microlayer evaporation may also contribute significantly to the overall bubble growth and its presence or not change the wall temperature and heat fluxes distributions.

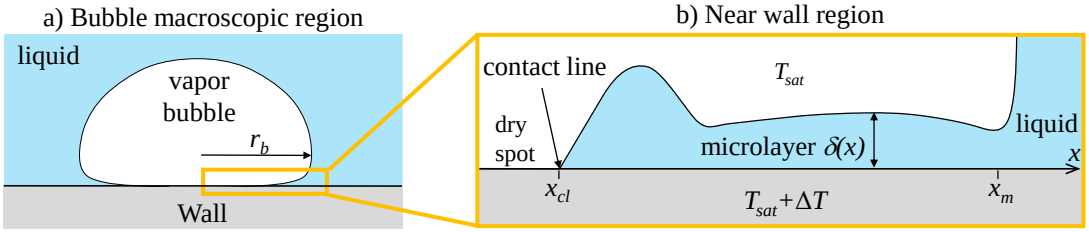

Figure 1.3: Bubble macroscopic and near-wall regions in a single bubble.

1.3 Motivation, scope and objectives

This work focuses on physical phenomena in the near-wall. More specifically, we study experimentally the dynamics of the microlayer, dry spot and the heat transfer within this region. The first motivation to focus in this region is that the microlayer profile can be as complex as depicted in schematics of Fig. 1.3b, which physical formation mechanisms are still under debate. The second motivation is that even direct numerical simulations of a single bubble require models to fully describe the near-wall phenomena. Therefore, experimental data must be provided to validate these models.

To understand the physics within such a short region, the experiments have to be performed at high spatial resolution. Therefore, one needs to concentrate the investigation during the growth of a single bubble.

The main objectives of this thesis are the following:

(i) Develop and validate a novel experimental installation for pool boiling studies.

(ii) Produce experimentally a single bubble.

(iii) Provide a physical description of the microlayer dynamics.

(iv) Characterize the wall heat transfer.

To achieve the aforementioned objectives the novel experimental installation uses state-of-the-art high speed and resolution optical diagnostics. It is conceived to measure the following:

(i) Spatio-temporal evolution of microlayer thickness by white light interferometry.

(ii) Spatio-temporal evolution of microlayer radius.

(iii) Dry spot temporal evolution.

(iv) Spatio-temporal evolution of temperature on the bubble base by infrared thermography.

(v) Temporal bubble radius by sidewise shadowgraphy.

1.4 Thesis structure

Apart of this chapter, the thesis is organized as follows.

- Chapter 2. This chapter presents a literature review consisting of theoretical aspects, state-of-the-art investigations on microscale boiling phenomena as well as the main experimental techniques applied in similar studies.
- Chapter 3. The pool boiling cell is presented along with important practical issues and solutions proposed for the experiments.

- Chapter 4. This chapter is devoted to the optical measurements. A detailed description of the three techniques, namely as white light interferometry, IR thermography and shadowgraphy is provided.
- Chapter 5. In this chapter, the results of near-wall phenomena at bubble growth in boiling are presented along with physical descriptions of the phenomena.
- Chapter 6. Conclusions and perspectives. The main findings of this work are highlighted and future perspectives are given.

Chapter 2

Boiling at the microscale: state of the art

2.1 Relevant physical phenomena . . . 7
2.1.1 Contact line phenomena . . . 7
2.1.2 Contact angle hysteresis . . . 8
2.1.3 Kelvin effect . . . 9
2.1.4 Interface slope variation in microregion . . . 9
2.1.5 Interfacial thermal resistance . . . 10
2.1.6 Vapor recoil . . . 11
2.1.7 Hydrodynamic slip . . . 11
2.1.8 Intermediate region and dewetting ridge . . . 12
2.2 Microlayer . . . 13
2.2.1 Physics of microlayer formation . . . 15
2.2.2 Description of the flow in the microlayer . . . 16
2.3 Bubble growth regimes: microlayer and contact line . . . 16
2.4 Near-wall heat transfer . . . 17
2.4.1 Determination of the heat flux toward the liquid . . . 17
2.4.2 Heat transfer in the microlayer . . . 19
2.4.3 Heat transfer in porthole . . . 19
2.5 Experimental issues . . . 20
2.5.1 Multiple bubbles versus single bubble . . . 20
2.5.2 Choice of the boiling surface . . . 21
2.6 Experimental techniques . . . 21
2.6.1 Microlayer thickness measurement . . . 21
2.6.2 Dry and wet areas . . . 23
2.6.3 Wall temperature and heat flux . . . 24
2.7 Summary and concluding remarks . . . 24

2.1 Relevant physical phenomena

2.1.1 Contact line phenomena

Near the wall, the slope of the liquid-vapor interface can strongly vary in boiling. Here, we define the contact angle at the liquid side being formed between the wall and the liquid-vapor interface. Fig. 2.1 shows three characteristic slopes ("contact angles") depending on the length scale in consideration.

In Fig. 2.1a, a microscopic region (microregion) near the wall is shown. Its typical size $l_V \sim 100\,\text{nm}$ is

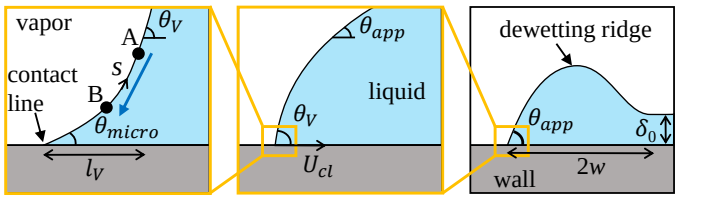

(a) Microregion (b) Intermediate region (c) Macroregion (dewetting ridge scale)

Figure 2.1: Contact angles in boiling.

called the Voinov length (by the reasons that will be evident later, in subsection 2.1.8). Very close to the wall (within few nm), the vapor-liquid interface forms a slope θ_{micro} with the solid wall. This is the true contact angle called also the microscopic contact angle. Its value is defined by the intermolecular forces that are very strong in this region. Therefore, it can be assumed independent of the fluid flows caused by wall superheating, evaporation and bubble motion. θ_{micro} defines the wettability of the surface and corresponds to the Young-Laplace contact angle, given by

$$\theta_{micro} = (\sigma_{SG} - \sigma_{SL})/\sigma \tag{2.1}$$

where σ_{SG}, σ_{SL} and σ represent the surface tension of the solid-vapor, solid-liquid and liquid-vapor interfaces, respectively. It can be shown [10] that the slope of the liquid-vapor interface within this region is defined by the fluid flow induced by the phase exchange only and is independent of the contact line motion and bubble deformation due to buoyancy.

2.1.2 Contact angle hysteresis

In the case of boiling, one needs to account for the solid surface heterogeneity, both chemical and geometrical (surface roughness). It leads to the wetting hysteresis, i.e. non-uniqueness of the static contact angle [11] that can take any value between two limits. They are named as advancing (θ_{adv}) and receding (θ_{rec}) contact angles. As illustrated in the schematics of Fig. 2.2, θ_{adv} is measured just before the wetted wall area starts increasing (contact line motion towards the vapor side) whereas θ_{rec} is measured just before the wetted wall area starts decreasing (contact line motion towards the liquid side). During the bubble growth in boiling, both situations occur. At the initial stages of the growth, one observes θ_{rec} before the dry spot spreading on the wall [12]. At the later stages of the bubble growth, the dry spot shrinks. One can thus see θ_{adv}.

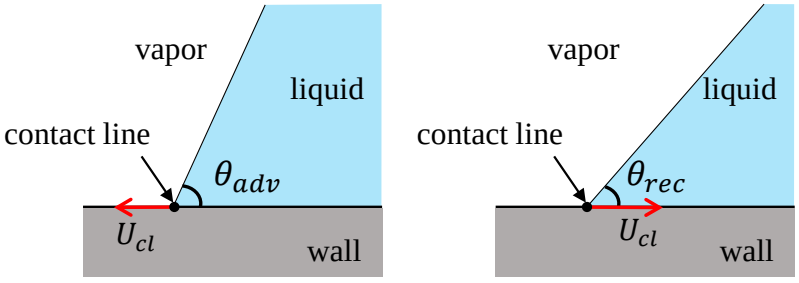

(a) Advancing. (b) Receding.

Figure 2.2: Advancing (θ_{adv}) and receding (θ_{rec}) contact angles.

The difference given by

$$\Delta\theta = \theta_{adv} - \theta_{rec}, \tag{2.2}$$

is defined as wetting hysteresis [13].

2.1.3 Kelvin effect

The Kelvin effect describes the dependence of the interfacial temperature, T^i, on the pressure jump across a liquid-vapor interface. It can be shown that this dependence is expressed by

$$T^i = T_{sat}\left(1 + \frac{\Delta p}{\mathcal{L}\rho_l}\right), \tag{2.3}$$

where Δp is the pressure jump across the interface given by the Laplace equation as

$$\Delta p = p_v - p_l = \sigma K, \tag{2.4}$$

where K is the local curvature of the interface. $\mathcal{L}$ and ρ_l represent the latent heat of vaporization and liquid density, respectively. This effect is only relevant in a close vicinity of the contact line, where the interface is strongly curved and the liquid film thickness is up to tens of nm. One notes the importance of the accounting for this effect as it relaxes the dynamic contact line singularity by providing a finite liquid pressure value at the contact line [10, 14].

2.1.4 Interface slope variation in microregion

One can analyze the slope theoretically as follows. In Fig. 2.1a, we take the points A and B located at the liquid-vapor interface with B closer to the contact line. Applying Eq. (2.4) at A and B and subtracting one from another (the pressure p_v is spatially homogeneous inside the vapor so $p_v^A > p_v^B$) one writes

$$p_l^A - p_l^B = \sigma(K^B - K^A) \tag{2.5}$$

In order to provide a fluid flow towards the contact line to replenish the liquid loss caused by intensive evaporation on it, $p_l^A > p_l^B$ resulting in $K^B > K^A$ so the curvature increases toward the contact line. As, according to its geometrical definition, the curvature is a rate of local slope variation along the curvilinear coordinate s running along the interface (Fig. 2.1a), the slope θ_V formed at the end of microregion that we call the Voinov angle (by the reasons that will be evident later, in subsection 2.1.8) can be considerably larger at evaporation than θ_{micro}. The Voinov angle is the apparent contact angle caused by evaporation only (i.e., when the contact line is immobile).

It is possible to obtain analytical expressions for θ_V under some simplifying assumptions, in particular, accounting for the Kelvin effect only (without accounting for other nanoscale effects). For small ΔT, Janeček [15] derived an expression

$$\theta_V = \theta_{micro} + \frac{\pi\Delta T}{2\sigma\theta_{micro}^2}\sqrt{\frac{3\mu_l k_l}{T_{sat}}}, \tag{2.6}$$

where k_l and μ_l stand for the liquid thermal conductivity and dynamic viscosity, respectively. One can see that θ_V is a function of the fluid properties, θ_{micro} and ΔT. For high ΔT, Janeček et al. [10] show that

$$\theta_V = \left(\frac{\sqrt{3\mu_l k_l T_{sat}}}{b\sigma}\frac{\Delta T}{T_{sat}}\right)^{1/3}, \tag{2.7}$$

where $b \simeq 0.3$. One can see that θ_V becomes independent of θ_{micro} when ΔT is high enough.

2.1.5 Interfacial thermal resistance

The high local heat flux in the vicinity of the contact line produces high vapor velocities. The interfacial thermal resistance represents a resistance to the evaporation flux at the liquid-vapor interface due to the limitation of velocity of vapor molecules during phase change. The heat flux at a flat liquid-vapor interface can be derived using the gas kinetic theory as [16]:

$$q''^{i} = \frac{2}{2-\mathcal{F}_C}\frac{\mathcal{L}}{\sqrt{2\pi\mathbb{R}_g/\mathbb{M}}}\left(\mathcal{F}_C\frac{p_v^i}{\sqrt{T^i}} - \mathcal{F}_E\frac{p_v}{\sqrt{T_{sat}(p_v)}}\right), \tag{2.8}$$

where $\mathbb{M}$ and $\mathbb{R}_g$ stand for molecular mass and universal gas constant, respectively. $\mathcal{F}_C$ and $\mathcal{F}_E$ represent the evaporation and condensation accommodation coefficients, respectively. These coefficients characterize the sticking of the molecules to the interface. For an interface in equilibrium, *i.e.* equal number of evaporating and condensing molecules, one can assume that $\mathcal{F}_C \equiv \mathcal{F}_E$. However, for a non-equilibrium interface this assumption might not be valid [17]. A more general concept of energy accommodation coefficient was first introduced by Maxwell [18] and later defined by Knudsen [19]. Further, the evaporation accommodation coefficient was given by Knudsen [20] as:

$$\mathcal{F}_E = \frac{\text{Number of molecules transferred to the vapor phase}}{\text{Number of molecules emitted from the liquid phase}}, \tag{2.9}$$

where $\mathcal{F}_E < 1$ means that some molecules emitted from the liquid have not been transferred to the vapor due to the effects of reflection, for instance. Complete evaporation is achieved when $\mathcal{F}_E = 1$. The condensation accommodation coefficient is analogous. As presented by Eames et al. [21], for pure water, $\mathcal{F}_E$ can be assumed as unity, regardless the pressure and temperature.

By assuming that $\mathcal{F}_C \equiv \mathcal{F}_E \equiv \mathcal{F}$ and a negligible temperature difference between interfacial and saturation temperatures if compared to their absolute values, Eq. (2.8) is simplified as

$$q''^{i} = \frac{2\mathcal{F}}{2-\mathcal{F}}\frac{\mathcal{L}\left[p_{sat}(T^i) - p_v\right]}{\sqrt{2\pi\mathbb{R}_g T_{sat}/\mathbb{M}}}. \tag{2.10}$$

From Clausius-Clapeyron equation and assuming $\rho_l \gg \rho_v$ one can write:

$$p_{sat}(T^i) - p_v = \left[T^i - T_{sat}(p_v)\right]\frac{\mathcal{L}\rho_v}{T_{sat}(p_v)}. \tag{2.11}$$

By combining Eqs. (2.11, 2.10) the interfacial temperature due to the interfacial resistance R^i is

$$T^i = T_{sat} + q''^{i}R^i, \tag{2.12}$$

where

$$R^i = \frac{2-\mathcal{F}}{2\mathcal{F}}\frac{T_{sat}\sqrt{2\pi\mathbb{R}_g T_{sat}/\mathbb{M}}}{\mathcal{L}^2\rho_v}. \tag{2.13}$$

If the interfacial thermal resistance is taken into account, $T^i > T_{sat}$. The theoretical value of R^i is $0.637\,\mu\text{Km}^2/\text{W}$, obtained via Eq. (2.13) for $\mathcal{F} = 1$ and water at 100 °C. By combining the interfacial thermal resistance with the Kelvin expression (2.3), one writes

$$T^i = T_{sat}\left(1 + \frac{\Delta p}{\mathcal{L}\rho_l}\right) + q''^{i}R^i. \tag{2.14}$$

By assuming a linear temperature distribution in the vertical direction,

$$q''^{i} = k_l\frac{T_w - T^i}{\delta}, \tag{2.15}$$

where q''^i is the heat flux at the liquid side of the interface. The interfacial energy balance (neglecting the heat flux towards the vapor) is

$$\mathcal{J}\mathcal{L} = q''^i, \tag{2.16}$$

where $\mathcal{J}$ stands for the mass flux at the interface. Finally, the latter can be expressed as

$$\mathcal{J} = k_l \frac{\Delta T - \dfrac{T_{sat}\Delta p}{\mathcal{L}\rho_l}}{(\delta + k_l R^i)\mathcal{L}}. \tag{2.17}$$

One notes that the interfacial thermal resistance remains to be controversial, in particular for polar fluids like water, where even tiny volume contamination comes up to the interface, which results in its strong contamination. Because of it, one observes a reduced interfacial mass flux evaporation rate that can be described with Eq. (2.17) but with a value of R^i, larger than that given by Eq. (2.13).

2.1.6 Vapor recoil

The vapor recoil, also known as the differential recoil pressure, is a consequence of the momentum transfer to the liquid-vapor interface when the fluid molecules vaporize or condense. Due to the rapid expansion of the fluid while evaporating the recoil pressure acts normal to the liquid-vapor interface pushing it towards the liquid side. The recoil pressure is expressed as

$$\vec{p_r} = -\vec{n}\mathcal{J}^2 \left(\frac{1}{\rho_v} - \frac{1}{\rho_l}\right), \tag{2.18}$$

In Fig. 2.1, for instance, the vapor recoil acts to maintain the interface closer to the solid, and its effect is accounted by adding it as an extra term in the Laplace equation, Eq. (2.4), as given by Nikolayev [14]:

$$\sigma K = \Delta p + p_r. \tag{2.19}$$

The recoil pressure strongly increases with $\mathcal{J}$. As the latter strongly varies in the vicinity of the contact line at evaporation, the vapor recoil leads to an additional contribution to the curvature and thus to an additional difference between θ_V and θ_{micro} [22].

The vapor recoil also contributes to increase T^i as [23, 24]

$$T^i = T_{sat}\left[1 + \frac{\mathcal{J}^2}{2\mathcal{L}}\left(\frac{1}{\rho_v^2} - \frac{1}{\rho_l^2}\right)\right], \tag{2.20}$$

so that the full T^i expression accounting all nanoscale effects reads

$$T^i = T_{sat}\left[\left(1 + \frac{\Delta p}{\mathcal{L}\rho_l}\right) + \frac{\mathcal{J}^2}{2\mathcal{L}}\left(\frac{1}{\rho_v^2} - \frac{1}{\rho_l^2}\right)\right] + q''^i R^i. \tag{2.21}$$

2.1.7 Hydrodynamic slip

Usually one considers that the liquid molecules stick to the solid so the tangential to the surface component u_x of the liquid velocity is zero on it, which is referred as the no-slip condition. When the surface is non-wettable, the molecular dynamic simulations show that the liquid can slide along the solid when the tangential hydrodynamic stress is large. This phenomenon is characterized by the slip length l_s defined with the Navier boundary condition

$$u_x = l_s \frac{\partial u_x}{\partial z}. \tag{2.22}$$

One needs to mention that the slip of liquid along the solid substrate is well confirmed experimentally [25], and measurements permit to determine the slip length within 10 nm accuracy [26]. More detailed discussion on this phenomenon may be found in the review articles [27, 28]. The characteristic value of l_s is of the order of 10-20 nm for the partial wetting case considered here. The slip effect is expected to be important at a (horizontal) distance $\sim l_s/\theta_{micro}$ from the contact line (the slip length is measured along the z axis).

2.1.8 Intermediate region and dewetting ridge

In Fig. 2.1b, the intermediate region is depicted. Its length scale is intermediate between l_V and the scale of microlayer, typically 10 μm. Within this region, the nanoscale effects discussed above are negligible. The liquid flow is mainly controlled by the contact line motion [10] and the evaporation effect is not as important. The interface slope θ is a function of the contact line velocity U_{cl} characterized with the dimensionless capillary number $Ca_{cl} = \mu_l U_{cl}/\sigma$. The slope is given by the Cox-Voinov asymptotic expression [14]

$$\theta^3(x) = \theta_V^3 - 9Ca_{cl}\ln\left(\frac{x}{l_V}\right). \tag{2.23}$$

The l_V value can be obtained theoretically by the asymptotic matching of the intermediate region and the microregion. For the isothermal contact line dynamics, Snoeijer and Eggers [29] have derived $l_V = l_s/(e\theta_{micro})$ within a theoretical approach based on the hydrodynamic slip. For the evaporation case, the model based on the Kelvin effect has been considered [10]. A recent study [30] shows however that the hydrodynamic slip is dominant for conventional fluids at evaporation and l_V can be approximated by the expression

$$l_V \approx 3l_s/(e\theta_V). \tag{2.24}$$

At its right end (Fig. 2.1c), the intermediate region matches the microlayer, which is a micrometric liquid film under the bubble discussed in the next section. The apparent contact angle θ_{app} measurable experimentally can be seen as the interface slope at their boundary.

When the contact line recedes, the dewetting phenomenon (i.e. wall drying via the lateral film removal from a previously wetted wall area) is observed. It is well known that because of a strong viscous shear in a thin film, the liquid does not flow into it but is collected in a ridge of circular cross-section along the film edge (Fig. 2.1c). The adiabatic dewetting (at $\Delta T = 0$) is commonly observed in the everyday life. Note that the dewetting ridge was observed in many experiments of adiabatic dewetting of liquid films [9, 31–36]. Snoeijer and Eggers [29] proposed an asymptotic theory for the adiabatic dewetting that resulted in two main expressions. The first defines θ_{app} as

$$\theta_{app}^3 = \theta_V^3 - 9Ca_{cl}\ln\left(\frac{2w}{el_V}\right), \tag{2.25}$$

where w is the ridge half-width. The second defines the dewetting velocity:

$$Ca_{cl} = \frac{\theta_V^3}{9}\left[\ln\left(\frac{4a}{e^2}Ca_{cl}^{1/3}\frac{w^2}{l_V\delta_0}\right)\right]^{-1}, \tag{2.26}$$

where $a \approx 1.094$ and δ_0 is the microlayer thickness at the end of the ridge (Fig. 2.1c). Recently, Zhang and Nikolayev [30] showed that such expressions describe the evaporation case provided the appropriate values of θ_V and l_V (from Eq. 2.24) were used. The results of such a theory showed a good agreement with the experimental data of Fourgeaud et al. [35, 36]. Note that the dewetting speed is mostly defined by $\theta_V = \theta_V(\Delta T)$, which means that it is controlled by the superheating.

2.2 Microlayer

A big effort was deployed by the scientific community to understand the hydrodynamics and heat transfer phenomena within the microlayer [37]. Pioneering investigations were performed in the 1950-70's [38–49] but still remain noteworthy references owing their relevance and quality. Snyder and Edwards [38] first suggested the existence of a thin liquid layer underneath of a growing bubble. Sharp [40], Jawurek [42, 43], Cooper and Lloyd [44] and Voutsinos and Judd [47] have performed optical measurements of the microlayer thickness during the nucleate boiling of a single bubble. The dry patch at the bubble base was also identified. The wedge-shaped microlayer with a thickness up to a few μm was observed. Such a strong interest to the microlayer is explained by the high heat transfer rate within it. A contribution of the microlayer evaporation to the bubble growth has been reported significant [44, 47] with very high heat transfer coefficients near the contact line [41]. Formulas for its initial thickness, δ_0, have been proposed [44, 48]. Under "initial thickness" one means the thickness at the instant of its creation (before its evaporation that leads to the microlayer thinning). It is usually assumed that this thickness is observed at the microlayer edge. Cooper and Lloyd [44] proposed

$$\delta_0 = C(\nu t_g)^{1/2}; \tag{2.27}$$

where C is an empirical constant which depends on the fluid [44, 50, 51]. t_g is the time of bubble growth (time of its residence on the heater) and ν is the kinematic viscosity of the microlayer fluid. Cooper and Lloyd [44] suggests $C = 0.8$ while van Ouwerkerk [45] and Olander and Watts [52] give 1.26 and 0.88, respectively.

More recently, several other authors have also measured the evolution of the microlayer thickness [12, 50, 51, 53–61]. Their results agree with the early observations regarding the microlayer shape and dynamics. In particular, the water nucleate pool boiling experiments performed by Jung and Kim [12] and Surtaev and co-authors [62, 63] describe in details the dynamics of the microlayer and dry spot: As the bubble nucleates the microlayer and the dry spot appear. The microlayer extends radially as fast as the bubble radius but it reaches a plateau a few moments later and then decreases slowly whereas the dry spot spreads over the surface slower and continuously. The microlayer is depleted when the dry spot reaches the microlayer outer edge. The contact line starts to move back towards the center of the bubble base until it reaches a zero radius at departure. A similar dynamics is observed in numerical simulations [64]. Jung and Kim [59] show that effects of surface tension, residual flow and non-hemispherical bubble shape should be considered into the initial microlayer thickness models in order to obtain a good agreement with the experimental data.

The contribution of microlayer evaporation to the bubble growth is still a controversial subject. Therefore, a full characterization of the heat transfer phenomena within this region is required. In particular, the knowledge of instantaneous temperature field at the bubble base, heat flux from the wall and heat transfer coefficients are of great importance. Several groups have addressed these parameters through numerical or experimental approaches [12, 55, 64–96]. Jung and Kim [12, 55] show that for a given time the heat flux through the microlayer extension is roughly constant and it drops significantly at the dry spot. The wall temperature increases with increasing the microlayer thickness. Just after nucleation, the temperature decreases at the center of the bubble and then increases as the dry spot is formed. The contribution of microlayer evaporation to the bubble growth accounts for about 17% of the total wall heat flow rate for water pool boiling at atmospheric pressure with a subcooling of 3 K and 20 K superheating. The highest heat transfer coefficient occurs during the microlayer evaporation stage of the bubble cycle near the contact line [12, 88]. The microlayer evaporation has been also investigated in flow boiling [89, 90, 94]. The authors partitioned the heat flux through the heating wall into the contributions to the vapor and liquid. They report that the contribution of the microlayer evaporation increases with the wall superheating, reaching about 50% at the CHF. A similar trend has been obtained in pool boiling simulations [97] and in experiments with water and ethanol [54, 75, 86].

Yabuki and co-authors [72, 73, 82] also confirm a significant contribution of the microlayer evaporation to the bubble growth in pool boiling (about 50%), however, this value remains roughly constant with wall superheating, which contradicts the other results. The subcooling was found to be unimportant to the microlayer evaporation. Several other authors also report a significant contribution of the microlayer evaporation up to about 50% of the total wall heat flow [50, 98–102].

Indeed, the contribution of the microlayer evaporation seems to be significant but different trends can still be found. One should, however, take great care with the comparisons since the Jakob number, $Ja = c\left(T_w - T_{sat}\right)/\mathcal{L}$, wettability and surface roughness may differ significantly. For instance, the experiments of Kangude and Srivastava [103] suggest that the bubble growth mechanism changes from microlayer evaporation in hydrophilic surfaces to contact-line evaporation-driven in hydrophobic surfaces. They also indicate that while a microlayer exists in hydrophilic boiling surfaces [42, 55, 57, 59], it no longer exists in hydrophobic surfaces. In microlayer evaporation mode heat is transferred from the wall to the vapor-liquid interface through the microlayer whereas in contact line the heat is mainly transferred by transient conduction from the superheated liquid surrounding the bubble [37, 103], see Fig. 2.4. Similar results have been reported in other studies [104–106]. It has been also shown that surface characteristics do have an impact on the microlayer thickness and heat transfer [104, 107–111].

The microlayer formation, extent, thickness, shape and depletion underneath a single bubble is widely discussed in the current literature. Colin and co-authors [7, 112–114] have made a significant contribution to the understanding of the near-wall phenomena in boiling. The results of a numerical simulation of Hänsch and Walker [115] suggests the microlayer depletion as a result of the dry spot dewetting, which contradicts other approaches where this is linked to the film evaporation [44, 64]. Their result also show an interesting feature in the microlayer geometry: the presence of a bump (dewetting ridge, see subsection 2.1.8) near the contact line formed in the early stages of the bubble growth. A similar shape has been found in subsequent boiling simulations [7, 116].

Chen et al. [57, 61] and Utaka et al. [86] observed experimentally a bumped shape but in a different bubble growth stage and location. They report a wedged-shaped microlayer during the initial stage of bubble growth, similar to other studies [44, 51, 59]. As the bubble approaches its departure, a bent shape near the microlayer outer edge appears. The authors suggest that this happens when the buoyancy force becomes larger than the liquid inertial effects.

Giustini and co-authors [92, 117, 118] performed a parametric study with the following remarks: As the bubble tends to become flatter with increasing the liquid density, the microlayer extent increases but without significant effect on its thickness. On the other hand, an increase in surface tension forms a more spherical bubble with smaller microlayer thickness and extent. Microlayer thickness increases with increasing viscosity but has unimportant effect on its extent. The bubble growth rate and the evaporative thermal resistance have been shown to be key features to microlayer formation [115, 119]. Giustini and co-authors [92, 117, 118] confirm that the evaporative thermal resistance becomes as important as the conductive one for an equivalent additional liquid film thickness of about 90 nm.

The results obtained for water pool boiling experiments by Zou [56, 120] are very surprising, as the authors say themselves. In subcooled conditions, they kept a single bubble at a quasi-steady state by balancing out evaporation and condensation rates. The interesting fact and also in contradiction to the observations mentioned above, is that a wetted bubble base is observed in hydrophilic and hydrophobic surfaces. That's it, the bubble nucleates above the heating surface and creates a microlayer that wets the entire bubble base. No dry spot is observed at the wall. As the bubble grows the microlayer thickness decreases and the dry region may appear at the wall, spreading radially afterwards. Molecular dynamics simulations performed by the authors revealed a similar behavior. A strong interaction between the liquid molecules and the solid surface near the interface has been identified. This forms a region of high liquid density near the wall, which increases the pressure locally. Thus, the bubble nucleates in the region above where the pressure is lower.

2.2.1 Physics of microlayer formation

To understand the formation of a microlayer, one can first take a look at the film deposition by a liquid meniscus receding in a capillary slot (Fig. 2.3a). The meniscus with a velocity U_b and a radius of curvature r_c leaves behind a liquid film of the thickness δ_0 between the walls and the vapor. In Fig. 2.3b we have an analogous case for boiling, where the liquid microlayer is created during the bubble growth, when the bubble foot edge expands with the radial velocity U_b. This analogy is justified by the fact that the Reynolds number $Re = \rho_l U_b \delta_0 / \mu_l$ is very small, so the inertial effects do not control the liquid thickness, just like the capillary case. The δ_0 value is thus controlled by the competition of the viscous and surface tension forces only. The viscosity tends to increase δ_0 to reduce the hydrodynamic stress in the microlayer. On the other hand, the surface tension tends to homogenize the meniscus radius of curvature thus leading to the decrease of δ_0.

The δ_0 expression can be determined from the following scaling analysis. In Fig. 2.3a, the interface

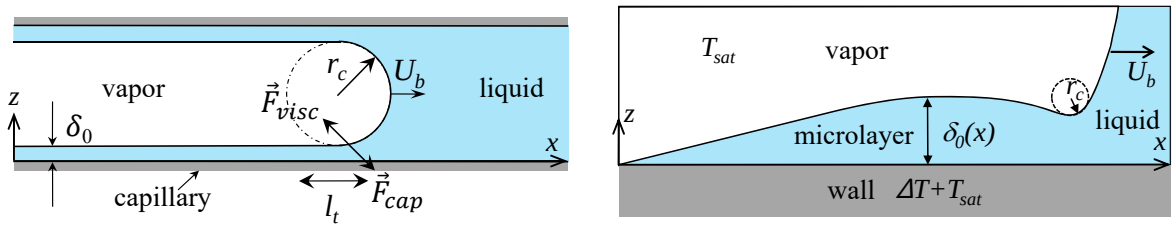

(a) Film deposition in meniscus receding.

(b) Microlayer formation during bubble growth.

Figure 2.3: Formation of a thin liquid film by receding liquid surface.

curvature changes from zero to r_c^{-1} within a length scale l_t of the transition region. Thus, curvature in this transition region scales as $\partial^2\delta/\partial x^2 \sim \delta_0/l_t^2$. At the end of the transition region, the curvature should match the meniscus curvature r_c^{-1}, which results in the first scaling relation

$$r_c^{-1} \sim \delta_0/l_t^2. \tag{2.28}$$

The viscous force F_{visc} acting in this transition region with the wall area $A_{visc} = Ll_t$ (where L is the slot depth in the direction perpendicular to the page) scales as

$$F_{visc} = \mu_l \frac{\partial u_x}{\partial z} A_{visc} \sim \frac{\mu_l U_b}{\delta_0} L l_t. \tag{2.29}$$

The capillary force F_{cap} acting in the transition region can be calculated as a product of its cross-section $A_{cap} \sim L\delta_0$ and the Laplace pressure $\sigma\delta_0/l_t^2$:

$$F_{cap} \sim \sigma L \delta_0^2 / l_t^2 \tag{2.30}$$

With $F_{visc} = F_{cap}$, the second scaling relation can be obtained. By solving them for δ_0, one gets

$$\delta_0 = C\, r_c Ca^{2/3}, \tag{2.31}$$

where the meniscus capillary number is

$$Ca = \frac{\mu_l U_b}{\sigma}, \tag{2.32}$$

and C is a numerical coefficient of the order of one. The deposited microlayer thickness is therefore a function of the capillary number. A similar analysis also holds for the boiling case, where r_c is the radius of curvature at the bubble foot edge, as illustrated in Fig. 2.3b. The coefficient C has been first found by Landau and Levich [121] for the case of the flat plate pulled from a liquid pool and then by Bretherton [122] for a meniscus receding in a capillary tube. Its precise value is $C = 1.337 \pm 0.001$.

2.2.2 Description of the flow in the microlayer

In Fig. 1.3b, δ_0 and r_m are of order of μm and mm, respectively. Therefore, one mentions that $\delta_0/r_m \ll 1$ with viscous effects being predominant over the inertial. The two-dimensional lubrication approximation theory is thus suitable to study the dynamics the microlayer thickness. More specifically, the set of equations presented by [30, 123] to study the dewetting by evaporation in 2D can represent all the relevant physical effects encountered in our experiment. The governing equation

$$\underbrace{\frac{\partial \delta}{\partial t}}_{\text{I}} + \frac{\partial}{\partial x}\left\{\frac{1}{\mu}\left[\underbrace{\frac{\delta}{2}(\delta + 2l_s)\frac{\partial \sigma}{\partial x}}_{\text{II}} + \underbrace{\frac{\delta^2}{3}(\delta + 3l_s)\frac{\partial \Delta p}{\partial x}}_{\text{III}}\right] - \underbrace{U_{cl}\delta}_{\text{IV}}\right\} = -\underbrace{\frac{\mathcal{J}}{\rho_l}}_{\text{V}}, \tag{2.33}$$

is written in the frame of reference of the contact line that recedes with the speed U_{cl} with respect to the wall. Eq. (2.33) includes all the hydrodynamic effects aforementioned. The main (capillary) term is (III). The Marangoni flow induced by surface tension gradients appearing in the microregion (and only in microregion for the pure fluid) because of the variation of the interfacial temperature (2.21) (term II). The contributions to the fluid flow due to the contact line receding and the evaporation are described by the terms (III) and (IV), respectively. The ridge growth is described by the term (I). Two more equations are required to fully describe Eq. (2.33). One is to represent Δp and another is for $\mathcal{J}$. The later is expressed by Eq. (2.17), whereas the interface temperature is given in Eq. (2.21), which includes the Kelvin, vapor recoil and interfacial thermal resistance (discussed in section 2.1). The singularity associated with the moving contact line is thus regularized [14]. The pressure jump across the interface is determined with Eq. (2.19).

Two physical phenomena can lead to the microlayer thinning over time: its evaporation and/or the radial liquid flow in it. The latter flow is expected to have a minor effect on $\delta(t)$ because of strong viscous stresses within the most of the microlayer extent (except in two areas: near the contact line and near the bubble foot edge). Therefore, one can neglected it in many cases. This is equivalent to neglecting the terms (II), (III) and (IV) in Eq. (2.33) that reduces to the equation

$$\mathcal{L}\rho_l \frac{\partial \delta}{\partial t} = -k_l \frac{\Delta T(t)}{\delta}. \tag{2.34}$$

widely used for the description of the microlayer evaporation.

By rearranging Eq. (2.34) so that δ can be integrated from $\delta_0 = \delta(t = 0)$ up to $\delta = \delta(t)$, with an average ΔT, one obtains

$$\delta_0(x) = \sqrt{\delta(x)^2 + \frac{2k_l \Delta T}{\mathcal{L}\rho} t}. \tag{2.35}$$

Therefore, by using Eq. (2.35) with a given microlayer profile $\delta(x)$ at the moment t and an average ΔT over time, the profile of the initial microlayer thickness $\delta_0(x)$ can be obtained considering the effects of microlayer thinning by evaporation. We emphasize that this approach can be applied only in the microlayer region where the fluid flow is negligible.

2.3 Bubble growth regimes: microlayer and contact line

One can distinguish two typical bubble growth modes: microlayer and contact line. The first takes place when the microlayer is present. The heat is transferred from the wall towards the liquid-vapor interface thus evaporating the liquid throughout the whole microlayer extent as depicted in Fig. 2.4a. In contact line mode, the microlayer does not exist and a strong evaporation maximum occurs only near the contact line as illustrated in Fig. 2.4b. This latter regime predominates for water at high

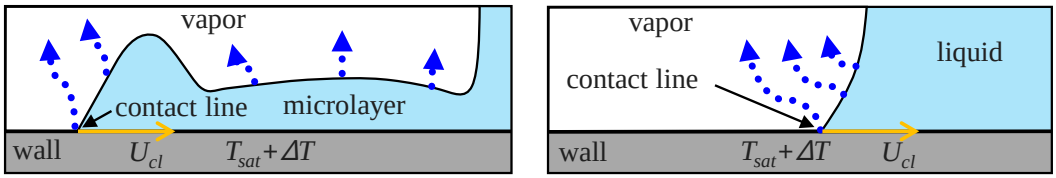

(a) Microlayer regime.

(b) Contact line regime.

Figure 2.4: Two kinds of interface shapes near the foot of growing bubble in nucleate boiling.

pressures and for refrigerants. A transition between microlayer and contact line regimes has been studied recently by Schweikert et al. [9]. They state that the microlayer formation depends on a critical value $U_{b,crit}$ of what they call "dewetting velocity" (which sounds like the velocity of the contact line) but which is in fact analogous to the liquid meniscus velocity with respect to the solid which is denoted here U_b. $U_{b,crit}$ increases with ΔT. They state the following conditions

$$\underline{\text{Microlayer regime:}}\ U_b \geq U_{b,crit}, \tag{2.36}$$

$$\underline{\text{Contact line regime:}}\ U_b < U_{b,crit}. \tag{2.37}$$

These two parameters determine the presence or not of the microlayer and thus the evaporation mode near the wall. Fischer et al. [111] also show results indicating that ΔT, latent heat of vaporization and interface velocity are relevant parameters to determine the microlayer formation. The numerical simulations of Urbano et al. [7] in the transition from contact line and microlayer boiling regimes show the existence of apparent contact angle threshold under which a microlayer will be formed. This threshold increases linearly with $Ja^{1/3}Ca^{1/3}$. Recently, Bureš and Sato [8] have modeled numerically this transition as a dewetting process with phase change. From Eq. (2.23) and establishing that this transition occurs when $\theta_{app} = 0$, the authors show that

$$U_{b,crit} = C\frac{\sigma}{\mu_l}\theta^3, \tag{2.38}$$

where $C \approx 0.01$ is used to fit the experimental data of Schweikert et al. [9]. A good agreement has been obtained with the numerical results of Urbano et al. [7] and experimental results of Schweikert et al. [9] for $Ja \lesssim 75$.

2.4 Near-wall heat transfer

The near-wall heat transfer at bubble growth in boiling is of great importance to determine the heat flux through the microlayer during the bubble growth. Figure 2.5 illustrates the heat transfer in the boiling surface with thickness given by h. One can understand the heat transfer in the film as follows. Part of the energy inserted in the boiling surface (by means of Joule or local heating) will be accumulated as internal energy thus raise up its temperature. As indicated by the horizontal arrows, radial flux through h can occur, depending on the temperature distribution on the wall. At the upper and lower surfaces, the heat fluxes q''_p and q''_l establish the amount of heat in $\mathrm{W/m^2}$ being exchanged at these interfaces, respectively. The later is the most important quantity in the wall heat transfer analysis. It represents the heat that provides evaporation of the liquid at the vapor-liquid interface. The subscripts l, p and w refer to liquid microlayer, porthole and wall boiling surface, respectively.

2.4.1 Determination of the heat flux toward the liquid

The wall heat transfer model presented here is based on Kenning and Yan [124], also used by Sielaff [125] for the study of pool boiling heat transfer on a thin heating wall (a thin film, of ITO in our case).

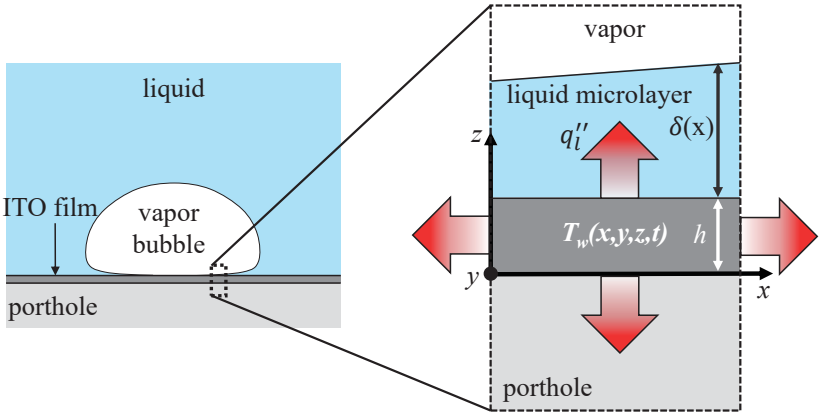

Figure 2.5: Schematics of the heat transfer at the boiling surface.

The temperature distribution $T_w = T_w(x, y, z, t)$ inside the wall obeys the transient heat diffusion equation

$$\rho_w c_w \frac{\partial T_w}{\partial t} = k_w \left(\frac{\partial^2 T_w}{\partial x^2} + \frac{\partial^2 T_w}{\partial y^2} + \frac{\partial^2 T_w}{\partial z^2} \right) + J, \tag{2.39}$$

where ρ_w, c_w and k_w represent the density, specific heat and thermal conductivity of the film, and J is the volume heat generation produced in the film either by Joule heating or IR radiation absorbtion. Time is represented by t, and x, y and z are the cartesian coordinates on boiling surface as shown in Fig. 2.5. The L.H.S of Eq. (2.39) represents the heat accumulation whereas the three first terms in the R.H.S stand for the heat diffusion. One can obtain mean values by integrating Eq. (2.39) from zero to h in the z direction, which thus reads

$$\frac{1}{h}\int_0^h \rho_w c_w \frac{\partial T_w}{\partial t} dz = \frac{1}{h}\int_0^h k_w \left(\frac{\partial^2 T_w}{\partial x^2} + \frac{\partial^2 T_w}{\partial y^2} + \frac{\partial^2 T_w}{\partial z^2} \right) dz + \frac{1}{h}\int_0^h J dz, \tag{2.40}$$

where all physical properties are considered invariable in space and time. Eq. (2.40) becomes

$$h\rho_w c_w \frac{\partial \bar{T}_w}{\partial t} = h k_w \left(\frac{\partial^2 \bar{T}_w}{\partial x^2} + \frac{\partial^2 \bar{T}_w}{\partial y^2} \right) + \int_0^h \frac{\partial}{\partial z}\left(k_w \frac{\partial T_w}{\partial z} \right) dz + \int_0^h J dz, \tag{2.41}$$

where

$$\bar{T}_w(x, y, t) = \frac{1}{h}\int_0^h T_w(x, y, z, t) dz$$

is the height-averaged temperature. Considering that film thickness h is very small (typically, $h < 1\,\mu$m), and the heat fluxes are large, the temperature variation across the film is minor and $\bar{T}_w(x, y, t)$ can be assimilated to the temperature measured experimentally at the bottom of the film with an IR camera. By mentioning that $q'' = -k_w \partial T_w/\partial z$ represents the heat flux, one gets at the boundary $z = h$ the corresponding heat flux $q''|_{z=h} = q_l''$ towards the microlayer, and at $z = 0$ the heat flux $q''|_{z=0} = q_p''$ towards the porthole, one can simplify Eq. (2.40):

$$h\rho_w c_w \frac{\partial T_w}{\partial t} = h k_w \left(\frac{\partial^2 T_w}{\partial x^2} + \frac{\partial^2 T_w}{\partial y^2} \right) - (q_l'' - q_p'') + q_0'', \tag{2.42}$$

where

$$q_0''(x, y) = \int_0^h J(x, y, z) dz, \tag{2.43}$$

is the equivalent surface heat flux induced externally by Joule heating or by the IR laser. Hereafter, we drop the bars over T_w for simplicity. By rewriting Eq. (2.42), one can determine the heat flux towards the liquid as

$$q_l'' = q_0'' + q_p'' + \underbrace{hk_w\left(\frac{\partial^2 T_w}{\partial x^2} + \frac{\partial^2 T_w}{\partial y^2}\right)}_{q_d''} - \underbrace{h\rho_w c_w \frac{\partial T_w}{\partial t}}_{q_a''}. \tag{2.44}$$

where q_d'' and q_a'' represent the heat diffusion and heat accumulation in the wall, respectively. Eq. (2.44) can be applied everywhere on the boiling surface (at any time moment) with or without the bubble growth. In its R.H.S, q_p'' and q_0'' need to be determined whereas the last three terms (heat diffusion and accumulation) can be obtained from the transient 2D temperature distribution on the boiling surface given by IR thermography measurements, for instance. In the works of Kenning and Yan [124] and Sielaff [125], $q_p'' = 0$ was assumed. However, if a porthole is used, $q_p'' \neq 0$ and one needs to determine its contribution to q_l''.

2.4.2 Heat transfer in the microlayer

Generally speaking, as the fluid flow effect on the heat transfer can be neglected because a small microlayer thickness, the temperature $T_l = T_l(x, y, z)$ inside the liquid (here: inside the microlayer) obeys the heat diffusion equation

$$\rho_l c_l \frac{\partial T_l}{\partial t} = k_l\left(\frac{\partial^2 T_l}{\partial x^2} + \frac{\partial^2 T_l}{\partial y^2} + \frac{\partial^2 T_l}{\partial z^2}\right). \tag{2.45}$$

The heat capacity of the microlayer can be neglected, as stated by Cooper and Lloyd [44], given that

$$\rho_l c_l \delta \frac{\partial T_l}{\partial t} \ll k_l \frac{\partial T_l}{\partial z}. \tag{2.46}$$

Therefore, the transient term on the L.H.S drops and the stationary heat conduction equation applies. Next, because of a small microlayer thickness, a linear temperature distribution along z can be assumed so the heat flux in the microlayer is [124]

$$q_l'' = k_l \frac{\Delta T}{\delta} \tag{2.47}$$

is constant along z. If the interfacial thermal resistance is taken into account, $T^i > T_{sat}$. Substituting T_{sat} in Eq. (2.47) (where $\Delta T = T_w - T_{sat}$) by T^i given by Eq. (2.12), one gets

$$q_l'' = k_l \frac{\Delta T}{\delta + k_l R^i}. \tag{2.48}$$

2.4.3 Heat transfer in porthole

One can obtain q_p'' by solving the transient, 3D heat conduction in the porthole such as proposed by Jung and Kim [12, 55]. The energy conservation equation for the porthole is expressed as

$$\rho_p c_p \frac{\partial T_p}{\partial t} = k_p\left(\frac{\partial^2 T_p}{\partial x^2} + \frac{\partial^2 T_p}{\partial y^2} + \frac{\partial^2 T_p}{\partial z^2}\right). \tag{2.49}$$

where ρ_p, c_p and k_p represent the density, specific heat and thermal conductivity of the porthole. Adequate boundary conditions must be applied to represent the real conditions.

For each time moment and each point on the $z = 0$ plane, the solution of Eq. (2.49) gives the 3D temperature distribution in the porthole. The wall heat flux to the porthole is:

$$q''_p(x, y, t) = -k_p \frac{\partial T_p}{\partial z}\bigg|_{z=0}. \tag{2.50}$$

The relevant scale is the depth of the temperature perturbation penetration into the porthole

$$l_p = \sqrt{D_p t}, \tag{2.51}$$

where $D_p = k_p/(\rho_p c_p)$ is the thermal diffusivity of the porthole and t is the characteristic time scale. Another important theoretical concept is the effusivity of the porthole, which is expressed as

$$e_p = \sqrt{\rho_p c_p k_p}. \tag{2.52}$$

It represents the ability of the porthole to exchange thermal energy with its surroundings.

2.5 Experimental issues

2.5.1 Multiple bubbles versus single bubble

In the current experimental boiling investigations two approaches are used: multiple bubbles [81, 90, 91, 94, 95, 126, 127] or a single isolated bubble [55, 59, 103, 128–133]. At low superheating, only a few spots on the boiling surface will be activated and one can usually obtain isolated single bubbles on an ordinary surface if the spacing between bubbles is sufficient large [55, 59]. However, at intermediate to high superheating multiple bubbles start to nucleate in a very close proximity. Hydrodynamics interactions between bubbles, coalescence and thermal interaction between nucleation sites occur [134–137]. The single bubble assumption is no longer valid. The dynamics of the collective bubbles behavior including merging, rewetting and spreading of the dry spots over the heating surface is usually observed [91, 94, 126]. The dynamics in the macroregion is also complex, including vertical and horizontal coalescence [136, 138–140] and condensation in subcooled cases [87, 95, 109].

To produce a single bubble at high superheating one needs a local triggering mechanism, known as artificial nucleation site [131, 133, 141–143]. Cavities and local heating are the two main approaches to create an artificial nucleation site. In the first, a tiny cavity (with dimensions much smaller than the bubble radius) is made on the surface to create a preferential spot for bubble nucleation [54, 74, 134, 136, 138, 141, 144, 145]. For instance, Shoji and Takagi [141] fabricated conical, cylindrical and reentrant geometries on copper disks. Pressing diamond bit and micro-electrical discharge machining were used for fabrication. Other advanced methods, such as micro-fabrication [138, 144, 145] laser ablation [130, 146] and Focused Ion Beam [147] can be used to create the cavity. In local heating, a power source is used to heat up locally the surface. Lasers with energy absorbing materials [88, 130, 141, 148] or hot jets [57] have been used. In the case of laser heating, optical elements are used to adjust the beam diameter in order to obtain small heating spots [88, 149]. A combination of both, *i.e*, cavities heated up locally, are also used to trigger a bubble [54, 130, 141, 150].

The first reason for current investigations are still using both multiple and single bubble approaches can be related to the boiling crisis. There is an undergoing discussion if its triggering mechanism is a local phenomenon associated to the dynamics of a single bubble or a collective one, in which the interaction between bubbles is a key feature to trigger the crisis. While several results point to the irreversible dry pots as nuclei for triggering the boiling crisis, we have a limited knowledge of its nature. Some studies with multiple bubbles indicate a collective mechanism of the crisis [91, 94, 126, 151, 152], while others show the dry spot spreading of a single bubble as the key factor [74, 128, 153]. The second reason is that in order to study the near-wall phenomena, high spatial resolution in both numerical and experimental approaches is required. Thus, one has to concentrate in a single bubble approach.

2.5.2 Choice of the boiling surface

Indium-tin oxide (ITO), a mixture of In_2O_3 and SnO_3(alloy of In doped SnO_2), is an electrical conductive material with low sheet resistance, usually hydrophilic, transparent in visible and opaque in IR spectra widely used in electronic displays, aircraft cockpit windows and solar photovoltaic cells. Its electrical and optical properties make the ITO suitable as a heater in boiling experiments [55, 59, 60, 81, 90, 91, 94, 95, 127], where non-intrusive optical measurements of the wall and near-wall phenomena are required. The ITO surface is usually in contact with the working fluid [12, 60, 95]. Electrical conductive busbars can provide contact between the ITO and the wires, which are connected to a power supply. The ITO is heated up by Joule effect to produce the bubbles on its surface [81]. Its thickness ranges from tens of nm up to about 1 μm [55, 61] so it has negligible thermal capacity and temperature gradient through its thickness. The active boiling area is of tens of mm [69, 78, 126] with sheet resistance from 2.5 up to 10 Ω/sq [59, 79]. The ITO surface usually has an equilibrium contact angle for a water droplet less than 90° [78, 126, 154] with a nanoscale roughness [55, 68, 154].

The opaque heaters in both visible and infrared spectra have also been employed in boiling investigations. Fischer et al. [111, 150] used a chromium coating as a heater. Theofanous et al. [65] used a titanium film as heating surface. Kim et al. [155] used a polyamide tape on the top of a silicon porthole. An IR opaque paint deposited on the tape served as the boiling surface. One should note that in these cases direct measurements of the microlayer thickness cannot be performed.

The ITO and the other heating materials are usually coated on optical portholes [12, 60, 81]. Calcium fluoride (CaF_2) and sapphire are the two most common materials [55, 61, 68, 78, 95, 150, 156]. Both are transparent to visible light. However, calcium fluoride has a flat and high transmittance curve (>90%) throughout the visible and infrared spectra (from 0.2 to 6 μm) whereas sapphire has an uneven spectral transmission from 3 to 5 μm, the typical bandwidth of mid-IR cameras used in boiling thermography [9, 12, 81]. Its transmittance drops from 95% at 3 μm to 60% at 5 μm. As discussed by Bucci et al. [81], sapphire partially absorbs and emits the radiation from the boiling surface. As a result, the radiation received by the camera is significantly modified by the porthole. Modeling of the radiation is required to obtain the correct temperature of the boiling surface [81]. With CaF_2, one can obtain a direct measurement of the temperature thanks to its high and even transmittance in IR [9, 12, 55, 150]. However, CaF_2 is a fragile material while sapphire has a much higher mechanical strength and a thermal diffusivity of almost twice that of CaF_2. Nevertheless, several experiments have been successful with CaF_2 [12, 55, 59, 150, 157, 158]. Magnesium fluoride (MgF_2) porthole can also be considered. It has similar optical properties as CaF_2 but better mechanical properties.

2.6 Experimental techniques

2.6.1 Microlayer thickness measurement

- Laser interferometry (LI): In this technique a monochromatic light is shone into the microlayer usually from below through a transparent heater. The light reflected from each interface will interfere with each other creating bright and dark fringes which geometry depends on the thickness of the microlayer as shown in Fig. 2.6a. Bright and dark fringes stand for constructive and destructive interference, respectively [159, 160]. The microlayer thickness is then computed counting the fringes. Jawurek [42, 43] was the pioneering in using this technique in boiling experiments and several groups worldwide still keep using it to measure the microlayer thickness in boiling experiments [51, 55–59, 61, 86, 120, 161, 162]. This method is extensively employed to measure the microlayer thickness in boiling experiments. Its features are the following: The minimum measurable thickness is roughly 100 nm for water microlayer. This value also represents the thickness resolution of measurements [43]. The uncertainty on the thickness depends on the precision of the spatial calibration and on the spatial resolution. The long coherence length of lasers creates spurious interference from the

thicker porthole and can contaminate the fringe map. A 2D thickness profile of the microlayer can be obtained from the fringe pattern. A spatial calibration is required to detect the location where each fringe take place.

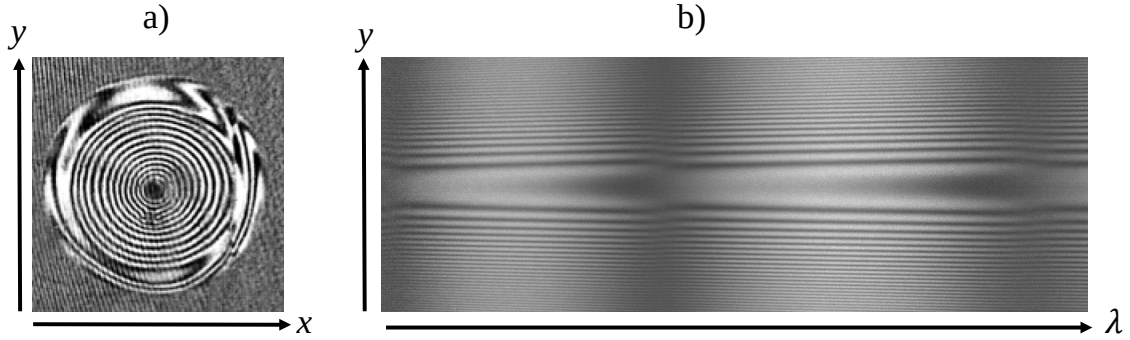

Figure 2.6: Light interference. a) fringe pattern in LI [162] and b) WLI.

- Laser extinction: This method consists on measuring the intensity of the transmitted light through the microlayer, which decreases with increasing the thickness due to the light absorption in the microlayer. Beer Lambert's equation applies in these cases, which is defined as given in Eq. 4.30. Utaka et al. [54, 75] and Morokuma et al. [161] used an infrared laser owing the light absorbance of water and ethanol within the IR spectrum. Morokuma et al. [161] measured a minimum thickness of 300 nm. The thickness can be computed for each pixel, which improves its resolution. However, in boiling this technique has a major practical difficulty. The head of the laser beam has to be immersed into the bulk and attached to the vapor bubble; see Utaka et al. [54]. Otherwise, light would be absorbed by the liquid above the bubble. This, first, requires extra care to not damage the optical laser head because of the hot liquid in contact with it and second, it is too intrusive to the bubble behavior.

- Infrared interferometry: Kim and Buongiorno [163] have measured the microlayer thickness by infrared interferometry. The working principle is the same as the one explained for laser interferometry. However, an infrared camera records the fringes within the IR spectrum. The minimum measurable thickness was about 1 μm. However, this is 10 times higher than LI. Infrared spectrum is indeed not advantageous to measure thinner thicknesses because $\delta \propto \lambda$.

- Confocal optical sensor: This technique uses a broadband light source (white light) and a set of lenses to disperse the white light into a series of monochromatic beams. Each dispersed light ray is then shone into the film contact with a different wavelength. At the two interfaces which define the film thickness the monochromatic rays get reflected. But only two wavelengths are directed back to a spectrometer through the optical path thanks to the confocal configuration. These two are the wavelengths focused at the upper and lower interfaces of the film thickness. All the others will be out of focus and will not be observed. The spectrometer will then reveal two intensity peaks corresponding to the two wavelengths. One can measure thicknesses ranging from a few μm up to mm [164]. Gong et al. [164, 165] and Zhou et al. [166] have measured the thickness dynamics of an evaporating film and a falling liquid, respectively, using confocal optical sensor. The main limitation of this technique is that the two peak signals overlap when a thin film thickness ($<1\,\mu$m) is measured and the wavelengths can no longer be distinguished. Moreover, only a few (1 to 5) spatial measurements points were obtained by the above mentioned studies. These are important drawbacks for the measurements of the microlayer thickness.

- White light interferometry: Similarly to laser interferometry, the physical principle of this technique is also the observation of light interference. However, a broadband collimated beam is shone into

the film to create a colorful interference pattern instead. There are several different apparatus using this physical principle.

- **Scanning white light interferometry** is widely used in to characterize stationary surfaces [167–170]. This method comprises a controlled and known motion of a reference mirror by an actuator regarding the target surface to change the focal plane at the film contact [168]. A 3D thickness profile of the surface is obtained with the nanoscale precision [169]. However, this and other similar interferometry techniques such as phase shifting and coherence correlation require relative motion of the optics and are thus unsuitable for boiling experiments given the small time scale (ms) of the bubble growth.
- **Spectral white light interferometry** is the second variant. It has no moving parts, then suitable for fast dynamic phenomena. It is also denominated as fringes of equal chromatic order (FECO) [171]. In this work we call it simply as white light interferometry (WLI). In this method, the reflected colored fringes are sent to a spectrometer to be dispersed into wavelength. The output image is the spectrum map of the fringe interference [172, 173] along a line as shown in Fig. 2.6b. In this map, λ axis stands for the wavelength bandwidth and y is the spatial position along the film. Thus, a 1D film profile can be obtained. Connor and Horn [174, 175] have measured successfully film thicknesses with 0.3 nm resolution. Fung et al. [172] and Hou et al. [173] also used WLI to measure wetting films and nanoparticle adsorption, respectively. Fourgeaud et al. [35, 36] have used this technique to measure the thick film thickness in evaporating films. The condition interference is the same as LI. Fringes will not be formed for $\delta \lesssim 100\,\text{nm}$ [43, 176]. This occurs because the film thickness becomes too thin compared to the wavelength of the visible light to form constructive interference. Spikes and co-authors [176–179] then introduced a spacer-layer with known thickness between a thick porthole and the film in a FECO setup. The sum of the two, film and the spacer-layer, is then sufficiently thick to produce interference. Glovnea et al. [179] report measurements of thin lubricant films down to 0.3 nm. It is indeed a complex setup, but to the best of our knowledge WLI has never been used in boiling experiments.

2.6.2 Dry and wet areas

Measurements of phase distribution aim at distinguishing the dry from the wetted by the liquid areas on the heater surface. Two kinds of information can then be obtained: the dynamics of contact line and the dry area fraction.

- Light reflectance: It consists on illuminating the heating surface with a light source and imaging the reflected light from below with a high speed camera. Because the liquid and vapor have different indexes of refraction, the intensity of reflected light (or reflectance) at a given point depends if it is wet or dry. A dry spot will appear brighter than the wet region because of the higher reflectance. One should note that the porthole and the heater should be transparent to visible light. Recently, broadband light sources (white light) have been used for this purpose [180–182].
- IR absorbance: Kim and Buongiorno [163] used an IR camera to detect dry and wetted ares. The principle lies on the difference of IR absorbance between vapor and liquid water. At the dry spot, the low IR absorbance of vapor allows IR temperature measurements from the cooler bulk liquid above the bubble. At the wetted area, a high absorbance of the liquid allows IR measurements from the wetted area. The dry spot appears as a dark spot whereas the wetted region is brighter [80]. The interface between both determines the contact line. In this case the heater and the porthole should both be transparent to IR.
- Total internal reflection: This technique consists on shining a light beam to the boiling surface from below with a given incident angle in which total internal reflection takes place at the dry spot

whereas it is mostly transmitted at the wet area. Thus, dry spots appear brighter than the wet area. Again, this is possible thanks to the difference in indexes of refraction for liquid and vapor, which determines two different critical angles according to Snell's law. Several experiments have used successfully this method [12, 55, 154, 156, 183–185].

- IR thermography: This technique consists on measuring the temperature on an IR-opaque heater surface with an IR camera. Because the dry spots are hotter than the wet regions and promote a very low heat exchange, one can distinguish these two by the gradients in temperature or heat flux. Even though the contact line location is less precise compared to the previous approaches, one can still observe the dynamics of dry spots [87, 95, 127, 155]

2.6.3 Wall temperature and heat flux

The heat transfer from the heating surface to the microlayer, dry area and bulk liquid is characterized with the measurements of wall temperature, heat flux and heat transfer coefficients. Below we summarize the most employed techniques to do so.

- Infrared thermography: This technique has been extensively used in boiling experiments. It consists of using an IR fast camera to capture the infrared radiation emitted by the heater [12, 81, 155, 186]. The radiation received by the camera can then be accurately converted into temperature; see IR calibration procedures for ITO and sapphire [81] or CaF_2 [150, 158]. Jung and Kim [12, 55] and Fischer et al. [111, 150] measured the temperature at the bubble base using thin opaque heaters (ITO and Chromium, for instance) deposited on CaF_2 portholes. In this case, the output result is directly the 2D temperature map at the bubble base. The heat flux at the heater surface is determined by solving numerically the transient 3D heat conduction problem within the porthole with the temperature measurements as boundary condition on the top. As mentioned in section 2.5.2, sapphire is also widely used in boiling investigations. In these cases, temperature measurements are not straightforward. Bucci et al. [81] presented a detailed description of the required post-processing to recover temperature and heat flux. Radiation and conduction have to be coupled and solved iteratively. Once temperature and heat flux are computed, local heat transfer coefficient can be determined by Newton's law of cooling.

- Microsensors: Thanks to advanced manufacturing techniques fast micro-temperature sensors have been developed to investigate boiling phenomena. Platinum micro-heater arrays were fabricated to supply a controlled heat flux and measure the surface temperature at the same time [101, 187–190]. Yabuki and co-authors [72, 73, 82, 191, 192] developed a micro-electro-mechanical system (MEMS) sensor consisting of thin film thermocouples with a data acquisition rate of 50 kHz and a spatial resolution of $20\,\mu$m [144].

- Time-Domain thermoreflectance: This technique has been used by Mehrvand and Putnam [88, 149] to determine the local heat flux and heat transfer coefficient during the bubble growth. It consists in measuring the temporal reflectance of the boiling surface. A pump laser beam is used to heat up locally the surface and trigger the bubble. A second laser probes the amount of light that is reflected from the boiling surface which depends on the local temperature by its thermoreflectance coefficient of the heating surface.

2.7 Summary and concluding remarks

In this chapter we have provided a review on the main characteristics of the microscale boiling phenomena. Theoretical features and state of the art research have also been explored. We highlight here

the following remarks on nucleate boiling regime: In the near-wall vicinity, viscous and surface tension forces are predominant and the dynamics in this region is independent of macro hydrodynamics around the bubble. The microlayer can be formed, depending on the surface properties such as wettability, dewetting velocity and wall superheating. Its profile can vary. While most of the experimental approaches show wedged-shapes, numerical simulations depict the presence of dewetting ridge near the contact line. The evaporation of the microlayer can contribute significantly to the overall bubble growth. While some results indicate that the microlayer depletion occurs due to hydrodynamics effects other show that its thinning is due to evaporation. High heat transfer fluxes occur near the contact line. The conclusion here is that the near-wall phenomena still requires more fundamental understanding.

In order to have optical access through the wall to measure the microlayer thickness, transparent portholes and heaters are used. CaF_2 and MgF_2 are both transparent in visible and IR spectra and are thus considered for portholes in this work. ITO films served as heaters in most advanced experimental installations. They are transparent in visible but opaque in IR spectra. They are thus suitable for IR thermography and visible light interferometry. They can also serve as heater either by means of Joule effect or by using IR laser local absorption. In this work, ITO has been chosen as a heater.

Special means are required to produce a single bubble. Our review shows that artificial nucleation site and local laser heating are the most used techniques. In this work, we have chosen to use an IR laser to heat up locally the ITO. More details are given in chapter 3.

A wide range of state of the art experimental techniques employed to study the microscopic features at bubble growth have been discussed. Optical methods are advantageous given that they are non-intrusive and high speed cameras can be used to capture the phenomena with sufficient temporal resolution. Our literature review shows that LI is the most used technique in boiling investigations while WLI is still not explored. Moreover, to the best of our knowledge, we have not found detailed studies on the advantages and disadvantages of each one of these techniques for microscopic boiling studies. In this work, LI and WLI features are therefore revealed by means of a comparison study in static conditions using a novel experimental setup. To measure the wall temperature, the use of an IR camera is the most suitable. Side-wide shadowgraphy can be used to measure the macroscopic behavior of the bubble. These methods are discussed in details in chapter 4.

Chapter 3

Experimental Apparatus

3.1 Introduction 27
3.2 The boiling cell 27
3.2.1 Boiling surface: Practical issues and solutions 28
3.3 ITO surface state 31
3.4 Optical apparatus arrangement 31
3.4.1 Visible-IR light beam splitter 32
3.5 Characterization of the IR laser heating 34
3.5.1 Source heat flux 35
3.5.2 Measurement of ITO absorption 36
3.5.3 Measurement of the angle of incidence of IR laser 37
3.5.4 Measurement of angle β 39
3.5.5 Measurement of heat source profile 39
3.6 Microlayer heating estimation 39
3.7 Experimental protocol 40
3.8 Summary and concluding remarks 41

3.1 Introduction

In this chapter, we present the experimental apparatus. It consists of a boiling cell and a series of optical elements devoted to perform microscopic scale measurements during the growth of a single bubble in boiling. Here, we give focus on the design of the boiling surface (porthole and heating surface) and on the characterization of the heating mode. It is noteworthy to mention that the whole experimental installation herein presented is novel. Therefore, the implementation and validation of the optical instrumentation apparatus as well as the design of the boiling surface have been developed during the framework of this thesis.

3.2 The boiling cell

The experimental apparatus is illustrated in Fig 3.1. The boiling cell comprises a water pool boiling chamber at atmospheric pressure surrounded by a temperature homogenizer and a boiling surface at the bottom. A thermal bath provides continuous flow of heated oil to the inlet of the homogenizer in order to minimize the temperature gradients inside the pool. The water pool boiling is isolated from the oil by sealed walls. Thermal insulated hoses connect the inlet and outlet of the homogenizer to the thermal bath. The external walls of the homogenizer are also insulated to minimize heat losses to the

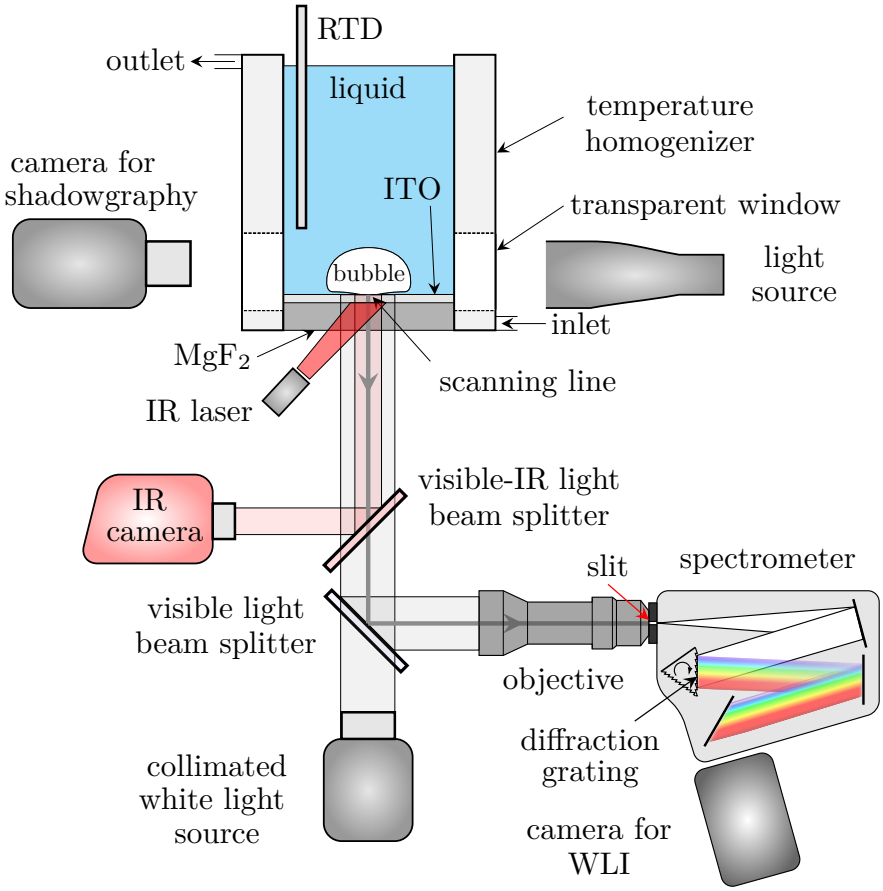

Figure 3.1: Schematics of the boiling cell and optical measurement apparatus.

environment. A resistance thermal detector (RTD) is placed inside the boiling chamber to monitor the temperature of the liquid pool. Four lateral optical windows transparent to visible light provide optical access to the macro dynamics of the bubble.

The boiling surface consists of a roughly 950 nm thick ITO deposited on a magnesium fluoride (MgF_2) optical porthole. MgF_2 is transparent in visible and IR spectra whereas ITO is transparent in visible but opaque in the IR bandwidth. A continuous IR laser triggers a single bubble on ITO by local heating from below thanks to the high absorbance of ITO to IR radiation. An optical fiber guides it from the laser to the head collimator positioned below the cell.

3.2.1 Boiling surface: Practical issues and solutions

The ITO film is used as a heater and is placed on the liquid side of the porthole. As ITO is an electrical conductor, we attempted initially to combine uniform electrical heating by Joule effect with local laser heating to trigger a single bubble. There are, however, many noteworthy practical issues that arise in this case such as ITO adhesion to the porthole surface and electrochemical effects. Several preliminary tests under boiling conditions have been performed to understand these issues in order to ensure a stable bubble generation during experiments. These issues and solutions are presented here.

Figure 3.2 shows our initial design of the porthole in the holder. A rectangular ITO film deposited on a 25 mm diameter and 3 mm thick porthole. An internal hole on the holder fits the porthole diameter. The red ring around the porthole is a high-temperature silicone which is used to glue the porthole to the holder and seal it to avoid water leaking from the pool. This holder is then installed

below the boiling cell as illustrated in Fig. 3.1. In Fig. 3.2a, silver (Ag) busbars are deposited on the ITO. They provide electrical contact between the ITO and the wires, which are brazed to the busbars. The wires are then connected to a power supply, which heats up the ITO by Joule effect. Silicone is used to cover the wires and the busbars in order to protect the them from the water.

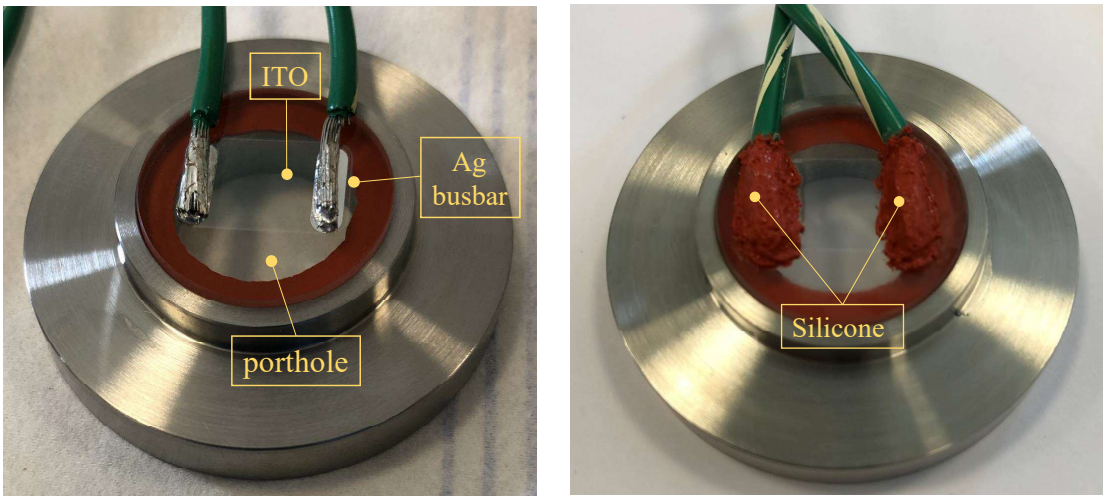

(a) ITO deposited on the porthole.

(b) Silicone protects the busbars and wires.

Figure 3.2: Initial design of ITO deposited on a porthole. Ag busbars provide electrical contact between the ITO and the wires for Joule heating.

The main practical issues and solutions are described as follows:

- Quality of ITO deposition. We have initially requested ITO samples from two well-known companies with expertise on ITO deposition. They are: Diamond Coatings (UK) and Solems (France). Unfortunately, both have not attained our technical requirements. Significant irregularities on the ITO thickness and on its adhesion were observed. This has lead us to a partnership with the Laboratory of physics of interfaces and thin films (LPICM, Laboratoire de physique des Interfaces et des couches minces) at Institut Polytechnique de Paris, aiming at a more detailed study on the ITO deposition. A large number of the cycles of film depositions and tests under boiling conditions have been performed in order to determine the right deposition procedure that provides high ITO adhesion to the porthole. At LPICM, the ITO is deposited by radio frequency magnetron sputtering. Each one of theses issues and the solutions for them are discussed below.

- Porthole fragility. CaF_2 was initially considered as a porthole as it was used by other research groups in similar experiments [59, 150]. Because of the CaF_2 fragility, it does not handle mechanical stresses and can easily fracture. As discussed by Bucci et al. [81], thermal stresses imposed during boiling might also cause the fracture of CaF_2. During our trial test campaigns, fissures on CaF_2 have been observed in boiling and many samples have been damaged during handling. This led us to switching to MgF_2 for safety purposes, whose Young's modulus (the ratio between stress and strain) is roughly twice that for CaF_2 (see Table C.4). Such fissures have not been observed on MgF_2 even during high local heating, which ensured safe operation for boiling experiments.

- Liquid electrochemical reactions. If the wires or busbars are in contact with the water inside the pool they work as electrodes and promote water electrolysis under Joule heating. Therefore, in order to avoid the production of hydrogen inside the boiling cell we cover the busbars and the wires with silicone as depicted in Fig. 3.2b.

- Substrate dissolution. At boiling conditions, the temperature of the MgF_2 porthole can be considered as the saturation temperature of water, $T_{sat} \approx 100°C$. At this temperature, one needs to take into consideration the MgF_2 solubility in water. It is roughly 0.1 g/L at 25 °C [193]. Since solubility increases with temperature, the dissolution of MgF_2 at T_{sat} increases. This can be seen in Fig. 3.3b. When a part of the porthole is exposed to water as depicted in the design of Fig. 3.2a, particles of MgF_2 are deposited on the ITO surface due the MgF_2 dissolution. To solve this issue, we cover the whole surface with ITO in order to protect it from water.

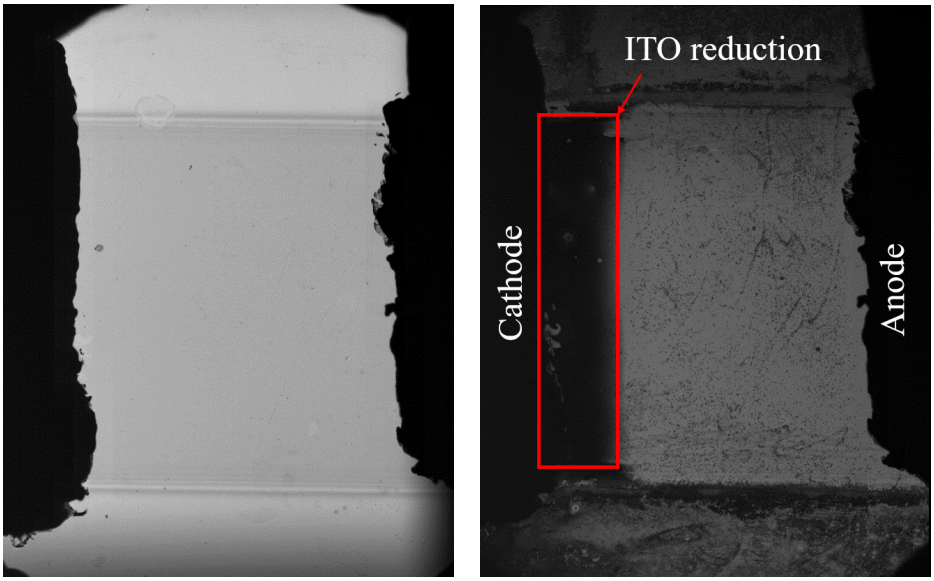

(a) Before. (b) After.

Figure 3.3: ITO before and after the boiling test with Joule heating.

- ITO adhesion. We first deposited a rectangular ITO film on the optical porthole as in Fig. 3.2a by using a mask. However, our experiments showed important peeling off near the film edges under boiling conditions. The ITO adhesion gets weaker in this region. We believe this is related to an edge effect during the deposition process. By covering the whole porthole surface with ITO, the use of a mask is no longer required and ITO presented a stronger adhesion throughout the whole surface of MgF_2 during boiling experiments. No peeling off was observed.

- ITO reduction. It is well known that ITO can undergo through electrochemical reduction from oxide to metallic when submitted to anodic or cathodic polarization [194–196] if Joule heating is used to heat up the ITO. The consequences include significant changes in its optical, electrical and morphological properties such as loss in transparency and conductivity as well as increase in absorbance. The chemical reduction reads [195]

$$In_2O_3 + 6H^+ + 6e^- \rightarrow 2In + 3H_2O; \tag{3.1}$$

$$SnO_2 + 4H^+ + 4e^- \rightarrow Sn + 2H_2O. \tag{3.2}$$

The RHS of Eqs. (3.1,3.2) shows the products from the ITO reduction, which correspond to tin (Sn) and indium (In) opaque metallic particles. ITO turns into a gray-dark color as a result of its reduction [194]. This can be seen in Fig.3.3b for our experiment with Joule heating, where a dark region near the cathode has been formed and covers roughly 20% of the ITO area. The power supplied by DC was 1 W during a few minutes, which corresponds to roughly 1.6 Volts and 0.6

Amperes. This represents an input power of $10\,\mathrm{kW/m^2}$, which was insufficient to onset the nucleate boiling. To avoid this issue, we adopt only local laser heating.

Given the issues and solutions aforementioned, our final design for the boiling surface consists simply of ITO deposited on the whole surface of the MgF_2 porthole. The heating source is provided solely by the local IR laser. Our preliminary boiling tests show that the ITO absorption is high enough to overcome the nucleation energy barrier and trigger a single bubble.

3.3 ITO surface state

One has to have an ITO surface as homogeneous as possible to avoid contact line pinning at imperfections (holes) which can lead to highly heterogeneous dynamics of contact line motion during the bubble growth. It is also helpful to know the heater surface state. For this purpose, the surface topography measurements by means of atomic force microscopy (AFM) have been performed at SPEC/CEA with the gracious help of Cindy Rountree. It is well known that a thermal treatment can change the surface roughness (through changing the grain size) of ITO films [197]. To check the effects of annealing, the surface was analyzed twice: before and after the annealing. The heating protocol for the annealing is as follows. The sample is placed inside an oven where the temperature is risen progressively, with a rate of $3\,\mathrm{K/min}$. When it reaches the $50\,^\circ\mathrm{C}$, and $70\,^\circ\mathrm{C}$, the temperature is kept constant before the next rise for 60 min, and 20 min, respectively. The last increase reaches $120\,^\circ\mathrm{C}$, where it is kept constant during 120 min. Then, the oven is turned off and the sample cools down to ambient temperature. As shown by Wu and Chiou [198], the ITO reflectance in IR (at 3-5μm) increases with increasing annealing temperature thus decreasing the ITO emissivity, as defined in Eq. (4.69). This is not advantageous for the IR thermometry measurements as ITO emissivity is low $(0.1 - 0.3)$. Therefore, higher annealing temperatures have been avoided.

The ITO surface is depicted before and after annealing in Figs. 3.4a and 3.4b, respectively. The respective surface profiles along a line show that the annealing reduces the grain size and the root mean square roughness of the ITO film. The later is 13 nm for the sample without annealing and 11 nm with annealing. The surface is highly homogeneous in both cases. The absence of holes (larger than 100 nm) ensures a smooth contact line motion. Annealing effect is minor; we thus chose to use no ITO thermal treatment for boiling experiments.

3.4 Optical apparatus arrangement

The optical arrangement is also depicted in Fig. 3.1. Three simultaneous and synchronous optical measurements are performed aiming at revealing the near-wall microscale features of boiling and the macro dynamics of the bubble. WLI, IR thermography and sidewise shadowgraphy measure the microlayer spatially varying thickness, 2D temporal distribution of temperature on the bubble base and the macroscopic diameter of the bubble, respectively.

The WLI optical apparatus consists of a collimated white light, a visible light beam splitter, a sigma 800 mm focal length objective installed at the entrance of a spectrometer (Horiba iHR550) and a gray-scale camera (Phantom v2011) at its output. A LED white light source model Solis-3C (Thorlabs) provides illumination from below towards the bubble while the beam splitter redirects the reflected fringe pattern created by light interference at the interfaces defined by MgF_2, ITO, microlayer and vapor towards the spectrometer.

A visible-IR beam splitter transparent to visible and reflective to the bandwidth of our IR camera (FLIR X6901sc, 3-5 μm) is used to reflect the IR radiation emitted by the ITO towards the IR camera during the bubble growth while letting the visible light passing through it. Therefore, it works as a spectral splitter. Because of room constrains the IR camera cannot be installed below the boiling cell.

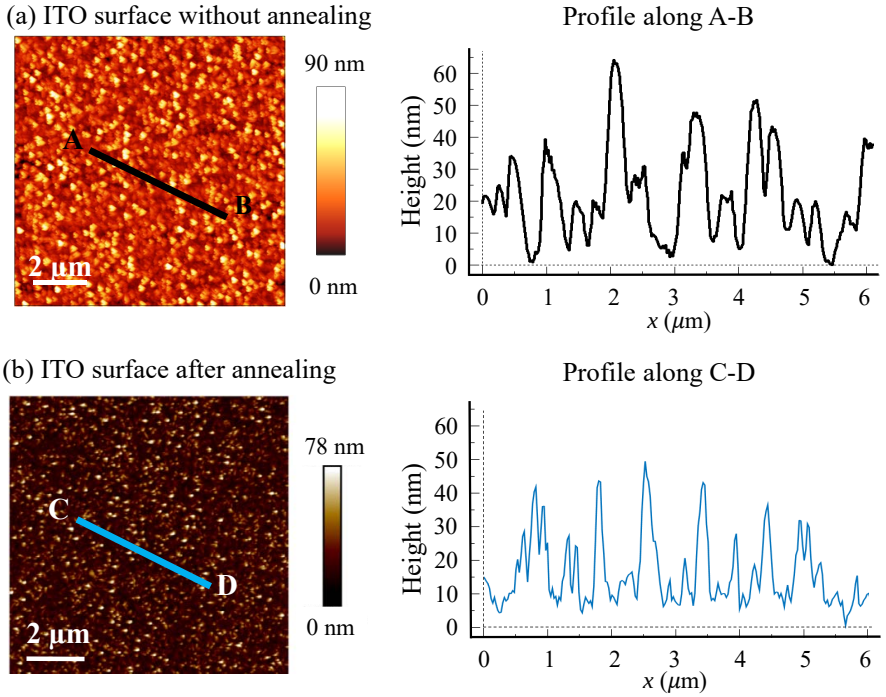

Figure 3.4: ITO surface imaged by atomic force microscopy with the help of Cindy Rountree at SPEC/CEA Paris-Saclay.

In addition, this arrangement avoids damage of the IR camera in case of a leakage from the cell. Both beam splitters have an incident angle of roughly 45°. More details of the visible-IR beam splitter are given in section 3.4.1.

The shadowgraphy consists of a telecentric collimated LED light source (Opto Engineering model OE LT CL HP 024-W) for background illumination and a fast camera (Photron SA3) positioned at opposites sides of the cell. Therefore, the source illuminates the bubble while the camera images its macro dynamics. The details of the three technique mentioned here are discussed in chapter 4.

3.4.1 Visible-IR light beam splitter

In this work, we perform synchronous and simultaneous IR thermography and WLI to measure the microlayer thickness and the associated heat transfer on the wall, respectively. One then needs a visible-IR beam splitter to reflect the IR radiation from the ITO towards the IR camera whereas it lets the visible light passes through to reach the WLI apparatus as shown in Fig. 3.5. This kind of mirror is also called as hot mirror. Gold or silver mirrors are typically used as hot mirrors because they have a reflectance of up to 0.98. However, such ordinary mirrors are not suitable because they also reflect visible light. Other commercially available hot mirrors do transmit visible light but they do not reflect enough within the bandwidth of our IR camera. A high reflectance, is a must as the radiation reaching the IR camera is limited by the low emissivity of ITO. Here, the reflectance and transmittance of the hot mirror are denoted as $\mathcal{R}_{hm}$ and $\mathcal{T}_{hm}$ and defined as given by Eq. (4.23) and Eq. (4.26), respectively.

Sibin et al. [199] developed a visible-IR spectral beam splitter consisting of a multilayer coating of ITO/Ag/ITO. The optimized by them thicknesses of ITO and Ag were 60 and 21 nm, respectively, with the transmittance of 0.88 within visible and reflectance of 0.9 in IR. It is well known that ITO reflects well the IR whereas being transparent to visible. A nano-metric layer of Ag is usually sandwiched between two layers of ITO in a multilayer coating structure to enhance $\mathcal{R}$ for IR applications [200, 201].

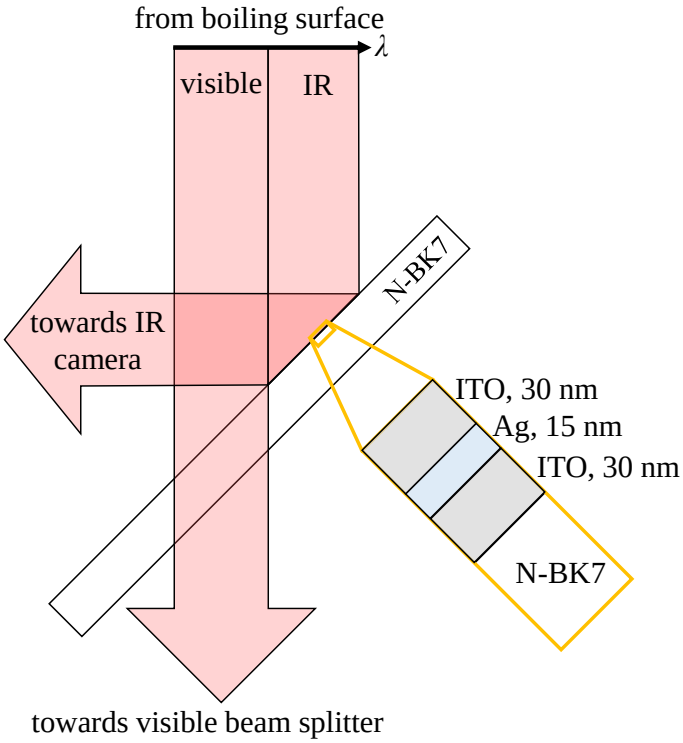

Figure 3.5: Design of visible-IR beam splitter (hot mirror).

Based on the ITO/Ag/ITO film stacking idea [199], our own visible-IR beam splitter was designed at LPICM by P. Bulkin. The ITO and Ag thicknesses were optimized to be 30 and 15 nm, respectively. These thicknesses enhanced $\mathcal{R}$ in IR and $\mathcal{T}$ in visible spectrum for our ITO and Ag optical properties. An N-BK7 optical glass transparent to visible light served as a substrate for deposition. Fig. 3.6 depicts $\mathcal{R}_{hm}$ within IR and $\mathcal{T}_{hm}$ in visible spectrum as functions of λ obtained by Fourier-transform infrared spectroscopy (FTIR), performed at Institut d'Optique (Palaiseau) by S. Vassant (SPEC/CEA Paris-Saclay), and visible spectroscopy using our WLI apparatus, respectively. The angle of incidence is 45°. One can observe a high $\mathcal{T}_{hm}$ throughout the visible spectrum whereas providing a $\mathcal{R}_{hm} \simeq 0.92$ within the IR camera bandwidth.

A high value of $\mathcal{R}_{hm}$ is a requirement to ensure a good signal to noise ratio (SNR) for the IR thermography measurements. The SNR, expressed in dB, is computed as

$$\mathrm{SNR} = 10 \log_{10}(\bar{I}/\sigma), \tag{3.3}$$

where $\bar{I}$ and σ stand for the average and standard deviation of the IR intensity recorded by the camera, respectively. From the IR intensity depicted in Fig. 3.7 we obtain an SNR of 29.25 dB. This value is similar to other experimental approach using IR thermography in boiling studies [125]. The high $\mathcal{R}_{hm}$ thus ensures a high SNR so that the IR camera can used for the thermography measurements in boiling experiments.

In Fig. 3.6a, $\mathcal{T}$ varies significantly within the visible spectrum. In WLI, this effect is compensated during the image post-processing as discussed in section 4.1.8. Its use however does reduce the intensity of light reaching the CCD of the camera for WLI, limiting the exposure time of image acquisition. Nevertheless, it does not change the pattern of the fringe map because the WLI optical system is focused on the bubble base, situated far enough from the IR-visible beam splitter. For the IR thermometry, roughly 8% of the IR radiation emitted by the ITO is therefore not reflected towards

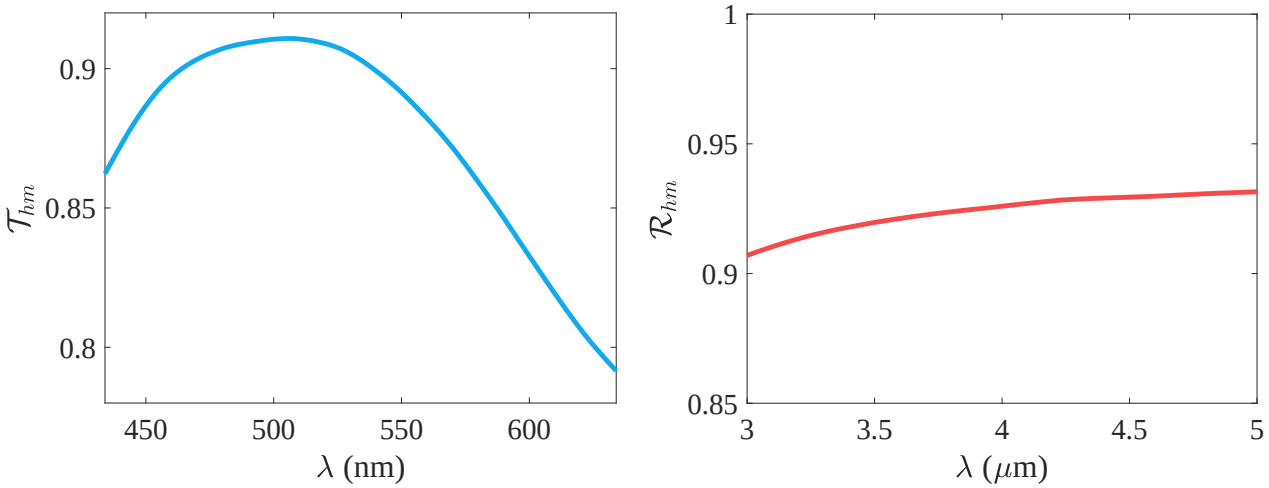

(a) Transmittance in visible spectrum.

(b) Reflectance within the bandwidth of IR camera measured by FTIR by S. Vassant (CEA/SPEC).

Figure 3.6: Transmittance and reflectance of the IR-visible beam splitter at an incident angle of 45°.

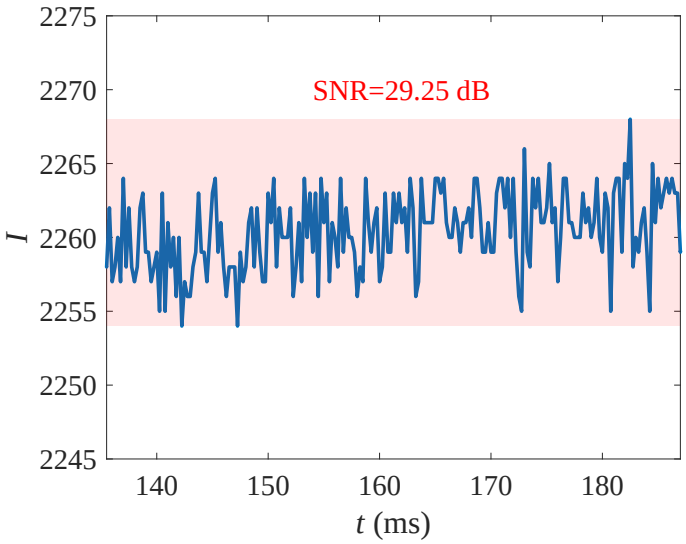

Figure 3.7: Signal to noise ratio(SNR) of the IR camera for a fixed pixel.

the IR camera by the visible-IR beam splitter. This is taken into account during the calibration of the IR camera and it has no practical effect on the temperature measurement. One should note that the substrate and the ITO/Ag/ITO films are of optical quality with a sufficient thickness uniformity and surface flatness so that imperfections are minor and do not impact the IR measurements.

3.5 Characterization of the IR laser heating

The IR laser (Changchun New Industries Optoelectronics, model FC-W-1208B-10W) emits continuously the irradiation at $\lambda = 1.208$ μm. The laser head consists of an optical collimator which allows the user to adjust the beam size. An optical fiber provided by the manufacturer connects the collimator to the IR radiation supply. Once the laser is enabled, a display shows the electric current of the laser. The output laser power $q_{i,IR}$ is a function of the laser current as shown in Fig. 3.8. The laser head is

equipped with a visible laser beam, which is used to guide the IR beam positioning and size.

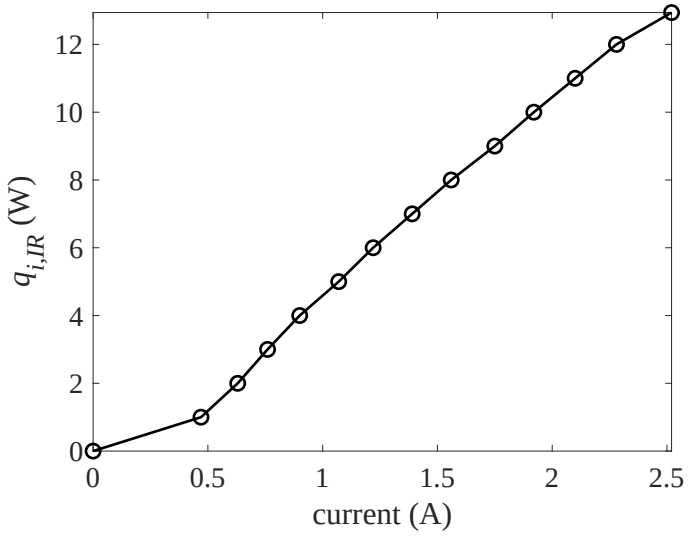

Figure 3.8: The IR laser beam power $q_{i,IR}$ as a function of the laser current as given by the manufacturer.

3.5.1 Source heat flux

One needs to know the heat flux distribution over the heating surface given by the laser heating. Fig. 3.9a presents an illustration of the heat source imposed on ITO. The IR laser beam strikes the ITO with an incidence angle θ. The cartesian coordinates are represented by x, y and z in the plane $x - y$ on the ITO. The coordinate system is centered at the point corresponding to maximum wall heat flux (center of the beam spot).

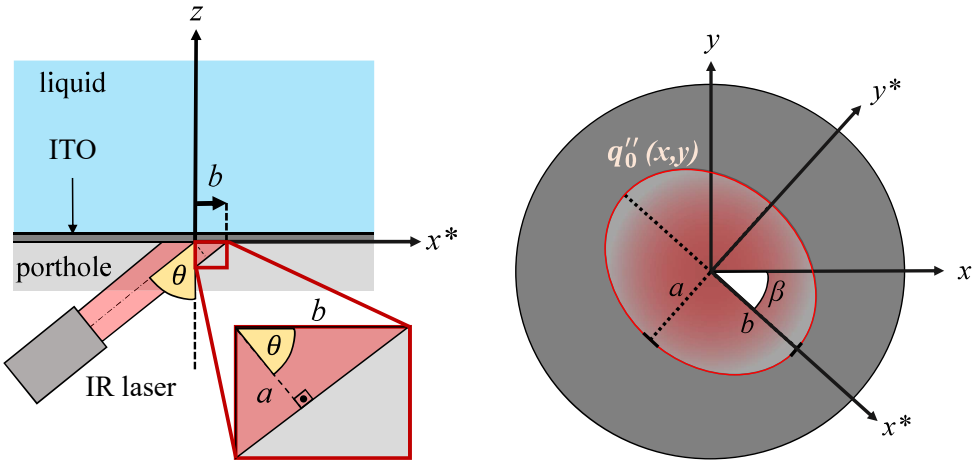

(a) Lateral view of beam incidence on ITO.

(b) Top view of beam spot on ITO.

Figure 3.9: Schematics of the heat source created on ITO by the IR laser.

The distribution of $q_0''(x, y)$ related to the volume IR laser absorbed power via Eq. (2.43), depends on the laser beam profile and θ whereas its amplitude is a function of the ITO absorbance and the incident power $q_{i,w}$. Therefore, one writes

$$q_0''(x, y) = Q\hat{q}_0''(x, y), \tag{3.4}$$

where Q is the maximum flux value in the laser center, and $\hat{q}_0''(x,y)$ the normalized heat source profile measured with the beam profiler (subsection 3.5.5). The ITO absorbance $\mathcal{A}_w$ is defined as

$$\mathcal{A}_w = \frac{q_0}{q_{i,IR}}. \tag{3.5}$$

One can get the total absorbed power q_0 by integrating $q_0''(x,y)$ over the ITO area as

$$q_0 = \int q_0''(x,y)dxdy. \tag{3.6}$$

Substituting Eq. (3.4) into Eq. (3.6)

$$q_0 = Q \int \hat{q}_0''(x,y)dxdy. \tag{3.7}$$

Substituting Eq. (3.7) into Eq. (3.5) and solving for Q, one obtains

$$Q = \frac{\mathcal{A}_w q_{i,IR}}{\int_S \hat{q}_0''(x,y)dxdy}, \tag{3.8}$$

where $q_{i,IR}$ is given in Fig. 3.8. Therefore, by determining $\mathcal{A}_w$ and $\hat{q}_0''(x,y)$ in two different experiments, one obtains $q_0''(x,y)$ by using Eqs. (3.4,3.8). We discuss next $\mathcal{A}_w$ while $\hat{q}_0''(x,y)$ is determined in section 3.5.5.

3.5.2 Measurement of ITO absorption

A dedicated optical power measurement installation (Fig. 3.10) has been conceived to determine $\mathcal{A}_w$ for the MgF_2 porthole with the deposited ITO film at $\lambda = 1.208\,\mu$m. One measures the power of the incident $q_{i,w}$, reflected $q_{r,w}$ and transmitted $q_{t,w}$ beams by using an IR optical power meter. The sensor consists of a Germanium photodiode detector model 918D-IR (Newport Corporation) with spectral range of 0.78 – 1.8 μm. The minimum power it can measure is 5 nW and its uncertainty is $\pm 2\%$ at $\lambda = 1.208\,\mu$m. An optical density filter is placed after the IR laser to decrease the beam power in order to ensure that the power density at the sensor and at the ITO are below the damage thresholds. A convergent lens focuses the transmitted beam into the sensor's area. Convergent lens and power sensor are both mounted on a on a rotatable plate so it can be moved near the reflected beam to measure $q_{r,w}$. The MgF_2/ITO sample is mounted on a rotatable platform with angular graduation so that the required θ can be imposed.

The energy conservation law for the laser beam after the filter reads

$$q_{i,w} = q_0 + q_{r,w} + q_{t,w}. \tag{3.9}$$

Dividing Eq. (3.9) by $q_{i,w}$ it yields

$$\mathcal{A}_w = 1 - \mathcal{T}_w - \mathcal{R}_w, \tag{3.10}$$

where $\mathcal{T}_w = q_{t,w}/q_{i,w}$ and $\mathcal{R}_w = q_{r,w}/q_{i,w}$ are the transmittance and reflectance, respectively.

The measurement procedure is as follows. First, without MgF_2/ITO in the optical path, $q_{i,w}$ can be measured. Next, the MgF_2/ITO is introduced between the laser and the IR power sensor with an incident angle θ with respect to the beam, as shown in Fig. 3.10. The transmitted power is then measured. The last step consists in displacing the mounting plate towards the reflected beam (as shown by the arrow in Fig. 3.10) to measure $q_{r,w}$. The incident power is kept the same during the measurements. The filter and the convergent lens have no effect on $\mathcal{A}_w$ as they are present in the optical path for all three measurements.

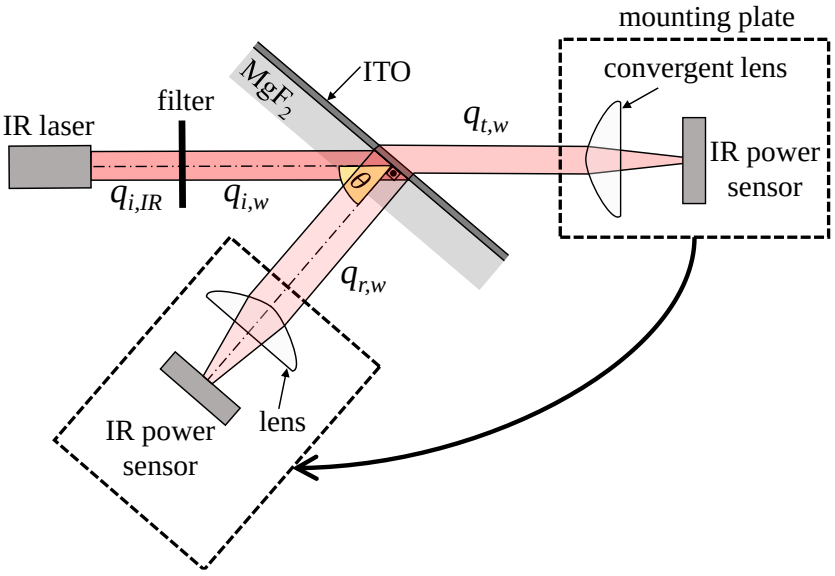

Figure 3.10: Illustration of the optical installation to determine $\mathcal{A}_w$.

Two practical issues should be mentioned. First, in order to avoid the ITO damage produced by heat accumulation, the data is acquired within a few seconds and then the laser is turned off. Second, the environment in which the measurements are performed (illumination, equipment, operator, etc) also emits IR radiation and thus contributes to the power being measured by the sensor. To compensate it, a small power from the environment, q_{env}, is measured with the laser switched off. One can then correct $q_{i,w}$, $q_{r,w}$ and $q_{t,w}$ by subtracting q_{env} from each of three measured quantities.

Figure 3.11a shows $\mathcal{A}_w$ as a function of θ. The ITO absorption increases with θ because the optical path through ITO also increases with θ. The absorption reaches approximately 43% and 50% at θ of 15° and 45°, respectively. Our experiments show that $\mathcal{A}_w$ provides enough superheating to overcome the energy barrier for bubble nucleation. The remaining power is mostly transmitted whereas just a small fraction (3 to 5%) is reflected.

The absorbance of the ITO deposited in the same apparatus as the samples used for the boiling experiment but on a thin glass substrate has also been determined by FTIR measurements performed at Institut d'Optique (Palaiseau) by S. Vassant (SPEC/CEA Paris-Saclay). $\mathcal{A}_w$ is determined following a similar procedure as described for the case of IR power sensor. Fig. 3.11b shows A_w as a function of λ for $\theta = 40°$. One obtains $\mathcal{A}_w = 0.6$ at $\lambda = 1.2\,\mu$m. In Fig. 3.11a, $\mathcal{A}_w = 0.49$ for $\theta = 40°$ with the power meter. This difference can arise from the combined experimental error from both measurements and slightly different ITO thickness of the samples. We thus rely on the measurements of IR power meter that can be performed *in situ* with the sample used for the boiling experiment.

3.5.3 Measurement of the angle of incidence of IR laser

To get θ, we use a normalized temperature distribution $\hat{T}^0_w(x,y) = T^0_w(x,y)/T^0_{w,max}$ obtained during the boiling experiment by the IR thermometry measurements. The superscript 0 represents the time moment $t = 0$ just before bubble nucleation and $T^0_{w,max}$ is the maximum temperature. Both ITO and MgF_2 are isotropic in the $x-y$ plane so there is no preferential direction of heat diffusion. Therefore, any isoline of $\hat{T}^0_w(x,y)$ shown Fig. 3.12, should have the same ellipticity f as $\hat{q}''_0(x,y)$. The ellipticity is

$$f = 1 - a/b, \tag{3.11}$$

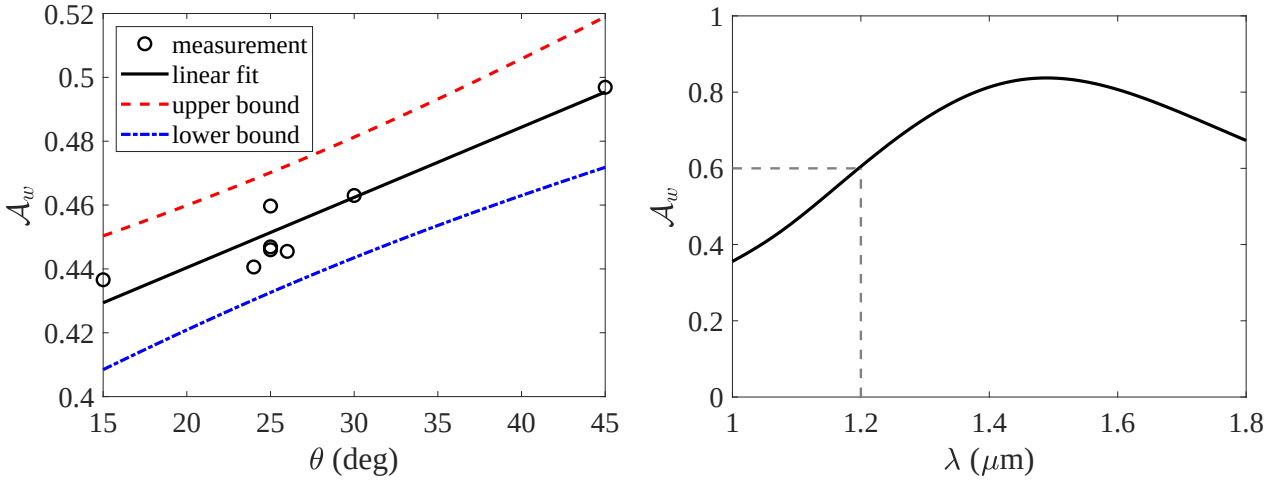

(a) $\mathcal{A}_w(\theta)$ $\lambda = 1.2\,\mu$m measured with IR power meter. (b) $\mathcal{A}_w(\lambda)$ at $\theta = 40°$ measured with FTIR by S. Vassant.

Figure 3.11: ITO absorbance determined by IR power meter and FTIR measurements.

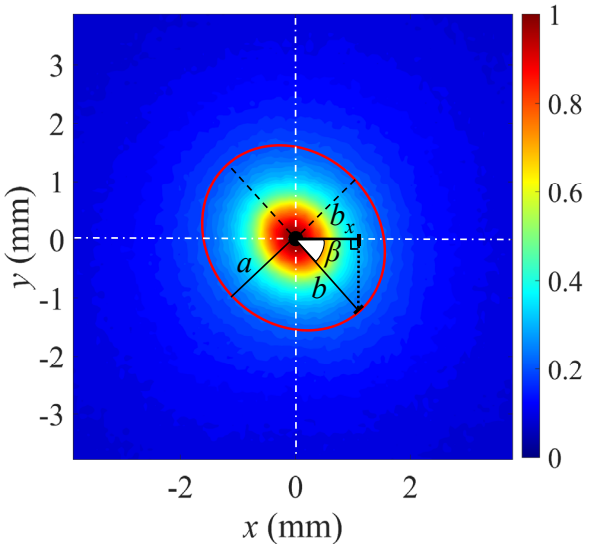

Figure 3.12: Distribution of $\hat{T}_w^0(x, y)$. Its value is shown with a color scale. The ellipse is the $\hat{T}_w^0(x, y) = 0.3$ isoline fit.

where a and b stand for the minor and major half-axes. The ellipticity of the T_w^0 distribution is therefore a measure of θ. From Fig. 3.9a, one can write

$$\theta = \arccos(a/b). \tag{3.12}$$

Therefore, one would have $f = 0$ representing a circle ($a = b$) at $\theta = 0°$.

The isolines are fitted with the ellipses. The root mean square of error for the fit is roughly ± 1 px. Figure 3.13 shows that f is (within the experimental error) the same for different values of $\hat{T}_w^0(x, y)$) for the IR thermography measurements shown in Fig. 3.12. One gets $f \approx 0.15$. From Eq. (3.12) one obtains $\theta = 32°$. By using it, from Fig. 3.11a one determines the ITO absorbance $\mathcal{A}_w = 0.47$.

One can also obtain a rough estimation of θ by the light reflected from the ITO on the optical table. θ is thus given by measuring the vertical Δz and horizontal Δx distances from the beam spot on the table under the boiling surface. Therefore, $\theta = \arctan(\Delta x/\Delta z)$. One finds $\theta = 36°$. Because of

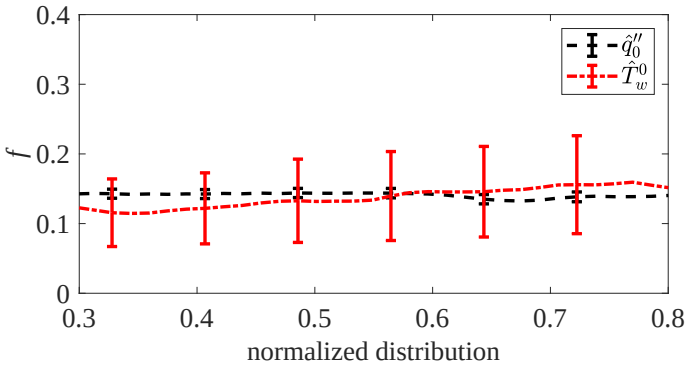

Figure 3.13: Ellipticity f as a function of $\hat{T}_w^0(x,y)$ and $\hat{q}_0''(x,y)$.

a strongly limited room under the porthole (the components are strongly packaged) this measurement is not expected to be precise. We thus rely on θ given by Eq. (3.12).

3.5.4 Measurement of angle β

The laser optical axis is turned with respect to the projection of the x-axis of the IR camera sensor to the heater. Therefore, the heated spot is elongated along a direction (Fig. 3.12) forming an angle β with the x axis. β can be expressed as

$$\beta = \arccos(b_x/b), \tag{3.13}$$

where b_x is the projection of b on the x axis, which is the horizontal axis of the thermal image. Therefore, β can be determined from the semi-major axis of any isoline-fitting ellipse. One finds $\beta = 40°$.

3.5.5 Measurement of heat source profile

An IR laser beam profiler is used to measure $\hat{q}_0''(x,y)$ as shown in Fig. 3.14. The beam profiler, model DAT-BladeCam2-HR-1310 (Dataray), consists of a CMOS sensor with 5.2 μm pixel size, spectral sensitivity of 355 - 1350 nm and 3.1 Mpx resolution. The angle θ and the distance from the laser to the beam profiler are the same as during the boiling experiments. Figure 3.15a depicts $\hat{q}_0''(x,y)$. We proceed similarly to the previous section to fit the isolines of $\hat{q}_0''(x,y)$ with ellipses. In Fig. 3.13, one can verify that f agrees well with the one obtained from the thermal images so that the angle of the beam profiler has been set correctly for the measurements of $\hat{q}_0''(x,y)$.

Figures 3.15 show $\hat{q}_0''(x,y)$ and $q_0''(x,y)$. We have rotated Fig. 3.15b by the angle β determined earlier and translated it with respect to Fig. 3.15a so that both the orientation of the axes of the elliptical flux isoline fit and the flux maximum point match the temperature distribution in Fig. 3.12. This is needed for the future use of the $q_0''(x,y)$ distribution in Eq. (2.44). The heat flux provided by the laser in the experimental run under consideration is $Q = 0.62\,\mathrm{MW/m^2}$ at its maximum (central point).

3.6 Microlayer heating estimation

For the boiling case, the power $q_{t,w}$ transmitted through the ITO film is incident to the liquid, $q_{i,l} = q_{t,w}$. As it corresponds to more than 50% of $q_{i,w}$ one needs to determine if the microlayer heating by $q_{t,w}$ is significant. The ratio of power transmitted through the microlayer with thickness δ to the incident power, $q_{t,l}/q_{i,l}$, is given similarly as in Eq. (4.30) for $\mathcal{T}$. For liquid water, $\varpi_l \approx 125\,\mathrm{m^{-1}}$ [202]

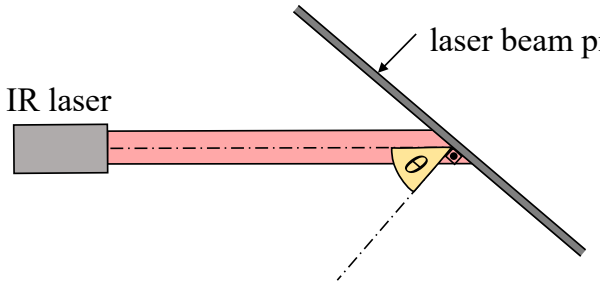

Figure 3.14: Schematics of the optical installation to determine laser beam profile.

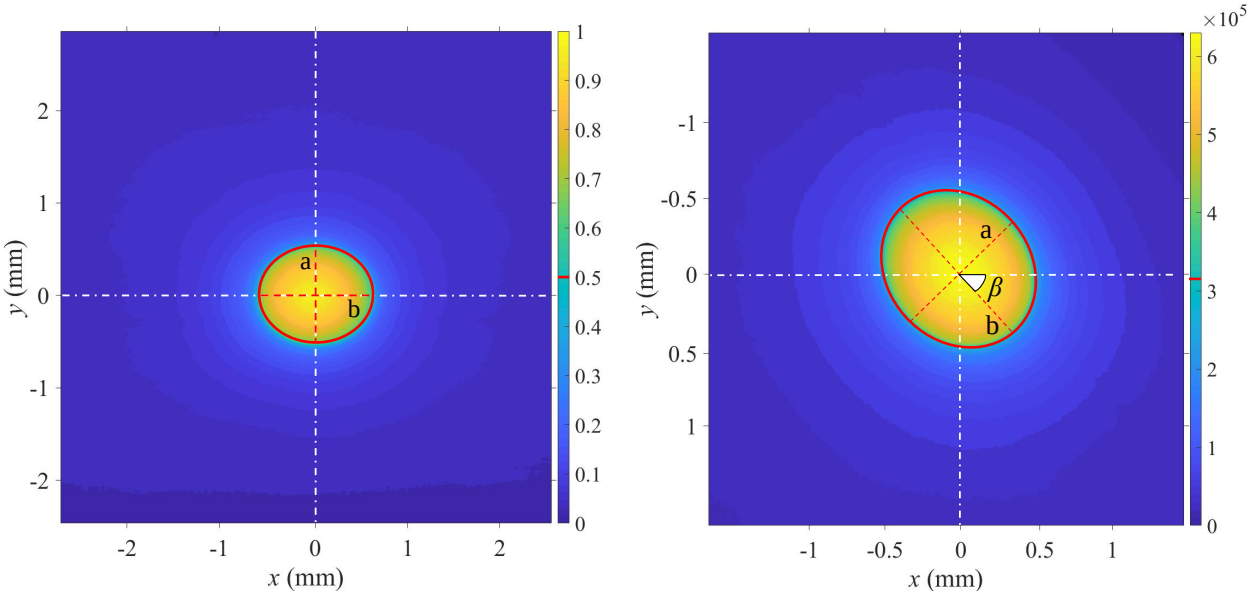

(a) The normalized source flux distribution $\hat{q}''_0(x, y)$ turned in such a way that the larger half-axis is horizontal.

(b) The source flux distribution $q''_0(x, y)$.

Figure 3.15: Heat source profile. The ellipses correspond to the value of flux that is a half of the maximum.

for $\lambda = 1.2\,\mu$m at $T = 27\,^{\circ}$C. With $\delta = 10\,\mu$m, one gets $q_{t,l}/q_{i,l} = 0.999$. Therefore, only about 0.1% is absorbed by the microlayer. This power will produce a temperature increase

$$\Delta T_l = \frac{q_{0,l} t_m}{\rho_l c_l \mathcal{V}_l}, \tag{3.14}$$

where $q_{0,l} = (1 - q_{t,l}/q_{i,l})\mathcal{T}_w q_{i,w}$ is the power absorbed in the microlayer, $\mathcal{V}_l = \pi r_m^2 \delta$ is the microlayer volume, t_m stands for its lifetime(typically $\approx 10\,$ms), ρ_l is the density and c_l is the specific heat of the liquid. Here, r_m represents the radius of the microlayer. One gets $\Delta T_l \approx 0.05\,$K, which is much smaller than the ITO superheating. Therefore, the microlayer heating due to the IR light absorption through its thickness is negligible. The wall heat transfer from the ITO is thus the major mechanism of microlayer heating, which shows the equivalence of the IR laser heating mode to the conventional in boiling heating from below.

3.7 Experimental protocol

The following steps are performed for the boiling test:

- The porthole is glued to the porthole holder.
- The interior of the cell is cleaned by removing the dust with inert clean gas.
- The porthole holder is installed and sealed at the bottom of the cell.
- The cell is filled in with osmosed and deionized water obtained from a milli-Q purification unit at the Physical Chemistry Department (DPC) of CEA Paris-Saclay, kindly supplied by Romain Abadie.
- The thermal bath is turned on. It heats up the cell so that the liquid pool temperature rises from ambient to saturation progressively.
- Once the liquid pool reaches T_{sat}, we wait one more hour before starting the experiment to ensure a homogeneous temperature distribution in the entire liquid pool, which is checked by four auxiliary thermocouples inside the boiling reservoir.
- All three cameras, light sources and the IR laser are turned on. Before triggering the bubble, we wait roughly 15 min for the equipment warming up.
- The pilot beam is then used to adjust the position and size of the IR laser beam at the center of the ITO.
- The IR laser power is turned on. One then locates the heating spot on the ITO film with an instantaneous image of the temperature distribution on the ITO film given by the IR camera as shown in Fig. 3.12.
- We move the laser head along the ITO film using micrometric translation stages to find a preferential nucleation site that triggers a single bubble.
- Once a single bubble is triggered, the cameras are synchronized and focalized to ensure maximum contrast.
- Finally, the synchronous frame acquisition by all three cameras is triggered by an oscilloscope.

3.8 Summary and concluding remarks

In this chapter we have presented the boiling cell and the optical arrangement for measurements. The boiling surface consists of an ITO film deposited on a MgF_2 porthole. ITO film is transparent to visible and opaque to IR irradiation whereas the porthole is transparent in both visible and IR spectrum. Thus, WLI and IR thermography can be employed simultaneously to measure the microlayer thickness and the bubble base temperature, respectively. A visible-IR beam splitter reflects the IR irradiation emitted by the ITO film towards the IR camera while being transparent to visible light. The single bubble is triggered by local heating using an IR laser thanks to the high absorbance of the ITO in IR spectrum.

Practical issues concerning the ITO and the porthole have been addressed and understood by means of preliminary tests to ensure their mechanical, thermal and chemical stability at boiling conditions. Our final design choice lies on the deposition of ITO on the whole surface of MgF_2 porthole. It ensures that both are stable under boiling conditions without impacting the physics of the near-wall phenomena.

The IR heating has also been characterized. Experiments were performed to measure the ITO absorbance and to determine the laser beam profile. The source heat flux induced by the laser heating of ITO is found. In addition, we have shown that, under boiling conditions, the transmitted power through the ITO does not affect the microlayer heat transfer.

Chapter 4

Optics study

4.1 Interferometry . . . 43
4.1.1 Introduction . . . 43
4.1.2 Scalar beam interference theory . . . 45
4.1.3 Reflectance, transmittance and absorbance . . . 48
4.1.4 Intensity of the fringe map . . . 50
4.1.5 Comparison with the electromagnetic theory . . . 51
4.1.6 Spectral and spatial calibration of the setup . . . 52
4.1.7 Fringe geometry as a function of the thickness profile . . . 53
4.1.8 Image processing: Map compensation and symmetry analysis . . . 55
4.1.9 Image processing: Determination of the microlayer thickness $\delta(x)$ in validation 60
4.1.10 Image processing: Determination of microlayer thickness $\delta(x)$ in boiling . . . 62
4.1.11 Validation: air layer thickness without spacer layer . . . 64
4.1.12 Validation: air microlayer thickness with spacer layer . . . 67
4.1.13 Thickness resolution of measurements . . . 68
4.1.14 Fringe quality . . . 70
4.1.15 Microlayer maximum slope limit . . . 71
4.2 Infrared thermography . . . 73
4.2.1 Theory . . . 73
4.2.2 Sources of IR radiation . . . 75
4.2.3 Calibration . . . 77
4.3 Sidewise shadowgraphy . . . 79
4.3.1 Image post-processing . . . 80
4.4 Summary and concluding remarks . . . 81

4.1 Interferometry

4.1.1 Introduction

Optical interferometry is a measurement technique based on the interference phenomenon of light waves which is used, in particular, to measure the thickness of thin films. Two kinds of interferometry techniques can be distinguished: laser interferometry (LI) and white light interferometry (WLI). Laser is monochromatic, so the interference pattern between reflected rays produces a gray-scale image. A large coherency length of lasers that causes unwanted interference patterns from thick optical parts used in the experiment is one of the main drawbacks of LI. On the other hand, WLI produces a colored

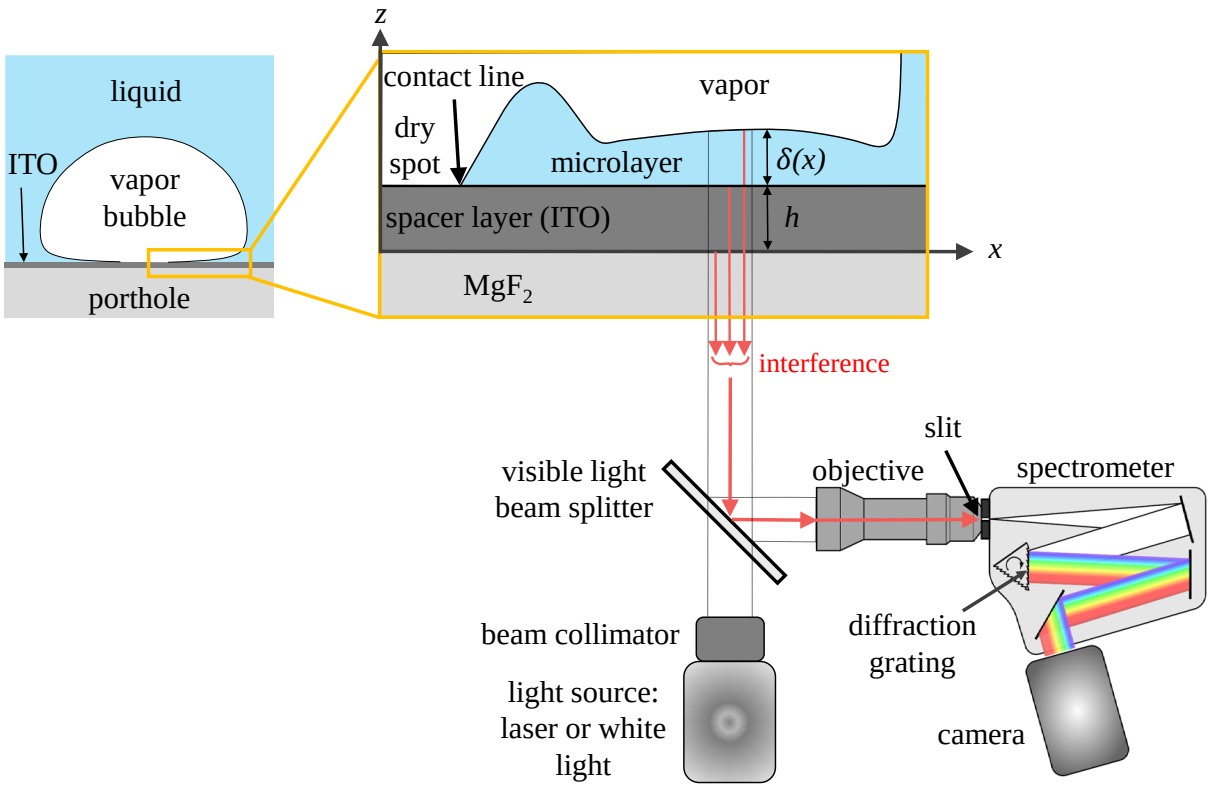

Figure 4.1: Schematics of the interferometry part of the experimental setup fully represented in Fig. 3.1.

image with less spurious interference due to the shorter coherency length of the white light, typically of the order of μm [159].

A schematics of the interferometry installation is depicted in Fig. 4.1. A collimated white light or laser is directed towards the bubble with perpendicular incidence from below. The light rays reflected from the interfaces of MgF_2/ITO, ITO/microlayer and microlayer/vapor interfere with each other thus producing a fringe pattern consisting of constructive and destructive interference. This fringe map is then reflected by the visible light beam splitter. In WLI, it enters into a spectrometer through a slit, which selects a very narrow part of the ITO surface along a line that we call scanning line. It is parallel to the x axis. Its position is tuned in such a way that it passes through the center of bubble at $y = 0$, where y is the coordinate axis perpendicular to the paper plane in Fig. 4.1. The incoming light is then dispersed by a diffraction grating inside the spectrometer. This configuration is called diffraction mode. The output image is a spectral intensity fringe map $I = I(x, \lambda)$ shown in Fig. 4.2a, where the vertical and horizontal axes correspond to wavelength λ' and the spatial direction x' along the scanning line, respectively, both in pixels. The thickness spatial distribution $\delta = \delta(x)$ is obtained from the analysis of the fringe pattern [176, 178]. Thanks to the difference in indexes of refraction of vapor and liquid, the intensity of light reaching the CCD depends on the phase distribution on the wall. Therefore, the dry spot can also be recognized by WLI as a brighter zone in the center while the microlayer region is identified by the presence of interference fringes and is darker. However the microlayer is brighter than the bulk liquid beyond it because the rays of light do not return after the reflection on the vapor-liquid interface in this part, see Fig. 4.2a. One should note that due to the use of the slit, WLI gives the 1D thickness distribution.

The diffraction grating and a mirror are mounted on a turret inside the spectrometer, which can be rotated with a motor. Therefore, one can open the slit to full image width and turn the turret to replace the diffraction grating in the optical path by the mirror to get a 2D representation of the

reflected light as shown in Fig. 4.2b. We call this configuration "mirror mode". The extent of the dry spot, microlayer and the contact line position can be identified by the intensity of the white light reflected from the bubble foot similarly to the diffraction mode.

In LI, the spectrometer is not needed and the image that corresponds to the 2D thickness distribution is directly sent to the camera. The output image is an intensity fringe map $I = I(x, y)$ as shown in Fig. 4.2c. The microlayer thickness can also be obtained from the fringe pattern.

As presented in chapter 3, the ITO works as a heating surface to nucleate the bubble by absorbing the local IR power radiation emitted by a laser. In this section, we explore the ITO's additional feature. It works as a spacer layer reducing the minimum measurable thickness of the microlayer [179]. This will be discussed theoretically and experimentally in more details in sections 4.1.2 and 4.1.12, respectively.

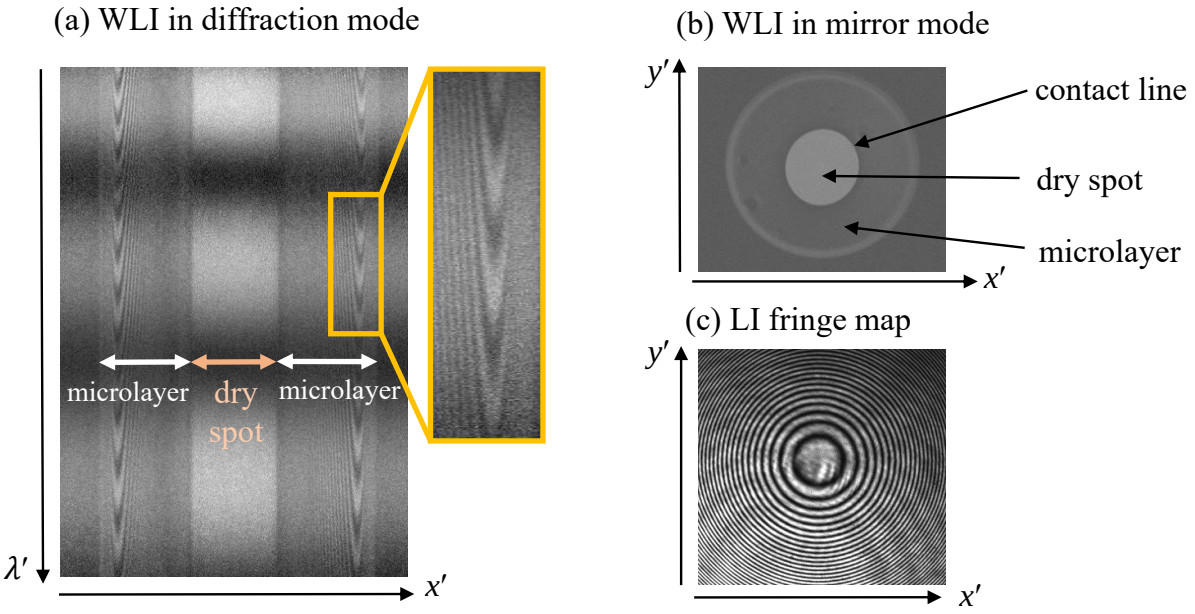

Figure 4.2: Fringe maps obtained in interferometry.

4.1.2 Scalar beam interference theory

In Fig. 4.3b, the rays R_1, R_2 and R_3 represent the interfering electromagnetic waves reflected from respective interfaces. The ray R_0 does not interfere with the others because the porthole thickness H is much larger than the length of coherence. Assuming that the incoming light is unpolarized and at normal incidence, so that there is no effect of polarization upon reflection, the electrical fields associated to them are given by

$$I = |E_1 + E_2 + E_3|^2 + I_0, \tag{4.1}$$

where

$$E_1 = \sqrt{I_1}, \tag{4.2}$$

$$E_2 = \sqrt{I_2}\exp(i\Omega_{12}), \tag{4.3}$$

$$E_3 = \sqrt{I_3}\exp(i\Omega_{13}). \tag{4.4}$$

Here Ω_{ij} accounts for the path difference between rays i and j, so that $\Omega_{ij} = 2\pi\Delta_{ij}/\lambda$, where Δ_{ij} is the path difference between the rays j and i given by

$$\Delta_{ij} = \mathcal{P}_{ij} + \phi_{ij}\lambda = \mathcal{P}_{ij} + \frac{\varphi_j - \varphi_i}{2\pi}\lambda, \tag{4.5}$$

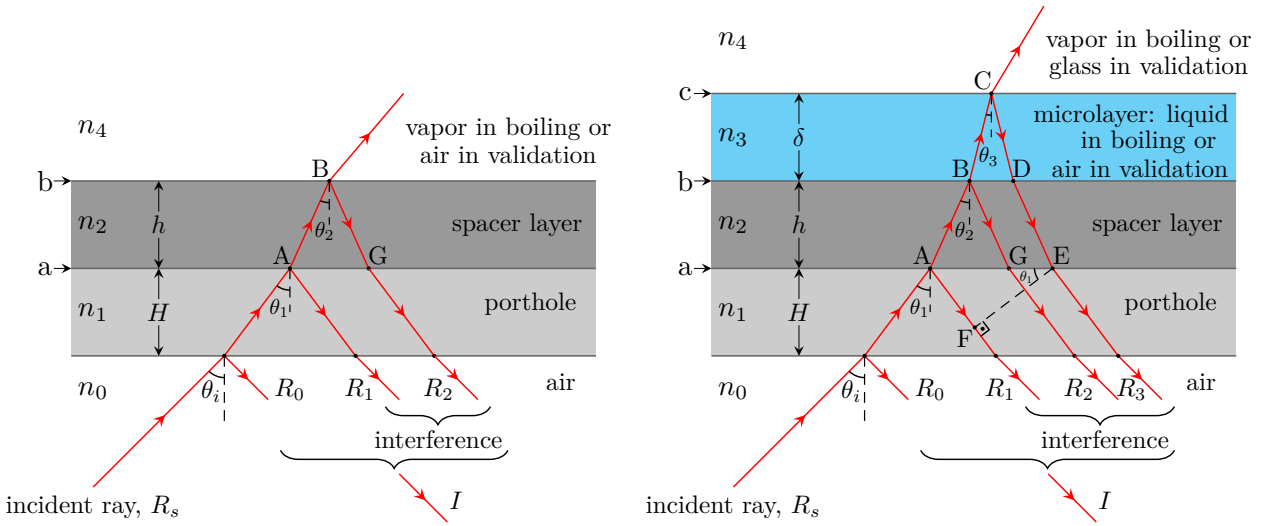

(a) Single layer interference: spacer.

(b) Two layer interference: spacer and microlayer.

Figure 4.3: Schematic of the light path in the porthole, spacer layer and microlayer. The y-axis is perpendicular to the paper plane.

which accounts for the contributions of the optical path difference $\mathcal{P}_{ij}$ and the phase shifts φ_i and φ_j gained by the rays R_i and R_j at reflection. ϕ_{ij} stands for the net phase shift coefficient. A reflected light ray undergoes a π phase shift when it is reflected from a medium of higher index of refraction and zero phase shift when it is reflected from a medium of lower index of refraction [159].

Eq. (4.1) can be rewritten as

$$I = I_0 + I_1 + I_2 + I_3 + 2\sqrt{I_1 I_2}\cos\Omega_{12} + 2\sqrt{I_1 I_3}\cos\Omega_{13} + 2\sqrt{I_2 I_3}\cos\Omega_{23}. \tag{4.6}$$

In a more compact format,

$$I = \sum_{i=0}^{3} I_i + \sum_{\substack{i=1 \\ j>i}}^{3} \left(2\sqrt{I_i I_j}\cos\frac{2\pi\Delta_{ij}}{\lambda} \right), \tag{4.7}$$

where the indexes i and j correspond to the light rays R_i and R_j, respectively. The terms in the second sum in Eq. (4.7) represent the interference between R_i and R_j. One can see that this scalar theory corresponds to two-beam interference model that neglects the multiple reflections of the beams inside each layer. To evaluate a validity of such approach, it can be compared to the full electromagnetic theory of interference in multilayer stacks (subsection 4.1.5).

In Eq. (4.7), I reaches its maxima and minima when the cosine terms are equal to 1 and -1, representing the constructive and destructive interferences, respectively. Therefore, for the maxima, $2\pi\Delta_{ij}/\lambda = 2N\pi$, and for the minima, $2\pi\Delta_{ij}/\lambda = 2N\pi - \pi$, where N is an entire number (positive, zero, or negative) that identifies the fringe order as

$$\underline{\text{Constructive:}}\ \Delta_{ij} = \mathcal{P}_{ij} + \phi_{ij}\lambda = N\lambda, \tag{4.8}$$

$$\underline{\text{Destructive:}}\ \Delta_{ij} = \mathcal{P}_{ij} + \phi_{ij}\lambda = (N - 1/2)\,\lambda, \tag{4.9}$$

Note that the N-th minimum precedes the neighboring N-th maximum. Based on the geometry depicted in Fig. 4.3b, the optical path difference between R_3 and R_1 can be expressed as

$$\mathcal{P}_{13} = n_2(\overline{\text{AB}} + \overline{\text{DE}}) + n_3(\overline{\text{BC}} + \overline{\text{CD}}) - n_1\overline{\text{AF}}. \tag{4.10}$$

Eq. (4.10) can be rewritten as

$$\mathcal{P}_{13} = 2n_2\frac{h}{\cos\theta_2} + 2n_3\frac{\delta}{\cos\theta_3} - 2n_1\sin\theta_1\left(\delta\tan\theta_3 + h\tan\theta_2\right). \tag{4.11}$$

The Snell-Descartes law states that

$$n_1\sin\theta_1 = n_2\sin\theta_2, \tag{4.12}$$
$$n_2\sin\theta_2 = n_3\sin\theta_3. \tag{4.13}$$

Therefore one can conclude that

$$n_1\sin\theta_1 = n_3\sin\theta_3. \tag{4.14}$$

By substituting Eq. (4.14) and Eq. (4.12) into the last two terms of the R.H.S of Eq. (4.11) it yields

$$\mathcal{P}_{13} = 2\left(n_2 h\cos\theta_2 + n_3\delta\cos\theta_3\right). \tag{4.15}$$

Following a similar procedure, one can also obtain expressions for $\mathcal{P}_{12}$ and $\mathcal{P}_{23}$. At normal incidence we have $\theta_i \approx \theta_2 \approx \theta_3 \approx 0$, resulting in

$$\mathcal{P}_{13} = 2\left(n_2 h + n_3\delta\right), \tag{4.16}$$
$$\mathcal{P}_{12} = 2n_2 h, \tag{4.17}$$
$$\mathcal{P}_{23} = 2n_3\delta. \tag{4.18}$$

Therefore, one can conclude that $\mathcal{P}_{13} = \mathcal{P}_{12} + \mathcal{P}_{23}$. Substituting Eq. (4.16) into Eqs. (4.8) and (4.9), it yields two conditions:

$$\underline{\text{Constructive:}}\ 2\left(n_2 h + n_3\delta\right) = (N - \phi_{13})\lambda, \tag{4.19}$$
$$\underline{\text{Destructive:}}\ 2\left(n_2 h + n_3\delta\right) = (N - 1/2 - \phi_{13})\lambda. \tag{4.20}$$

Their significance is different for LI and WLI. For LI, $\lambda = \lambda_{laser}$ is the same in Eqs. (4.19,4.20) so they define $\delta_{max,N}$ and $\delta_{min,N}$ corresponding to the maxima and minima of intensity. As the fringes formed when a lens is placed on top of the flat porthole are circular (cf. Fig. 4.9 below), the corresponding radii $r'_{max,N}$ and $r'_{min,N}$ are determined from the image. The corresponding points on the film are found by using the calibration line slope K (Fig. B.3b), $r = \mathsf{K}_{laser} r'$.

The difference in microlayer thickness between two neighboring maximum and minimum interference can be obtained by subtracting Eq. (4.19) with $\delta = \delta_{max,N}$ from Eq. (4.20) with $\delta = \delta_{min,N}$ and solving for $\delta_{max,N} - \delta_{min,N}$. With the N-th minimum preceding the adjacent N-th maximum one obtains

$$\delta_{max,N} - \delta_{min,N} = \frac{\lambda}{4n_3}; \tag{4.21}$$

One can see that for a fixed λ a new fringe appears at every $\lambda/(4n_3)$ increment or decrement in δ. At $\lambda = 437\,\text{nm}$ this represents roughly 110 and 82 nm for a microlayer of air ($n_3 = 1$) and water ($n_3 = 1.33$), respectively.

For WLI, the maxima are attained at $\lambda = \lambda_{max,N}$ given by Eq. (4.19), where the constructive interference takes place. Eq. (4.19) can then be rewritten as:

$$n_2 h + n_3\delta = \frac{\lambda_{max,N}}{2}(N - \phi_{13}), \tag{4.22}$$

From this equation, one can see the rationale of the spacer use. Indeed, when $h = 0$ (without spacer), the minimum measurable thickness, δ^{min}, is achieved when $N = 1$ and $\lambda = \lambda^{min}$ yields $\delta^{min} = \lambda^{min}/4n_3$ which values are the same as those obtained from Eq. (4.21). By introducing the

spacer layer, δ^{min} can be reduced with h being thick enough to produce maxima. Then, the film thickness is determined by solving Eq. (4.22) for δ with known h, n_2 and n_3.

From Eqs. (4.19,4.20), one can see the range of valid N values for a given ϕ_{13}. In the lens case with $h = 0$ and $\phi_{13} = 0.5$, the condition $\delta \geq 0$ results in $N \geq 1$. For the vapor bubble with $h > 0$, $N \geq 0$. For the lens case, $N \geq 1$. Table 4.1 summarizes the phase shifts φ_1, φ_3, ϕ_{13} and the range of N values for the lens and vapor bubble cases.

Table 4.1: Phase shifts at reflections and range of N values.

Case	h	Fig.	φ_1	φ_3	ϕ_{13}	N
Lens	0	4.7	0	π	1/2	$N \geq 1$
Lens	> 0	4.3b	π	π	0	$N \geq 1$
Bubble	> 0	4.3b	π	0	-1/2	$N \geq 0$

4.1.2.1 Spacer layer thickness

The ITO spacer layer should be thick enough to allow, at least, one maximum or minimum within the spectrometer bandwidth, 437 nm – 645 nm. To address this, first Eq. (4.7) is solved to find λ_{max} for a desired minimum thickness, δ^{min} to be measured. Then, Eq. (4.22) determines the corresponding N. The parameters n_3, n_2 and ϕ_{13} are known. Fig. 4.4 shows the plots for different h for the vapor bubble case. Similar curves can be obtained for the lens case. The total number of maxima that fall within the bandwidth (shaded area) increases as h increases. Indeed, the more maxima the better. However, one has a constraint on the maximum h. It should be chosen so that the total optical path difference (Eq. (4.22)) is within the coherence length of white light (typically a few μm) so that interference is still possible. Since, in boiling, $\delta_{max} \approx 7\,\mu$m our ITO thickness should be within $800 \leq h(\text{nm}) \leq 1000$.

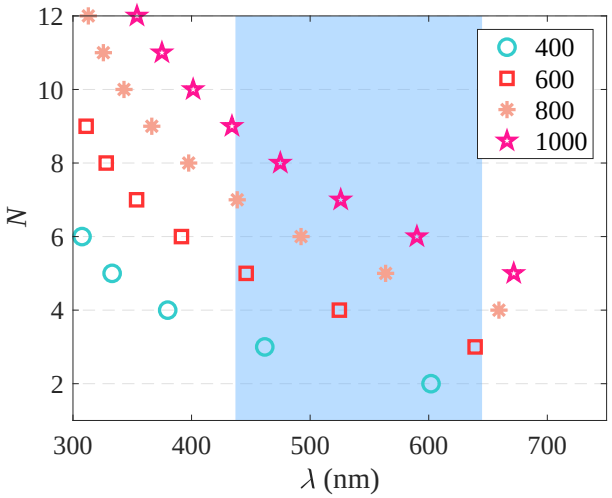

Figure 4.4: Positions of interference maxima calculated for $\delta^{min} = 0.5$ nm. The symbols correspond to h in nm. The shaded interval of λ indicates the spectrometer bandwidth.

4.1.3 Reflectance, transmittance and absorbance

Up to now, we considered only the positions of maxima and minima. To consider the variation of the intensity, one needs to study first the light attenuation by different interfaces.

4.1.3.1 Reflectance

The reflectance $\mathcal{R}$ is defined as

$$\mathcal{R} = I_r/I_s, \tag{4.23}$$

where I_r and I_s stand for intensities of reflected and incident light from the source, respectively. Our WLI setup depicted in Fig. 4.1 uses the reflected light. One then needs to maximize the $\mathcal{R}$ in order to obtain a good fringe contrast. Here, two cases are analyzed: with and without the spacer layer. Transparent to visible light materials typically used for boiling investigations such as sapphire, fused silica, CaF_2 and MgF_2, and fluids for the film such as air and water are considered.

For normal incidence and non-polarizing light, the reflectance $\mathcal{R}_i$ due to the presence of the interface between the media i and $i+1$, is given by the Fresnel equation as [159]

$$\mathcal{R}_i = \left(\frac{n_{i+1} - n_i}{n_{i+1} + n_i}\right)^2. \tag{4.24}$$

For the case of the air on the top of porthole,

$$\mathcal{R}_1^{air} = \left(\frac{n_1 - n_0}{n_1 + n_0}\right)^2. \tag{4.25}$$

Since the indexes of refraction of the portholes, fluids and lens show a minor variation with λ, their values have been taken for $\lambda = 550\,\text{nm}$; (indexes of refraction are given in appendix C). Tables 4.2 and 4.3 show the cases without and with spacer layer, respectively. In table 4.2, the highest values of $\mathcal{R}_1$ and $\mathcal{R}_3$ are achieved when using sapphire and air. With the spacer layer, table 4.3 shows that the use of a MgF_2 is advantageous and can be thus selected for boiling experiments. One should note that the use of sapphire is therefore highly discouraged given the low $\mathcal{R}_1$.

Table 4.2: $\mathcal{R}$ values for the case with lens and without spacer layer (Fig. 4.7).

			Film	
			Water	Air
$\mathcal{R}_1$, [%]	Porthole	Sapphire	1.99	7.73
		Fused silica	0.21	3.50
		CaF_2	0.14	3.19
		MgF_2	0.03	2.53
$\mathcal{R}_3$, [%]	Lens	N-BK7	0.42	4.24

Values computed for $\lambda = 550\,\text{nm}$.

4.1.3.2 Transmittance

The transmittance $\mathcal{T}$ is defined as

$$\mathcal{T} = I_t/I_s, \tag{4.26}$$

where I_t is the intensity of the transmitted light. For normal incidence and non-polarizing light, the transmittance through the boundary between the media i and $i+1$ in Fig. 4.3b is expressed with the Fresnel equation as

$$\mathcal{T}_i = \frac{4n_i n_{i+1}}{(n_i + n_{i+1})^2}, \tag{4.27}$$

for any i. The indexes of refraction used in this work are given in appendix C.

Table 4.3: $\mathcal{R}$ values for the case with ITO spacer layer (Fig.4.3b).

$\mathcal{R}_1$, [%]	Porthole	Sapphire	0.24	
		Fused silica	2.09	
		CaF_2	2.35	
		MgF_2	2.98	
$\mathcal{R}_2$, [%]	Film	Water (boiling)	3.54	
		Air (validation)	10.43	
			Vapor (boiling)	Lens (validation)
$\mathcal{R}_3$, [%]	Film	Water (boiling)	2.04	0.42
		Air (validation)	-	4.24

Values computed for $\lambda = 550\,\text{nm}$.

4.1.3.3 Absorbance

The absorbance A quantifies the light that is absorbed in a medium. It is given as

$$\mathcal{A} = 1 - \mathcal{T} - \mathcal{R}. \tag{4.28}$$

The ability of a medium to absorb the light is defined by its absorption coefficient, expressed as

$$\varpi_i = \frac{4\pi\kappa_i}{\lambda}, \tag{4.29}$$

for any i. Here, κ stands for the extinction coefficient. The transmittance depends on much the light that is absorbed in the medium. These two are related by the Beer-Lambert law, which is expressed as

$$\mathcal{T}_i = \exp(-\varpi_i d_i), \tag{4.30}$$

where d_i is the the distance traveled by the light in the medium i. For our MgF_2 porthole, as informed by its manufacturer (Crystran Optics, UK), it has high transmittance in visible and IR spectra ($\mathcal{T}_p \approx 0.95$), so that $\mathcal{A}_p$ is negligible. For the microlayer liquid water($d_i = \delta$) in visible spectrum, $\kappa_l \sim 1 \times 10^{-9}$ [203]. Taking $\delta \sim 10\,\mu$m (order of magnitude of microlayer thickness in boiling) one obtains $\mathcal{T} \sim 0.99$. Therefore, it also has negligible absorbance. Fig. C.1 shows the values of n_w and κ_w in visible spectrum for the ITO. They have been determined by the ellipsometry measurements performed by Pavel Bulkin (LPICM/Ecole Polytechnique). With $h \sim 1\,\mu$m, one gets $\mathcal{T}_w = 0.8$. Therefore, the ITO film (spacer layer) is the only element in the light optical path illustrated in Fig. 4.3b with a non-negligible absorbance. This is taken into account by A_2 in Eqs. (4.34,4.35). It accounts for the actual light absorption during the boiling conditions so it enters as a fitting parameter during the image-processing as discussed in section 4.1.10. It is worthy to mention that A_2 has no effect on the determination of δ for a high quality fit such as the one shown in Fig. 4.20b. This is because it modifies the value of I without a shift of the profile with respect to λ.

4.1.4 Intensity of the fringe map

Each term in the R.H.S of Eq. (4.7) depends, in practice, on the incident light from the source $I_s(\lambda)$, which can vary strongly with λ, and on the Fresnel equations for transmittance $\mathcal{T}$ and reflectance $\mathcal{R}$. Thus, one writes

$$I_i = I_s(\lambda)\mathcal{I}_i, \tag{4.31}$$

with $i = 0, 1, 2, 3$ and $\mathcal{I}_i$ being a product of the Fresnel reflectance and transmittance coefficients, given as

$$\mathcal{I}_0 = \mathcal{R}_0, \tag{4.32}$$

$$\mathcal{I}_1 = \mathcal{T}_0^2 \mathcal{R}_1, \tag{4.33}$$

$$\mathcal{I}_2 = \mathcal{T}_0^2 \sqrt{\mathsf{A}_2^2} \mathcal{T}_1^2 \mathcal{R}_2, \tag{4.34}$$

$$\mathcal{I}_3 = \mathcal{T}_0^2 \sqrt{\mathsf{A}_2^2} \mathcal{T}_1^2 \mathcal{T}_2^2 \mathcal{R}_3, \tag{4.35}$$

where $\mathcal{R}_i$ is given by Eq. (4.24) whereas $\mathcal{T}_i$ is expressed by Eq. (4.27). A_2 accounts for the light absorbance in the spacer layer, as discussed in subsection 4.1.3.3. In the particular case when only the porthole is used (without spacer layer and microlayer on top of it), Eq. (4.7) reduces to

$$I = I_s(\lambda) \left[\mathcal{I}_0 + \mathcal{I}_1^{air} \right], \tag{4.36}$$

where

$$\mathcal{I}_1^{air} = \mathcal{T}_0^2 \mathcal{R}_1^{air}. \tag{4.37}$$

with $\mathcal{R}_i^{air}$ is expressed by Eq. (4.25).

4.1.4.1 Interference in multilayer films

When the ITO spacer layer is introduced as shown Fig. 4.3b, one has an interference pattern from a multilayer system. It is given by R_1, R_2 and R_3 rays. First, we rewrite Eq. (4.7) as:

$$I = \sum_{i=0}^{3} I_i + I_{12}(\lambda, h) + I_{13}(\lambda, h, \delta) + I_{23}(\lambda, \delta), \text{ where } I_{ij} = 2\sqrt{I_i I_j} \cos \frac{2\pi \Delta_{ij}}{\lambda} \tag{4.38}$$

with I_i defined by Eq. (4.31). Since $I_s(\lambda)$ dependence is much weaker than that of the I_{12} terms, it will be neglected for the moment (so I_s will be assumed constant= 1; this approximation will be abandoned in the following sections). Note that I_{12} is independent of δ and it can be measured separately, as shown further in Fig. (4.11a). Let us analyze the two remaining interference terms in the R.H.S of Eq. (4.38), $I_{13}(\lambda, h, \delta)$ and $I_{23}(\lambda, \delta)$. In section 4.1.2, we have shown that for $\delta \leq 82$ nm, no fringes corresponding to I_{23} are visible within our wavelength bandwidth for a microlayer of liquid water. This means the maxima and minima are provided only by I_{13}. For $\delta > 82\,\text{nm}$, on the other hand, both terms should have at least one maximum or minimum. This is verified in Fig. 4.5, where theoretical I_{13} and I_{23} profiles are shown for $\delta = 80\,\text{nm}$ and $300\,\text{nm}$ in Figs. 4.5a and 4.5b, respectively. For $\delta = 80\,\text{nm}$, only I_{13} presents maxima and minima of interference whereas for $\delta = 300\,\text{nm}$ I_{23} has a minimum. This confirms that indeed when $\delta \leq 82\,\text{nm}$ the microlayer thickness is too thin to produce maxima or minima and fringe will not be visible.

Equation (4.22) is written taking into account only $I_{13}(\lambda, h, \delta)$. However, we obtain experimentally the superposition of I_{12}, I_{13} and I_{23}. Therefore, one cannot use Eq. (4.22) to compute δ. Indeed, the interference from a multilayer system imposes difficulties to recover δ. A strategy to deal with this issue will be presented further in section 4.1.12.

4.1.5 Comparison with the electromagnetic theory

To validate our scalar beam interference model we compare it with the classical electromagnetic theory of interference in multilayer stacks presented in Appendix A. We make a comparison for the case of the 3-layer system for the case of a vapor bubble with a liquid microlayer between the ITO and the vapor phase. The substrate is MgF_2. For the electromagnetic theory, we use Eqs. (A.2,A.25); for the scalar

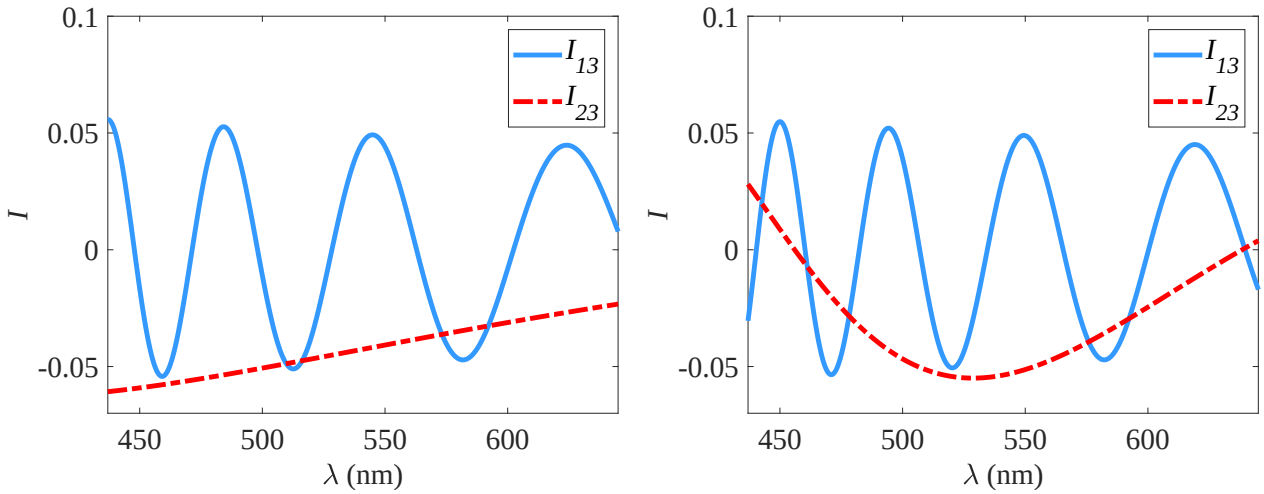

(a) $\delta = 80\,\text{nm}$ and $h = 850\,\text{nm}$. (b) $\delta = 300\,\text{nm}$ and $h = 850\,\text{nm}$.

Figure 4.5: Theoretical I_{13} and I_{23} for two different values of δ.

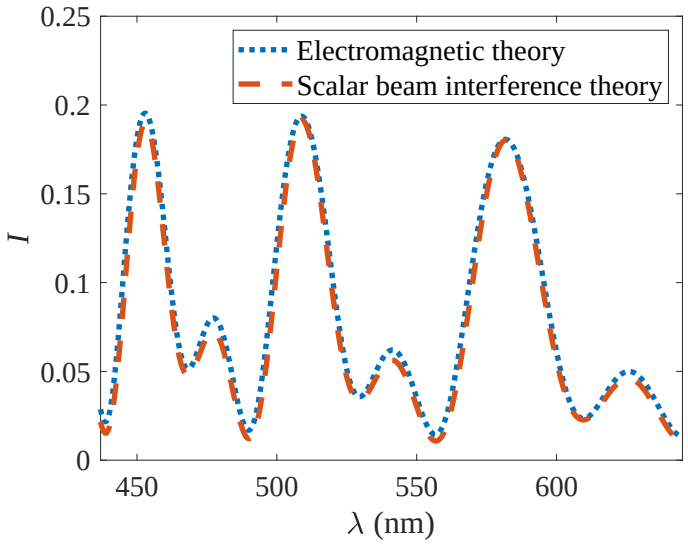

Figure 4.6: Normalized by I_s intensity for the microlayer case calculated for $h = 850\,\text{nm}$ and δ =1.5μm.

theory, Eqs. (4.7,4.32-4.35). Fig. 4.6 shows $I(\lambda)$ obtained by solving the characteristic matrix given by Eq. (A.24) and by the scalar interference model given by Eq. (4.7). A good agreement between both curves is observed with zero phase shift. The slight difference at the maxima has no practical issues since to fit $I(\lambda)$ experimental to $I(\lambda)$ theoretical one needs to insert a scale factor to account for the different span range of the experimental intensity that depends on the gray-scale, optical settings, frame rate and slit width, for instance.

4.1.6 Spectral and spatial calibration of the setup

As shown in Fig. 4.2 a, in WLI images the vertical axis λ' is linked to the wavelength and the horizontal axis, x', represents the physical positioning x along the bubble base. Then, a calibration procedure is required to determine the relation of λ' and x', both measured in pixels, to λ and x, both in meters, respectively. In LI, the output is a $x' - y'$ image where x' and y' are linked to the physical film coordinates x and y, respectively. A spatial calibration relates x' and y' in pixels to x and y in meters.

A detailed description of these calibration procedures can be found in appendix B.

The spectrum follows a linear regression in the form

$$\lambda = a(\lambda' - 1) + \lambda_0, \tag{4.39}$$

where the slope a is 0.1624 nm/px and it represents the spectral resolution of our optical system (the smallest difference in λ that can be distinguished). $\lambda_0 = 437.24$ nm is the lowest visible wavelength. λ' ranges from 1 to 1280 px. The visible spectrum bandwidth is then $\lambda_0 \leq \lambda \leq 644.95$ nm.

The horizontal axis follows a relation in the form of

$$x = \mathsf{K}x', \tag{4.40}$$

where $\mathsf{K}_{WLI} = 14.09\,\mu$m/px, i.e., each horizontal pixel in the image corresponds to $14.09\,\mu$m in the spacer layer for WLI (see Fig. 4.2). In LI, due to the use of a lens with a different magnification factor, $\mathsf{K}_{LI} = 7.18\,\mu$m/px. The same calibration factor has been obtained for the y' axis. The optical magnifications are also given in appendix, section B.3.

4.1.7 Fringe geometry as a function of the thickness profile

It is known that the fringe geometry observed in the CCD camera depends on the film geometry. The first goal is to check, qualitatively, if the fringe experimental profile corresponds to the one predicted theoretically.

4.1.7.1 Theory

For a given fringe, N is constant and n_3 has a negligible change within the visible spectrum. ϕ_{13} is constant for a given setup. From Eq. (4.22)

$$\lambda_{max} = C_1\delta(x), \text{ where } C_1 = [(N - \phi_{13})/(2n_3)]^{-1}. \tag{4.41}$$

For a wedge film geometry, $\delta(x) \sim x$ so the fringes should appear as slanted straight lines. For a lens placed on the flat porthole, in the fringe image, $x' = 0$ can be determined as a position of the axis of symmetry, so $x' = 0$ corresponds to $x = 0$ in the porthole, which is the center of the lens. Then $\delta(x) = a + bx^2$ for a fixed y so the fringes should appear as parabolas.

For the WLI setup in the boiling case of Fig. 4.3b, the fringe map of the spacer layer is first obtained when there is no bubble on the ITO. In this case, to measure its thickness h, $\delta = 0$ should be used in Eq. (4.19), which yields

$$\lambda_{max} = C_2 h, \text{ where } C_2 = [(N - \phi_{13})/(2n_2)]^{-1}. \tag{4.42}$$

In this expression, h varies within a few nm as given by the ITO deposition specifications, so it can be considered as a constant for a qualitative analysis. Then, for a given fringe N, λ_{max} is constant. The fringes should appear as horizontal lines.

In LI, $\lambda_{max} = \lambda_{laser}$ and $\delta = \delta(x, y)$, so that for $h = 0$ Eq. (4.22) becomes:

$$\delta(x, y) = C_3, \text{ where } C_3 = \lambda_{laser}(N - \phi_{13})/(2n_3). \tag{4.43}$$

It means that the fringes are the thickness isolines. For the wedge geometry, $\delta(x, y) \sim x + y$ so the fringes should also appear as straight lines. In the lens case of Fig. 4.7, $\delta(x, y) = a + x^2 + y^2$. Then, the fringe map should be seen as a set of concentric circles. Note that $a = 0$ when $\delta(x, y) \approx 0$.

4.1.7.2 Comparison to the experiment

We aim at comparing the features of LI and WLI techniques. To do so, we place a plano-convex lens on a flat porthole as illustrated in Fig. 4.7. For the quantitative comparison, we measure the thickness of a thin film of air formed between them. The theoretical lens shape is known from its radius of curvature, $\mathtt{R}$, given by the manufacturer. Therefore, the goal is to recover the lens theoretical profile by measuring $\delta = \delta(x)$ by WLI and LI. This comparison also serves to validate our experimental installation. For the lens case depicted in Fig. 4.7, the theoretical lens shape is obtained from

$$(\mathtt{R} - \delta)^2 + x^2 - \mathtt{R}^2 = 0, \tag{4.44}$$

where x is the horizontal coordinate axis on the porthole centered at the point of symmetry of the lens. The lens is a KPX124 model (Newport). It is made of N-BK7 glass material with $\mathtt{R} = 516.8\,\text{mm}$. The uncertainty on $\mathtt{R}$, as informed by the manufacturer, is $\pm 1\%$. The uncertainty on the theoretical δ is, therefore, also $\pm 1\%$.

- **Issues**. For the theoretical profile of the lens in Fig. 4.7, Eq. (4.44) gives $\delta = 0$ at $x = 0$. However, according to many of our experiments this hardly happens in practice (except maybe with very clean surfaces in a clean room). Even cleaning the porthole and lens in a ultrasonic bath before the experiment, dust particles with micrometric size always remain on the surface because the cleaning is not perfect. Therefore, the lens is shifted up thus creating a non-zero thickness at $x = 0$, as shown in Fig. 4.8a (the maxima at $x = 0$ indicates $\delta > 0$). To get $\delta \sim 0$ at $x = 0$ one then needs to employ "special means". We put a weight $m \simeq 100\,\text{g}$ on top of the lens to force the contact between lens and porthole. When this is done, we obtain the fringe map shown in Fig. 4.8b, where the dark region at the center indicates $\delta \sim 0$. In this case, a comparison with the theoretical profile can be done. However, its position remains uncertain, representing the major source of error when compared to the theoretical profile. Because of this, error bars will not be provided. Moreover, due to the local pressure imposed by the weight on the contact, small mechanical deformations will take place thus the contact is flattened and the whole lens profile is expected to be shifted down by $\Delta\delta = \delta_{theo} - \delta_{exp}$. This displacement can be estimated from the Hertz contact theory expressed as [204]

$$\Delta\delta = (9/16)^{1/3} \left[\mathtt{F}^2 \left(\frac{1}{\hat{\mathtt{E}}_1} + \frac{1}{\hat{\mathtt{E}}_4} \right)^2 \frac{1}{\mathtt{R}} \right]^{1/3}, \tag{4.45}$$

  where $\hat{\mathtt{E}}_i = \mathtt{E}_i/(1-\nu_i^2)$ is the Young's modulus normalized by the Poisson coefficient ν_i of the porthole (sapphire) and lens (N-BK7). The force promoted by the weight is $\mathtt{F} = mg$. For the mechanical properties given in table C.4, one obtains $\Delta\delta = 60\,\text{nm}$. This is the order of the error expected on the comparison between experimental and theoretical lens thicknesses.

- **Qualitative comparison**. First, we consider the fringes for the microlayer film formed with a lens on top of the porthole depicted in Fig. 4.8b. A wide destructive interference area appears around $x' = 0$. It represents the contact area determined by the lens on the porthole at $x = 0$. It also includes the very close vicinity around this point where δ is much smaller than any wavelength within the bandwidth capable of producing any maximum. The same feature is observed in Fig. 4.9b around $x' = 0$ and $y' = 0$. On the other hand, in Fig. 4.8a, multiple maxima appear throughout λ at $x' = 0$. $\delta = 11.3\,\mu\text{m}$ at $x' = 0$ (determined using Eq. (4.51)). This occurs because the lens is shifted up due to the presence of dust between the porthole surface and the lens. Similarly, in Fig. 4.9a, the center shows a constructive interference in LI.

  According to the theory presented in section 4.1.7.1, the fringes should be seen as bell-shaped parabolas in WLI, which is confirmed qualitatively in Figs. 4.8. One should note that the

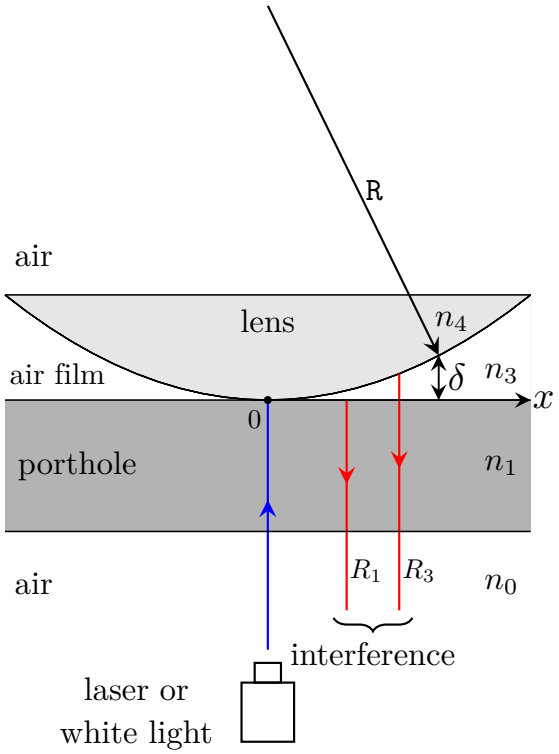

Figure 4.7: Plano-convex lens with on a flat optical porthole for validation and comparison of WLI and LI.

wavelength axis λ is downward. In Fig. 4.8b the parabolas present a very steep parabolic shape. In LI, the fringes theoretical geometry is confirmed as concentric circles in Figs. 4.9.

In the case of a flat plate on the porthole, the presence of dust creates a wedge-shaped film. The slanted lines predicted theoretically by the beam interference model are observed in WLI and LI in Figs. 4.10a and 4.10b, respectively. The plate inclination angles with regards to the horizontal can be determined as presented in section D.3 (α is not the same because the experiments were performed in two different conditions). In WLI, for the case of the ITO film over the porthole, the horizontal strips predicted by the theory are confirmed in Fig. 4.11a.

We can now highlight the first advantage of WLI over LI. We have verified theoretically, with Eqs. (4.41, 4.43), and experimentally, in Figs. (4.8,4.9,4.10), that indeed $\delta(x) \propto \lambda$. This means that the fringe geometry does correspond to the film profile. However, this is only possible in WLI thanks to the λ axis, where the fringes spectrum is obtained. In LI, the light is monochromatic and this feature therefore does not exist. As a result, one can have a quick qualitative information about the microlayer profile in WLI based on the fringe geometry without any image post-processing. The qualitative comparison between LI and WLI is performed in next sections.

4.1.8 Image processing: Map compensation and symmetry analysis

Two processing tasks must be performed before computing $\delta(x)$ from the fringe map in WLI. The first consists in compensating an uneven spectral light intensity distribution of the light source, $I_s(\lambda)$. The second task is meant to check the optical alignment of the interferometry installation and to determine the axis of symmetry in the fringe image that corresponds to $x = 0$. The optical alignment protocol for the WLI setup is described in the appendix section F.

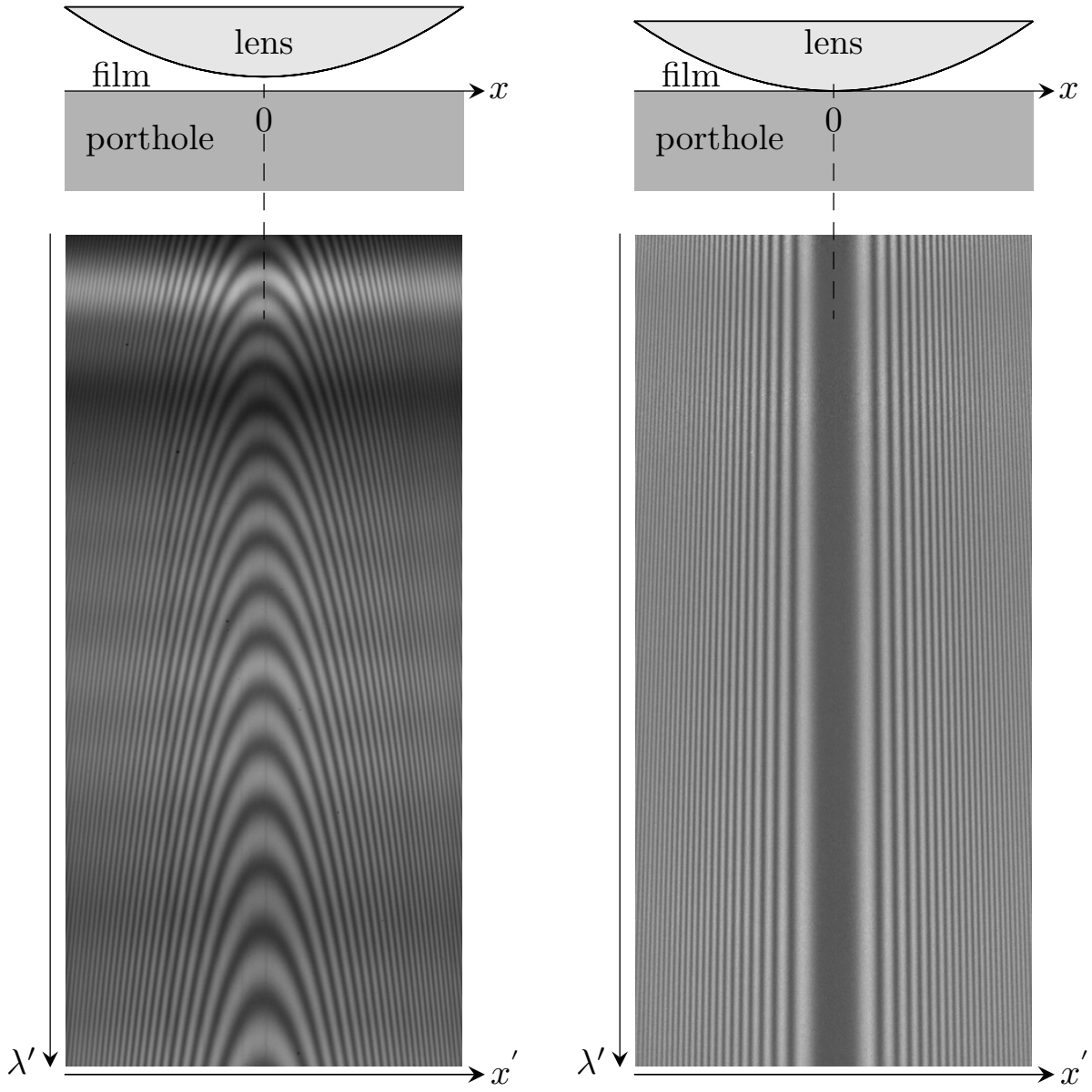

(a) Non-compensated fringe map for the plano-convex lens without cleaning procedure and without weight on top of the lens. $\delta = 11.3\,\mu$m at $x = 0$.

(b) Compensated fringe map for the plano-convex lens with ultra-sonic bath cleaning and with weight. $\delta = 0$ at $x = 0$.

Figure 4.8: WLI fringe maps for the lens.

- **Fringe map compensation.** As shown by Eq. 4.31, the resultant intensity seen by the CCD is proportional to $I_s(\lambda)$. Therefore, to compensate the uneven intensity distribution of the light source, one has first to find a way to measure $I_s(\lambda)$ and divide Eq. (4.7) by $I_s(\lambda)$ to obtain the compensated intensity as

$$I_c(\lambda) = \frac{I(\lambda)}{I_s(\lambda)} = \frac{1}{\mathcal{I}_0 + \mathcal{I}_1^{air}} \left[\sum_{i=0}^{3} \mathcal{I}_i + \sum_{\substack{i \geq 1 \\ j > i}}^{3} \left(2\sqrt{\mathcal{I}_i \mathcal{I}_j} \cos \frac{2\pi \Delta_{ij}}{\lambda} \right) \right]. \tag{4.46}$$

One can see that R.H.S. of Eq. (4.46) is independent of $I_s(\lambda)$ now. In practice, one obtains $I_c(\lambda)$

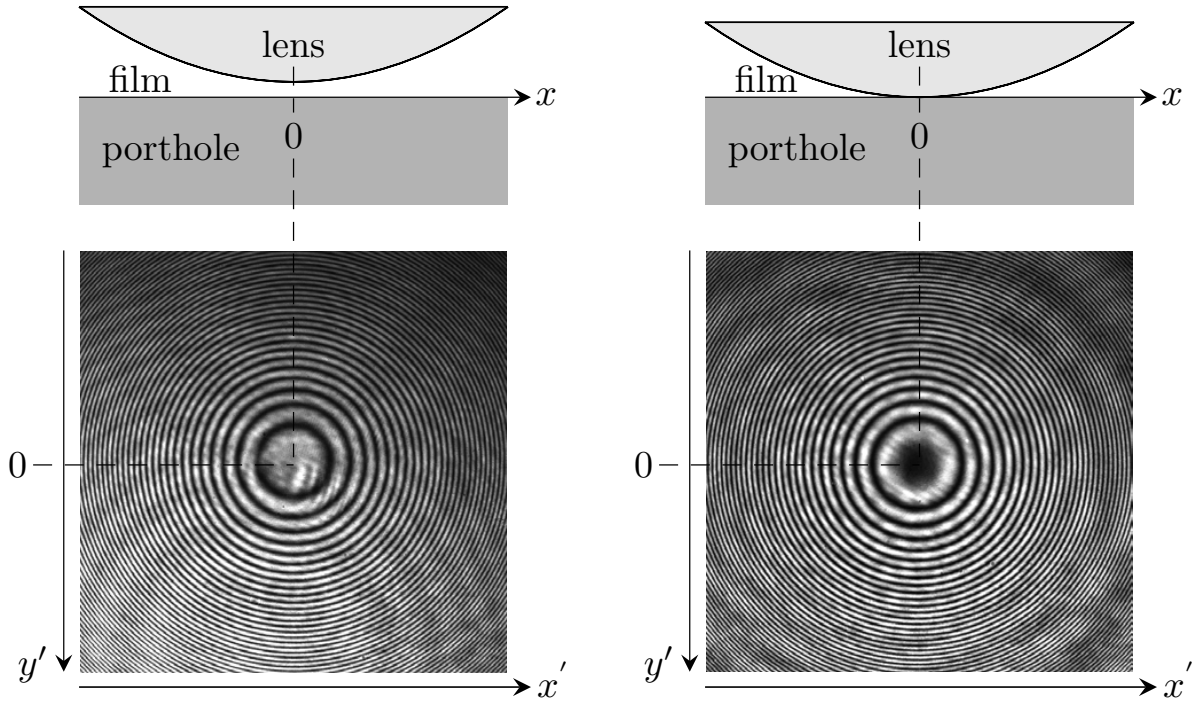

(a) Fringe map for the lens without cleaning procedure.

(b) Fringe map for the lens with ultra-sonic cleaning procedure.

Figure 4.9: LI fringe maps for the lens.

by performing a pixel-wise(*i.e*, pixel by pixel) compensation by dividing the intensity of the non-compensated fringe map (as given by the CCD camera) by the intensity of the light source $I_s(\lambda)$. So, how to get $I_s(\lambda)$?. We measure it using only the porthole (without ITO, bubble or lens on it, thus we are free of interference fringe) so that one obtains only the spectral distribution of the light source. That is the reason why the term $\mathcal{I}_0 + \mathcal{I}_1^{air}$ in the denominator of the R.H.S of Eq. 4.46 appears, which accounts for the reflectance response of the porthole only.

An example of the compensated map can be seen in Fig. 4.8b whereas a non-compensated map is shown in Fig. 4.8a. This compensation also eliminates two other spectral effects: the CCD response sensitivity and the transmittance of the visible-IR beam splitter. Equation (4.46) applies for the case illustrated when spacer layer and microlayer are present (Fig. 4.3b). The compensated intensity for the ITO fringe map only (obtained without the bubble in boiling or without the lens in validation) is given similarly:

$$I_c^{ITO}(\lambda) = \frac{I(\lambda)}{I_s(\lambda)} = \frac{1}{\mathcal{I}_0 + \mathcal{I}_1^{air}} \left[\mathcal{I}_0 + \mathcal{I}_1 + \mathcal{I}_2 + \left(2\sqrt{\mathcal{I}_1 \mathcal{I}_2} \cos \frac{2\pi \Delta_{12}}{\lambda} \right) \right]. \tag{4.47}$$

One should note that Eq. (4.47) includes only the interference from the ITO film thus suitable to compute its thickness because the R.H.S of it only has h as unknown parameter.

- **Optical alignment and axis of symmetry.** A minor misalignment in the setup (for instance, a tilt of the camera's axis with respect to the slit) might lead to a significant error of the film thickness. The alignment can be checked by verifying the symmetry of the fringe map for the lens case of Fig. 4.8b with respect to λ' axis, which is the vertical axis of the camera that corresponds to the lens symmetry axis. If the alignment procedure described in appendix F is properly done, one should obtain a symmetric fringe map. The symmetry check is performed as follows:

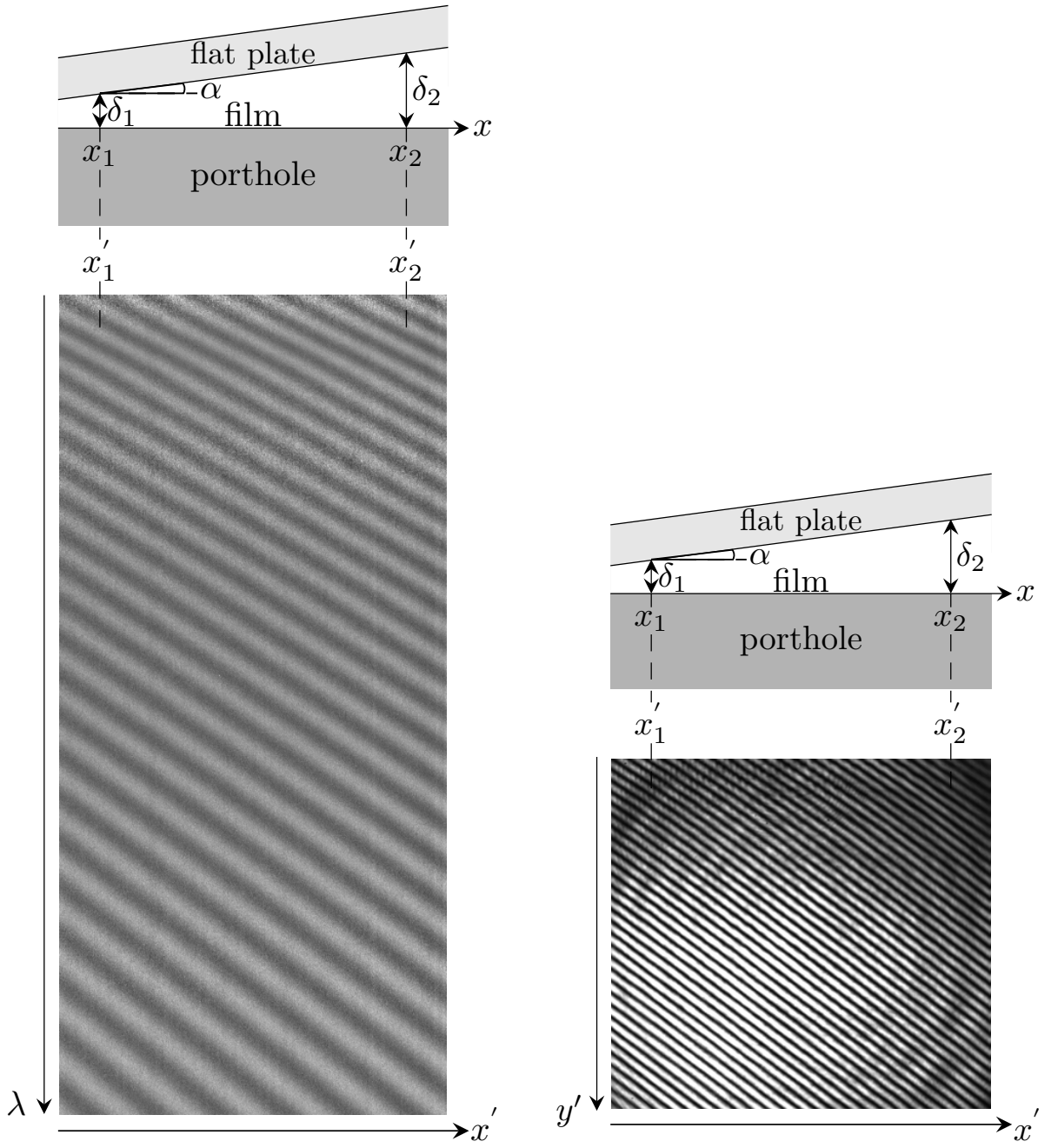

(a) WLI fringe map for a flat plate over the porthole. $\alpha = 0.021°$.

(b) LI fringe map for a flat plate over the porthole. $\alpha = 0.065°$.

Figure 4.10: WLI and LI fringe maps for wedge films.

– 1. Horizontal $I(x')$ profiles at a fixed λ are taken to locate the first five maxima ($N = 1, 2, 3, 4, 5$) at each side of the fringe map as shown in Fig. 4.12a. A lowpass filter (with zero phase shift) is applied to the raw $I(x')$ profile to reduce the high-frequency noise. The position of the symmetry axis is computed from each pair of maxima with the same N as a midpoint.

– 2. Step 1 is repeated throughout the wavelength bandwidth to obtain the midpoints for each λ and N as depicted in Fig. 4.12b. If the points form a straight vertical line, the map is considered symmetric. Fig. 4.13 shows that in our case 98% of the midpoints fall within

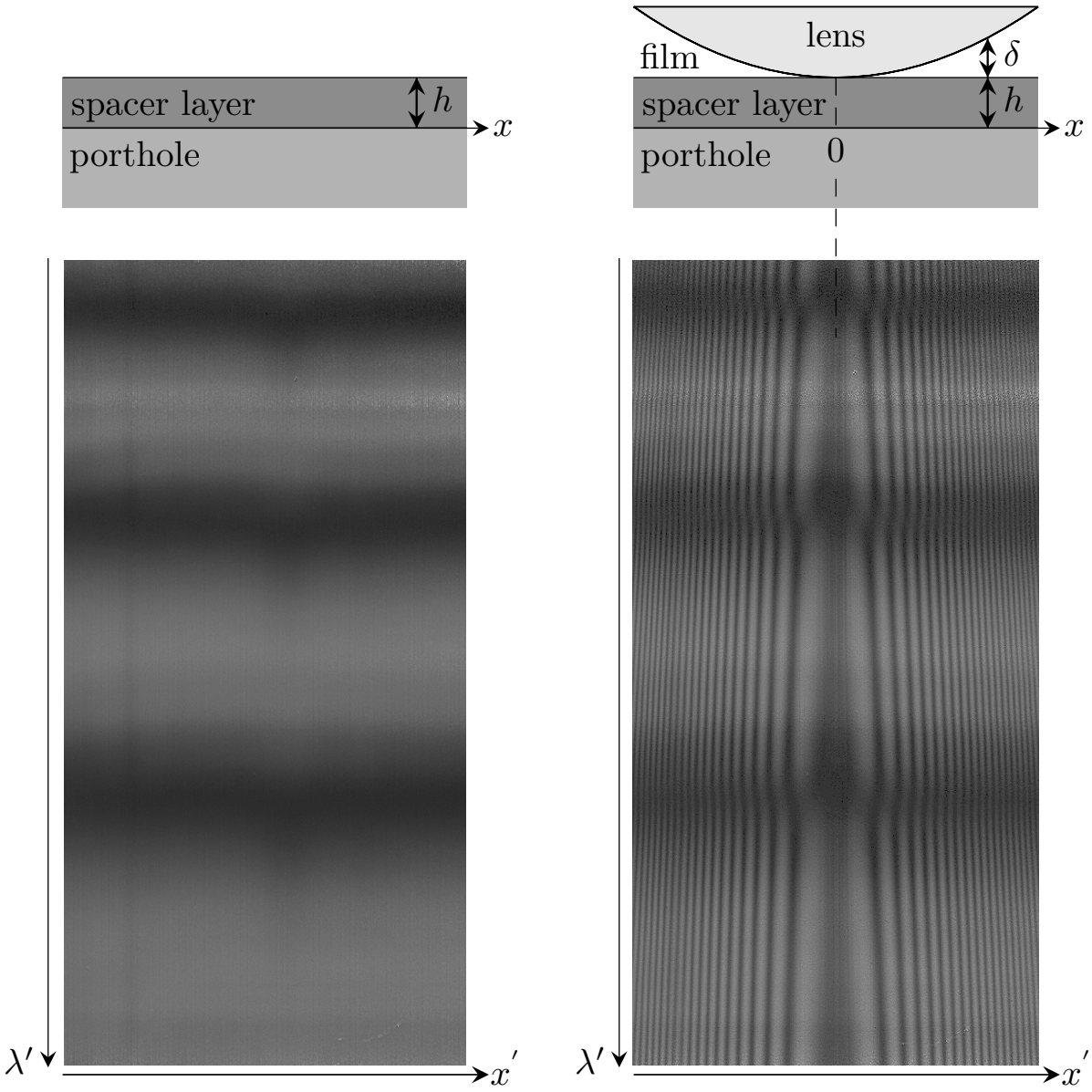

(a) WLI fringe map for spacer layer.

(b) WLI fringe map for the validation case with lens on the spacer layer.

Figure 4.11: WLI fringe maps for spacer layer and lens.

$360.5\,\text{px} \leq x' \leq 361.5\,\text{px}$. This represents a misalignment of roughly $28\,\mu\text{m}$, which is the size of a pixel. It represents an error on the thickness of 1 to 2%. Therefore, one can considered it minor, the fringe map is therefore symmetric and the alignment is indeed properly done. The axis of symmetry is considered to be at $x' = 361\,\text{px}$ and it corresponds to $x = 0$.

For the LI case shown in Figs. 4.9, the circular symmetry has been verified, which indicates that the porthole and the lens are well aligned.

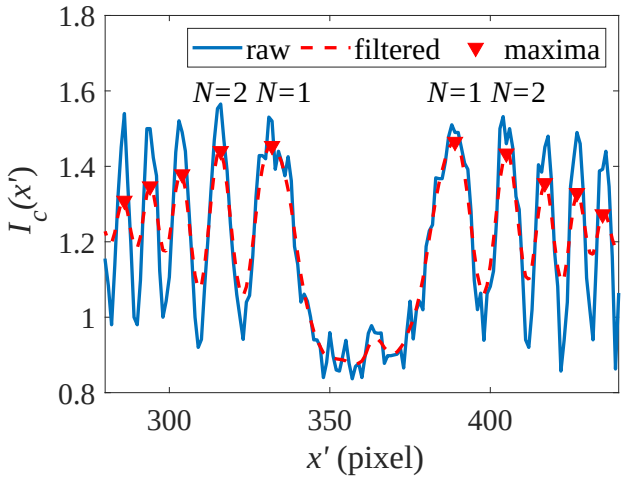

(a) $I(x')$ profiles for $\lambda = 573.49\,\text{nm}$.

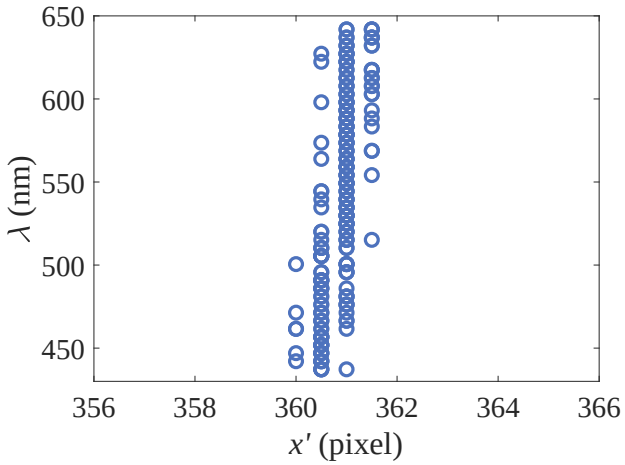

(b) Position of the symmetry midpoints for each pair of interference maxima throughout the wavelength bandwidth.

Figure 4.12: Fringe symmetry analysis.

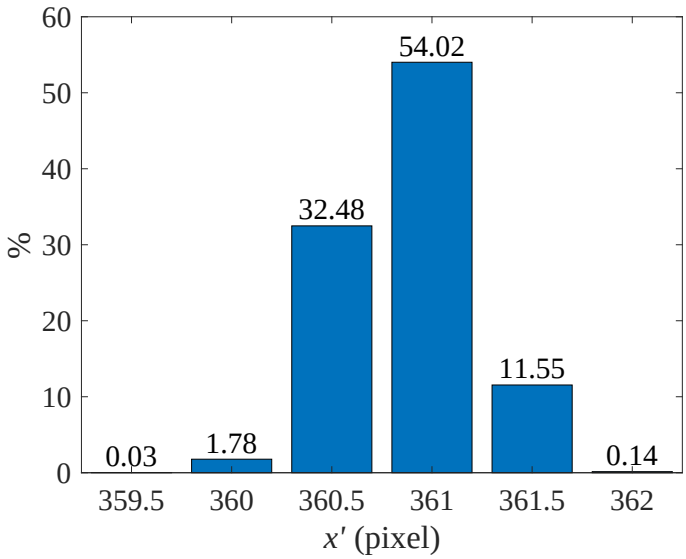

Figure 4.13: Normalized distribution of midpoints with respect to x'.

4.1.9 Image processing: Determination of the microlayer thickness $\delta(x)$ in validation

The WLI fringe map shown in Fig. 4.8b can be processed by two different ways. One can take horizontal $I(x)$ profiles for given λ or, the other way around, take vertical $I(\lambda)$ profile for a constant x. The post-processing for these two approaches is given as follows.

- $I(x)$. To compute $\delta(x)$ with $I(x)$ profiles we proceed as shown by the flowchart in Fig. 4.14. First, we get the compensated fringe map I_c depicted in Fig. 4.8b and we take a $I(x)$ profile for a given λ as shown, for instance, in Fig. 4.15 at $\lambda = 573.49\,\text{nm}$. We filtered out $I(x)$ only where the $I(x)$ is noisy with a low-pass and zero phase shift filter. The maxima are then located at x^i_{max} from the filtered profile, where the filter is applied, and from the raw $I(x)$ where the filter is not requested. In Fig. 4.15, the red triangles represent the maxima. Due to the nearly vertical orientation of the fringes along λ' in Fig. 4.8b, the maxima of $I(x)$ are very sharp

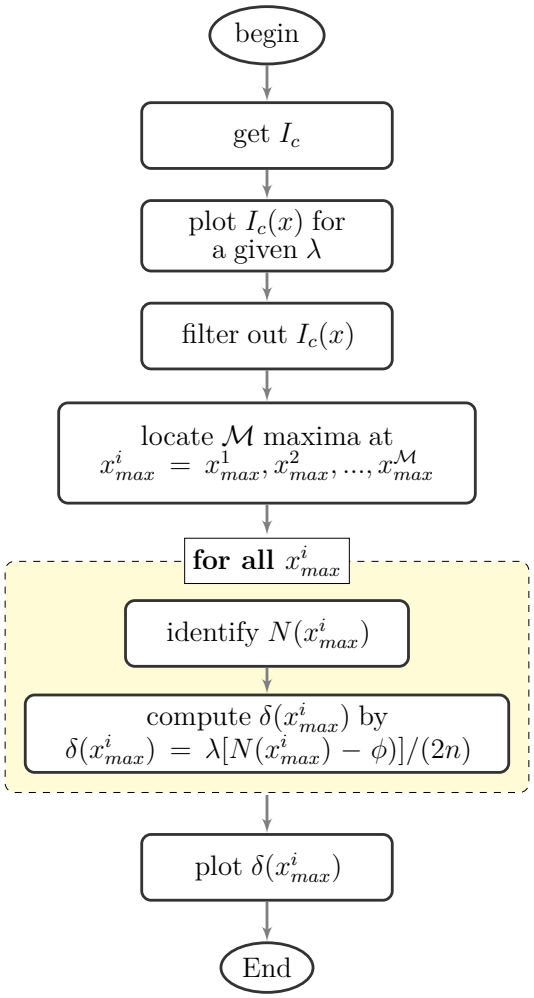

Figure 4.14: Flowchart to compute $\delta(x)$ from the maxima of $I(x)$ for the case without spacer layer. The steps inside the yellow rectangle are repeated for all maxima.

and nearly noiseless for $x > 0.8\,\text{mm}$. Next, the fringe sequential order N is identified for each x^i_{max} by counting them up, where each maximum stands for a value of N. In Fig. 4.8b for instance, the first maxima taking place at $x^1_{max} \approx 0.45\,\text{mm}$ is identified with $N = 1$ and second at $x^2_{max} \approx 0.7\,\text{mm}$ with $N = 2$ and so on. Next, we compute $\delta(x^i_{max})$ using Eq. 4.19 (with $h = 0$) where the corresponding $N(x^i_{max})$ is known. A similar procedure can be applied if the minima are accounted for. One should note that the full film thickness profile can be extracted from a single $I(x)$ profile. Since λ is constant in $I(x)$ profiles, this methodology also applies for the LI fringe map shown in Fig. 4.9, where $\lambda_{laser} = 633\,\text{nm}$. Similar $I(x)$ profiles are obtained.

- $I(\lambda)$. Vertical intensity profiles represent the $I(\lambda)$ variation at a fixed x. The procedure to compute δ is depicted in the flowchart of Fig 4.16. First, we take I_c and plot $I_c(\lambda)$ for a fixed x. The whole profile is then filtered out by a low-pass and zero phase shift filter to remove the high frequency noise. Next, we locate $\mathcal{M}$ maxima and $\mathcal{N}$ minima at λ^i_{max} and λ^i_{min}, respectively, from the filtered profile. The fringe sequential order is then identified for each λ^i_{max} and λ^i_{min} by counting up the maxima and minima. In the next step, two cases are possible:

  - Single minimum or maximum: In Fig. 4.8b, this occurs only for the few first x values close to $x = 0$ because of nearly vertical orientation of fringes and their large thickness. For this

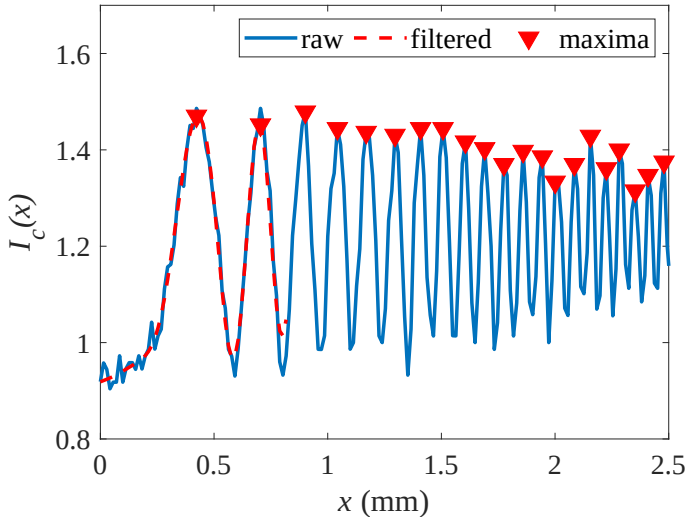

Figure 4.15: $I(x)$ profile by WLI at $\lambda = 573.49\,\text{nm}$.

reason, we are unable to identify the location of the first maximum in the spectrum. On the other hand, its adjacent minimum was the first fringe that could be identified. Its $I(\lambda)$ profile is shown in Fig. 4.17a. Therefore, to compute δ we use

$$\text{for single minimum: } \delta = \frac{\lambda^j_{min}}{2n}\left[N(\lambda^j_{min}) - 1/2 - \phi\right], \tag{4.48}$$

$$\text{for single maximum: } \delta = \frac{\lambda^i_{max}}{2n}\left[N(\lambda^i_{max}) - \phi\right], \tag{4.49}$$

where λ^j_{min} and λ^i_{max} are taken from the single minimum and maximum, respectively, and $N(\lambda^j_{min})$ and $N(\lambda^i_{max})$ are the corresponding fringe sequential order.

– Maxima and minima: If there is no single maximum or minimum, there must exist, at least, one maximum and one minimum in $I(\lambda)$. This can be seen in Fig. 4.8b, where the bending of fringes increases with increasing x whereas their thickness decreases. Maxima and minima start appearing in the spectrum. See for instance Fig. 4.17b, where the $I(\lambda)$ profile is shown for $x = 2.324$ mm. Several maxima and minima appear. To compute δ in this case, we have evaluated many different formulas by simply rearranging Eq. (4.19). They are presented in section E.3 along with an error analysis, which shows that the lowest error is given by computing δ for each individual maxima and minima and then take an average as given by

$$\delta = \frac{1}{4n}\left\{\frac{1}{\mathcal{M}}\sum_{i=1}^{\mathcal{M}}\lambda^i_{max}\left[N(\lambda^i_{max}) - \phi\right] + \frac{1}{\mathcal{N}}\sum_{j=1}^{\mathcal{N}}\lambda^j_{min}\left[N(\lambda^j_{min}) - 1/2 - \phi\right]\right\}, \tag{4.50}$$

where $\mathcal{M}$ and $\mathcal{N}$ stand for the total number of maxima and minima, respectively.

To compute the full film profile, this procedure is repeated by taking $I(\lambda)$ profiles for each x.

4.1.10 Image processing: Determination of microlayer thickness $\delta(x)$ in boiling

We now describe the procedure to determine $\delta(x)$ for the boiling case (with ITO space layer and bubble). A similar procedure is used for the case of spacer layer and lens for the validation experiment

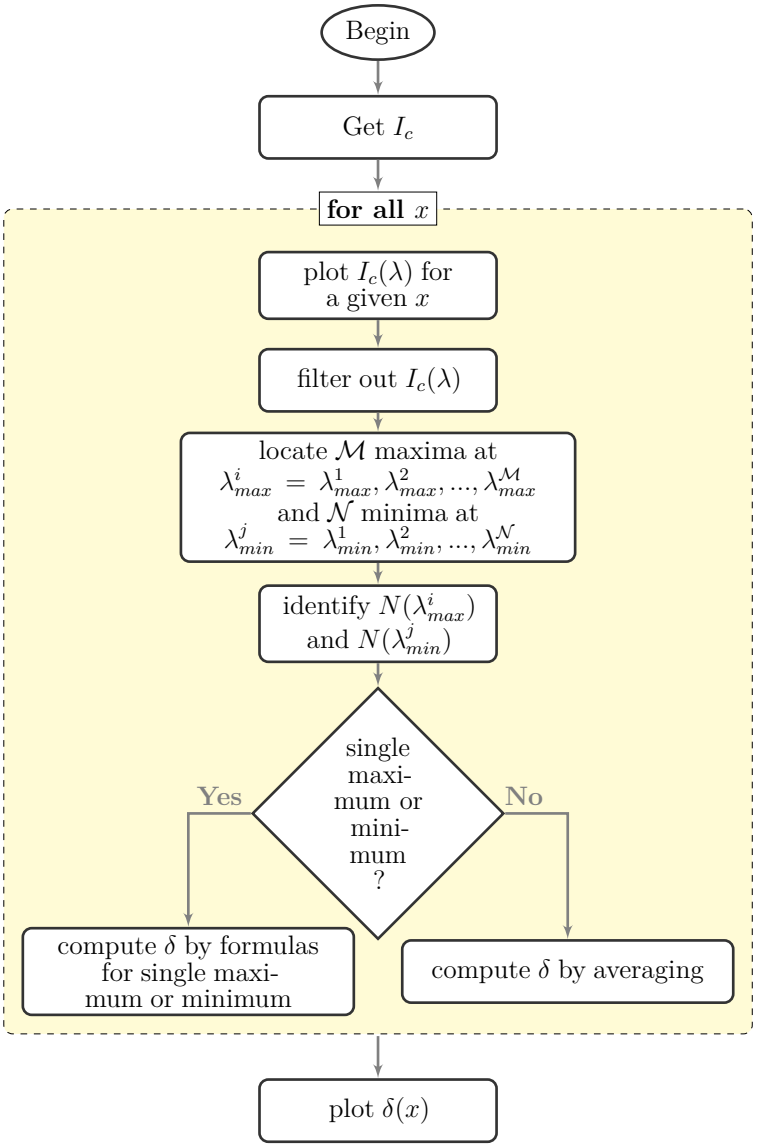

Figure 4.16: Flowchart to compute $\delta(x)$ using $I(\lambda)$ profiles for the validation case without spacer layer. The steps inside the yellow rectangle are repeated for all x.

(section 4.1.12). In these cases, h and δ are both unknown. The procedure to determine them is illustrated in the flowchart of Fig. 4.18. First, we obtain the ITO fringe map I_c at $t = 0$, corresponding to the frame just before the bubble nucleation ($\delta = 0$). For the validation case, this is equivalent of taking the fringe map without the lens on ITO. Only the interference produced by h is then observed in both cases, as shown in Fig. 4.11a. However, N is unknown. Eqs. (4.19,4.20) cannot be used. To address this issue we use the theoretical profile, $I_{c,theo}(\lambda)$, obtained by solving Eq. (4.47) to fit it to the experimental profile, $I_{c,exp}(\lambda)$. h is then determined by solving a minimization problem where the function F, defined as

$$F = \sum_{\text{all }\lambda} \left[I_{c,exp}(\lambda) - \mathcal{K} I_{c,theo}(\lambda) \right]^2 , \tag{4.51}$$

is minimized. $\mathcal{K}$ is a scaling factor that accounts for the different intensity span in the measurements. The minimization is then solved for each point along x to get $h(x)$. A Levenberg–Marquardt algorithm **REF?** is used to find $h(x)$ that minimizes F at x. Figure 4.19a depicts one fit example for the $I_c(\lambda)$

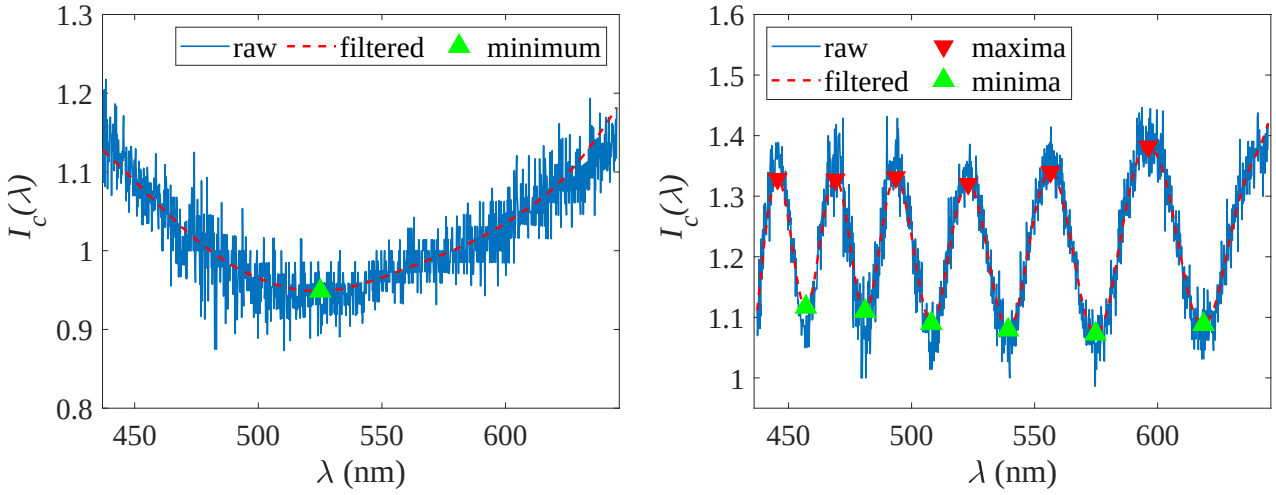

(a) $I(\lambda)$ profile with single minima at $x = 0.563\,\text{mm}$. (b) $I(\lambda)$ profile with minima and maxima at $x = 2.324\,\text{mm}$.

Figure 4.17: $I(\lambda)$ profiles for two points over x.

at $x' = 1\,\text{px}$ for the boiling case. The $h(x')$ profile is shown in Fig. 4.19b. For the lens case a similar distribution is obtained with $h \approx 710\,\text{nm}$. Next, we obtain the fringe map with bubble and ITO (lens on top of ITO for the validation case) I_c at a given t for $0 < t \leq t_{end}$ where t_{end} is the bubble life time from nucleation to departure from the wall. The following steps are similar as for the ITO where δ is the only unknown and $h(x)$ is known. A temporal sweeping is done for all the images during the bubble lifetime to get $\delta(x, t)$.

See for instance in Figs. 4.20a and 4.20b the fits between experimental and theoretical $I(\lambda)$ profiles for the validation and boiling cases, respectively. In these cases, $\delta = 34\,\text{nm}$ and $\delta = 6.48\,\mu\text{m}$ provided the best fits for the lens and for the boiling, respectively.

As discussed by Glovnea et al. [179], this methodology has two main benefits. First, the high frequency noise in the experimental data often requires the use of filters, smoothing or fitting curves. The task is then to find a curve that fits the experimental data the best. Second, the use of the entire intensity profile instead of just a few points of maxima or minima reduces the fitting error. For these reasons, this approach is chosen to compute δ in the case of boiling.

4.1.11 Validation: air layer thickness without spacer layer

The fringe maps shown in Fig. 4.8b and in Fig. 4.9b are now used to compute the thickness profiles by WLI and LI, respectively. They will be quantitatively compared to the actual film thickness calculated from the known lens curvature given by Eq. (4.44). For WLI, we determine $\delta(x)$ by $I(x)$ and $I(\lambda)$, as discussed in section 4.1.9. In LI, $I(x)$ is used.

4.1.11.1 WLI and LI: $I(x)$ profiles

The measurement of $\delta(x)$ for $\lambda = 573.49\,\text{nm}$ is shown in Fig. 4.21a. The lens curvature has been recovered successfully with a minimum measurable thickness δ^{min} of about 143.33 nm and 111 nm at $\lambda = 573.49$ and 443.57 nm, respectively. This is in accordance with the theoretical prediction of δ^{min} given in section 4.1.2. Fig. 4.21b shows that the relative measurement error, $\epsilon = (|\delta_{exp} - \delta_{theo}|)/\delta_{theo}$, decreases slightly with increasing λ. Overall, ϵ decreases exponentially from about 20% at a $\delta \approx 0.11\,\mu\text{m}$ to less than 5% for $\delta \geq 1\,\mu\text{m}$. For a fixed δ, one can also observe that ϵ varies only 5% within our spectral bandwidth thanks to the achromatic optical system which reduces the chromatic aberrations.

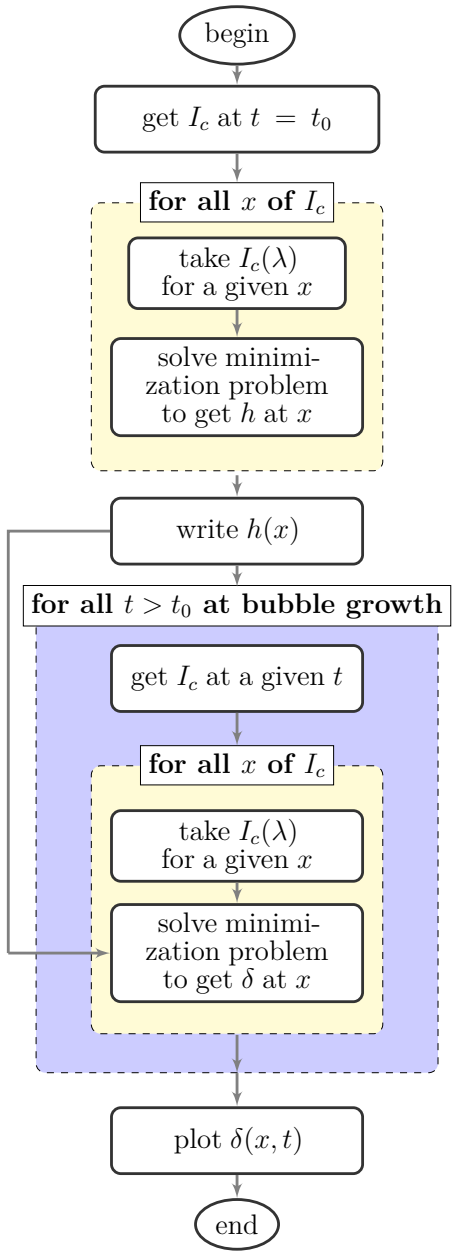

Figure 4.18: Flowchart to determine $\delta(x, t)$ in the case of ITO, spacer layer and bubble.

Figure 4.22a shows a good agreement of the experimental LI measurements with the reference data. The error decreases exponentially from about 16% at $\delta \approx 100\,\text{nm}$ to less than 5% for $\delta \geq 1\,\mu\text{m}$, see Fig. 4.22b.

The experimental thickness profiles are actually below the theoretical one, as shown in more details in Fig. 4.25. The lower thickness is explained by the use of the weights on top of the lens, as discussed in section 4.1.7.2. The absolute error is in the order of 50 nm, which is in a good agreement with the theoretical estimation (60 nm) given in section 4.1.7.2.

4.1.11.2 WLI: vertical ($I(\lambda)$) profiles

Fig. 4.23a shows that with such a method it is possible to recover the lens profile successfully with a similar precision as for the $I(x)$ profiles.

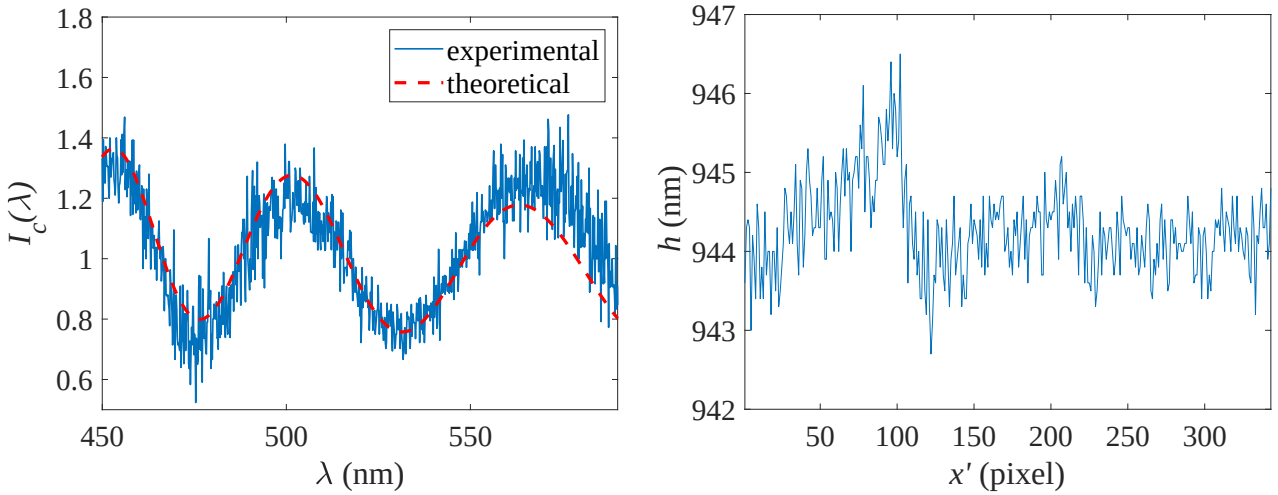

(a) Theoretical fit to experimental profile.

(b) ITO thickness along x'

Figure 4.19: Fringe profile and thickness of ITO film used for the boiling case at $t = 0$ just before the bubble nucleation ($\delta = 0$).

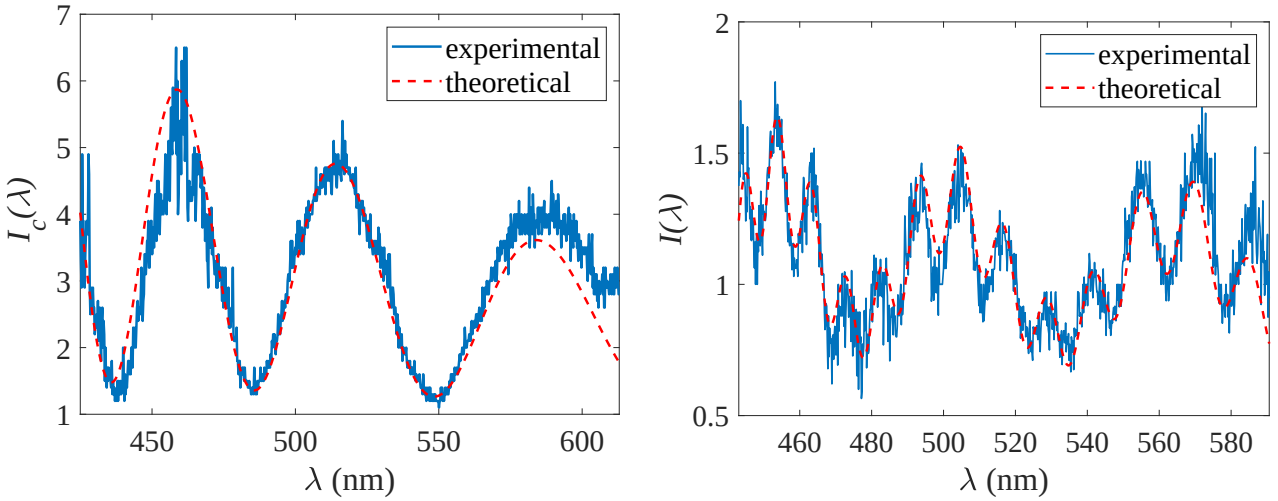

(a) Validation case (lens): $h = 710\,\text{nm}$ and $\delta = 34\,\text{nm}$.

(b) Boiling case: $h = 944\,\text{nm}$ and $\delta = 6.48\,\mu\text{m}$.

Figure 4.20: Fit of theoretical $I(\lambda)$ profiles to the experiment.

The measurement error of the film thickness is depicted in Fig. 4.23b. The maximum error is approximately 15% and it decreases to less than 5% for $\delta \geq 1\,\mu\text{m}$. Here, it should be mentioned that the $\delta^{min} = 262\,\text{nm}$. This occurs because of the nearly vertical orientation of the first constructive fringe (near the center) and its large thickness. However, we show in section 4.1.12 that this issue is overcame if the space layer is used because its thickness solely produces maxima and minima.

We have here the second advantage of WLI over LI. Thanks again to the λ axis, WLI provides more data points to compute δ for a fixed x. While LI the thickness is computed based on a single point, in WLI one can used as many points as the amount of maxima plus minima taking place within the visible wavelength bandwidth. Therefore, reducing the random error.

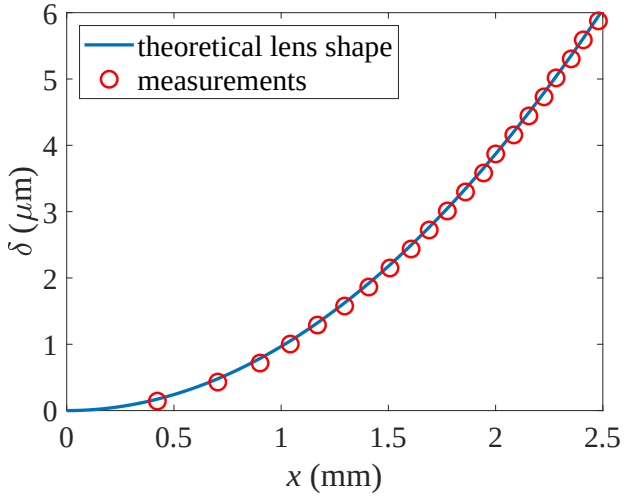

(a) Microlayer thickness under the lens of known curvature (line) and the experimental data (circles) for $\lambda = 573.49\,\text{nm}$.

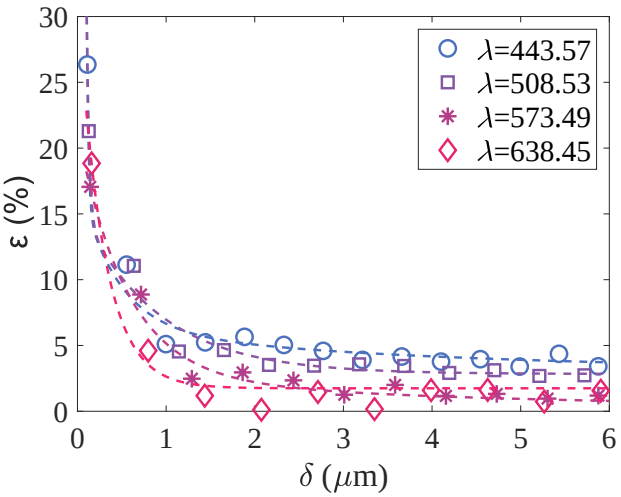

(b) Relative error (symbols) on the measurement of δ for different λ in nm. The dashed lines represent exponential fits.

Figure 4.21: Film thickness obtained by WLI from $I(x)$ profiles and its relative experimental error.

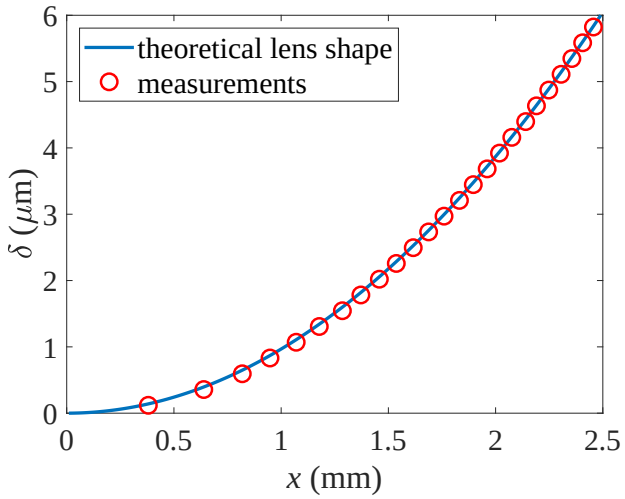

(a) Microlayer thickness under the lens of known curvature (line) and the experimental data (circles).

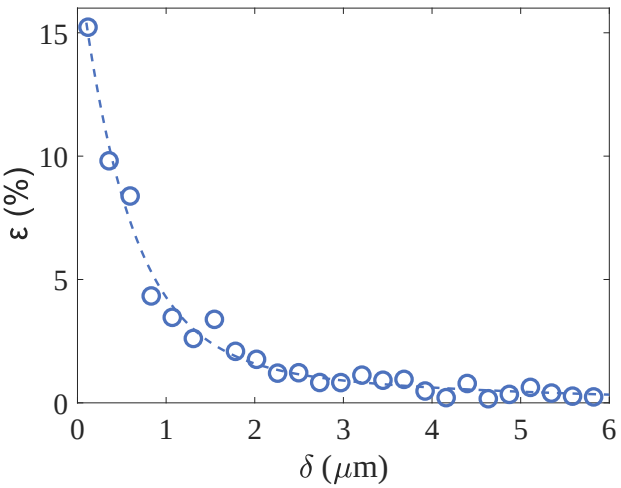

(b) Relative error on the measurement of the film thickness (circles). The dashed line represents an exponential fit.

Figure 4.22: Film thickness by LI and its relative error.

4.1.12 Validation: air microlayer thickness with spacer layer

Figure. 4.11b shows the fringe map for the ITO and lens case. In this particular case, the spatial resolution is roughly $7.2\,\mu\text{m/px}$ because of the use of a different camera with a smaller pixel size. The horizontal fringes in Fig. 4.11b are due to the interference from the ITO thickness, as seen in Fig. 4.11a, whereas the nearly vertical ones represent a contribution of ITO and the film. The width of the dark central region in Fig. 4.11b is smaller by half in comparison with the lens case without the spacer layer of Fig. 4.8b, creating fringes closer to $x = 0$. Fig. 4.20a shows a $I(\lambda)$ profile taken from the fringe map of Fig. 4.11b that corresponds to $\delta = 34\,\text{nm}$. Maxima and minima are now produced for $\delta < 100\,\text{nm}$ thanks to the spacer layer. The usefullness of the ITO film as a spacer layer is thus evident.

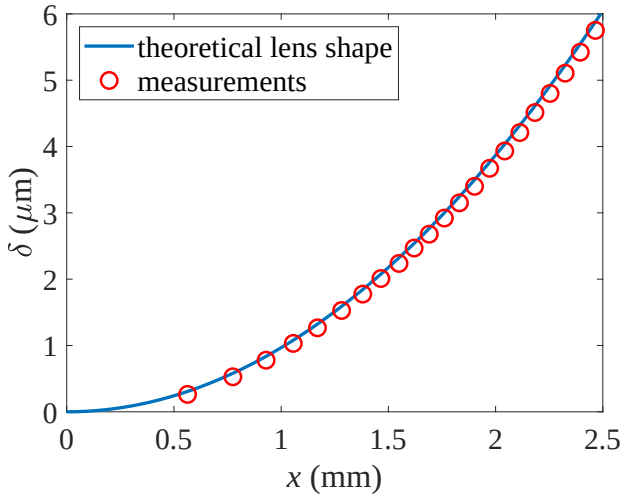

(a) Microlayer thickness under the lens of known curvature (line) and the experimental data (circles).

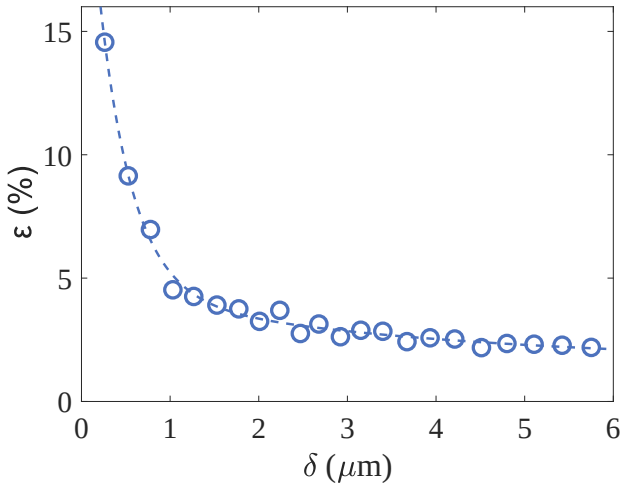

(b) Relative error of the measurement of film thickness. The line represents an exponential fit.

Figure 4.23: Film thickness by WLI and its relative error by $I(\lambda)$ profiles.

Fig. 4.24a shows the film thickness by WLI with spacer layer for the validation case. A good agreement between the experimental data and the theoretical lens shape is observed. The maximum relative error is approximately 60%, see Fig. 4.24b and decreases to about 10% at $\delta = 100\,\text{nm}$. The use of the spacer layer in WLI decreased δ_{min} from 100 nm to roughly 20 nm. This new limit is imposed by the spatial and spectral resolutions. It was possible to obtain thanks to a careful cleaning of the surfaces in the ultrasound bath so the thickness at the contact between ITO and lens is close to zero. Fringes for $x \leq 0.1\,\text{mm}$ are therefore not visible, which corresponds to the dark region around at $x = 0$ in Fig. 4.11b. This is another indication that indeed $\delta \sim 0$ at the contact point thus the shift of the lens with regards to its theoretical profile is minor. This is confirmed in Fig. 4.24a.

One should note that the (lateral) spatial resolution of our WLI is much rougher than the typical width of peaks on the ITO surface (shown as less than $0.5\,\mu\text{m}$ in Fig. 3.4). Our optical system thus works as a spatial filter taking the center line of the ITO surface height as its interface, which is roughly $20 - 30\,\text{nm}$ in Fig. 3.4a. Using Eq. (4.45), an estimation of the ITO displacement due to the use of the weight on top of the lens gives $\Delta\delta = 73\,\text{nm}$. One should note that the maximum height of the peaks is around 90 nm. Therefore, the weight displaces the lens downwards at the center line of surface height so that a zero thickness is seen by the WLI at the contact area. This explains why the dark region at the center of the fringe map appears and also the good agreement between theoretical and experimental lens shape. The microlayer thickness for the boiling case will be discussed in the next chapter.

4.1.13 Thickness resolution of measurements

The thickness resolution χ represents the smallest difference in thickness that can be measured between two experimental points. In LI, we define the thickness resolution as

$$\chi_{LI} = 1/(\delta_{max,N} - \delta_{min,N}) = 4n_3/\lambda_{laser}, \tag{4.52}$$

where $\delta_{max,N}$ and $\delta_{min,N}$ are the thicknesses determined from the maximum and its neighboring minimum defined by Eqs. (4.19,4.20). One gets $\chi_{LI} \approx 0.01\,\text{nm}^{-1}$ for the air-lens film. In WLI and for a given $I(x)$ profile (constant λ), it is the same value, regardless of calibration or camera resolution. On the other hand, in $I(\lambda)$ profiles (constant x), the thickness resolution, r_{WLI}, is obtained experimentally

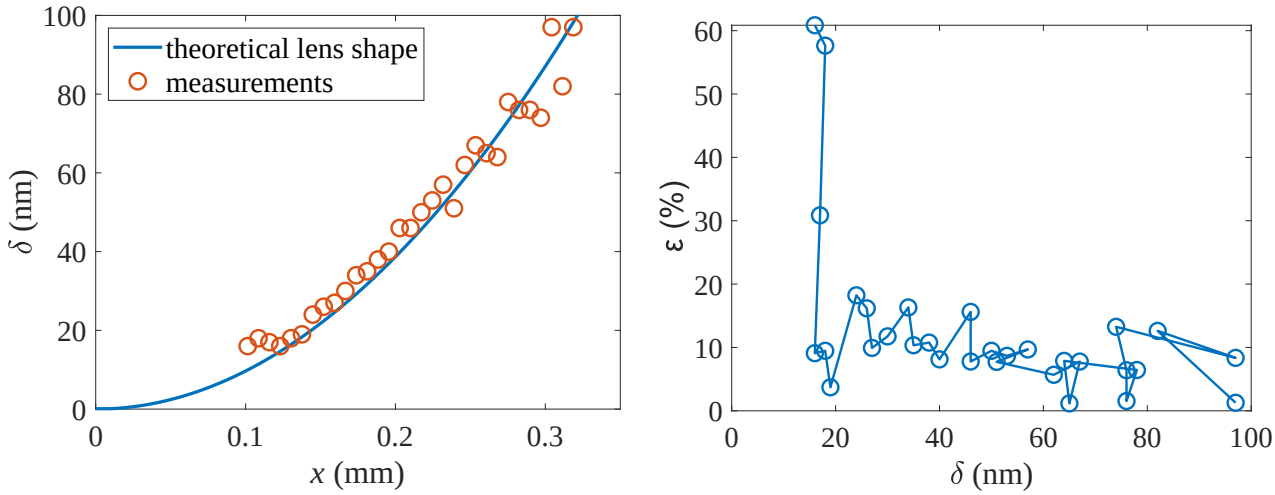

(a) Film thickness.

(b) Relative error.

Figure 4.24: Comparison between theoretical lens shape and WLI for $\delta < 100\,\text{nm}$.

by

$$\chi_{WLI} = 1/(\delta_{x_2'} - \delta_{x_1'}), \tag{4.53}$$

where $\delta_{x_2'}$ and $\delta_{x_1'}$ are measured at the adjacent pixels in x' axis, i.e. $x_2' - x_1' = 1\,\text{px}$. From the calibration of the x axis in Fig. B.3, this corresponds to one measurement roughly each 0.01 mm. Fig. 4.25 shows neighboring measurements of δ by LI and WLI for $1\,\text{mm} \leq x \leq 1.2\,\text{mm}$. In this particular case, the spatial resolution of WLI was roughly $11\,\mu\text{m/px}$. χ_{WLI} is higher than χ_{LI} by roughly a factor of six. Actually, χ_{WLI} by $I(\lambda)$ profiles is higher than χ_{laser} within the entire measurable thickness range in the lens case. One should note that in WLI, the thickness resolution can even be increased by increasing the resolution of the x axis. In LI, on the other hand, this feature does not exist. We have therefore, the third advantage of WLI over LI: The higher thickness resolution.

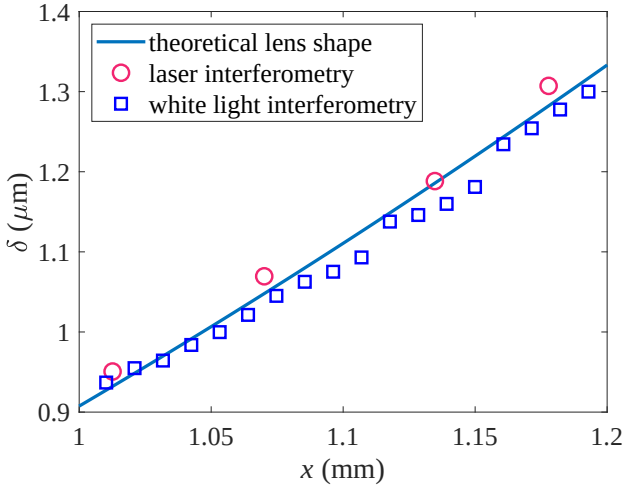

Figure 4.25: Measurements of neighboring thicknesses in the lens case without spacer layer by LI and WLI by $I(\lambda)$. The theoretical lens shape has been corrected to take into account the lens displacement in the experiment due to the Hertz contact as discussed in subsection 4.1.7.2.

4.1.14 Fringe quality

The experiments presented above were all carried out at steady-state conditions. However, boiling is a dynamic phenomenon with a timescale of ms. Therefore, to have enough temporal resolution one needs a frame rate acquisition of ms as well. In practice, this imposes an important issue in terms of fringe quality. Here, we mean as fringe quality its visibility V, and sharpness S, given, respectively, by

$$V = \frac{I_{max} - I_{min}}{I_{max} + I_{min}}, \tag{4.54}$$

$$S = \frac{1}{\xi}, \tag{4.55}$$

where I_{max} and I_{min} stand for the maximum and minimum intensities of the fringe, respectively. V is a measure of the fringe contrast ranging from 0 to 1 where $V = 1$ represents the maximum and $V = 0$ the absence of contrast. When V is sufficiently low, maxima and minima can no longer be distinguished. ξ stands for the full width in pixels between points where the intensity of a fringe falls to half of its amplitude.

In general, the light intensity decreases significantly with decreasing the exposure time (increasing the frame rate). Fringe quality also depends on the width of the slit at the entrance of the spectrometer. It determines the amount of light entering into it. The more open it is the more light it will be available. On the other hand, if the entrance is too narrow, less light reaches the CCD and effects of diffraction may blur the fringes.

To address the effect of the slit width and the exposure time on the fringe quality we use again the setup shown in Fig. 4.7 at steady-state condition. Fringe maps such as the one shown in Fig. 4.8b are obtained for several exposure times and slit widths.

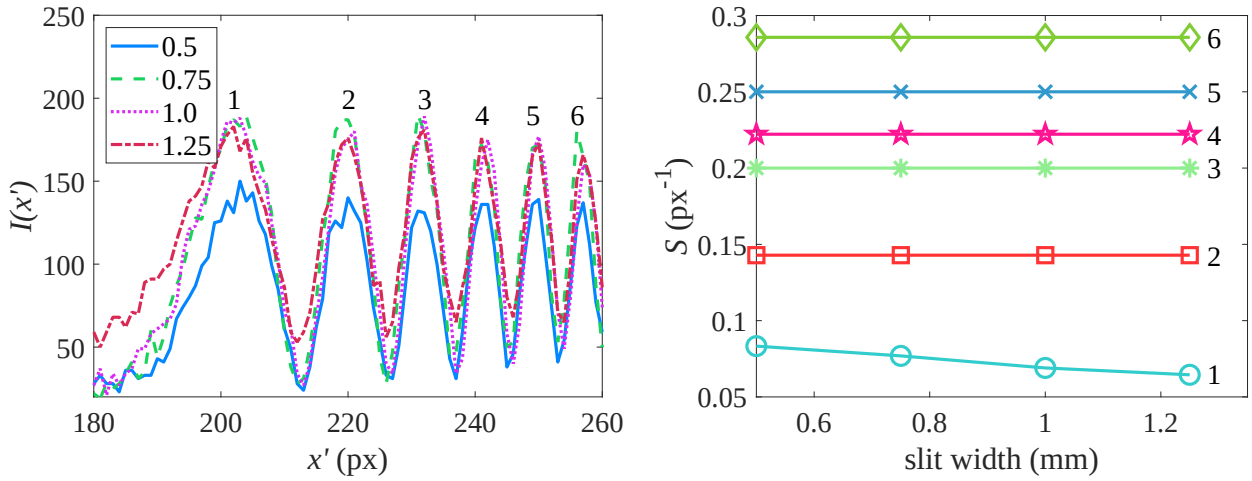

(a) $I(x')$ fringe profiles. The lines indicate the slit width in mm.

(b) Fringe sharpness. The symbols indicate the fringe order.

Figure 4.26: $I(x')$ profiles and fringe sharpness for different slit widths. The exposure time is 0.25 ms.

We first evaluate the fringe sharpness for a exposure time when the slit width is varied. $I(x')$ profiles of the six first fringes and their sharpness are shown in Figs. 4.26b and 4.26a, respectively, for slit widths of 0.5, 0.75, 1.0 and 1.25 mm. The exposure time is 0.25 ms. In Fig. 4.26b, the change in S is unimportant with the increase in the slit width. Similar results are observed for other exposure times. The increase in S with increasing N is due to the increase of the lens slope with x'.

The visibility is now computed for the exposure time of 0.25, 0.1, 0.067 and 0.05 ms. To simplify the analysis we compute the mean visibility, $\overline{V}$, of the first six fringes, which is shown in Fig. 4.27. On

can observe that setting the slit width to 1 mm provides the highest $\overline{V}$ for all exposure times. Also, $\overline{V}$ decreases when the slit width is increased from 1 to 1.25 mm. This effect is more pronounced for the exposure time of 0.25 ms due to a higher light intensity reaching the camera, which increases I_{min} but not I_{max}, see Fig. 4.26a.

We therefore set the slit width at 1 mm for our boiling experiments as it gives the highest V. However, we have verified a significant reduction in V during our boiling experiments with respect to the ones shown in Fig. 4.27. This is mainly caused by the use of the visible-IR beam splitter (not used for the study of fringe quality). Since the visible light beam for WLI has to cross it twice, the curves are shifted down. For this reason, our experiments were limited at exposure times of 0.25 ms.

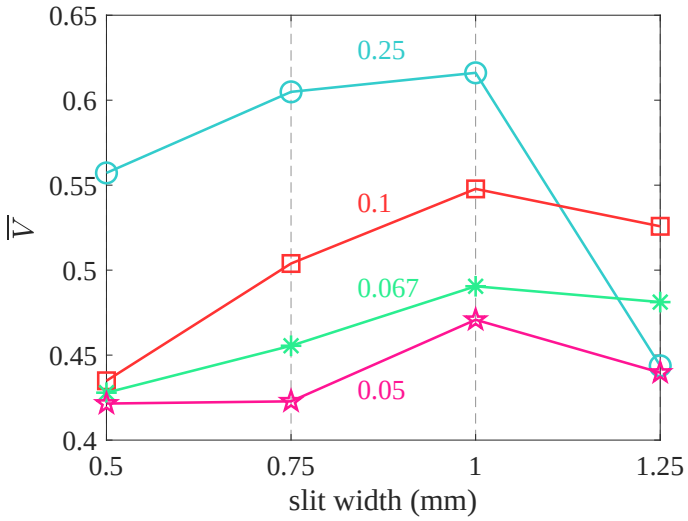

Figure 4.27: Mean visibility as a function of exposure time and slit width. The different symbols indicate different exposure times in ms.

4.1.15 Microlayer maximum slope limit

4.1.15.1 Theory

As any other experimental method, interferometry has its own limitations. Here, we address the microlayer maximum slope limit at which one can still observe and distinguish constructive from destructive fringes. This limit arises because the distance along x between two neighboring maximum and minimum, $x_{max} - x_{min}$, decreases with increasing with slope of the microlayer, see Figs. 4.15 and 4.21a. There exist then a maximum slope limit, θ_{lim}, at which the intensities of neighboring maxima $I(x_{max})$ and minima $I(x_{min})$ are attained at x_{max} and x_{min}, respectively, with $x_{max} - x_{min} = \mathsf{K}_{WLI}$, *i.e* the maximum and minimum are separated by a pixel at θ_{lim}. For $\theta > \theta_{lim}$, the spatial resolution is no longer capable of resolving the fringes. The schematics depicted in Fig. 4.28 illustrates this slope limit. Using the result of Eq. (4.21) for $\delta(x_{max}) - \delta(x_{min})$, the theoretical θ_{lim} is given by

$$\theta_{lim} = \arctan\left(\frac{\lambda}{4n\mathsf{K}_{WLI}}\right), \tag{4.56}$$

where K_{WLI} is given in section 4.1.6. The theoretical θ_{lim} computed by Eq. 4.56 is shown in Fig. 4.29 as a function of λ. For a microlayer of air, $0.45° \leq \theta_{lim} \leq 0.66°$. For the water microlayer in the boiling case, $0.33° \leq \theta_{lim} \leq 0.49°$.

For the lens case in Fig. 4.7, the relationship between δ and the coordinate x is given by Eq. 4.44.

By solving for δ and taking the first derivative with respect to x one obtains

$$\frac{\mathrm{d}\delta}{\mathrm{d}x} = \tan\theta = \frac{x}{\mathtt{R} - \delta}. \tag{4.57}$$

At $\theta = \theta_{lim}$, $x = x_{lim}$ and for the lens case, $\mathtt{R} \gg \delta$, θ_{lim} is then given by

$$\theta_{lim} = \arctan\left(\frac{x_{lim}}{\mathtt{R}}\right). \tag{4.58}$$

Substituting this result into Eq. (4.56), one obtains

$$\lambda_{lim} = \frac{4n\mathsf{K}_{WLI}}{\mathtt{R}} x_{lim}. \tag{4.59}$$

This expression locates the position of θ_{lim} as a line in the $I(x, \lambda)$ fringe map with a slope of $4n\mathsf{K}_{WLI}/\mathtt{R}$.

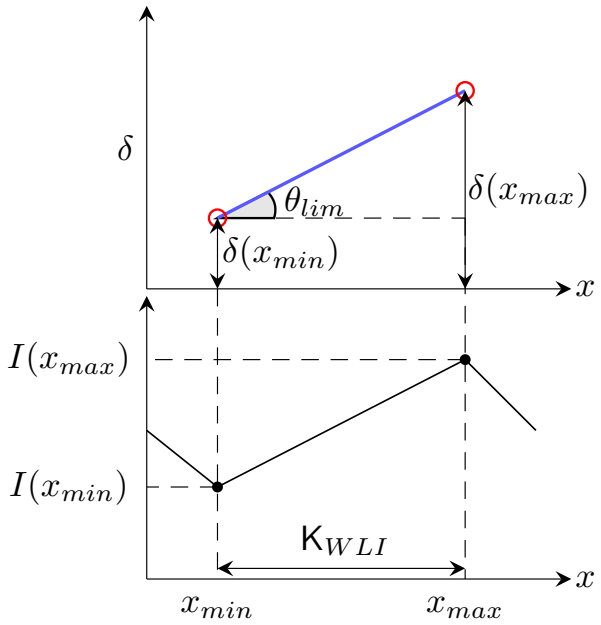

Figure 4.28: Schematics of maximum slope limit θ_{lim}.

4.1.15.2 Experiment

In Fig. 4.8, however, we were not able to determine θ_{lim} experimentally because of its high $\mathtt{R}$ thus $\theta < \theta_{lim}$ for the whole x axis. We used then a second plano-convex lens (Thorlabs model LA1461) with $\mathtt{R} = 128.8\,\mathrm{mm}$. The fringe map obtained is shown in Fig. 4.30. The axis of fringe symmetry is centered at $x = 0$. One can distinguish two regions. One, closer to $x = 0$ with visible fringe patterns and another at $x > x_{lim}$ where fringe can not be seen so one can say that they are invisible to our optical system. To identify $x_{lim}(\lambda)$, we try to recover the lens profile by $I(x)$ as discussed in section 4.1.9. Fig 4.31a shows one example for $\lambda = 463.04\,\mathrm{nm}$. Indeed, one can not recover the lens shape for $x \gtrapprox 1\,\mu\mathrm{m}$ because maxima and minima can no longer be distinguished when $\theta \geq \theta_{lim}$. To improve the accuracy on x_{lim} determination, we plot the relative error as a function of x, as shown in Fig 4.31b. For $x < 1.036\,\mathrm{mm}$, $\theta < \theta_{lim}$ and ε decreases with increasing x. This is the typical trend seen when fringes are still visible. However, at $x = 1.036\,\mathrm{mm}$, ε increases sharply since the fringes are no longer observed (one measures only the noise of the CCD) thus the error increases. This point corresponds to x_{lim} of θ_{lim}. On then knows the experimental x_{lim} at a given λ. This procedure is then repeated for many λ so that one can have x_{lim} along the visible spectrum.

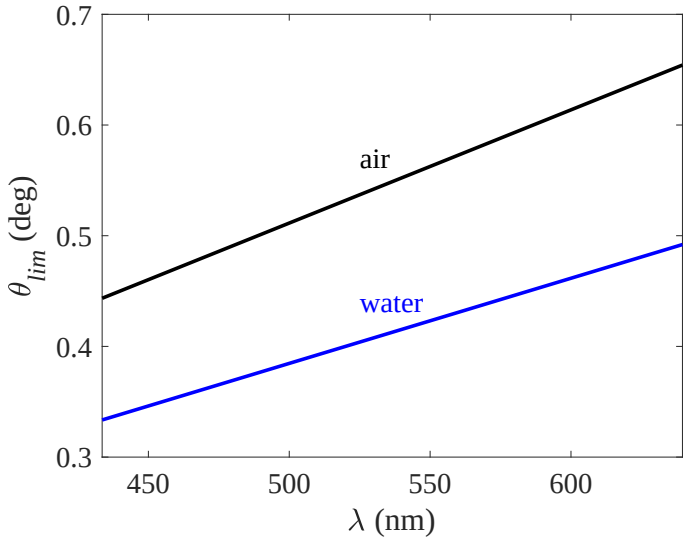

Figure 4.29: Theoretical θ_{lim} as a function of λ for layers of air and water.

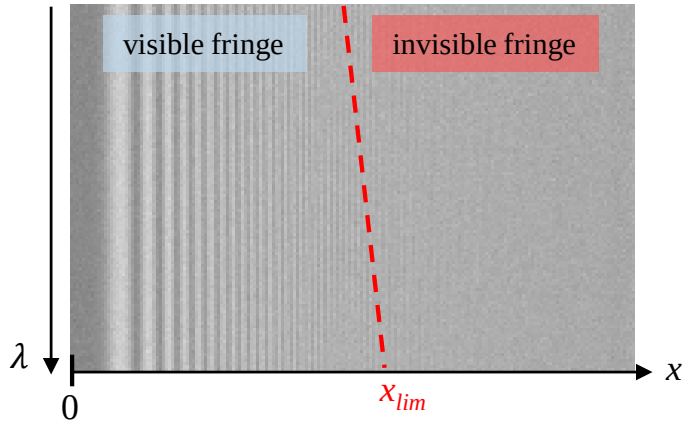

Figure 4.30: Fringe map showing visible and invisible fringe regions.

In Fig 4.32, we plot the theoretical and experimental positions of θ_{lim} at a $x - \lambda$ figure that represents the $x - \lambda$ fringe map for our visible bandwidth and for half the width of our x axis. The theoretical position is determined by Eq. (4.59). For $x < x_{lim}$ the fringes are visible with our optical system. However, for $x > x_{lim}$, the fringes can not be distinguished. The linear relationship between x_{lim} and λ is confirmed by the experiments. One should note that the good agreement between theory and experiment shown in Fig 4.32 for the lens case validates our theoretical θ_{lim} depicted in Fig 4.29. Therefore, one is expected to observe the fringe in the whole WLI spectrum only for microlayer slopes below 0.3° in boiling.

4.2 Infrared thermography

4.2.1 Theory

Electromagnetic radiation with wavelength ranging from 780 nm up to 1 mm is classified as infrared (IR) radiation. Stefan-Boltzmann law states that the hotter the object is, the more IR radiation it will emit. Temperature measurements are then possible by reading the intensity of this radiation with an infrared thermal camera. Based on a calibration curve it is possible to know the target's

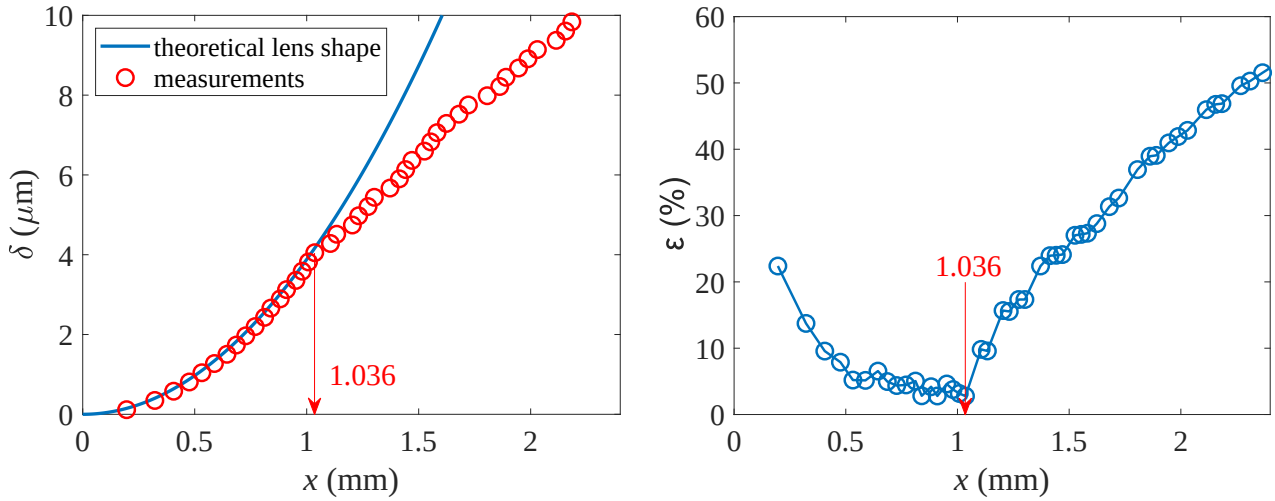

(a) Experimental lens profile.

(b) Relative error.

Figure 4.31: Experimental WLI maximum slope limit of measurements at $\lambda = 463.04\,\text{nm}$. At this λ, $\theta_{lim} = 0.451°$.

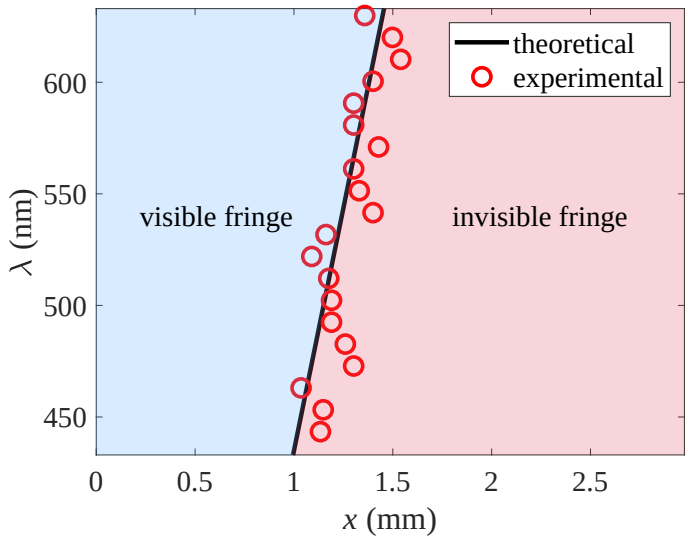

Figure 4.32: Theoretical and experimental x_{lim} in the $x - \lambda$ map.

temperature. This calibration can be performed by the camera's manufacture, for instance, by using standard sources of radiation known as black bodies in a controlled laboratory environment. A black body is defined as an object capable of absorbing all the radiation impinging on it at any wavelength. It is also an ideal emitter. It means that only another black body can emit as much IR radiation at same temperature. However, most of the materials are non-black body radiators, known as gray bodies. They are related by the emissivity, $\varepsilon_w(\lambda, T_w)$, defined as:

$$\varepsilon_w(\lambda, T_w) = \frac{W(\lambda, T_w)}{W^b(\lambda, T_w)}, \tag{4.60}$$

where $W(\lambda, T_w)$ and $W^b(\lambda, T_w)$ stand for the spectral emitted powers of the object and black body, respectively. Thus, the emissivity $\varepsilon_w(\lambda, T_w)$ characterizes the capability of an object to emit thermal radiation compared to the black body at the same temperature and wavelength. It varies according

to the material, surface treatment and oxidization level, for instance. It also depends on wavelength and temperature.

The Plank's law describes $W^b(\lambda, T_w)$ at thermal equilibrium at temperature T_w. It is expressed as [205]

$$W^b(\lambda, T_w) = \frac{C_1}{\lambda^5 \left[\exp\left(\frac{C_2}{\lambda T_w}\right) - 1\right]}; \tag{4.61}$$

where $C_1 = 3.74 \times 10^{-16}\,\mathrm{W\,m^2}$ and $C_2 = 1.44 \times 10^{-2}\,\mathrm{m\,K}$ represent the first and second radiation constants. By integrating Plank's distribution, Eq. (4.61), in the whole spectral range one obtains the Boltzmann equation:

$$\mathcal{W}^b(T_w) = \int_0^\infty W^b(\lambda, T_w) d\lambda = \boldsymbol{\sigma} T_w^4; \tag{4.62}$$

which express the total emitted power of a black body, where $\boldsymbol{\sigma} = 5.67 \times 10^{-8}\,\mathrm{W/(m^2\,K^4)}$ is the Boltzmann constant. For a gray body the emissivity is introduced and the Boltzmann equation becomes:

$$\mathcal{W}(T_w) = \varepsilon_w \boldsymbol{\sigma} T_w^4. \tag{4.63}$$

Kirchhoff's law states that the spectral emissivity $\varepsilon_w(\lambda)$ of a given material at temperature T_w is the same as its spectral absorbance $\mathcal{A}_w(\lambda)$ at the same T_w. Thus, one writes [205]

$$\varepsilon_w(\lambda) = \mathcal{A}_w(\lambda), \tag{4.64}$$

for a diffuse irradiation or a emitter with diffuse surface.

4.2.2 Sources of IR radiation

Fig. 4.33 shows a schematics of the thermal radiation sources in our experimental setup. Our object to be measured is the ITO deposited on top of the MgF_2 optical porthole. Here, we denote IR as the mid-infrared bandwidth from 3 to 5 μm. This corresponds to the spectral range of our IR camera. The goal is to use the camera to capture the IR radiation emitted by the ITO. However, the environment where the measurements are performed also has influence on the IR radiation entering the camera. One can mention first the surrounding objects, which comprises the boiling cell, other cameras, optical table, computers and laser that are in a close vicinity, that also emit or reflect an amount of radiation W_s that strikes the ITO. Most of this impinging radiation will be reflected by the ITO towards the camera owing its high reflectivity to IR ($\mathcal{R}_w \approx 0.7 - 0.85$, cf.). Second, the atmosphere between the porthole and the camera has two effects: It emits a thermal radiation W_{atm} and attenuates the radiation reflected and emitted from the ITO, denoted as W_r' and W_w', respectively. Here, the subscripts w, p, hm, r, atm and sur indicate the wall (ITO), MgF_2 porthole, hot mirror (visible-IR beam splitter), reflected light by the ITO, atmosphere and surroundings, respectively. The total power radiation entering the camera is then given by:

$$W_{tot} = \mathcal{R}_{hm} \left(W_r + W_w + W_{atm}\right), \tag{4.65}$$

where $\mathcal{R}_{hm}$ stands for the reflectance of the hot mirror (visible-IR beam splitter) given in section 3.4.1. Considering that the atmosphere has a transmittance $\mathcal{T}_{atm}$, the ITO an emissivity and reflectance ε_w and $\mathcal{R}_w$, respectively, and the porthole has a transmittance $\mathcal{T}_p$, one can use Eq.(4.60) to rewrite each term on the R.H.S of Eq.(4.65) as

$$W_r = \mathcal{T}_{atm} W_r' = \mathcal{T}_{atm} \mathcal{T}_p^2 \mathcal{R}_w \varepsilon_{sur} W_{sur}^b, \tag{4.66}$$

$$W_w = \mathcal{T}_{atm} W_w' = \mathcal{T}_{atm} \mathcal{T}_p \varepsilon_w W_w^b, \tag{4.67}$$

$$W_{atm} = \varepsilon_{atm} W_{atm}^b, \tag{4.68}$$

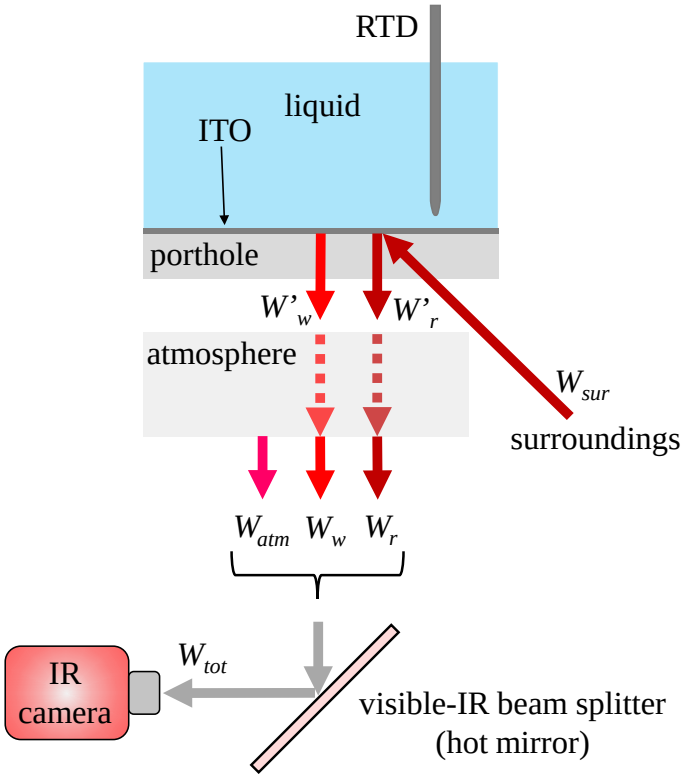

Figure 4.33: Schematics of the infrared radiation sources. The hot mirror is at 45° with regards to the optical axis of the IR camera.

where ε_{sur} stands for the emissivity of the surroundings. The incident radiation at any medium can be absorbed, transmitted and reflected. For the ITO, opaque to IR, we have $\mathcal{T}_w = 0$ and using Eqs. (3.10,4.64), the ITO reflectance is given as

$$\mathcal{R}_w = 1 - \varepsilon_w. \tag{4.69}$$

For the atmosphere, $\mathcal{R}_{atm} = 0$. Using Eqs. (3.10,4.64) for the atmosphere, one thus writes

$$\varepsilon_{atm} = 1 - \mathcal{T}_{atm}. \tag{4.70}$$

Substituting Eqs.(4.69) and (4.70) into Eqs.(4.66) and (4.68), respectively, and considering that all the radiation impinging on the surrounding surfaces will be absorbed by the same surfaces, $\mathcal{A}_{sur} = \varepsilon_{sur} = 1$, one obtains

$$W_r = \mathcal{T}_{atm}\mathcal{T}_p^2(1-\varepsilon_w)W^b_{sur}, \tag{4.71}$$

$$W_{atm} = (1-\mathcal{T}_{atm})W^b_{atm}. \tag{4.72}$$

Substituting Eqs.(4.67,4.71,4.72) into Eq.(4.65) and solving it for W^b_w, one obtains the expression for the radiation emitted from the ITO, given by

$$W^b_w = \frac{1}{\mathcal{R}_{hm}\mathcal{T}_{atm}\mathcal{T}_p\varepsilon_w}W_{tot} - \frac{\mathcal{T}_p(1-\varepsilon_w)}{\varepsilon_w}W^b_{sur} - \frac{(1-\mathcal{T}_{atm})}{\mathcal{T}_{atm}\mathcal{T}_p\varepsilon_w}W^b_{atm}. \tag{4.73}$$

where W^b_w is related to T_w by a calibration curve. In the R.H.S of Eq. (4.73), W_{tot} is the overall IR radiation captured by the camera whereas all the other parameters are unknown. It shows that one should know ε_w and compensate the contribution of the surroundings and atmosphere on the measurement. The calibration procedures are discussed below.

4.2.3 Calibration

There are essentially three different methods to calibrate an IR camera for boiling investigations. Here, we describe them briefly.

- **Method 1: Using the camera build-in curve.** One can uses the camera calibration curve to relate W_w^b to T_w. In this case, the first disadvantage is that all the parameters in the R.H.S of Eq. (4.73), except W_{tot}, have to be informed. Measurements of the atmosphere humidity and temperature(for W_{atm}^b) and ε_w are required. The second disadvantage is that the calibration curves used by the camera depend on the temperature range being measured, which may not be known *a priori*. The third complication is that the determination of W_{sur}^b isn't straightforward. For instance, it requires the MgF_2 to be replaced by a gold or silver mirror so that all the impinging radiation from the surroundings is reflected to the camera and a measure of W_{sur}^b can be given in terms of an apparent reflected temperature [206].

- **Method 2: Modelling the IR radiation**. This method consists of modeling the whole IR radiation problem as presented by Bucci et al. [81]. This is indicated when sapphire portholes are used, for instance. Sapphire has an uneven spectral absorption of the IR radiation emitted by the ITO. As a result, the sapphire emits IR radiation towards the camera, contaminating the measurement. The disadvantage is that a series of extra measurements is also required for the calibration.

- **Method 3: Intensity-Temperature.** An alternative method is to perform an in-situ calibration at steady-state conditions using a RTD inside the cell as depicted in Fig. 4.33. A relationship between the overall radiation W_{tot}(expressed as intensity in this case) and T_w (given by the RTD) can be established. The advantage of this method is that no extra measurements are required.

Given that MgF_2 is transparent to IR, the most suitable and less time consuming approach is the intensity-temperature method, which has been also used by other groups for similar studies [9, 12, 125]. The calibration procedure of our IR camera is the following: with the ITO at steady-state and the boiling cell at uniform temperature, the intensity I of each pixel is recorded by the IR camera. The temperature T_w of the ITO is given by the measurement from a resistance thermal detector (RTD) positioned inside the boiling cell, as shown in Fig. 4.33. This is done for different temperatures within the range $40\,°C \leq T \leq 100\,°C$. T_w and I are then related by a physical based calibration formula which is obtained from the theory of IR radiation presented in section 4.2.1.

Important practical issues should be mentioned here. The pixel wise calibration avoids effects of vignetting and bad pixels on the measurements. Vignetting is a radial intensity attenuation from the center to the edges of the camera's sensor due the multiple optical elements in the objective. Bad pixels represent a sharp drop in intensity, which can be due the presence of dust particles in the sensor or a malfunctioning of the pixel, for instance. Also, the hot mirror in Fig. 4.33 has to be slightly tilted so that the Narcissus effect is avoided. It occurs when the detector sees itself by the reflection from the ITO owing its high reflectance in IR. The detector is cooled down, so that an intensity much lower than the expected will be displayed. This tilting has no practical effects on the temperature measurement once calibration and measurements have been performed with the same tilting angle.

4.2.3.1 Theoretical calibration

Considering the optical path of the IR radiation from the ITO up to sensor of the IR camera as illustrated in Fig. 4.33, one can mention the reflectance of the hot mirror $\mathcal{R}_{hm}(\lambda)$, the transmittance $\mathcal{T}_{IR,obj}(\lambda)$ of the IR camera's objective and the normalized response sensitiveness $\mathcal{S}_{IR,det}(\lambda)$ of the IR

detector. They are included into Eq. (4.62), which is integrated from λ_1 to λ_2 for a given temperature T_w. Therefore, one writes

$$I(T_w) = \int_{\lambda_1}^{\lambda_2} \mathcal{R}_{hm}(\lambda)\mathcal{S}_{IR,det}(\lambda)\mathcal{T}_{IR,obj}(\lambda)W^b(\lambda, T_w)d\lambda; \tag{4.74}$$

where $\mathcal{W}^b(T) = I(T_w)$ because, in practice, $\mathcal{W}^b(T)$ represents the intensity of the IR radiation recorded by the camera. The integration is performed from $\lambda_1 = 2.5\,\mu$m up to $\lambda_2 = 3.5\,\mu$m because $\mathcal{S}_{IR,det}(\lambda)$ and $\mathcal{T}_{IR,obj}$ do not increase sharply at $3\,\mu$m and suddenly drops to zero at $5\,\mu$m as shown in Fig. 4.34. $\mathcal{S}_{IR,det}(\lambda)$ and $\mathcal{T}_{obj}(\lambda)$ were obtained from the camera's manufacturer. $\mathcal{R}_{hm}(\lambda)$ is given in Fig. 3.6b. Given that we measure I to get T_w, it is appropriate to work with $T_w = f(I)$. As discussed by Sielaff [125] and Schweikert et al. [207], the best fitting curve that relates T_w(K) with I is expressed as

$$T_w = A_1\left[(I + A_2)^{1/4} + A_3\right]; \tag{4.75}$$

where A_1, A_2 and A_3 are fitting constants that account for the surrounding radiation, emissivity of the ITO and atmosphere attenuation. One should note that the calibration is pixel-wise. This means that each pixel has its own fitting coefficients. Figure 4.35a shows the integral of Plank's law (obtained with Eq. (4.74)) and the fit given by Eq. (4.75) for a wide range of T_w. The fit represents the integral of Plank's law with a root mean square error of 0.07 °C. Therefore, the formula expressed by Eq. (4.75) represents well the theory of Eq. (4.74) and one can use it for fitting the experimental calibration points. The uncertainty on T_w is estimated to be ± 0.75 K.

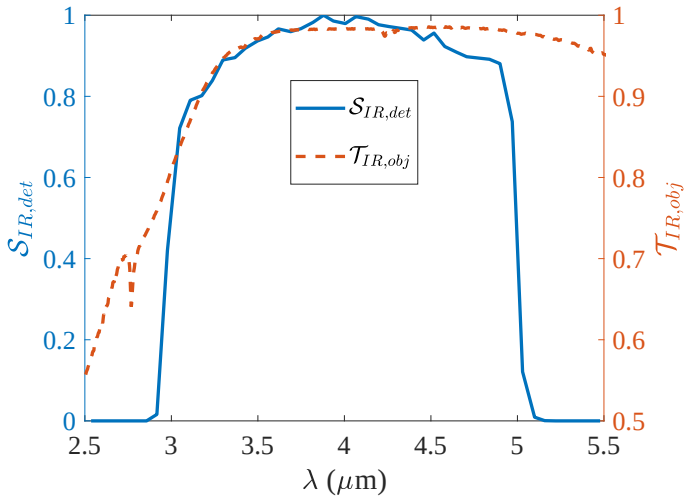

Figure 4.34: Spectral transmittance of the IR camera's objective and sensibility of the IR camera detector. Data provided by FLIR.

4.2.3.2 Experimental calibration

Figure 4.35b shows the experimental calibration points for a given pixel. Six calibration points are obtained within the range of temperature of $50(°C) \leq T \leq 100(°C)$. Equation (4.75) is used to fit the data. The fit represents the calibration points with a root mean square error of 0.4 K. One should note that the cell is at atmospheric pressure thus calibration points beyond the saturation temperature ($T_{sat} = 100$ °C) are not possible. During the bubble growth, the wall temperature will be higher than T_{sat} and we need to extrapolate the calibration range. However, the error is expected to be minor thanks to the use of a physical based fitting curve.

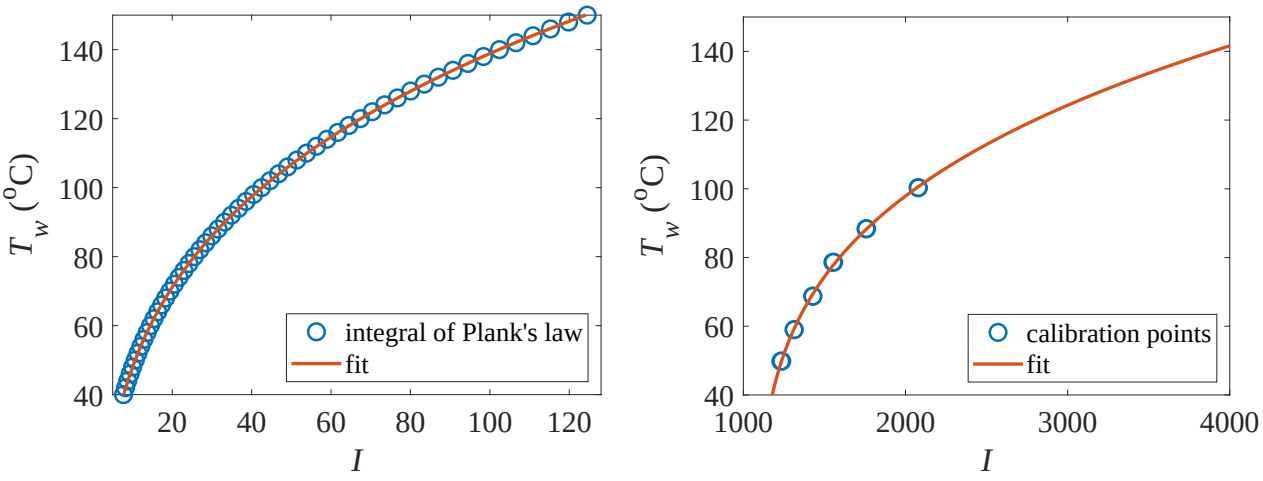

(a) Theoretical fit.

(b) Experimental fit.

Figure 4.35: IR thermometry calibration fits.

The spatial resolution for the IR thermometry is 84 μm/px. It has been obtained by imaging the hole (with known diameter) of the porthole in which the MgF_2 is glued on such as shown in Fig. 4.36. A circle fits well the circular hole thus one can conclude that the optical deformation on the temperature distribution due to the tilting of the hot mirror is negligible.

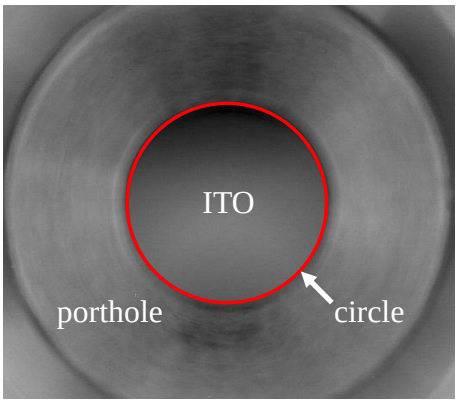

Figure 4.36: IR image of the hole into which the MgF_2 porthole is installed.

4.3 Sidewise shadowgraphy

The optical observation by sidewise shadowgraphy (SWS) consists in shining light at one side of the boiling cell towards the bubble through the lateral transparent optical windows to record the macroscopic bubble dynamics with a high speed camera at the opposite side, as the schematics depicted in Fig. 4.37. Due to the bubble's curvature, the light striking its interface will be deviated and it does not reach the CCD. The light rays that do not cross the bubble will travel straight through the liquid pool reaching the CCD. Therefore, the bubble's shadow is projected towards the camera and one sees it as a black area while the surrounding liquid is white as shown in Fig. 4.38a.

We use a collimated LED (light emitting diode) light source for background illumination and a telecentric objective. It only collects the light rays parallel to its optical axis and has fixed magnification factor, working distance and field of view. This optical apparatus provides a few advantages

in comparison to ordinary lenses. First, it increases the sharpness of the bubble's image at its interface as seen in Fig. 4.38a. Second, it increases the depth of field (the distance between the nearest and furthest points along the bubble diameter where its interface is still sharp), facilitating the focus adjustment during the experiment. Third, it eliminates the error due to parallax (perspective error) because its magnification does not change with the distance to object.

The spatial calibration of the camera has been performed similarly as described for the WLI in section 4.1.6. The spatial resolution for the SWS, expressed by K_{SWS}, is 32 μm/px.

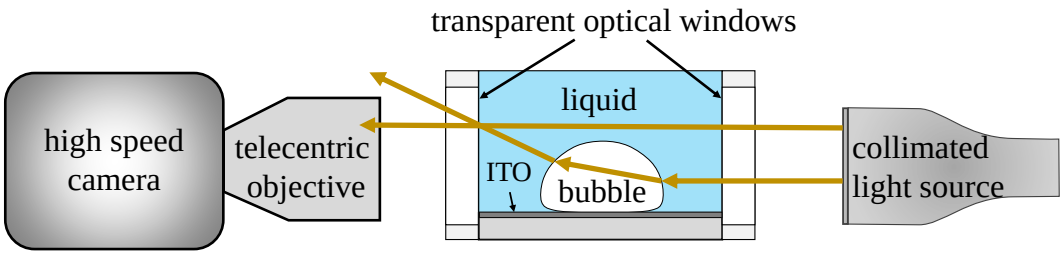

Figure 4.37: Illustration of the sidewise shadowgraphy observation.

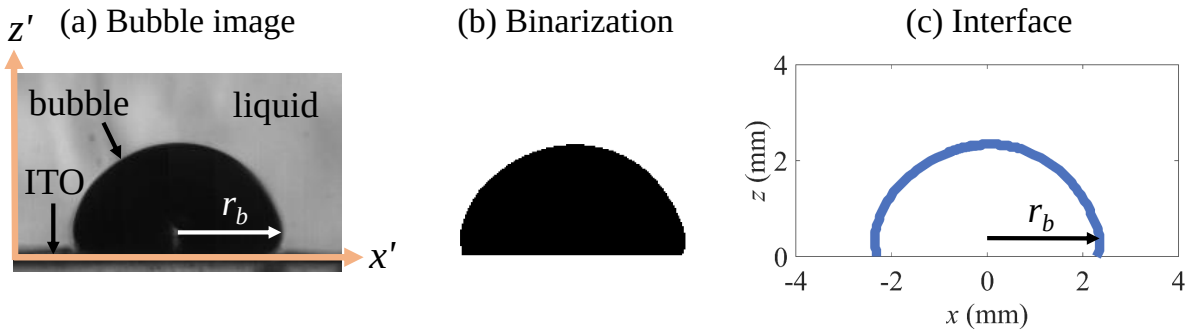

Figure 4.38: Image post-processing for sidewise shadowgraphy.

4.3.1 Image post-processing

The two main goals of using SWS are to measure the bubble radius and detect its macroscopic interface. The post-processing procedure is the following: First, we take horizontal $I(x')$ and vertical $I(z')$ intensity profiles across the bubble. Fig. 4.39 shows a $I(x')$ profile taken from the bubble image in Fig. 4.38a. In order to detect the bubble interface we define an intensity threshold value $I_{th} = I_{max}/2$ where I_{max} stands for the maximum intensity in the image, roughly 160 in Fig. 4.38(a). Therefore, the pixels x' which $I(x') \leq I_{th}$ are assigned as zero corresponding to vapor and one (liquid bulk) for $I(x') > I_{th}$. One obtains a binary image as shown in Fig. 4.38(b). The interface is then detected at neighboring dark and bright pixels as shown in Fig. 4.38(c), from which the bubble radius can be obtained. The uncertainty on the interface positioning is ± 0.16 mm which corresponds to a 10 pixels wide transition from high to low intensity in Fig. 4.39. For the $I(z')$ profiles the procedure is similar. However, $I(z')$ are taken only near the bubble cap where $I(x')$ cannot recover properly the interface because of the nearly local horizontal orientation.

From Fig. 4.38c) one can compute the volume of the bubble V_b. It is given by summing up the volume of all discs with diameter $x_{z,max} - x_{z,min}$ at the height z from the bubble base up to its cap. x_{max} and x_{min} are the coordinates of the points at the bubble interface in the right($x > 0$) and

left($x < 0$) sides, respectively, for a fixed z with the size of a pixel. Thus, one writes

$$V_b = \frac{\pi}{4} \sum_{z=1}^{z_{cap}} (x_{z,max} - x_{z,min})^2 \mathsf{K}_{SWS}. \tag{4.76}$$

where $z = 1$ and $z = z_{cap}$ correspond to the bubble base and cap, respectively.

The bubble growth rate is often expressed in the literature [12, 208] by an equivalent bubble radius $r_{b,eq}$. It represents the radius that a sphere of vapor would have with the volume V_b. Thus, one can write

$$r_{b,eq} = \left(\frac{3}{4\pi} V_b \right)^{1/3}. \tag{4.77}$$

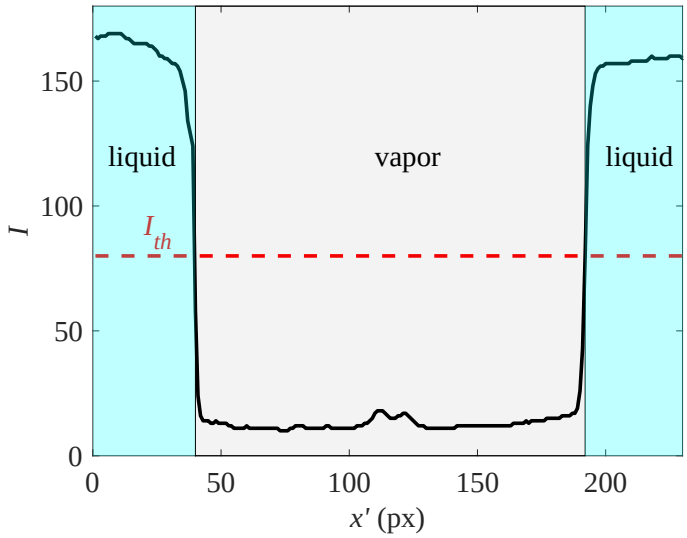

Figure 4.39: $I(x')$ profile across the bubble.

4.4 Summary and concluding remarks

In this chapter, film thickness measurements have been addressed by laser and white light interferometry. A test case is used to validate the experimental apparatus and methods. It consists on measuring the thickness of a film created between a flat porthole and plano-convex lens with well known curvature. The interference between reflected rays from the film creates a map with constructive and destructive fringes, which is used to determine the film thickness. We highlight the following remarks:

- WLI is free from unwanted interference caused by reflections from thick optical elements thus the fringe map is not contaminated.
- WLI and LI can both recover the theoretical lens shape with similar errors. Thus, our WLI experimental setup has been successfully validated.
- We have shown that in WLI $\delta(x) \propto \lambda$ so that the spectrum of the fringes have the same geometry as the microlayer. A qualitative inference on the microlayer profile is therefore possible without any image post-processing.
- More data for computing the film thickness is obtained in WLI compared to LI thus reducing the random error.

- The thickness resolution by WLI is higher than LI.
- In WLI, the ITO works as spacer layer reducing the minimum thickness that can be measured.

We also present a pixel-wise calibration procedure to measure the wall temperature by IR thermometry. A physical based fitting curve relates the intensity of the IR radiation pixel by pixel on the camera with the actual temperature at the wall.

Our sidewise shadowgraphy apparatus is also presented. The use of a collimated light source with a telecentric objective eliminates many sources of error due to optical aberration and thus provides an better precision of detection of the bubble macroscopic interface.

Chapter 5

Near-wall phenomena in nucleate boiling

5.1 Generalities . . . 83
5.2 Bubble nucleation, growth and departure . . . 84
5.3 Bubble, dry spot and microlayer radii . . . 85
5.4 Microlayer dynamics . . . 85
5.4.1 Simple bump model . . . 87
5.4.2 Numerical simulation of the microlayer dynamics . . . 88
5.5 Wall temperature . . . 89
5.6 Wall heat flux . . . 92
5.6.1 Heat transfer in ITO . . . 92
5.6.2 Heat transfer in MgF_2 . . . 93
5.6.3 Heat flux reconstruction and interfacial resistance . . . 94
5.7 Microlayer evaporation contribution to bubble growth . . . 97
5.8 Dewetting dynamics . . . 98
5.9 Discussion . . . 99
5.9.1 Microlayer and contact line evaporation regimes . . . 99
5.9.2 Homogeneous versus local heating: effect on contact line dynamics . . . 100
5.9.3 Effects of enlarged heating spot . . . 102
5.10 Summary and concluding remarks . . . 102

5.1 Generalities

In this section we present the dynamics of the microscale physical phenomena of a single bubble in nucleate boiling regime. The bubble is triggered by local heating with the IR laser, as depicted in Fig. 5.1. As discussed in section 3.3, the heating surface is nanometrically smooth so a strong laser power is needed to induce nucleation. However, in this case the bubble growth is very fast. In addition, the local heat flux may exceed the CHF so the heater burns out very quickly as soon as the bubble nucleates. It was found out that a defect is needed, cf. subsection 2.5.1. It was created *in situ*, by slightly burning the heater. This has been achieved by carefully choosing the smallest possibly power to overcome the nucleation barrier.

As mentioned before, about a hundred of bubble nucleation events for a dozen of boiling surfaces and at different positions over the heater were carried out. We have selected only one for presentation here, many others being similar. It was selected because of several reasons:

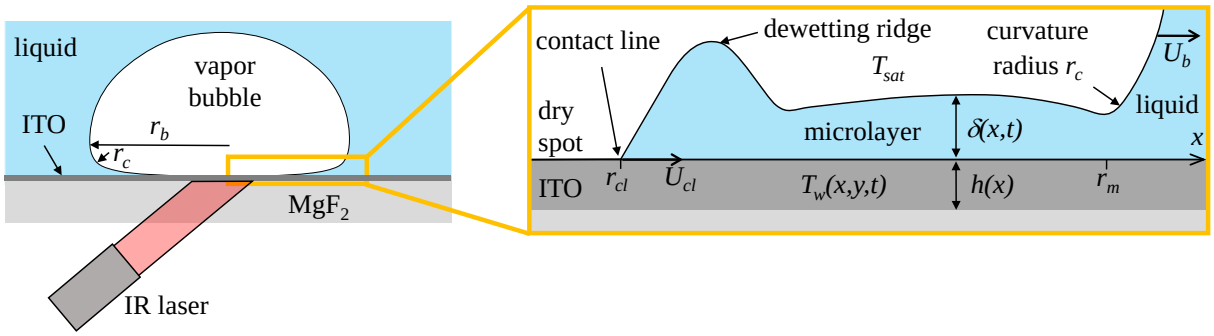

Figure 5.1: Schematics of the microlayer underneath a single bubble.

(*i*) The defect on which the bubbles are generated is deep enough so the bubbles are produced at small enough superheating (as explained above).

(*ii*) There is only one such defect on the heater so a single bubble is nucleated at a time.

(*iii*) The defect is in the middle of the heater so the bubble is not affected by other bubbles, which can be generated at the heater edge. This produces symmetric bubbles and circular dry spots.

The bubble is nucleated at the center of the heating spot on the ITO thus producing radially symmetric bubbles. This is achieved by displacing the IR laser with a micrometric stage until the point of maximum intensity of the wall temperature coincides with the nucleation site.

In order to understand our experimental observations, we also present a theoretical analysis. All the relevant variables that will be used throughout this chapter are presented in the schematics of Fig. 5.1. During the initial stages of bubble growth, the bubble base has a receding velocity U_b and a curvature radius of r_c at the edge. The apparent and equivalent macroscopic bubble radii are r_b and $r_{b,eq}$, respectively. The extents of the dry spot and the microlayer on the wall are given by r_{cl} and r_m, respectively. The contact line has a velocity U_{cl}. The ITO has an average thickness $\overline{h}$ of 954 nm, as shown in Fig. 4.19b. Its spatial variation is however taken into account for the determination of $\delta(x,t)$. $T_w(x,y,z)$ stands for the wall temperature on the upper ITO surface. $\Delta T = T_w - T_{sat}$ is the wall superheating with $T_{sat} \approx 100\,^{\circ}\mathrm{C}$ which has been verified by the liquid pool temperature at saturation measured by the RTD as illustrated in Fig. 3.1. WLI, IR thermography and side-wise shadowgraphy measurements were carried out simultaneously and synchronously at 4000 fps.

5.2 Bubble nucleation, growth and departure

Fig. 5.2a shows the ΔT time evolution obtained by IR thermography for the point on the wall where the bubble is nucleated. The time comprises a few nucleation cycles with the shaded area corresponding to the bubble growth period, which is shown in details in Fig. 5.2b. The boiling cycles are periodical with approximately 248 ms between two consecutive bubble nucleation. The ΔT required to overcome the nucleation energy barrier and thus trigger the bubble is roughly 32 K. In Fig. 5.2b, the bubble growth period, given by the time interval between bubble nucleation and departure from the wall, is approximately 19 ms. ΔT drops sharply at nucleation thanks to the wall heat removal promoted by the latent heat of vaporization. However, the rapid dry spot formation results in a sharp increase of ΔT. This increase is slowed down after a few ms thanks to the radial heat diffusion towards the contact line, where high evaporation rates occurs. At bubble departure from the wall, ΔT decreases thanks to wall rewetting by the liquid from the bulk.

Because of these repetitive nucleation cycles characteristics as depicted in Fig. 5.2a, we can concentrate our analysis on the near-wall phenomena during the bubble growth of one of them.

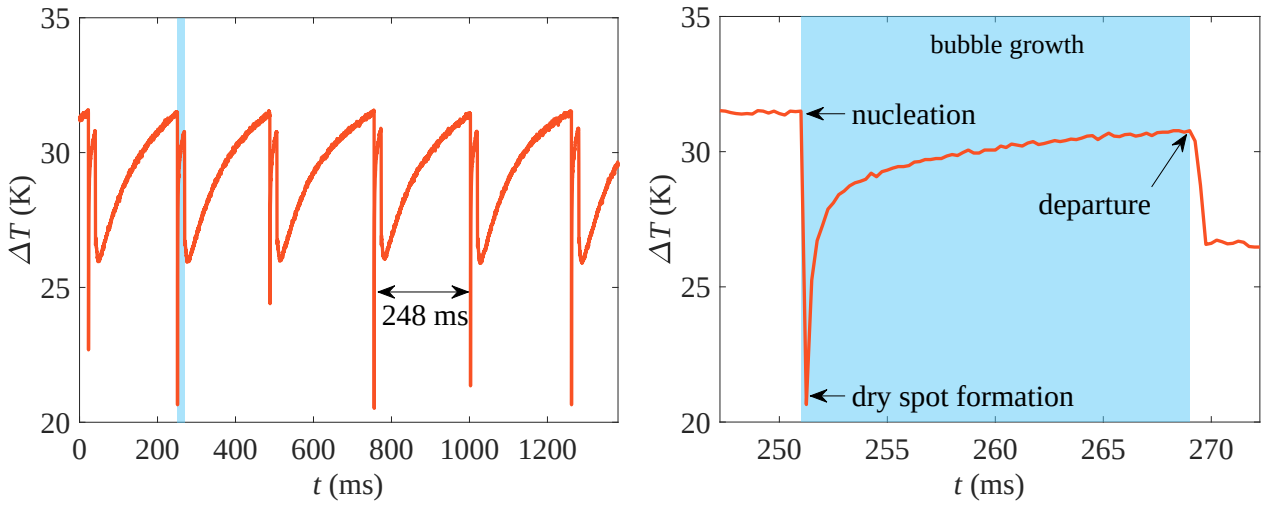

(a) Nucleation cycles.

(b) Bubble growth.

Figure 5.2: Wall superheating evolution at the center of the bubble. The shaded zone indicates the bubble growth period.

5.3 Bubble, dry spot and microlayer radii

The bubble equivalent radius $r_{b,eq}$ is obtained as described in section 4.3.1. From WLI fringe images as those shown in Fig. 5.3 one identifies the dry spot r_{cl} and the microlayer r_m radii as explained in section 4.1. Here, r denotes the radial coordinate along x. $x = 0$ corresponds to the center of the bubble (center of the dry spot in WLI fringe map of Fig. 5.3).

Fig. 5.4 shows an example of the time evolution of the radii. $t = 0$ corresponds to the moment just before nucleation; the bubble departs from the wall at $t = 19.5$ ms. For $0 \leq t \leq 1$ ms the dynamics of the bubble and microlayer radii are similar thanks to the inertial bubble expansion, which results in a nearly hemispherical bubble shape. The microlayer radius attains 90% of its maximum ($\sim$2 mm) within the first 10% of bubble growth period. Its depletion occurs at $t = 12.5$ ms, where the dry spot and microlayer radii coincide. Therefore, for $0 \leq t \leq 12.5$ ms the microlayer exists and its evaporation over time can contribute to the overall bubble growth. For the remaining bubble lifetime, the microlayer no longer exists. The contact-line evaporation regime occurs(according to the classification discussed in section 2.3).

The dynamics of $r_{b,eq}$, r_m and r_{cl} shown in Fig. 5.4 is qualitatively similar to the one obtained by Jung and Kim [12], depicted in Fig. 5.5, using Joule heating(uniform heating) in nucleate boiling of a single bubble. Quantitatively, it can be noticed that r_m is roughly two times larger in our case. This is associated with the strong inertial forces acting during the early moments of bubble expansion promoted by the laser heating. During the microlayer existence, r_{cl} has a linear behavior with Joule heating (Fig. 5.5) whereas with laser heating(Fig. 5.4) it grows faster for $0 \leq t \leq 2.5$ ms and then slows down for $2.5 < t \leq 12.5$ ms, where it increases with a constant rate. The reason for this behavior is linked to the evaporation rate at the contact line. This is explained in details in section 5.8.

5.4 Microlayer dynamics

The experimental "bumped" profile is shown in Fig. 5.6. The microlayer thickness is obtained from the WLI images like those shown in Fig. 5.3. The method to recover the shape from the fringe analysis is discussed in subsection 4.1.10. The microlayer profile could be recovered only partly(where the fringe

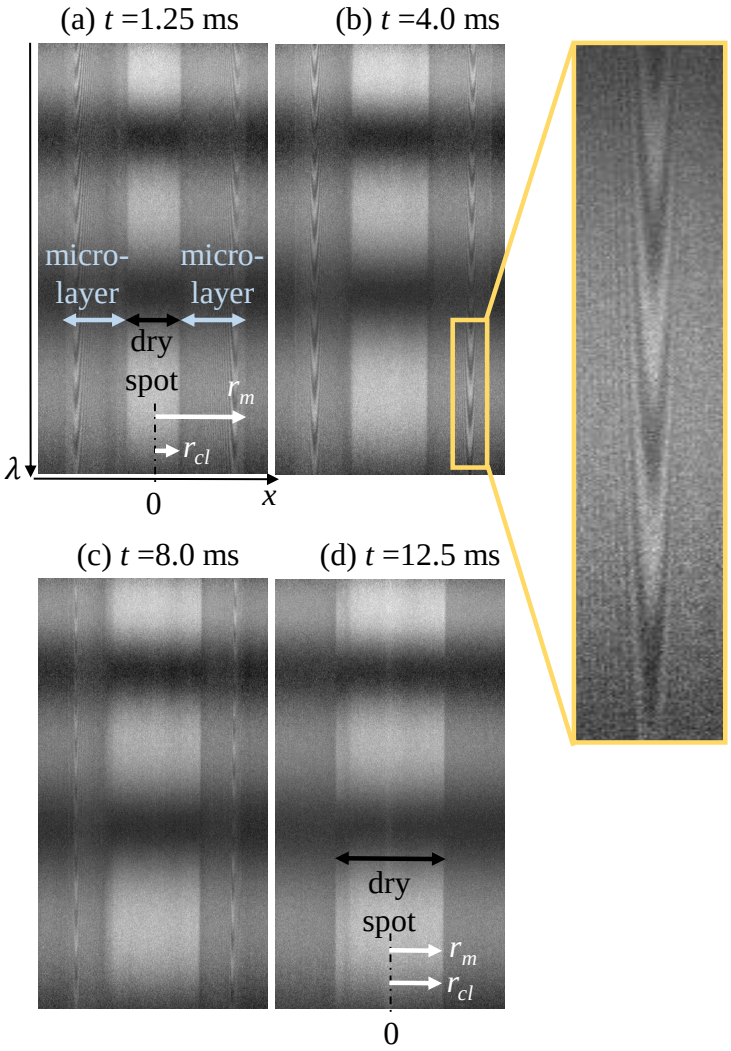

Figure 5.3: Typical WLI fringe maps observed throughout the microlayer existence.

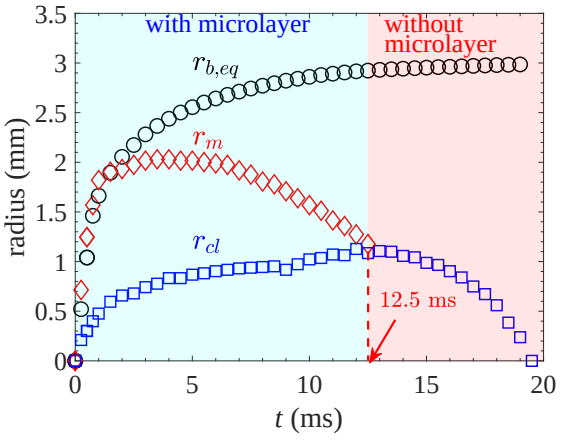

Figure 5.4: Experimental time evolution $r_{b,eq}$, microlayer radius r_m and dry spot (contact line) radius r_{cl} with laser heating.

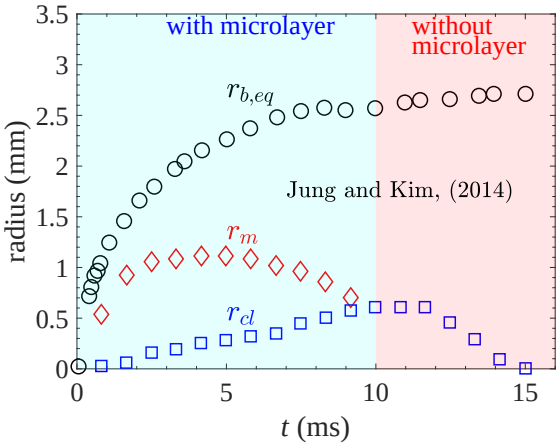

Figure 5.5: Experimental data of Jung and Kim [12] for the time evolution of $r_{b,eq}$, r_m and r_{cl} with Joule heating.

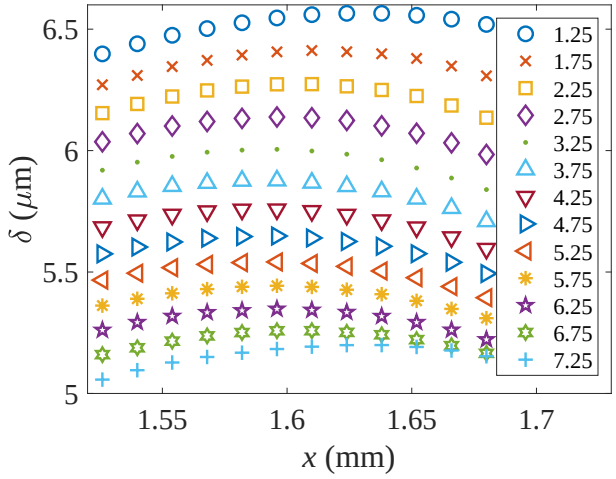

Figure 5.6: Experimental microlayer profiles obtained by WLI for different growth times in ms indicated as curve parameters.

pattern is visible) because in its other part, the interface slope is too big (or the optical resolution is insufficient, which is equivalent, so that the fringes are not visible, see subsection 4.1.15).

The WLI fringe map shown in Fig. 5.3a is the first image that presents fringes that can be post-processed. The position of the fringes does not change with time. Their parabolic shape, as depicted in Fig. 5.3b, indicates the presence of a "bumped" profile. Even though the microlayer region can still be detected thanks to the reflected light from it, the width of the parabolic fringe pattern becomes thinner at $t = 8\,\text{ms}$ (Fig. 5.3c) so that the post-processing can no longer distinguish maxima and minima. Therefore, the experimental microlayer profile can only be obtained between 1.25 ms and 8 ms. The microlayer is also not resolved for $t < 1.25\,\text{ms}$ because of the fast inertial dynamics so that the fringes are not observed by WLI camera. In Fig. 5.3d, microlayer and dry spot radii coincide at $t = 12.5\,\text{ms}$, corresponding to the microlayer depletion (i.e. disappearance via its shortening).

The parabolic microlayer profile shown in Fig. 5.6 corresponds to the fringe bump geometry seen in Fig. 5.3. This profile is observed as soon as the microlayer is fully formed at $t = 1.25\,\text{ms}$. Its thickness attains a maximum at $x_{max} \simeq 1.6\,\text{mm}$. Although δ decreases with time due to evaporation, x_{max} remains nearly unchanged.

5.4.1 Simple bump model

A simple theoretical approach [209] to analyze the initial microlayer thickness as a function of x can be developed based on the idea that the microlayer formation is analogous to the Landau-Levich film left behind by the bubble foot edge receding during the initial stages of bubble growth (subsection 2.2.1). Therefore, Eq. (2.31) can be used to determine the deposited microlayer thickness (Fig. 5.1). As illustrated in Fig. 5.1, r_c differs from the bubble radius r_b. The bubble foot is flattened by the inertial forces acting on the bubble downwards thanks to the rapid bubble growth. Therefore, the portion of interface between the bubble foot and its dome has a much larger curvature r_c^{-1} than that of the bubble dome (r_b^{-1}). The ratio

$$\gamma = r_c/r_b, \tag{5.1}$$

is thus expected to be much smaller than unity. By assuming this factor to be constant, the initial microlayer thickness given by the bubble foot edge receding (Eq. (2.31)) becomes

$$\delta_0 = 1.337\gamma r_b Ca^{2/3}, \tag{5.2}$$

where one can obtain δ_0 from the data fit as follows.

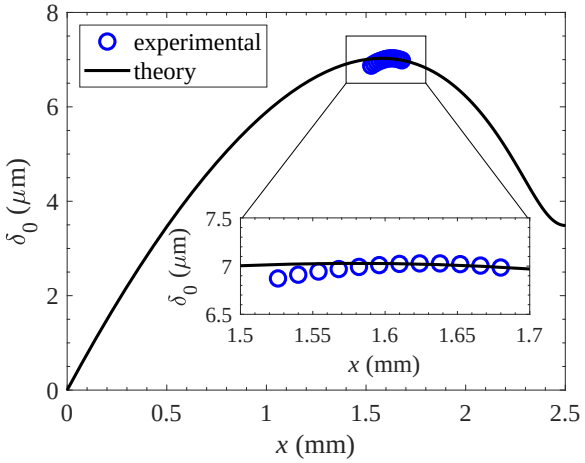

(a) Theoretical initial microlayer profile given by the simple bump model of Eq (5.2).

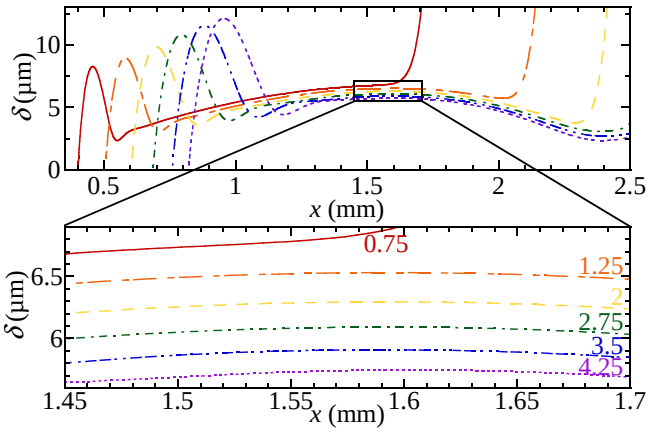

(b) Numerical simulation results showing the temporal evolution of the microlayer profile. Time moments are labeled in ms. A low-slope part that is possible to be measured by interferometry is zoomed in.

Figure 5.7: Theoretical microlayer profiles.

One can assume that the initial thickness at a point x forms at a time moment where the bubble edge (i.e. the point with $x = r_b$) passes over it. In other words, for each time moment t corresponding to the increasing r_b in Fig. 5.4 (i.e. while the microlayer forms), one takes U_b, and r_b and determines $\delta_0' = 1.337 r_b Ca^{2/3}$, where Ca is given by Eq. (2.32) with $U_b = dr_b/dt$ (Fig. 5.1). One finds the maximum value $\delta'_{0,max}$ of δ_0'. One then takes the experimental microlayer profile (Fig. 5.6) at $t = 1.25$ ms and uses Eq. (2.35) to correct the microlayer thinning over time due to its evaporation by assuming an average ΔT of 8 K up to $t = 1.25$ ms. One then obtains the maximum experimental value $\delta_{0,max}$ of $\delta_0(x)$ and compute $\gamma = \delta_{0,max}/\delta'_{0,max}$. The assumption that experimental $\delta_{0,max}$ corresponds to the maximum initial microlayer thickness is reasonable because δ decreases with time so it is maximal right after the meniscus deposition.

Once $\gamma = 0.084$ is obtained, one can determine $\delta_0(x)$ from Eq. (5.2). According to the above hypothesis, this thickness should be initial at the position $x = r_b$. The plot $\delta_0(x)$ obtained in this way is shown in Fig. 5.7a. Its particularity is a maximum (a "bump") at $x \simeq 1.6$ mm. It can be explained as follows. δ_0 is proportional to the product of $U_b^{2/3}$ that monotonously decreases with time (cf. Fig. 5.4) and r_b that monotonously grows. As a consequence, a maximum of δ_0 can occur. Such a theory represents the initial thickness of the deposited microlayer. In reality it varies in time because of capillary action and evaporation. However, because of the thinness of the film, the axial fluid flow caused by capillary action is expected to be small. The only thickness change is its local reduction due to evaporation governed by Eq. (2.34) that cannot change the position of the maximum and it is taken into account via Eq. (2.35). This situation is analogous to the bumped film deposited by the oscillating meniscus [210]. In Fig. 5.7a, the positions of the theoretical and experimental microlayer maximum thickness agrees well. This shows the validity of this simple model, in which the initial microlayer thickness is controlled by capillary and viscous effects.

5.4.2 Numerical simulation of the microlayer dynamics

We discuss here a numerical simulation [209] based on the lubrication theory approach by Zhang and Nikolayev [123]. The set of equations has been discussed in subsection 2.2.2. The boundary conditions

for the boiling case (Fig. 5.1) are the following:

$$\delta(x = r_{cl}) = 0, \tag{5.3}$$

$$\left.\frac{\partial \delta}{\partial x}\right|_{x=r_{cl}} = \tan(\theta_{micro}), \tag{5.4}$$

$$\left.\frac{\partial \Delta p}{\partial x}\right|_{x=r_{cl}} = 0, \tag{5.5}$$

$$K(x = r_m) = r_c^{-1}. \tag{5.6}$$

The first condition, Eq. (5.3), establishes the zero film thickness at the contact line whereas the second, Eq. (5.4), imposes the microscopic contact angle θ_{micro} (at the contact line), which is obtained comparing experimental and theoretical data of the contact line speed as a function of wall superheating, see Fig. 5.19d, we obtained $\theta_{micro} = 10°$ for water. The pressure finiteness at the contact line is imposed by Eq. (5.5). It is made possible thanks to accounting for the Kelvin effect (subsection 2.1.3) [10, 14, 30]. The last boundary condition establishes that the interface curvature at the bubble foot edge is given by r_c^{-1} determined as described in subsection 5.4.1. The simulation is performed only for the initial stage of the microlayer existence where both r_m and r_b grow ($t < 3\,\text{ms}$). For larger times, r_m decreases while r_b grows. As our simulation boundary should be defined at $r = r_b$ (i.e. at a height much larger than the film thickness), the curvature boundary condition becomes uncertain.

Equation (2.33) accounts both for the triple contact line receding caused by capillary effects amplified by evaporation [123] and for the decelerated motion of the meniscus created at the bubble foot edge [210]. The problem is solved numerically within the spatial interval determined by (r_{cl}, r_b). The contact line dynamics (position and velocity derived from the position) is linked to the mass evaporation rate at the contact line and it is an output of the numerical simulation. The bubble radius is imposed by using the experimental data from Fig. 5.4. The experimental data are fitted for $t < 3\,\text{ms}$ as

$$r_b(t) = -6.534 \times 10^{-6} + 3.920t - 2.525 \times 10^3 t^2 + 7.783 \times 10^5 t^3 - 8.967 \times 10^7 t^4 \tag{5.7}$$

The wall superheating is assumed to be spatially homogeneous (isothermal heater) however varying in time to mimic the ΔT at the contact line (see section 5.5). It is imposed by the fit curve of the wall superheating at the contact line, $\Delta T_{cl}(t)$, which is shown in Fig. 5.17. For $t < 0.25\,\text{ms}$, $\Delta T = 31\,\text{K}$. For $0.25\,\text{ms} < t < 3\,\text{ms}$, it is assumed to decline exponentially to $3.3\,\text{K}$ at $t = 5\,\text{ms}$.

Figure 5.7b(top) shows the simulated evolution of the liquid film (microlayer) deposited by the bubble edge during its receding. The latter is caused by the bubble growth. The simultaneous contact line receding leads to formation of a growing in time ridge near the contact line (the dewetting ridge) that collects the liquid previously situated on the dry spot to the left of the microlayer. One observes the dewetting ridge expected from the physics of dewetting (subsection 2.1.8). It has also been observed in boiling simulations with the high enough spatial resolution to model the microlayer, see [7, 115, 116]. The dewetting ridge is not however possible to be measured by interferometry as the maximum observable slope is $\sim 0.4°$, which is the maximum slope limit determined in section 4.1.15. Only a nearly flat middle part of the microlayer is measurable. It is zoomed in in the bottom part of Fig. 5.7b. One can compare it to the experimental profile in Fig. 5.6. One can see that the position of the maximum in the bump, the absolute value of thickness, and its dynamics agree very well.

5.5 Wall temperature

In this section we discuss the wall superheating distribution $\Delta T(x, y, t)$ during the bubble growth. The orientation of x and y axes is assumed hereafter to be different from previous section (where the x axis coincided with the WLI scanning line) while the point $x = 0$, $y = 0$ still coincides with the bubble center. Now, the axes directions are defined by the IR camera orientation.

Figs. 5.8a and 5.8b show $\Delta T(x, y)$ for $t = 0$ (just before the bubble nucleation) and $t = 6.25\,\text{ms}$, respectively, obtained from the IR images. In Fig. 5.8a, one can understand the temperature distribution as a combination of the following effects: the heat generation in the ITO provided by the IR laser heating, the heat diffusion towards the porthole and radial in the ITO and the convection into the liquid pool. In Fig. 5.8b, the dry spot and microlayer dynamics change significantly this distribution. Therefore, we use $\Delta T(x, y, t = 0)$ as a reference to address how the microlayer and dry spot presence modifies $\Delta T(x, y, t)$.

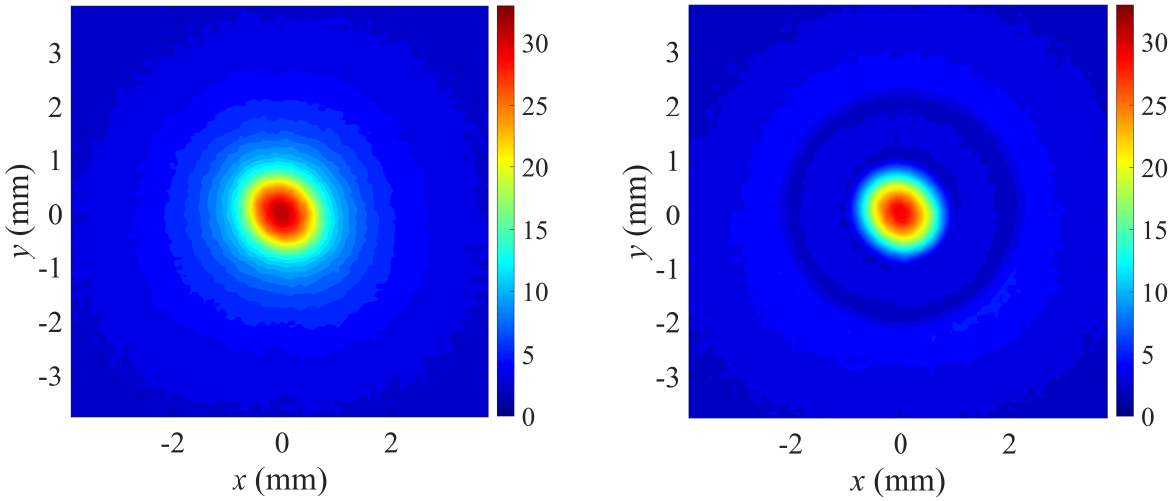

(a) At $t = 0$. (b) At $t = 6.25\,\text{ms}$.

Figure 5.8: Superheating ΔT distribution on the wall. The color bar represents ΔT in K.

For the sake of simplicity and due to nearly radial symmetry of the temperature distribution on the wall, as one can observe in Figs. 5.8a,b, the spatial distribution of ΔT is presented by profiles of $\Delta T(x, t)$ at $y = 0$. First, we focus on the wall dynamics at the early stages of bubble growth during the microlayer formation.

Figure 5.9 depicts the wall superheating for $0\,\text{ms} \leq t \leq 1.25\,\text{ms}$. In Fig. 5.9a, we identify the extents of dry spot and microlayer along x as follows. As the microlayer is formed during the inertial bubble growth, evaporation of the liquid underneath the bubble takes place and leads to a ΔT decrease along its extent. This occurs because the depth $l_m \simeq 6.5\,\mu\text{m}$ of temperature penetration into the microlayer is defined similarly to Eq. (2.51), with $t = 0.25\,\text{ms}$ (time between two consecutive frames). Therefore, $l_m \approx \delta_0$ and the heat diffuses from the wall throughout the whole microlayer thickness within 0.25 ms, thus promoting an effective and rapid heat removal from the wall. As a result, the point where $\Delta T(t = 0.25\,\text{ms})$ starts to deviate from $\Delta T(t = 0)$ corresponds to the ending point $x = r_m$ of the microlayer(bubble foot edge).

ΔT distribution is nonmonotonous inside the microlayer. This is a combined result of evaporation and nonuniform heating by the IR laser. While the high wall heat removal rate near the contact line works to decrease ΔT, the IR laser heating tends to increase it. The laser heating is maximum inside the dry spot thus producing high temperature gradients on the wall in this region. As a result, we identify the dry spot radius r_{cl} by two points where ΔT decreases sharply. These points correspond to the contact line position.

As one can observe in Figs. 5.9, $\Delta T(t)$ is a decreasing function along the whole extent of the microlayer as the bubble grows. In particular, at $t = 1.25\,\text{ms}$, $\Delta T(x)$ is nearly uniform inside the microlayer. One can relate $\Delta T(x) = T_w(x) - T_{sat}$ to the wall heat flux towards the liquid $q_l''(x)$ with

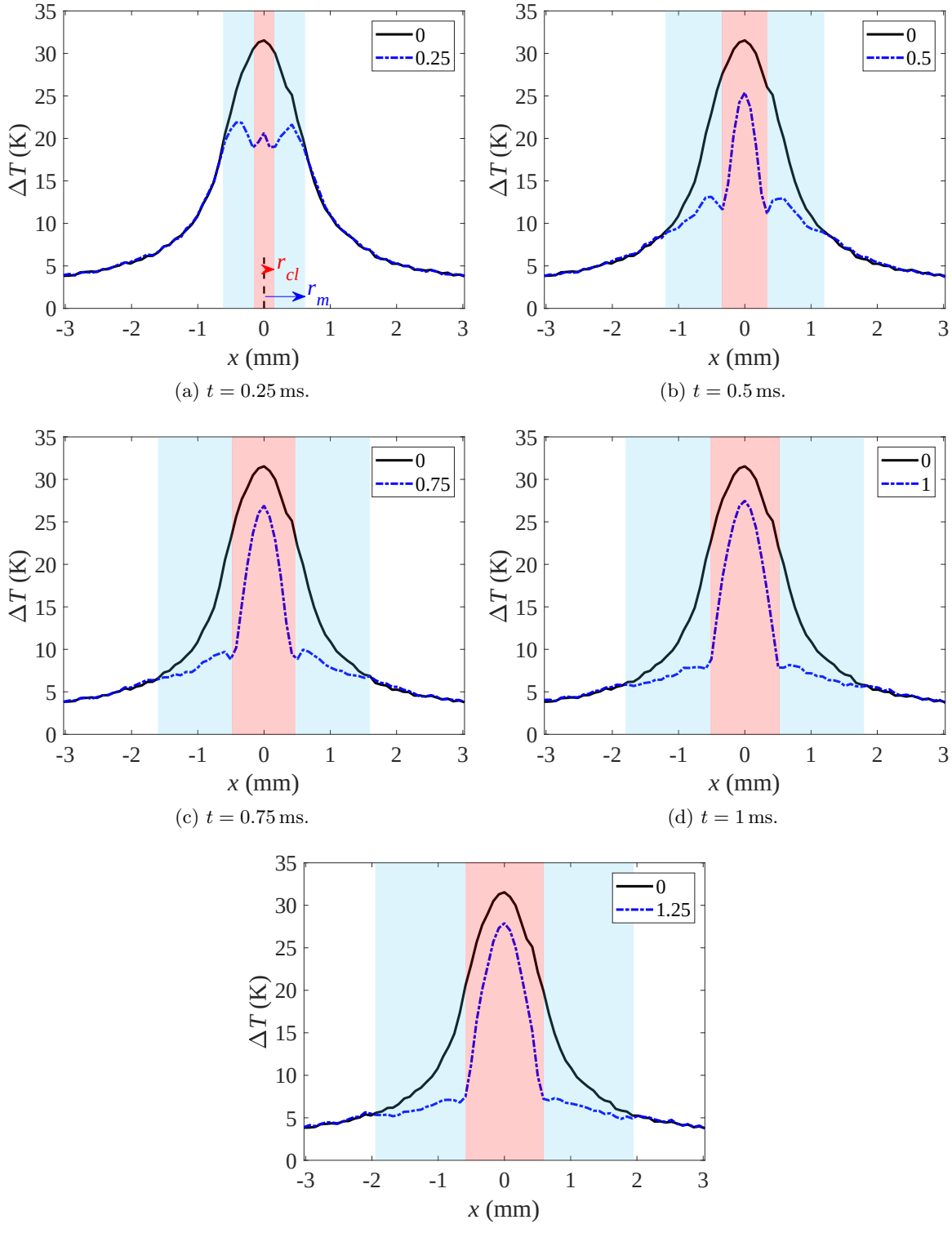

(a) $t = 0.25$ ms. (b) $t = 0.5$ ms.

(c) $t = 0.75$ ms. (d) $t = 1$ ms.

(e) $t = 1.25$ ms.

Figure 5.9: Spatial distributions $\Delta T(x)$ (blue dotted lines) for different t during the microlayer formation as compared to $\Delta T(x, t = 0)$ (black lines). The shaded areas at the center and in the sides represent the extent of dry spot (in red) and microlayer (in blue).

Eq. (2.47). With $\Delta T(x)$ constant, $q_l''(x)$ and $\delta(x)$ should behave similarly.

Over the dry spot, the temperature profile follows approximately the shape of that at $t = 0$. The vapor represents a high heat transfer resistance and heat is accumulated into the wall and increases its temperature. As the microlayer approaches its full extent (at $t = 1.25\,\text{ms}$), the changes in ΔT along the dry spot become minor. This is a result of the effective wall heat removal at the contact line and also throughout the whole microlayer extent.

Figure 5.10 shows the ΔT distribution after the microlayer is fully developed. Here, its extent differs from the description given above. For $t = 6.25\,\text{ms}$ (Fig. 5.10a), ΔT is lower than the superheating at the periphery of microlayer. As a result, heat diffuses inwards. The point where the profiles start to deviate from each other no longer corresponds to r_m. Instead, at r_m ($x = 2\,\text{mm}$ for $x > 0$), and at the dry spot ($x = 1\,\text{mm}$) we then have two points of ΔT minima; the region between them corresponds to the microlayer. The minima at $x = 2\,\text{mm}$ and $-2\,\text{mm}$ correspond to the cold ring with a radius of $\approx 2\,\text{mm}$ in the $x - y$ map (cf. Fig. 5.8b). When the microlayer is depleted at $t = 12.5\,\text{ms}$ in Fig. 5.10b, the second pair of minima of ΔT at $x = -2\,\text{mm}$ and $2\,\text{mm}$ disappear. For $t > 12.5\,\text{ms}$, the temperature at the contact line increases due to the absence of the microlayer.

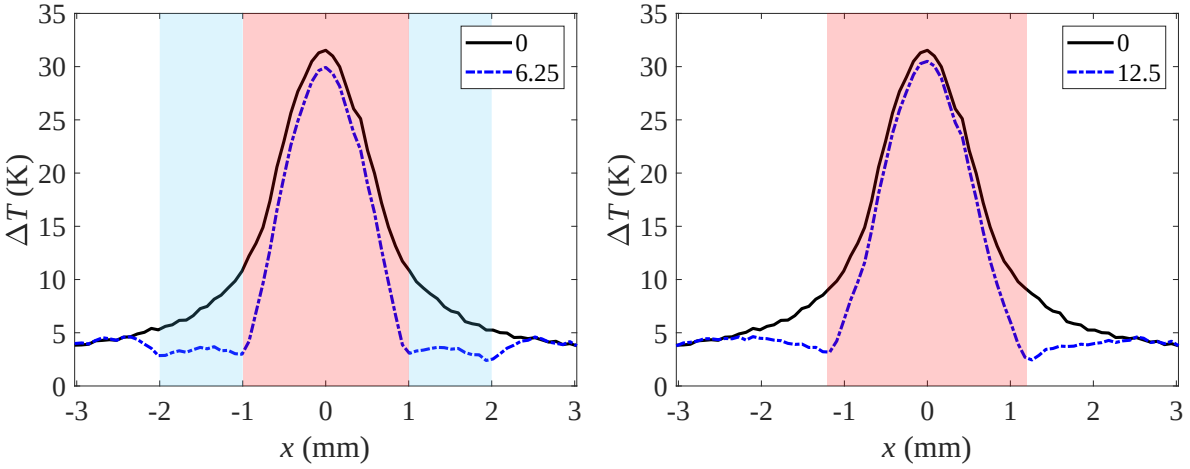

(a) $t = 6.25\,\text{ms}$. (b) $t = 12.5\,\text{ms}$.

Figure 5.10: Spatial distributions $\Delta T(x)$ for different t after the microlayer development as compared to $\Delta T(x, t = 0)$. The shaded areas at the center and in the sides represent the extent of dry spot (in red) and microlayer (in blue).

The local superheating $\Delta T(t)$ can also be obtained by using the microlayer thickness δ (measured by WLI) in Eq. (2.34). Figure 5.11 shows a comparison of $\Delta T(t)$ at the position $x = 1.6\,\text{mm}$ (in the microlayer) obtained from the IR thermography and the one obtained from Eq. (2.34) by using the WLI $\delta(t)$ data from Fig. 5.6. A good agreement between these two curves indicates that the microlayer thinning is a result of its evaporation only, and therefore the relaxation of the microlayer shape by radial flow is indeed negligible as expected from the theoretical considerations given in section 2.2.2.

5.6 Wall heat flux

5.6.1 Heat transfer in ITO

We use Eq. (2.44) to model the transient two-dimensional heat transfer in the ITO film. The main goal is to reconstruct the heat flux $q_l''(x, y, t)$ towards the liquid from $\Delta T(x, y, t)$ (or, equivalently, $T_w(x, y, t)$) data discussed in the previous section. In Eq. (2.44), we use the $q_0''(x, y)$ distribution

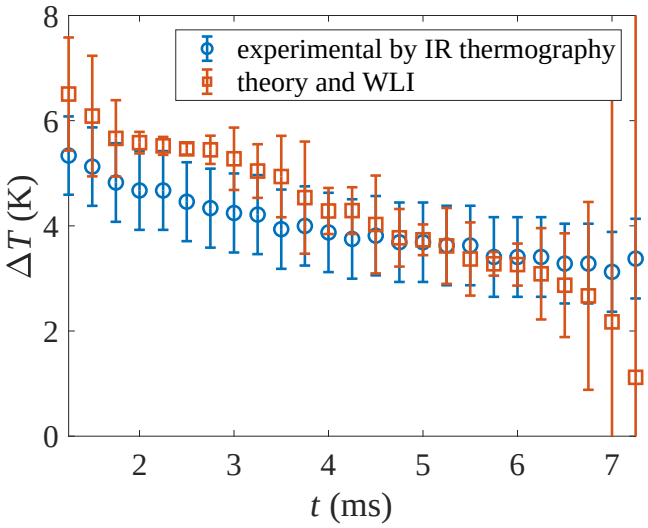

Figure 5.11: Comparison of ΔT at $x = 1.6\,\text{mm}$ obtained from the IR thermography with the theory (2.34) using δ from WLI.

presented in Fig. 3.15b. Two complications arise for the remaining terms. First, q''_p cannot be neglected as MgF_2 has a high thermal inertia. This is where one needs $\Delta T(x, y)$ data. $q''_p(x, y, t)$ is calculated based on $T_w(x, y, t)$ as discussed in subsection 5.6.2. Second, $T_w(x, y, t)$ is noisy, so one needs to smooth it to avoid the noise amplification in the diffusive term q''_d. We implement a two-dimensional Savitzky-Golay algorithm (Appendix H.2) to filter out the noise. In essence, the temperature distribution is represented by polynomial equations that fit the experimental data so that a faithful representation of the original data is obtained (see, for instance, Fig. H.3). q''_d in Eq. (2.44) is obtained by second order derivation of the fit. We do not filter the measured temperature in time because sharp time variation that occurs at early growth stages is difficult to be well represented by a smoothing algorithm, so that we keep the original data. More details on the spatial temperature smoothing can be found in Appendix H.2.

5.6.2 Heat transfer in MgF_2

Equation (2.49) is used to determine the transient temperature distribution in the porthole; one obtains q''_p from Eq. (2.50). The boundary conditions are shown in the schematics of Fig. 5.12. At the top boundary, $T_p(x, y, z = 0, t) = T_w(x, y, t)$ is the temperature distribution over ITO obtained by the IR thermography data. At the other boundaries, one can consider adiabatic conditions $q''_p = 0$, given that the heat exchange at these surfaces is much smaller than at the top surface. The porthole radius and thickness are 12.5 mm and 3 mm, respectively.

To find a truly periodic regime of temperature change, several nucleation-departure cycles needs to be simulated. Therefore, the time interval for the porthole problem is different from that of subsection 2.4.1 that covers only one cycle. To reduce the simulation time, one needs to choose an initial condition as close to the periodical solution as possible. Thanks to the high thermal inertia of the porthole, the temperature T_p far from the nucleation site is nearly invariable in time. For this reason, one can choose the stationary thermal distribution $T_p^\infty(x, y, z)$ as $T_p(x, y, z, t = 0)$. It satisfies the equation

$$\frac{\partial^2 T_p^\infty}{\partial x^2} + \frac{\partial^2 T_p^\infty}{\partial y^2} + \frac{\partial^2 T_p^\infty}{\partial z^2} = 0. \tag{5.8}$$

with the boundary condition $T_p^\infty(x, y, z = 0) = T_w(x, y, t = 0)$ where the instant $t = 0$ corresponds to the T_w measurement just before the bubble nucleation. For the numerical time step, one can take

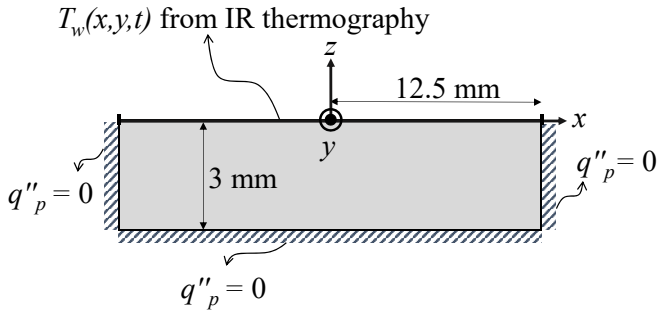

Figure 5.12: Schematics of the boundary conditions for the porthole heat transfer calculations.

the temporal resolution given by the acquisition image rate of experimental measurements. It turns out that the periodic regime is established right after the first cycle so $T_p^{\infty}(x, y, z)$ can be taken for $T_p(x, y, z, t = 0)$.

The above problem has been solved numerically by G. Bois and E. Sakali (STMF/CEA) to find the T_p time and space variation throughout periodic cycles of bubble nucleation, departure and waiting time. The calculation was performed with the Trio-CFD freeware. The spatial discretization in the numerical problem should provide the grid independence. For this, for the step Δz in the z direction, one needs to resolve the heat diffusion profile. The relevant scale is given by Eq. (2.51), where t is the time scale between bubble nucleation and departure from the wall. One finds $l_p \approx 0.2\,\text{mm}$. At least $N = 20$ points are required within l_p to describe the temperature distribution. Therefore, $\Delta z < l_p/N \leq 0.01\,\text{mm}$ is needed.

Similarly, Eq. (2.51) can be used to estimate l_p during the bubble cycle time (the time between two consecutive nucleations). One gets $l_p \approx 1\,\text{mm}$. This represents 1/3 of the porthole thickness. The MgF_2 has an effusivity given by Eq. (2.52) 3.5 times higher than that of liquid water. This means that the ITO film exchanges thermal energy more efficiently with the porthole than with the liquid (in the absence of evaporation). For this reason, q''_p cannot be neglected.

5.6.3 Heat flux reconstruction and interfacial resistance

The heat flux distribution on the wall follows a nearly (but not completely) symmetric pattern (Fig. 5.13) established by the temperature distribution so we can consider here all the quantities as functions of x and t at $y = 0$. Figure 5.14 shows the time evolution of heat flux for each term in the R.H.S of Eq. (2.44) at $x = 1.1\,\text{mm}$, which corresponds to the point on the wall where occurs the microlayer depletion (radius corresponding to $r_m = r_{cl}$ in Fig.5.4). q''_a and q''_d are negligible compared to q''_p and q''_0. This occurs because of the thinness of the ITO film, which provides a very small cross section area to the radial heat flux while having low heat capacity. At $t < 0.5\,\text{ms}$, this point is in the contact with the liquid so only convection occurs, which provides only a small heat exchange. q''_p increases sharply at around $t = 0.5\,\text{ms}$. At this time, $r_m = 1.1\,\text{mm}$ in Fig. 5.4, thus corresponding to the moment of formation of microlayer. The evaporation of the liquid microlayer produces a high heat transfer from the porthole towards the bubble. Note that q''_p becomes positive. This occurs because the massive porthole accumulates a big heat amount between the nucleation events so it becomes to be hotter than the ITO cooled by evaporation. During the microlayer evaporation at $0.5\,\text{ms} \leq t \leq 12.5\,\text{ms}$, q''_p represents the dominant contribution to q''_l (roughly 90% at $t = 0.5\,\text{ms}$ and 75% at $t = 12\,\text{ms}$), much larger than the source term q''_0.

At $t = 12.5\,\text{ms}$, the receding contact line reaches the point $x = 1.1\,\text{mm}$. Note that in this particular position, the superheating at this time is very small so there is no heat transfer peak. For $t > 12.5\,\text{ms}$, the contact line changes the motion direction (begins to advance) so $r_{cl} < 1.1\,\text{mm}$; the microlayer

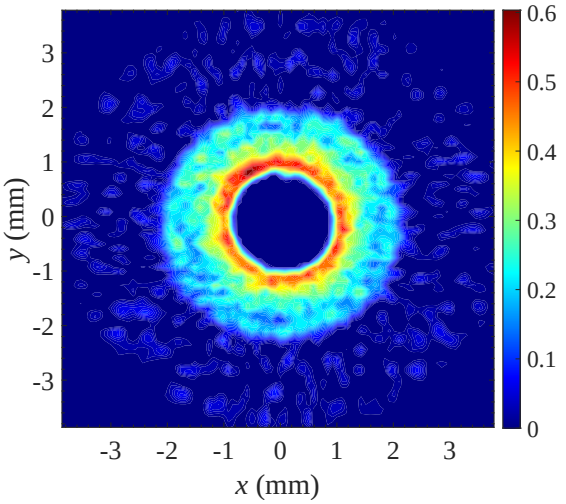

Figure 5.13: Reconstructed heat flux spatial distribution $q_l''(x, y)$ at $t = 6.25\,\text{ms}$ corresponding to Fig. 5.8b. The color bar represents the heat flux value in MW/m^2.

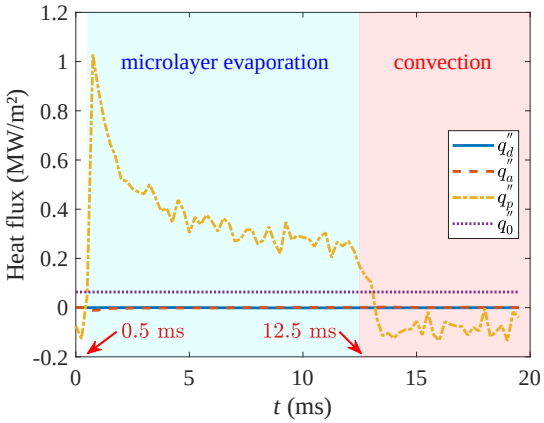

Figure 5.14: Heat flux contributions as a function of time at $x = 1.1\,\text{mm}$ and $y = 0$.

disappears (see Fig. 5.4). The point $x = 1.1\,\text{mm}$ comes to the contact with the bulk liquid. The heat generated in ITO is transferred to the porthole (negative q_p'') because of its higher effusivity comparing to liquid water.

A similar trend is observed for other points along the heater. The only difference is the presence of the heat transfer peak at the instant where the contact line passes the point (in which case it happens at a positive local superheating).

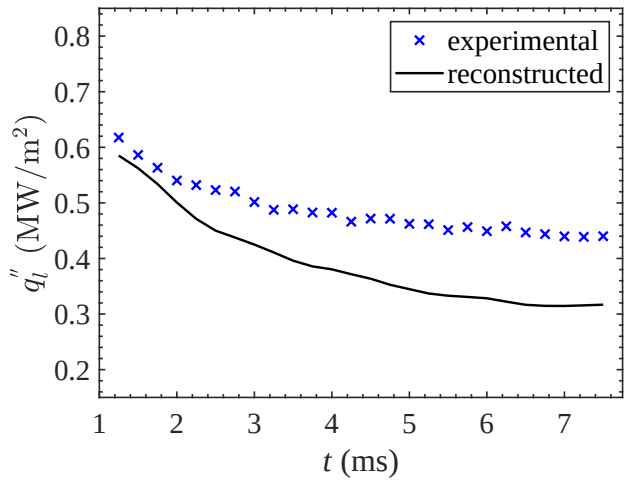

(a) Comparison of $q_l''(t)$ reconstructed with Eq. (2.44) and $q_l''(t)$ experimental calculated with Eq. (2.47) at $x = 1.6\,\text{mm}$.

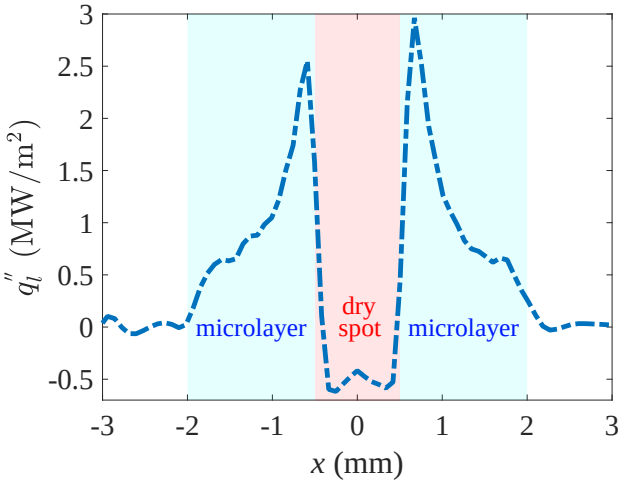

(b) $q_l''(x)$ at $t = 1.25\,\text{ms}$.

Figure 5.15: Spatio-temporal evolution of q_l''.

Figures 5.15 a) and b) depict q_l'' as a function of time and x, respectively. In Fig. 5.15a we compare q_l'' computed by two different methods. The first method is the flux reconstruction from the IR thermography data with Eq. (2.44) as discussed above. The second is the experimental q_l'' calculated

with Eq. (2.47) by using ΔT from the IR thermography and δ from WLI. A significant difference between the numerical and experimental heat fluxes exists. It indicates the effect of interfacial thermal resistance discussed in subsection 2.1.5. q_l'' decreases in time due to the thermal diffusion into the porthole. It also decreases with increasing x due to the nonuniform laser heating distribution on the wall. In Fig. 5.15b, the maxima of $q_l''(x)$ correspond to the contact line positions and it agrees with recent numerical simulations [7] of pool boiling dynamics. $q_l'' \approx 0$ at the dry spot due to the low thermal conductivity of vapor.

The issue of interfacial thermal resistance in water is important but highly controversial; it is under active discussion in the literature [7, 117, 211]. R^i can be expressed from Eq. (2.48) and calculated by using the experimental ΔT, q_l'', and δ data. The ΔT and δ data come from the IR thermography and WLI, respectively. The q_l'' data are reconstructed from ΔT with Eq. (2.44) as discussed above. Fig. 5.16a shows the time evolution of R^i values normalized by the theoretical interfacial thermal resistance ($R^i_{theo} = 0.637\,\mu\mathrm{K\,m^2/W}$) coming from Eq. (2.13). The average value $\langle R^i \rangle \approx 3.6 R^i_{theo}$ is comparable to the result of Bucci [212], who reported $R^i = 5.65 R^i_{theo}$. Our average value is closer to the theoretical value, but the instantaneous one is still up to 5.6 times higher than it. This difference can be explained by the electrochemical properties of water that facilitate the accumulation of all impurities present in the liquid at the liquid-vapor interface as the bubble grows in spite of extra-high purity of water used in the experiments (it is difficult to avoid completely the water contamination by the boiling cell itself). Therefore, R^i/R^i_{theo} can grow with time. This is also suggested by the data in Fig. 5.16a. The simplest hypothetical law is a linear increase

$$R^i(t) = Ct + R^i_{theo}, \tag{5.9}$$

where $C = 0.4\,\mathrm{mK\,m^2/(W\,s)}$ can be determined with the least squares method (Fig. 5.16a). Figure 5.16b shows the effect of R^i on ΔT. Here, the experimental values are those obtained from the IR thermography. One can thus produce an equivalent inverse operation and express ΔT from Eq. (2.48) by using the reconstructed q_l'' and δ from WLI by using R^i_{theo}, $\langle R^i \rangle$ and $R^i(t)$. One can see that the time-dependent R^i gives the most precise result whereas the assumption of R^i_{theo} causes the underestimation over time. This comparison shows that one should take into account $R^i(t)$ caused by time-dependent water contamination to simulate water boiling.

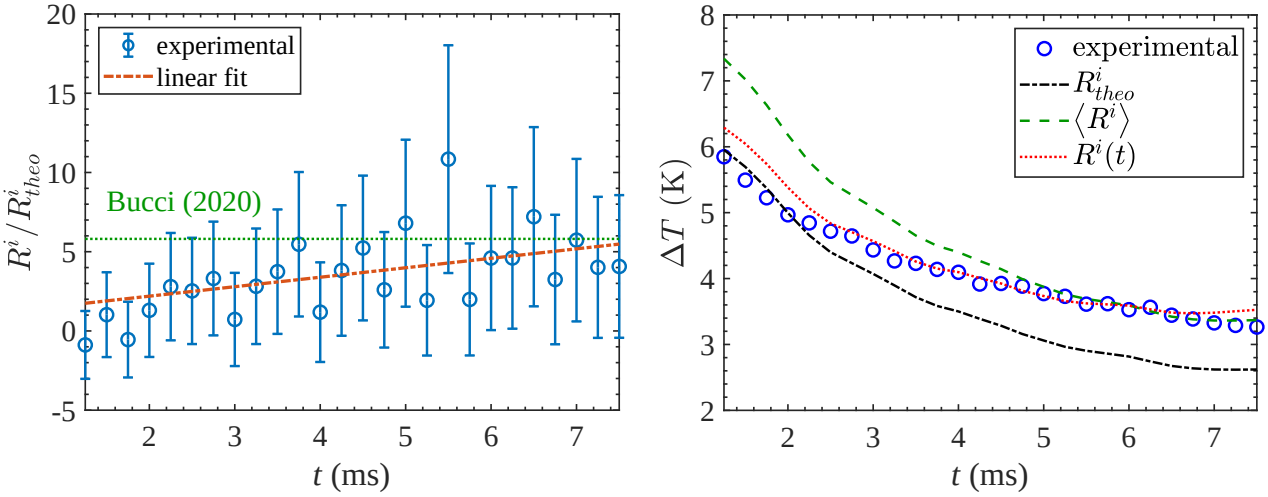

(a) R^i/R^i_{theo} as a function of t.

(b) Effect of R^i on ΔT.

Figure 5.16: R^i and its effect on ΔT at $x = 1.60\,\mathrm{mm}$.

The time evolution of the heat flux at the contact line $q''_{l,cl}$ is shown in Fig. 5.17. It follows a quick decay at the initial stage of its receding. This occurs because the contact line recedes over the

heater, the superheating of which decreases away from the laser spot center. The superheating ΔT_{cl} at the contact line is low and nearly constant for $t > 5\,\text{ms}$ until the end of the receding end so $q''_{l,cl}$ is constant. For $t > 12.5\,\text{ms}$, the contact line advances as the buoyancy forces pull the bubble up. $q''_{l,cl}$ thus increases as the contact line moves back towards the center of the heated area. The heat flux at the contact line is therefore highly dependent on the temperature distribution on the wall with a maximum at the very early moments of its receding stage. It should be noted however that the discussed heat flux is actually an averaged over the pixel size ($84\,\mu\text{m}$), which is much larger than the microregion (subsection 2.1.1). The local heat flux at the contact line can thus be considerably higher as suggested by the theoretical data [14].

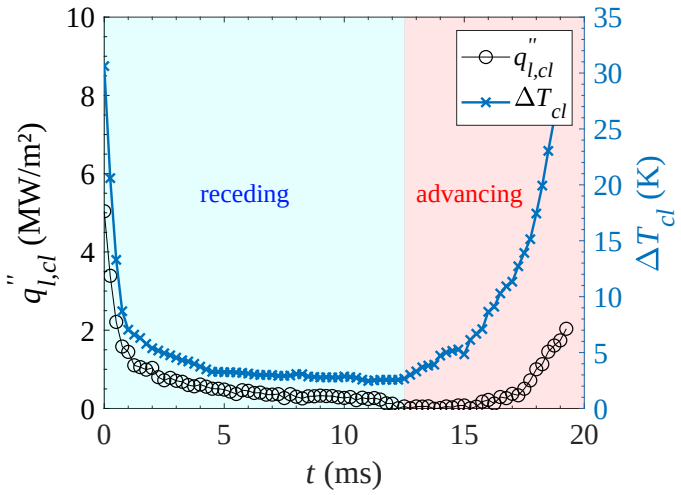

Figure 5.17: Time evolution of q''_l and ΔT at the contact line.

5.7 Microlayer evaporation contribution to bubble growth

To evaluate the contribution of the microlayer evaporation to the bubble growth one can define a parameter α that expresses the ratio between the integrated q''_l(reconstructed) over the microlayer area to the latent heat corresponding to the macroscopic bubble volume V_b as

$$\alpha(t) = \frac{2\pi \int_{t=0}^{t} \int_{r=r_{cl}}^{r_m} q''_l(r,t) r \mathrm{d}r \mathrm{d}t}{\mathcal{L}_v \rho_l V_b\,(t)}, \tag{5.10}$$

where q''_l is considered to be axisymmetric as can be observed in Fig. 5.13. V_b is obtained from the side-wise shadowgraphy measurements. $\alpha = 1$ represents a bubble growth entirely governed by the microlayer evaporation whereas $\alpha = 0$ represents a zero contribution coming from it. Fig. 5.18 shows α as a function of time during the microlayer evaporation. A contribution of about 18% is observed. This value is in good agreement with other similar experimental studies performed by Jung and Kim [12] and Myers et al. [101], $\alpha = 17\%$ and 23%, respectively. Within $0\,\text{ms} < t < 2\,\text{ms}$ the contact line is on the hot spot of the heating surface so that a transient behavior of α appears because of the non-uniform heating given by the IR laser on the boiling surface. For $t \geq 2\,\text{ms}$ the contact line is far enough from the hot spot and α attains a plateau.

This microlayer evaporation contribution seems therefore reasonable but it represents a lower limit due to the fact that the wall heat flux near the contact line, where q''_l attains a maximum (see

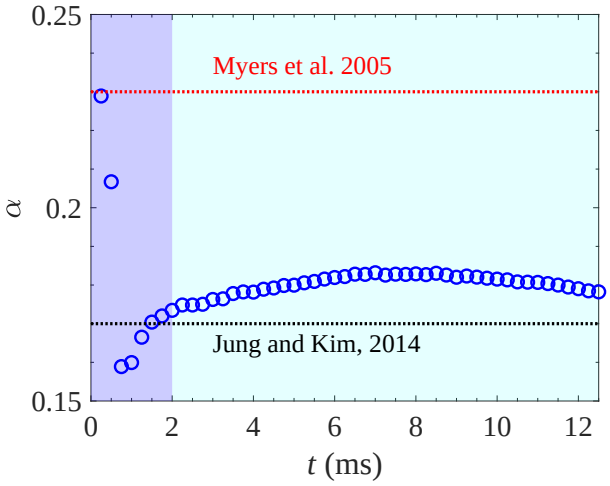

Figure 5.18: Microlayer evaporation contribution to the overall bubble growth.

Fig. 5.15b), is resolved within the pixel size given by the constrains in optical spatial resolution of the IR camera.

5.8 Dewetting dynamics

Figures 5.19a,b depict the capillary number $Ca_{cl} = \mu U_{cl}/\sigma$ based on the contact line receding speed and ΔT_{cl} at the contact line position at receding (i.e. a part of the curve in Fig. 5.17). Here, $U_{cl} = dr_{cl}/dt$, where r_{cl} is obtained from the experimental data shown in Fig. 5.4. Ca_{cl} and ΔT_{cl} present similar decays. The dewetting of the wall occurs faster at the initial stages of the bubble growth and then reaches a constant value when ΔT_{cl} becomes nearly constant. This is indeed an effect of the laser heating mode, which provides a highly non-uniform temperature distribution on the wall. For $t \leq 2$ ms, the contact line is located within the area of high input heat flux provided by the IR heating so that the high evaporation rates in this zone lead to fast contact line motion. Once the contact line is far enough from the heated spot, ΔT_{cl} decreases to a nearly constant value, which results in a constant Voinov angle (see subsection 2.1.8) thus causing a constant Ca_{cl}. These results show that the dewetting is indeed controlled by evaporation, which agrees well with the simulations of [30]. In Fig. 5.19a, we also show the numerical Ca_{cl} as a function of time, which is a result of the numerical simulation of the microlayer dynamics presented in section 5.4.2. The good agreement between the experimental and numerical Ca_{cl} shows the correct understanding of the near-wall phenomena.

We now use the experimental data from Figs. 5.19 to plot Ca_{cl} as a function of ΔT_{cl} shown in Fig. 5.19d. Note that ΔT_{cl} decreases with time, meaning that high ΔT_{cl} points correspond to early times. We compare with the theoretical curves [30, 123] showing the dewetting speed as functions of superheating for different microscopic contact angles θ_{micro}. From these curves one may have an impression that θ_{micro} varies in time. This is however wrong: θ_{micro} time variation caused by the surface temperature gradient cannot be that strong. The explanation is different. The theoretical curves (calculated under the assumption of the spatially uniform and constant in time ΔT) correspond to the averaged in time Ca_{cl}. However, even under these uniform conditions, Ca_{cl} decreases in time (Fig. 5.19c) because the ridge grows. This curve has been obtained for the quasi-stationary regime (after relaxation of the initial transients). The deviation of the experimental points from a single theoretical curve at early times can thus be explained by the transient effect and only the data at late times (for which ΔT_{cl} is nearly constant) should be accounted for while estimating θ_{micro}. One gets then $\theta_{micro} \approx 10°$, which should correspond to the receding contact angle (subsection 2.1.2).

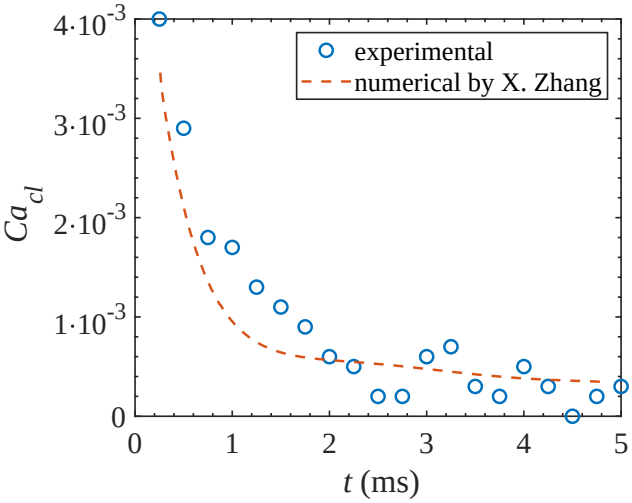

(a) Receding contact line speed as a function of time.

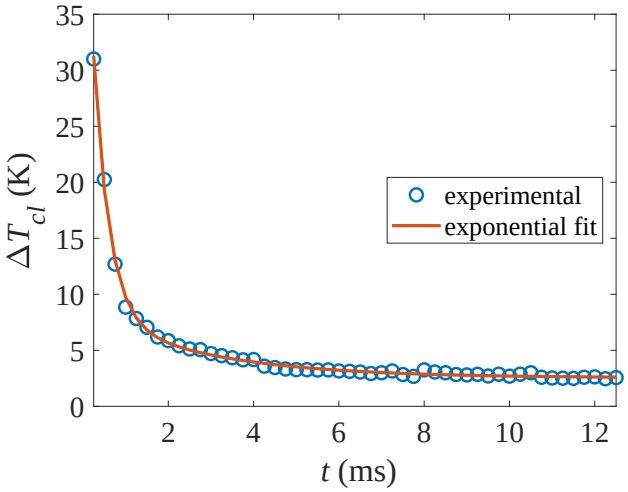

(b) The superheating at the contact line as a function of time.

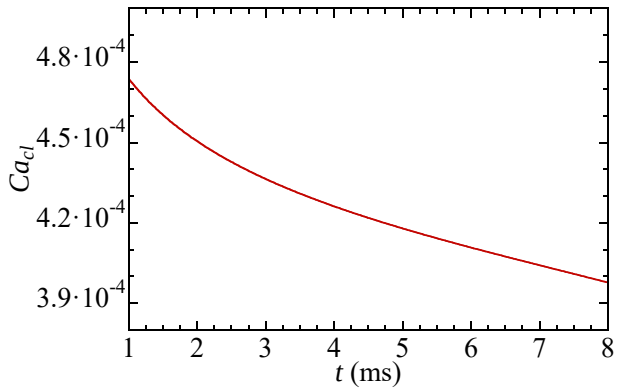

(c) An example of Ca_{cl} variation with time calculated theoretically [30] for uniform $\delta_0 = 6\,\mu$m, $\theta_{micro} = 10°$, and uniform $\Delta T = 5\,$K.

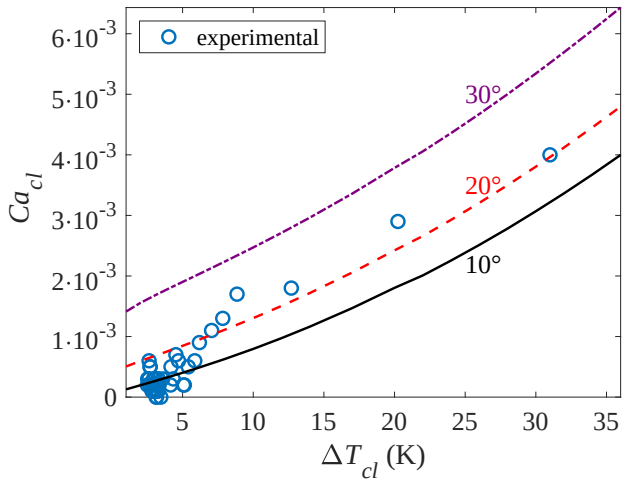

(d) Ca_{cl} as a function of ΔT_{cl}. The lines correspond to the theoretical data [123] computed for different values of the microscopic contact angle θ_{micro} and for $\delta_0 = 6\,\mu$m while the dots are experimental points.

Figure 5.19: Ca_{cl} and ΔT_{cl} at the contact line during its receding.

5.9 Discussion

We have performed many more boiling experiments apart from the one reported here in details. In this section, we discuss some of them aiming at two objectives. First, we describe how the boiling phenomenon, in particular the bubble triggered by local laser heating, can impose limitations on the optical observations. Second, both a transition from microlayer to contact line evaporation regimes and the dewetting phenomenon are addressed.

5.9.1 Microlayer and contact line evaporation regimes

In most boiling experiments, the formation of microlayer has not been observed. In these cases, the boiling dynamics is described as follows. When the IR laser beam heats up the ITO on surface with low roughness (of the order of several nm) and without any significant defects, the laser power

required to trigger the first bubble on a fresh ITO film is very high. We thus increase the IR laser power progressively until we observe a bubble nucleation. Figure 5.20 shows the macroscopic shape (obtained by sidewise shadowgraphy) and the wall phase distribution (obtained with the WLI in mirror mode as discussed in subsection 4.1.1) for the first nucleated bubble. The images correspond to the initial stage of bubble growth, 0.5 ms after nucleation. The wall phase distribution shows the presence of a microlayer and a dry spot. The inertial forces are large at high heat flux thus causing a stronger adhesion and large bubbles. Nevertheless, the main boiling features are similar to those described earlier in this chapter.

Figure 5.21a shows the bubble macroscopic shape and its respective phase distribution on the wall at a given time moment t' close to the bubble departure from the wall. At $t = t' + 0.25$ ms (Fig.5.21b), the bubble macroscopic shape shows the formation of a new dry patch on the wall that occurs before the previous bubble departs thus preventing the wall rewetting with the liquid from the bulk. The wall phase distribution in Fig. 5.21b and confirms the appearance of a new dry spot on the wall, which merges with the previous dry spot at $t = t' + 0.5$ ms. The rings around the dry spot (a signature of the microlayer seen e.g. Fig. 4.2b), are not observed. This signifies the bubble growth in the contact line evaporation regime.

Therefore, the first nucleated bubble does present a microlayer evaporation regime during its growth thanks mainly to a high receding velocity of the bubble foot edge induced by the inertial effects. However, the power is sufficiently high to reach the boiling crisis and the contact line regime predominates for the next bubbles nucleated on the same spot. We also have observed that even after decreasing the IR laser power the microlayer is not formed any longer. We thus believe that the wall overheating introduces significant changes of the wall properties, in particular deteriorates its wettability, thus preventing the formation of microlayer.

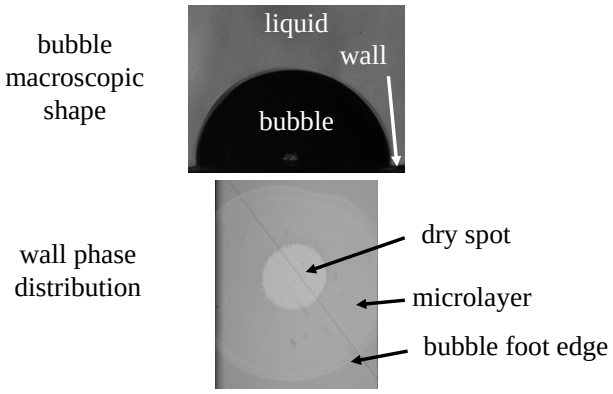

Figure 5.20: First nucleated bubble on a uniform heater without defects. Bubble macroscopic shape and wall phase distribution. The image corresponds to its receding moment 0.5 ms after bubble nucleation.

5.9.2 Homogeneous versus local heating: effect on contact line dynamics

As illustrated in Fig. 5.1 and also shown by state-of-the-art numerical simulations of nucleate pool boiling [7, 8, 209] the formation of a dewetting ridge results in high interfacial slopes near the contact line. To the best of our knowledge, the dewetting ridge has never been observed experimentally in boiling. We believe that the slopes are too high so the experimental techniques based on light reflectance such as interferometry cannot detect it. This can happen due to several reasons. First, the light being reflected from the liquid-vapor interface is deflected thus not interfering with the other reflected rays. The second possible reason is that the fringe can not be resolved by the optical measurements because of limited spatial resolution, such as discussed in section 4.1.15. Nevertheless,

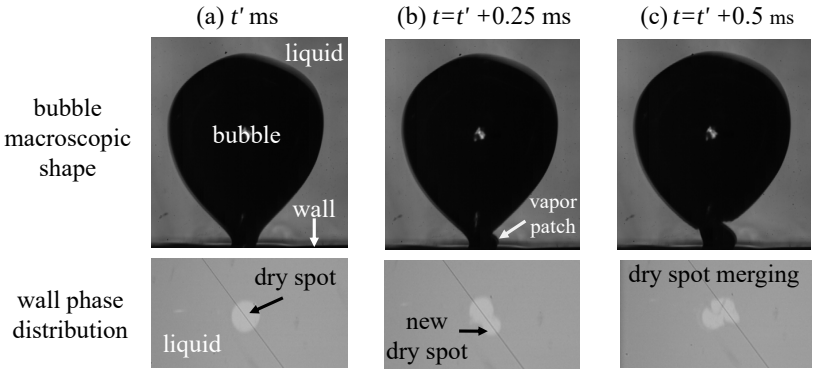

Figure 5.21: Bubble macroscopic shape and wall phase distribution near boiling crisis at single bubble growth.

in both cases the high local interfacial slope is a physical limitation preventing the observation of interference fringes. These two reasons can explain the impossibility to observe the fringes near the contact line.

We believe that the size of dewetting ridge is even bigger in our experimental setup due to the use of local heating. In order to compare the dewetting phenomenon that creates the ridge, one can cite a similar to our's experiment by Jung and Kim [12] with uniform Joule heating. From their experimental data, one obtains $Ca_{cl} \approx 3 \times 10^{-4}$ which is constant throughout the whole period of microlayer evaporation (constant U_{cl} during the contact line receding). In their experiment, $\Delta T \approx 23\,\mathrm{K}$ at bubble nucleation. In the our's, $\Delta T \approx 32\,\mathrm{K}$ with $Ca_{cl} \approx 4 \times 10^{-3}$, following an exponential decay over time as shown in Fig. 5.19a. As the contact line moves away 10 times faster at the very initial stages of bubble growth in our case, the liquid that previously situated at the dry spot is swept over by the contact line motion, getting accumulated in the ridge and forming a dome with slopes many times larger than our WLI installation could resolve. Therefore, the fringes are not observed within the extent of the ridge.

Another indication of high interfacial slopes can be obtained from Eqs. (2.6,2.7). One deduces from them that θ_{app} increases as ΔT and $(\Delta T)^{1/3}$ for low and high ΔT, respectively. At the bubble receding stage, ΔT is rather high ($\Delta T > 5\,\mathrm{K}$) as shown in Fig. 5.9. By using Eq. 2.7 one gets $\theta_{app} \approx 50°$ with $\Delta T = 5\,\mathrm{K}$. Such a slope is order of magnitude larger than the maximum slope limit that WLI is capable of measuring. We remind that the latter is determined in subsection 4.1.15 as $0.33° \leq \theta_{lim} \leq 0.49°$. Therefore, our experiments comply to the physical reasoning that suggests the presence of a big dewetting ridge near the contact line.

However, it is still a matter of discussion why experimental approaches using laser interferometry such as Jung and Kim [12] report a wedge-shaped microlayer (without mentioning the presence of dewetting ridge). Even though special optics are used to maximize the white light collimation, one could argue, for instance, that the absence of fringes in our WLI measurements could possibly come from the white light diffusion induced by imprecise collimation. In order to check this, we have also performed laser interferometry measurements with a highly collimated laser beam. Fig. 5.22 shows the obtained fringe pattern. The absence of fringes near the contact line is also observed with laser interferometry. This indicates that the absence of fringes is not linked to the optical method (LI or WLI) but rather agrees to the hypothesis that it is an effect of high slopes in the large ridge formed due to the IR laser heating mode.

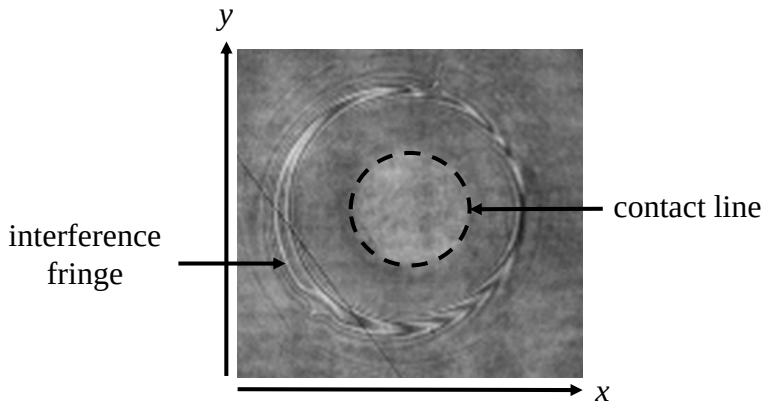

Figure 5.22: Fringe of interference by laser interferometry.

5.9.3 Effects of enlarged heating spot

We also have performed a few experiments enlarging the size of the IR laser beam aiming at providing a more uniform heating of the ITO film. However, when heating spot is enlarged, the laser power has to be increased to overcome the energy barrier for bubble nucleation. Since the laser power is limited, one meets a limitation on the maximum size of heating spot that can trigger the bubble. Fig. 5.23a shows the fringe map obtained with the maximum diameter beam still capable of triggering the bubble nucleation. The heating spot is a few times larger than the one reported in section 3.5.5. In the very close vicinity of the dry spot one still does not observe the interference fringe. This region corresponds to the dewetting ridge as we deduced above. In such a case, two different geometries of fringes are observed in the microlayer. A linear profile appears closer to the contact line, followed by a parabolic shape similar to the one shown in Fig. 5.3. The linear fringe thus represents a linear microlayer profile after the dewetting ridge. In some experiments we have clearly observed the formation of a convex parabola following the concave one near the bubble foot edge as soon as the microlayer is formed, as shown in Fig. 5.23b. In Fig. 5.23a the convexity cannot be identified because its width is shorter so the spatial resolution is insufficient to observe it. Nevertheless, such a geometry indicates a change in interface curvature near the microlayer edge as illustrated in Fig. 5.23c. These two parabolas are a result of deceleration of the bubble foot edge. This indicates that the interface slope decreases with the beam diameter. However, this effect might be also linked to the fact that by enlarging the heating area one covers a larger area on the ITO thus increasing a possibility to find a defect on the wall that can trigger the bubble with a lower ΔT, which decreases the slope of the interface.

5.10 Summary and concluding remarks

We have presented novel experimental data on the single bubble growth in boiling obtained with the state-of-the-art fast and microscopic-scale measurements. A maximum (bump) in the middle of the microlayer that appears at the initial stage of the bubble growth has been discovered and understood. The bumped profile is a result of the deceleration of growth of the radial bubble size on one hand, and on the other, of viscous and surface tension forces acting within the microlayer. The bump we measure does not correspond to the dewetting ridge evidenced in earlier numerical simulations. The numerical simulations performed in our research group evidence both the dewetting ridge and the bump. The simulated bump shape agrees to the experiment. We show that the temporal microlayer thinning is a result of its local evaporation.

The wall heat transfer features during the bubble growth has been revealed. We reveal and discuss the effects of the dry spot and microlayer on the wall temperature and heat flux. In the microlayer

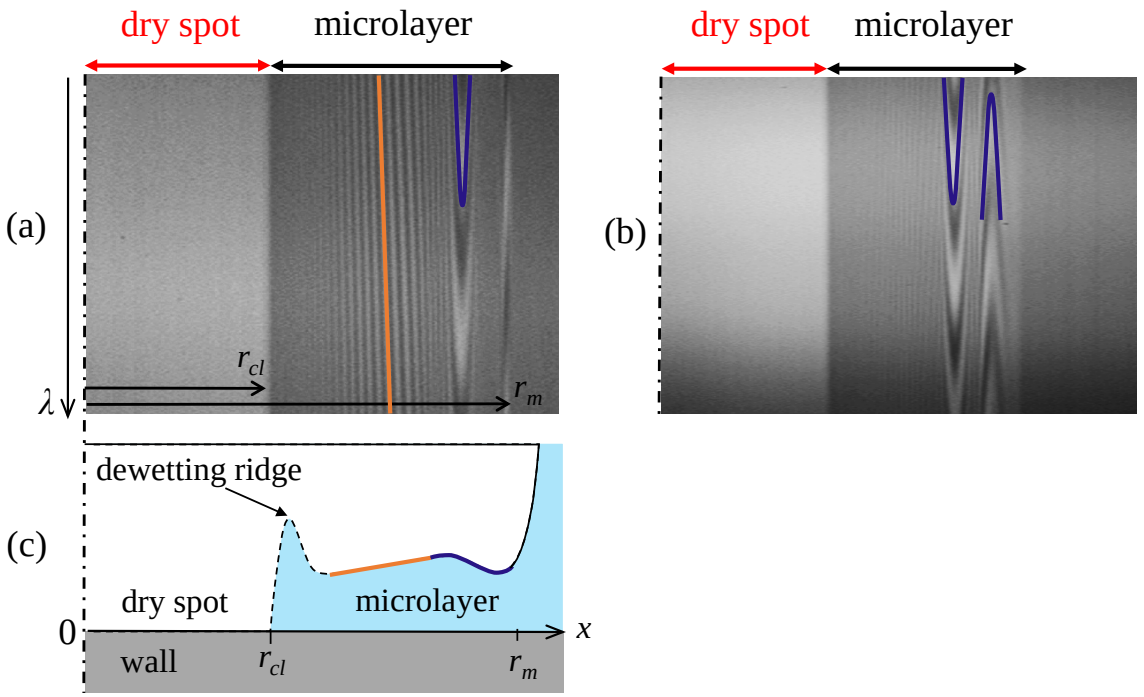

Figure 5.23: WLI fringe with enlarged IR laser beam. a) Linear and parabolic fringe b) two parabolic fringe and c) an illustrative description of microlayer profile.

extent, the wall temperature is nearly uniform with a low superheating. On the other hand, a high gradient is observed within the dry spot which is mainly caused by the non-uniform heating provided by the laser. The temporal heat flux distribution on the wall show similar trends observed in recent numerical simulation. We show that the heat flux coming from the porthole contributes the most for the wall heat flux towards the microlayer. By comparing the experimental heat flux and the one reconstructed numerically, we show that interfacial thermal resistance is important and it increases in time due to the accumulation of impurities at the interface.

We also evaluate the dewetting dynamics by comparing our experimental result with the theory. We particularly prove that the dewetting is accelerated by the evaporation and the microscopic contact angles were deduced from the comparison. By comparing with similar experiments that employ uniform Joule heating on the heating wall, we show that the acceleration of dewetting is related to the heating mode provided by the laser in our experiment.

We also have provided an extended discussion why interference fringes corresponding to the dewetting ridge cannot be observed in our experiment. However, our contact line velocity measurements correspond to the formation of a large dewetting ridge near the contact line, with high local slopes. In our case, this effect is even more pronounced given a high velocity of the contact line receding at early stages of bubble growth. The liquid previously situated at the dry spot area accumulates into the ridge. A full physical explanation of our experimental observations is therefore provided.

Chapter 6

Conclusions and perspectives

In this work, we performed microscale measurements of bubble growth in nucleate boiling regime. The focus is on the near-wall physical phenomena that occurs within the microlayer of thickness of few μm formed between the vapor bubble and the solid. The microlayer formation is still under debate in the scientific community studying boiling and only a limited number of precise experimental results are available. Novel high resolution and high speed optical diagnostic methods have been developed in the framework of this work to understand the physics of boiling. White light interferometry was used to study the dynamics of the microlayer thickness and the extents of the dry spot and microlayer on the wall while IR thermography and sidewise shadowgraphy give the wall temperature distribution and macroscopic shape of bubble, respectively.

The boiling surface consists of an ITO film deposited on a MgF_2. A single bubble is triggered by local heating with an IR laser thanks to the high absorbance of ITO in IR spectrum. A detailed study was carried out under boiling conditions to understand the electrochemical, mechanical and adhesion issues of the ITO on the porthole. In collaboration with LPCIM at Institut Polytechnique de Paris, who are the internationally recognized experts on the thin film physics, the right conditions for ITO deposition on such a difficult material as MgF_2 have been found. It ensures the ITO film that provides a strong adhesion during the bubble growth in boiling.

The first novelty of this work concerns the instrumentation used in this study. We implemented and validated a novel spectral white light interferometry apparatus to measure the dynamics of the microlayer thickness. To the best of our knowledge, this method has never been used in boiling studies. It has several notable advantages over the classical laser interferometry used for the boiling studies by several research groups. In particular, this approach provides a higher microlayer thickness resolution thus providing more data to compute the thickness, which ensures a higher precision. Most importantly, thanks to the wavelength dimension, the fringe geometry shows the microlayer profile at the observation time without any post-processing. This information is highly useful as it lets the observer to instantly evaluate the heater surface properties in the vicinity of a particular nucleation site and decide whether a neighboring site is more advantageous for observations or not. We have also optimized the arrangement of a large number of optical elements below the boiling cell so that all the three aforementioned measurements can be performed simultaneously and synchronously at 4000 fps with high spatial resolution. An extensive description of near-wall thermophysics and hydrodynamic phenomena is therefore achieved. We have also provided an extensive study of the optics issues that arise during adjustment and functioning of such an apparatus like physically-imposed limits of its functioning. We should also highlight here that the correct alignment of the optical elements the calibration of the cameras are indeed critical factors for the precision of our observations employed in this work. Even though we have followed strict alignment and calibration protocols, care must be taken and cross verification must be performed whenever is possible in order to ensure that misalignment and optical aberrations are at minimum.

Our experimental results show a novel feature on the microlayer profile: a "bump" in its central region that appears during its formation. We explain this bump as a result of interplay of viscous and capillary forces acting in the microlayer during the receding stage of the bubble foot edge. Within this description, the flow on the bubble scale defines the bubble edge dynamics that, on its turn, affects the microlayer formation. A very good agreement of these results have been found with numerical simulations performed in our research group thus confirming our physical understanding of microlayer formation. We also show that while the microlayer thinning occurs due to its evaporation, its depletion (disappearance) occurs because of its shortening provided by the contact line receding (a dewetting phenomenon).

The absence of interference fringe near the contact line in our experiment indicates a large dewetting ridge. Its existence in single bubble growth has been confirmed by our numerical simulations and those of other groups active in this field [7, 115, 116]. We show that the dewetting is faster under the IR laser heating mode compared to similar studies employing Joule heating. A rapid formation of the dry spot and the fast motion of the contact line sweeps the liquid situated in its surrounding thus causing an accumulation of a large liquid quantity in the ridge. Its width and thickness gets large thus leading to high slopes of the vapor-liquid interface. They are much higher than the maximum slope limit that WLI can measure so that the corresponding fringe pattern cannot be observed.

We were also able to compute the numerical heat flux towards the microlayer using the temperature distribution on the wall given by our IR thermometry measurements. A comparison with the heat flux determined from the microlayer thickness and the wall superheating show that an interfacial thermal resistance a few times higher than its theoretical value. Moreover, we show that it increases in time. This result indicates that in spite of the ultra-high purity of water used in the experiments, impurities exist in it and accumulate at the liquid-vapor interface as the bubble grows.

A large number of boiling tests have been performed to understand the bubble nucleation using IR laser local heating. In some of them, the microlayer was either partially observed or not observed at all. We believe that this is linked to the surface state of the heater and the characteristics (in particular depth) of the nucleation site. If the heater surface is so smooth that a large overheating is necessary to generate a bubble, the surface is immediately slightly damaged, which can cause a deterioration of its wettability thus increasing the microscopic contact angle. In order to better understand and confirm this hypothesis, experiments will be performed in the near future with an artificial microscopic nucleation site on the heater. By using it, we intend to decrease the energy required to trigger the bubble (nucleation barrier) so the heater stays homogeneous during subsequent bubble nucleation events.

We intend to explore in the future the physics of boiling crisis, preferably with a single bubble. Our preliminary experiments have shown that indeed the CHF can be achieved with a single bubble if the contact angle is high enough, which agrees with previous experiments of Kannengieser et al. [74]. However, the mechanisms leading to CHF are still poorly understood and our current experimental installation is able to give insightful data on them. We suggest that cameras with a higher resolution should be implemented to better describe the microlayer dynamics. Also, their sensitivity should be increased to capture with higher precision the very initial stages of microlayer formation because its dynamics is very fast.

Bibliography

[1] T. N. Dinh, T. G. Theofanous, Nucleation phenomena in boiling, Multiphase Sci. Technol. 15 (2003) 349 – 363.

[2] T. G. Theofanous, The boiling crisis in nuclear reactor safety and performance, Int. J. Multiphase Flow 6 (1980) 69 – 95.

[3] T. G. Theofanous, S. Syri, T. Salmassi, O. Kymäläinen, H. Tuomisto, Critical heat flux through curved, downward facing, thick walls, Nucl. Eng. Des. 151 (1994) 247 – 258.

[4] S. Angelini, J. P. Tu, Y. A. Buyevich, T. G. Theofanous, The mechanism and prediction of critical heat flux in inverted geometries, Nucl. Eng. Des. 200 (2000) 83 – 94.

[5] S. Nukiyama, The maximum and minimum values of the heat Q transmitted from metal to boiling water under atmospheric pressure, J. Soc. Mech. Eng. Jpn. 37 (1934) 367 – 374. (translated in Int. J. Heat Mass Transfer, **9**, 1419 - 1433 (1966)).

[6] S. M. Ghiaasiaan, Two-Phase Flow, Boiling and Condensation in Conventional and Miniature Systems, Cambridge University Press, 2008.

[7] A. Urbano, S. Tanguy, G. Huber, C. Colin, Direct numerical simulation of nucleate boiling in micro-layer regime, Int. J. Heat Mass Transfer 123 (2018) 1128 – 1137.

[8] L. Bureš, Y. Sato, Analysis of dynamics of microlayer formation and destruction in nucleate boiling, in: 5-6th Thermal Fluids Eng. Conf., 2021, pp. 97 – 106. 26-28 May.

[9] K. Schweikert, A. Sielaff, P. Stephan, On the transition between contact line evaporation and microlayer evaporation during the dewetting of a superheated wall, Int. J. Therm. Sci. 145 (2019) 106025.

[10] V. Janeček, B. Andreotti, D. Pražák, T. Bárta, V. S. Nikolayev, Moving contact line of a volatile fluid, Phys. Rev. E 88 (2013) 060404.

[11] P.-G. de Gennes, Wetting: statics and dynamics, Rev. Mod. Phys. 57 (1985) 827 – 863.

[12] S. Jung, H. Kim, An experimental method to simultaneously measure the dynamics and heat transfer associated with a single bubble during nucleate boiling on a horizontal surface, Int. J. Heat Mass Transfer 73 (2014) 365 – 375.

[13] C. W. Extrand, Contact angles and hysteresis on surfaces with chemically heterogeneous islands, Langmuir 19 (2003) 3793 – 3796.

[14] V. S. Nikolayev, Evaporation effect on the contact angle and contact line dynamics, in: M. Marengo, J. De Coninck (Eds.), The Surface Wettability Effect on Phase Change, Springer, 2022, pp. 133 – 187.

[15] V. Janeček, Evaporation at microscopic scale and at high heat flux, Ph.D. thesis, Université Pierre et Marie Curie Paris 6, 2012.

[16] V. P. Carey, Liquid-Vapor Phase Change Phenomena, Hemisphere, Washington D.C., 1992.

[17] R. Marek, J. Straub, The origin of thermocapillary convection in subcooled nucleate pool boiling, Int. J. Heat Mass Transfer 44 (2001) 619 – 632.

[18] J. C. Maxwell, On stresses in rarefied gases arising from inequalities of temperature, Proc. R. Soc. Lond. 27 (1878) 304 – 308.

[19] M. Knudsen, Die molekulare warmeleitung der gase und der akkommodationskoeffizient, Ann. Phy. 339 (1911) 593 – 656.

[20] M. Knudsen, Die maximale verdampfungsgeschwindigkeit des quecksilbers, Ann. Phy. 352 (1915) 697 – 708.

[21] I. W. Eames, N. J. Marr, H. Sabir, The evaporation coefficient of water: a review, Int. J. Heat Mass Transfer 40 (1997) 2963 – 2973.

[22] V. S. Nikolayev, D. A. Beysens, Boiling crisis and non-equilibrium drying transition, Europhys. Lett. 47 (1999) 345 – 351.

[23] D. M. Anderson, P. Cermelli, E. Fried, M. E. Gurtin, G. B. McFadden, General dynamical sharp-interface conditions for phase transformations in viscous heat-conducting fluids, J. Fluid Mech. 581 (2007) 323 – 370.

[24] M. Ishii, T. Hibiki, Thermo-Fluid Dynamics of Two-Phase Flow, Springer, 2006.

[25] R. Pit, H. Hervet, L. Léger, Direct experimental evidence of slip in hexadecane: solid interfaces, Phys. Rev. Lett. 85 (2000) 980 – 983.

[26] C. I. Bouzigues, P. Tabeling, L. Bocquet, Nanofluidics in the Debye layer at hydrophilic and hydrophobic surfaces, Phys. Rev. Lett. 101 (2008) 114503.

[27] E. Lauga, M. P. Brenner, H. A. Stone, Microfluidics: the no-slip boundary condition, in: C. Tropea, A. Yarin, J. Foss (Eds.), Springer Handbook of Experimental Fluid Dynamics, Springer, New York, 2007, pp. 1217 – 1240.

[28] J. Koplik, J. R. Banavar, Continuum deductions from molecular hydrodynamics, Annu. Rev. Fluid Mech. 27 (1995) 257 – 292.

[29] J. H. Snoeijer, J. Eggers, Asymptotic analysis of the dewetting rim, Phys. Rev. E 82 (2010) 056314.

[30] X. Zhang, V. S. Nikolayev, Dewetting acceleration by evaporation, J. Fluid Mech. (2022).

[31] C. Redon, F. Brochard-Wyart, F. Rondelez, Dynamics of dewetting, Phys. Rev. Lett. 66 (1991) 715 – 718.

[32] C. Redon, J. B. Brzoska, F. Brochard-Wyart, Dewetting and slippage of microscopic polymer films, Macromolecules 27 (1994) 468 – 471.

[33] G. Delon, M. Fermigier, J. H. Snoeijer, B. Andreotti, Relaxation of a dewetting contact line. Part 2: Experiments, J. Fluid Mech. 604 (2008) 55 – 75.

[34] A. M. J. Edwards, R. Ledesma-Aguilar, M. I. Newton, C. V. Brown, G. McHale, Not spreading in reverse: the dewetting of a liquid film into a single drop, Sci. Adv. 2 (2016) e1600183.

[35] L. Fourgeaud, E. Ercolani, J. Duplat, P. Gully, V. S. Nikolayev, Evaporation-driven dewetting of a liquid film, Phy. Rev. Fluids 1 (2016) 041901(R).

[36] L. Fourgeaud, V. S. Nikolayev, E. Ercolani, J. Duplat, P. Gully, In situ investigation of liquid films in pulsating heat pipe, App. Therm. Eng. 126 (2017) 1023 – 1028.

[37] J. Kim, Review of nucleate pool boiling bubble heat transfer mechanisms, Int. J. Multiphase Flow 35 (2009) 1067 – 1076.

[38] N. R. Snyder, D. K. Edwards, Summary of conference on bubble dynamics and boiling heat transfer. memo 20-137, jet propulsion laboratory, 1956.

[39] F. D. Moore, R. B. Mesler, The measurement of rapid surface temperature fluctuations during nucleate boiling of water, AIChE J. 7 (1961) 620 – 624.

[40] R. R. Sharp, The nature of liquid film evaporation during nucleate boiling, Technical Report, National Aeronautics and Space Administration, 1964. NASA Technical note TN D-1997.

[41] K. Torikai, Heat transfer in a contact area of a boiling bubble on a heating surface, Bull. JSME 10 (1967) 338 – 348.

[42] H. H. Jawurek, Simultaneous determination of microlayer geometry and bubble growth in nucleate boiling, Int. J. Heat Mass Transfer 12 (1969) 843 – 848.

[43] H. H. Jawurek, Latent heat transport and microlayer evaporation in nucleate boiling, Ph.D. thesis, University of the Witwatersrand - School of Mechanical Engineering, 1977.

[44] M. G. Cooper, A. J. P. Lloyd, The microlayer in nucleate pool boiling, Int. J. Heat Mass Transfer 12 (1969) 895 – 913.

[45] H. J. van Ouwerkerk, The rapid growth of a vapour bubble at a liquid-solid interface, Int. J. Heat Mass Transfer 14 (1971) 1415 – 1431.

[46] M. Akiyama, Dynamics of an isolated vapor bubble in saturated nucleate boiling: Part 3, Effect of thermal factors of a heater, Bull. JSME 14 (1971) 1313 – 1319.

[47] C. M. Voutsinos, R. L. Judd, Laser interferometric investigation of the microlayer evaporation phenomenon, J. Heat Transfer 97 (1975) 88 – 92.

[48] G. F. Smirnov, Calculation of the “initial” thickness of the “microlayer” during bubble boiling, J. Eng. Phys. 28 (1975) 369 – 374.

[49] T. G. Theofanous, T. H. Bohrer, M. C. Chang, P. D. Patel, Experiments and universal growth relations for vapor bubbles with microlayers, J. Heat Transfer 100 (1978) 41 – 48.

[50] L. D. Koffman, M. S. Plesset, Experimental observations of the microlayer in vapor bubble growth on a heated solid, J. Heat Transfer 105 (1983) 625 – 632.

[51] M. Gao, L. Zhang, P. Cheng, X. Quan, An investigation of microlayer beneath nucleation bubble by laser interferometric method, Int. J. Heat Mass Transfer 57 (2013) 183 – 189.

[52] R. R. Olander, R. G. Watts, An analytical expression of microlayer thickness in nucleate boiling, J. Heat Transfer 91 (1969) 178 – 180.

[53] Y. Zhang, Y. Utaka, Y. Kashiwabara, Formation mechanism and characteristics of a liquid microlayer in microchannel boiling system, J. Heat Transfer 132 (2010) 122403.

[54] Y. Utaka, Y. Kashiwabara, M. Ozaki, Microlayer structure in nucleate boiling of water and ethanol at atmospheric pressure, Int. J. Heat Mass Transfer 57 (2013) 222 – 230.

[55] S. Jung, H. Kim, An experimental study on heat transfer mechanisms in the microlayer using integrated total reflection, laser interferometry and infrared thermometry technique, Heat Transfer Eng. 36 (2015) 1002 – 1012.

[56] A. Zou, A. Chanana, A. Agrawal, P. C. Wayner, S. C. Maroo, Steady state vapor bubble in pool boiling, Sci. Rep. 6 (2016) 20240.

[57] Z. Chen, A. Haginiwa, Y. Utaka, Detailed structure of microlayer in nucleate pool boiling for water measured by laser interferometric method, Int. J. Heat Mass Transfer 108 (2017) 1285 – 1291.

[58] K. Hu, Z. Chen, Y. Utaka, Study on characteristics of formation and evaporation of microlayer using laser interferometry during nucleate pool boiling for water and ethanol, in: 16th Int. Heat Transfer Conf., 2018, pp. 917 – 924.

[59] S. Jung, H. Kim, Hydrodynamic formation of a microlayer underneath a boiling bubble, Int. J. Heat Mass Transfer 120 (2018) 1229 – 1240.

[60] J. nan Liu, M. Gao, L. shuang Zhang, L. xin Zhang, A laser interference/high-speed photography method for the study of triple phase contact-line movements and lateral rewetting flow during single bubble growth on a small hydrophilic heated surface, Int. Comm. Heat Mass Transfer 100 (2019) 111 – 117.

[61] Z. Chen, X. Hu, K. Hu, Y. Utaka, S. Mori, Measurement of the microlayer characteristics in the whole range of nucleate boiling for water by laser interferometry, Int. J. Heat Mass Transfer 146 (2020) 118856.

[62] A. S. Surtaev, V. S. Serdyukov, Investigation of contact line dynamics under a vapor bubble at boiling on the transparent heater, Thermophys. Aeromech. 25 (2018) 67 – 73.

[63] A. Surtaev, V. Serdyukov, J. Zhou, A. Pavlenko, V. Tumanov, An experimental study of vapor bubbles dynamics at water and ethanol pool boiling at low and high heat fluxes, Int. J. Heat Mass Transfer 126 (2018) 297 – 311.

[64] Y. Sato, B. Niceno, A depletable micro-layer model for nucleate pool boiling, J. Comput. Phys. 300 (2015) 20 – 52.

[65] T. G. Theofanous, T. N. Dinh, J. P. Tu, A. T. Dinh, The boiling crisis phenomenon. Part II: Dryout dynamics and burnout, Exp. Thermal Fluid Sci. 26 (2002) 793 – 810.

[66] J. Buongiorno, L.-W. Hu, C. Gerardi, T. J. McKrell, Experimental observation of the dynamic micro-and macro-layer during pool boiling, in: Proc. 2008 ASME Summer Heat Transf. Conf., Jacksonville, Florida USA, 2008.

[67] C. Gerardi, J. Buongiorno, L. W. Hu, T. McKrell, High-speed infrared thermography study of bubble growth in water pool boiling, Trans. Am. Nucl. Soc. 101 (2009) 905 – 906.

[68] C. Gerardi, J. Buongiorno, L. wen Hu, T. McKrell, Study of bubble growth in water pool boiling through synchronized, infrared thermometry and high-speed video, Int. J. Heat Mass Transfer 53 (2010) 4185 – 4192.

[69] C. Gerardi, J. Buongiorno, L.-w. Hu, T. McKrell, Infrared thermometry study of nanofluid pool boiling phenomena, Nanoscale Res. Lett. 6 (2011) 232.

[70] X. Duan, B. Phillips, J. Buongiorno, T. McKrell, Measurement of nucleate pool boiling with synchronized particle imaging velocimetry and infrared thermometry, in: 2011 ANS Winter Meeting and Nuclear Technology Expo: and Embedded Topical Meetings, Washington, D.C, 2011.

[71] X. Duan, B. Phillips, T. McKrell, J. Buongiorno, Synchronized high-speed video, infrared thermometry, and particle image velocimetry data for validation of interface-tracking simulations of nucleate boiling phenomena, Exp. Heat Transfer 26 (2013) 169 – 197.

[72] T. Yabuki, T. Saitoh, O. Nakabeppu, Contribution of microlayer evaporation to bubble growth in pool saturated boiling of water, in: ASME 2013 11th International Conference on Nanochannels, Microchannels, and Minichannels, ASME, 2013.

[73] T. Yabuki, O. Nakabeppu, Heat transfer mechanisms in isolated bubble boiling of water observed with MEMS sensor, Int. J. Heat Mass Transfer 76 (2014) 286 – 297.

[74] O. Kannengieser, W. Bergez, C. Colin, Boiling on an isolated nucleation site close to CHF conditions, in: Proc. 15th Int. Heat Transfer Conf., Kyoto, Japan, 2014. Paper IHTC15-8856.

[75] Y. Utaka, Y. Kashiwabara, M. Ozaki, Z. Chen, Heat transfer characteristics based on microlayer structure in nucleate pool boiling for water and ethanol, Int. J. Heat Mass Transfer 68 (2014) 479–488.

[76] R. Visentini, C. Colin, P. Ruyer, Experimental investigation of heat transfer in transient boiling, Exp. Therm. Fluid Sci. 55 (2014) 95 – 105.

[77] N. S. Dhillon, J. Buongiorno, K. K. Varanasi, Critical heat flux maxima during boiling crisis on textured surfaces, Nat. Commun. 6 (2015) 8247.

[78] G.-Y. Su, M. Bucci, T. McKrell, J. Buongiorno, Transient boiling of water under exponentially escalating heat inputs. Part I: Pool boiling, Int. J. Heat Mass Transfer 96 (2016) 667 – 684.

[79] G.-Y. Su, M. Bucci, T. McKrell, J. Buongiorno, Transient boiling of water under exponentially escalating heat inputs. part II: Flow boiling, Int. J. Heat Mass Transfer 96 (2016) 685 – 698.

[80] D. E. Kim, J. Song, H. Kim, Simultaneous observation of dynamics and thermal evolution of irreversible dry spot at critical heat flux in pool boiling, Int. J. Heat Mass Transfer 99 (2016) 409 – 424.

[81] M. Bucci, A. Richenderfer, G.-Y. Su, T. McKrell, J. Buongiorno, A mechanistic IR calibration technique for boiling heat transfer investigations, Int. J. Multiphase Flow 83 (2016) 115 – 127.

[82] T. Yabuki, O. Nakabeppu, Microscale wall heat transfer and bubble growth in single bubble subcooled boiling of water, Int. J. Heat Mass Transfer 100 (2016) 851 – 860.

[83] A. Surtaev, V. Serdyukov, A. Chernyavskiy, Study of thermal behavior of microlayer under vapor bubble at liquid boiling, EPJ Web Conf. 159 (2017) 00051.

[84] H. Kim, Y. Park, H. Kim, C. Lee, D. W. Jerng, D. E. Kim, Critical heat flux enhancement by single-layered metal wire mesh with micro and nano-sized pore structures, Int. J. Heat Mass Transfer 115 (2017) 439 – 449.

[85] V. S. Serdyukov, A. S. Surtaev, A. N. Pavlenko, A. N. Chernyavskiy, Study on local heat transfer in the vicinity of the contact line under vapor bubbles at pool boiling, High Temp. 56 (2018) 546 – 552.

[86] Y. Utaka, K. Hu, Z. Chen, T. Morokuma, Measurement of contribution of microlayer evaporation applying the microlayer volume change during nucleate pool boiling for water and ethanol, Int. J. Heat Mass Transfer 125 (2018) 243 – 247.

[87] M. A. Amidu, S. Jung, H. Kim, Direct experimental measurement for partitioning of wall heat flux during subcooled flow boiling: Effect of bubble areas of influence factor, Int. J. Heat Mass Transfer 127 (2018) 515 – 533.

[88] M. Mehrvand, S. A. Putnam, Transient and local two-phase heat transport at macro-scales to nano-scales, Commun. Phys. 1 (2018) 21.

[89] A. Richenderfer, A. Kossolapov, J. H. Seong, G. Saccone, E. Demarly, R. Kommajosyula, E. Baglietto, J. Buongiorno, M. Bucci, Investigation of subcooled flow boiling and CHF using high-resolution diagnostics, Exp. Therm. Fluid Sci. 99 (2018) 35 – 58.

[90] E. Baglietto, E. Demarly, R. Kommajosyula, Boiling crisis as the stability limit to wall heat partitioning, Appl. Phys. Lett. 114 (2019) 103701.

[91] L. Zhang, J. H. Seong, M. Bucci, Percolative scale-free behavior in the boiling crisis, Phys. Rev. Lett. 122 (2019) 134501.

[92] G. Giustini, S. Jung, H. Kim, K. H. Ardron, S. P. Walker, Microlayer evaporation during steam bubble growth, Int. J. Therm. Sci. 137 (2019) 45 – 54.

[93] G. Giustini, I. Kim, H. Kim, Comparison between modelled and measured heat transfer rates during the departure of a steam bubble from a solid surface, Int. J. Heat Mass Transfer 148 (2020) 119092.

[94] G.-Y. Su, C. Wang, L. Zhang, J. H. Seong, R. Kommajosyula, B. Phillips, M. Bucci, Investigation of flow boiling heat transfer and boiling crisis on a rough surface using infrared thermometry, Int. J. Heat Mass Transfer 160 (2020) 120134.

[95] A. Kossolapov, F. Chavagnat, R. Nop, N. Dorville, B. Phillips, J. Buongiorno, M. Bucci, The boiling crisis of water under exponentially escalating heat inputs in subcooled flow boiling at atmospheric pressure, Int. J. Heat Mass Transfer 160 (2020) 120137.

[96] A. Kossolapov, B. Phillips, M. Bucci, Can LED lights replace lasers for detailed investigations of boiling phenomena?, Int. J. Multiph. Flow 135 (2021) 103522.

[97] Y. Sato, B. Niceno, Pool boiling simulation using an interface tracking method: From nucleate boiling to film boiling regime through critical heat flux, Int. J. Heat Mass Transfer 125 (2018) 876 – 890.

[98] R. L. Judd, K. S. Hwang, A comprehensive model for nucleate pool boiling heat transfer including microlayer evaporation, J. Heat Transfer 98 (1976) 623 – 629.

[99] R. J. Benjamin, A. R. Balakrishnan, Nucleate pool boiling heat transfer of pure liquids at low to moderate heat fluxes, Int. J. Heat Mass Transfer 39 (1996) 2495 – 2504.

[100] G. Son, V. K. Dhir, N. Ramanujapu, Dynamics and heat transfer associated with a single bubble during nucleate boiling on a horizontal surface, J. Heat Transfer 121 (1999) 623 – 631.

[101] J. G. Myers, V. K. Yerramilli, S. W. Hussey, G. F. Yee, J. Kim, Time and space resolved wall temperature and heat flux measurements during nucleate boiling with constant heat flux boundary conditions, Int. J. Heat Mass Transfer 48 (2005) 2429 – 2442.

[102] W. Ding, E. Krepper, U. Hampel, Evaluation of the microlayer contribution to bubble growth in horizontal pool boiling with a mechanistic model that considers dynamic contact angle and base expansion, Int. J. Heat Fluid Flow 72 (2018) 274 – 287.

[103] P. Kangude, A. Srivastava, Understanding the growth mechanism of single vapor bubble on a hydrophobic surface: experiments under nucleate pool boiling regime, Int. J. Heat Mass Transfer 154 (2020) 119775.

[104] S. Gong, P. Cheng, Lattice Boltzmann simulations for surface wettability effects in saturated pool boiling heat transfer, Int. J. Heat Mass Transfer 85 (2015) 635 – 646.

[105] X. Ma, P. Cheng, 3D simulations of pool boiling above smooth horizontal heated surfaces by a phase-change lattice Boltzmann method, Int. J. Heat Mass Transfer 131 (2019) 1095 – 1108.

[106] A. Surtaev, V. Serdyukov, A. Safonov, Characteristics of boiling heat transfer on hydrophobic surface, EPJ Web of Conferences 196 (2019) 00054.

[107] W. Ding, D. Sarker, U. Hampel, Impact of surface characteristics on microlayer, bubble dimensions and departure in nucleate boiling, in: 16th Int. Heat Transfer Conf., 2018.

[108] D. Sarker, W. Ding, R. Franz, O. Varlamova, P. Kovats, K. Zähringer, U. Hampel, Investigations on the effects of heater surface characteristics on the bubble waiting period during nucleate boiling at low subcooling, Exp. Therm. Fluid Sci. 101 (2019) 76 – 86.

[109] D. Sarker, W. Ding, U. Hampel, Bubble growth during subcooled nucleate boiling on a vertical heater: A mechanistic attempt to evaluate the role of surface characteristics on microlayer evaporation, App. Therm. Eng. 153 (2019) 565 – 574.

[110] D. Sarker, W. Ding, C. Schneider, U. Hampel, Single bubble dynamics during nucleate flow boiling on a vertical heater: experimental and theoretical analysis of the effect of surface wettability, roughness and bulk liquid velocity, Int. J. Heat Mass Transfer 142 (2019) 118481.

[111] S. Fischer, T. Gambaryan-Roisman, P. Stephan, On the development of a thin evaporating liquid film at a receding liquid/vapour-interface, Int. J. Heat Mass Transfer 88 (2015) 346 – 356.

[112] S. Tanguy, M. Sagan, B. Lalanne, F. Couderc, C. Colin, Benchmarks and numerical methods for the simulation of boiling flows, J. Comput. Phys. 264 (2014) 1 – 22.

[113] G. Huber, S. Tanguy, M. Sagan, C. Colin, Direct numerical simulation of nucleate pool boiling at large microscopic contact angle and moderate Jakob number, Int. J. Heat Mass Transfer 113 (2017) 662 – 682.

[114] A. Urbano, S. Tanguy, C. Colin, Direct numerical simulation of nucleate boiling in zero gravity conditions, Int. J. Heat Mass Transfer 143 (2019) 118521.

[115] S. Hänsch, S. Walker, The hydrodynamics of microlayer formation beneath vapour bubbles, Int. J. Heat Mass Transfer 102 (2016) 1282 – 1292.

[116] L. Bureš, Y. Sato, On the modelling of the transition between contact-line and microlayer evaporation regimes in nucleate boiling, J. Fluid Mech. 916 (2021) A53.

[117] G. Giustini, S. Jung, H. Kim, S. P. Walker, Evaporative thermal resistance and its influence on microscopic bubble growth, Int. J. Heat Mass Transfer 101 (2016) 733 – 741.

[118] G. Giustini, V. Badalassi, S. P. Walker, Analysis of the liquid film formed beneath a vapour bubble growing at a heated wall without neglect of evaporative thermal resistance, in: Int. Congr. Adv. Nuclear Power Plants, 2016.

[119] S. Hänsch, S. Walker, Microlayer formation and depletion beneath growing steam bubbles, Int. J. Multiphase Flow 111 (2019) 241 – 263.

[120] A. Zou, M. Gupta, S. C. Maroo, Origin, evolution, and movement of microlayer in pool boiling, J. Phys. Chem. Lett. 9 (2018) 3863 – 3869.

[121] L. D. Landau, B. V. Levich, Dragging of a liquid by a moving plate, Acta physico-chimica USSR 17 (1942) 42 – 54.

[122] F. P. Bretherton, The motion of long bubbles in tubes, J. Fluid Mech. 10 (1961) 166 – 188.

[123] X. Zhang, V. S. Nikolayev, Dewetting accelerated by evaporation, in: Proc. 16th Int. Conf. Heat Transfer Fluid Mech. Thermodynamics (HEFAT-ATE 2022), 2022, pp. 311 – 316.

[124] D. B. R. Kenning, Y. Yan, Pool boiling heat transfer on a thin plate: features revealed by liquid crystal thermography, Int. J. Heat Mass Transfer 39 (1996) 3117 – 3137.

[125] A. Sielaff, Experimental investigation of single bubbles and bubble interactions in nucleate boiling, Ph.D. thesis, Technical University of Darmstadt, 2014.

[126] S. Jung, H. Kim, Observation of the mechanism triggering critical heat flux in pool boiling of saturated water under atmospheric pressure, Int. J. Heat Mass Transfer 128 (2019) 229 – 238.

[127] J. Jung, J. Kim, H. Lee, S. J. Kim, Measurement of phase distributions on the surface in subcooled pool boiling of FC-72, Int. J. Heat Mass Transfer 115 (2017) 62 – 72.

[128] V. Nikolayev, D. Beysens, Y. Garrabos, C. Lecoutre, D. Chatain, Bubble spreading during the boiling crisis: modelling and experimenting in microgravity, Microgravity Sci. Technol. 18 (2006) 34 – 37.

[129] V. S. Nikolayev, D. Chatain, Y. Garrabos, D. Beysens, Experimental evidence of the vapor recoil mechanism in the boiling crisis, Phys. Rev. Lett. 97 (2006) 184503.

[130] M. E. Pasquini, Étude expérimentale de la dynamique d'une bulle de vapeur, Ph.D. thesis, Université Pierre et Marie Curie, 2015.

[131] Y. Nam, E. Aktinol, V. K. Dhir, Y. S. Ju, Single bubble dynamics on a superhydrophilic surface with artificial nucleation sites, Int. J. Heat Mass Transfer 54 (2011) 1572 – 1577.

[132] I. Nejati, A. Sielaff, B. Franz, M. Zimmermann, P. Hänichen, K. Schweikert, J. Krempel, P. Stephan, A. Martin, H. Scheerer, T. Engler, M. Oechsner, Experimental investigation of single bubble nucleate boiling in microgravity, Microgravity Sci. Technol. 32 (2020) 597 – 607.

[133] S. Vafaei, H. Kim, Single bubble boiling from an artificial cavity, J. Nanofluids 8 (2019) 1617 – 1631.

[134] L. Zhang, M. Shoji, Nucleation site interaction in pool boiling on the artificial surface, Int. J. Heat Mass Transfer 46 (2003) 513 – 522.

[135] S. Chatpun, M. Watanabe, M. Shoji, Nucleation site interaction in pool nucleate boiling on a heated surface with triple artificial cavities, Int. J. Heat Mass Transfer 47 (2004) 3583 – 3587.

[136] J. Bonjour, M. Clausse, M. Lallemand, Experimental study of the coalescence phenomenon during nucleate pool boiling, Exp. Therm. Fluid Sci. 20 (2000) 180 – 187.

[137] C. Hutter, K. Sefiane, T. G. Karayiannis, A. J. Walton, R. A. Nelson, D. B. R. Kenning, Nucleation site interaction between artificial cavities during nucleate pool boiling on silicon with integrated micro-heater and temperature micro-sensors, Int. J. Heat Mass Transfer 55 (2012) 2769 – 2778.

[138] C. Hutter, A. Sanna, T. G. Karayiannis, D. B. R. Kenning, R. A. Nelson, K. Sefiane, A. J. Walton, Vertical coalescence during nucleate boiling from a single artificial cavity, Exp. Therm. Fluid Sci. 51 (2013) 94 – 102.

[139] I. Golobic, J. Petkovsek, H. Gjerkes, D. B. R. Kenning, Horizontal chain coalescence of bubbles in saturated pool boiling on a thin foil, Int. J. Heat Mass Transfer 54 (2011) 5517 – 5526.

[140] A. Mukherjee, V. K. Dhir, Study of lateral merger of vapor bubbles during nucleate pool boiling, J. Heat Transfer 126 (2004) 1023 – 1039.

[141] M. Shoji, Y. Takagi, Bubbling features from a single artificial cavity, Int. J. Heat Mass Transfer 44 (2001) 2763 – 2776.

[142] W. M. Sluyter, P. C. Slooten, C. A. Copraij, A. K. Chesters, The departure size of pool boiling bubbles from artificial cavities at moderate and high pressures, Int. J. Multiphase Flow 17 (1991) 153 – 158.

[143] S. Siedel, S. Cioulachtjian, J. Bonjour, Experimental analysis of bubble growth, departure and interactions during pool boiling on artificial nucleation sites, Exp. Therm. Fluid Sci. 32 (2008) 1504 – 1511.

[144] C. Hutter, D. B. R. Kenning, K. Sefiane, T. G. Karayiannis, H. Lin, G. Cummins, A. J. Walton, Experimental pool boiling investigations of FC-72 on silicon with artificial cavities and integrated temperature microsensors, Exp. Therm. Fluid Sci. 34 (2010) 422 – 433.

[145] A. Sanna, T. G. Karayiannis, D. B. R. Kenning, C. Hutter, K. Sefiane, A. J. Walton, I. Golobič, E. Pavlovič, R. A. Nelson, Steps towards the development of an experimentally verified simulation of pool nucleate boiling on a silicon wafer with artificial sites, Appl. Therm. Eng. 29 (2009) 1327 – 1337.

[146] I. Golobič, M. Zupančič, Wall-temperature distributions of nucleate pool boiling surfaces vs. boiling curves: A new approach, Int. J. Heat Mass Transfer 99 (2016) 541 – 547.

[147] V. Voulgaropoulos, G. M. Aguiar, C. N. Markides, M. Bucci, Simultaneous laser-induced fluorescence, particle image velocimetry and infrared thermography for the investigation of the flow and heat transfer characteristics of nucleating vapour bubbles, Int. J. Heat Mass Transfer 187 (2022) 122525.

[148] I. Golobič, H. Gjerkeš, Interactions between laser-activated nucleation sites in pool boiling, Int. J. Heat Mass Transfer 44 (2001) 143 – 153.

[149] M. Mehrvand, S. A. Putnam, Probing the local heat transfer coefficient of water-cooled microchannels using time-domain thermoreflectance, J. Heat Transfer 139 (2017) 112403.

[150] S. Fischer, S. Herbert, A. Sielaff, E. M. Slomski, P. Stephan, M. Oechsner, Experimental investigation of nucleate boiling on a thermal capacitive heater under variable gravity conditions, Microgravity Sci. Technol. 24 (2011) 139 – 146.

[151] T. Charignon, P. Lloveras, D. Chatain, L. Truskinovsky, E. Vives, D. Beysens, V. S. Nikolayev, Criticality in the slowed-down boiling crisis at zero gravity, Phys. Rev. E 91 (2015) 053007.

[152] K. Wang, C.-Y. Li, M. Pellegrini, N. Erkan, K. Okamoto, Extended development of a bubble percolation method to predict boiling crisis of flow boiling, Int. J. Heat Mass Transfer 165 (2021) 120660.

[153] S. Gong, L. Zhang, P. Cheng, E. N. Wang, Understanding triggering mechanisms for critical heat flux in pool boiling based on direct numerical simulations, Int. J. Heat Mass Transfer 163 (2020) 120546.

[154] I.-C. Chu, H. C. No, C.-H. Song, Visualization of boiling structure and critical heat flux phenomenon for a narrow heating surface in a horizontal pool of saturated water, Int. J. Heat Mass Transfer 62 (2013) 142 – 152.

[155] B. S. Kim, H. Lee, S. Shin, G. Choi, H. H. Cho, Interfacial wicking dynamics and its impact on critical heat flux of boiling heat transfer, Appl. Phys. Lett. 105 (2014) 191601.

[156] I.-C. Chu, N. O. Hee Cheon, C.-H. Song, D. J. Euh, Observation of critical heat flux mechanism in horizontal pool boiling of saturated water, Nucl. Eng. Des. 279 (2014) 189 – 199.

[157] S. Fischer, S. Herbert, E. M. Slomski, P. Stephan, M. Oechsner, Local heat flux investigation during pool boiling single bubble cycles under reduced gravity, Heat Transfer Eng. 35 (2013) 482 – 491.

[158] P. Stephan, A. Sielaff, S. Fischer, J. Dietl, S. Herbert, A contribution to the basic understanding of nucleate boiling phenomena: generic experiments and numerical simulations, Therm. Sci. Eng. 21 (2013) 39–57.

[159] E. Hecht, Optics, 5th ed., Pearson, 2017.

[160] P. Hariharan, Basics of Interferometry, 2nd ed., Elsevier, 2007.

[161] T. Morokuma, T. Ohara, Y. Utaka, Combination of laser interferometric and laser extinction methods for precise thickness measurement of liquid film between coalescing twin air bubbles, Int. J. Heat Mass Transfer 127 (2018) 154 – 160.

[162] G. K. Sinha, S. Narayan, A. Srivastava, Microlayer dynamics during the growth process of a single vapour bubble under subcooled flow boiling conditions, J. Fluid Mech. 931 (2022) A23.

[163] H. Kim, J. Buongiorno, Detection of liquid-vapor-solid triple contact line in two-phase heat transfer phenomena using high-speed infrared thermometry, Int. J. Multiphase Flow 37 (2011) 166 – 172.

[164] S. Gong, W. Ma, T.-N. Dinh, Diagnostic techniques for the dynamics of a thin liquid film under forced flow and evaporating conditions, Microfluid Nanofluid 9 (2010) 1077 – 1089.

[165] S. Gong, W. Ma, T.-N. Dinh, An experimental study of rupture dynamics of evaporating liquid films on different heater surfaces, Int. J. Heat Mass Transfer 54 (2011) 1538 – 1547.

[166] D. W. Zhou, T. Gambaryan-Roisman, P. Stephan, Measurement of water falling film thickness to flat plate using confocal chromatic sensoring technique, Exp. Therm. Fluid Sci. 33 (2009) 273 – 283.

[167] P. J. de Groot, X. C. de Lega, Transparent film profiling and analysis by interference microscopy, in: Proc. SPIE 7064, Interferometry XIV: Applications, 2008.

[168] P. de Groot, L. Deck, Three-dimensional imaging by sub-Nyquist sampling of white-light interferograms, Opt. Lett. 18 (1993) 1462.

[169] B. Maniscalco, P. M. Kaminski, J. M. Walls, Thin film thickness measurements using scanning white light interferometry, Thin Solid Films 550 (2014) 10 – 16.

[170] S.-W. Kim, G.-H. Kim, Thickness-profile measurement of transparent thin-film layers by white-light scanning interferometry, Appl. Opt. 38 (1999) 5968 – 5973.

[171] E. P. Goodwin, J. C. Wyant, Fringes of equal chromatic order (FECO), in: Field Guide to Interferometric Optical Testing, SPIE, 2006, p. 48.

[172] C. Y. K. Fung, R. Sedev, J. N. Connor, Wetting films: a technique for probing the microscopic meniscus using white light interferometry, Adv. Powder Technol. 25 (2014) 1171 – 1176.

[173] T. Hou, L. L. Martin, R. G. Horn, G. W. Greene, Use of optical interferometry to measure gold nanoparticle adsorption on silica, Colloid Surface A 506 (2016) 383 – 392.

[174] J. N. Connor, R. G. Horn, Measurement of aqueous film thickness between charged mercury and mica surfaces: a direct experimental probe of the poisson-boltzmann distribution, Langmuir 17 (2001) 7194 – 7197.

[175] J. N. Connor, R. G. Horn, Extending the surface force apparatus capabilities by using white light interferometry in reflection, Rev. Sci. Instrum. 74 (2003) 4601 – 4606.

[176] G. J. Johnston, R. Wayte, H. A. Spikes, The measurement and study of very thin lubricant films in concentrated contacts, Trib. Trans. 34 (1991) 187 – 194.

[177] H. A. Spikes, Direct observation of boundary layers, Langmuir 12 (1996) 4567 – 4573.

[178] H. A. Spikes, The study of very thin lubricant films in high pressure contacts using spacer layer interferometric methods, in: Fundamentals of Tribology and Bridging the Gap Between the Macro- and Micro/Nanoscales, Springer Netherlands, 2001, pp. 663 – 689.

[179] R. P. Glovnea, A. K. Forrest, A. V. Olver, H. A. Spikes, Measurement of sub-nanometer lubricant films using ultra-thin film interferometry, Tribol. Lett. 15 (2003) 217 – 230.

[180] H. Kim, D. E. Kim, Effects of surface wettability on pool boiling process: Dynamic and thermal behaviors of dry spots and relevant critical heat flux triggering mechanism, Int. J. Heat Mass Transfer 180 (2021) 121762.

[181] D. E. Kim, J. Park, Experimental study of critical heat flux in pool boiling using visible-ray optics, Int. J. Heat Mass Transfer 169 (2021) 120937.

[182] D. E. Kim, J. Park, Visualization study of phase distribution on a boiling surface, Exp. Therm. Fluid Sci. 121 (2021) 110261.

[183] S. Nishio, T. Gotoh, N. Nagai, Observation of boiling structures in high heat-flux boiling, Int. J. Heat Mass Transfer 41 (1998) 3191 – 3201.

[184] H. J. Chung, H. C. No, Simultaneous visualization of dry spots and bubbles for pool boiling of R-113 on a horizontal heater, Int. J. Heat Mass Transfer 46 (2003) 2239 – 2251.

[185] S. Nishio, H. Tanaka, Visualization of boiling structures in high heat-flux pool-boiling, Int. J. Heat Mass Transfer 47 (2004) 4559 – 4568.

[186] E. Wagner, P. Stephan, High-resolution measurements at nucleate boiling of pure FC-84 and FC-3284 and its binary mixtures, J. Heat Transfer 131 (2009) 121008.

[187] T. D. Rule, J. Kim, Heat transfer behavior on small horizontal heaters during pool boiling of FC-72, J. Heat Transfer 121 (1999) 386 – 393.

[188] F. Demiray, J. Kim, Heat transfer from a single bubble nucleation site during saturated pool boiling of FC-72 using an array of 100 micron heaters, in: 8th AIAA/ASME Joint Thermophysics and Heat Transfer Conference, American Institute of Aeronautics and Astronautics, St. Louis, Missouri, 2002.

[189] F. Demiray, J. Kim, Microscale heat transfer measurements during pool boiling of FC-72: effect of subcooling, Int. J. Heat Mass Transfer 47 (2004) 3257 – 3268.

[190] Z. Yin, A. Prosperetti, J. Kim, Bubble growth on an impulsively powered microheater, Int. J. Heat Mass Transfer 47 (2004) 1053 – 1067.

[191] T. Yabuki, O. Nakabeppu, Study on heat transfer mechanism of isolated bubble nucleate boiling with MEMS sensors, in: 14th Int. Heat Transfer Conf., 2010.

[192] T. Yabuki, O. Nakabeppu, Heat transfer characteristics of isolated bubble nucleate boiling of water, in: ASME/JSME 8th Thermal Eng. Joint Conf., ASMEDC, 2011.

[193] D. R. Lide, CRC handbook of chemistry and physics, CRC Press, Boca Raton, 2005.

[194] A. Liu, A numerical investigation of the dynamic wetting transition on a moving substrate, Procedia Eng. 126 (2015) 476 – 480.

[195] E. Matveeva, Electrochemistry of the indium-tin oxide electrode in 1 M NaOH electrolyte, J. Electrochem. Soc. 152 (2005) H138.

[196] C. A. Huang, K. C. Li, G. C. Tu, W. S. Wang, The electrochemical behavior of tin-doped indium oxide during reduction in 0.3 M hydrochloric acid, Electrochim. Acta 48 (2003) 3599 – 3605.

[197] N. A. Hamzah, R. I. M. Asri, M. A. Ahmad, M. A. A. Z. M. Sahar, S. N. Waheeda, Z. Hassan, Effect of post-annealing in oxygen environment on ITO thin films deposited using RF magnetron sputtering, J. Phys. Conf. Ser. 1535 (2020) 012036.

[198] W.-F. Wu, B.-S. Chiou, Effect of annealing on electrical and optical properties of RF magnetron sputtered indium tin oxide films, Appl. Surf. Sci. 68 (1993) 497 – 504.

[199] K. P. Sibin, N. Selvakumar, A. Kumar, A. Dey, N. Sridhara, H. D. Shashikala, A. K. Sharma, H. C. Barshilia, Design and development of ITO/Ag/ITO spectral beam splitter coating for photovoltaic-thermoelectric hybrid systems, Sol. Energy 141 (2017) 118 – 126.

[200] E. Kusano, J. Kawaguchi, K. Enjouji, Thermal stability of heat-reflective films consisting of oxide-Ag-oxide deposited by DC magnetron sputtering, J. Vac. Sci. Technol. A 4 (1986) 2907 – 2910.

[201] K. H. Choi, J. Y. Kim, Y. S. Lee, H. J. Kim, ITO/Ag/ITO multilayer films for the application of a very low resistance transparent electrode, Thin Solid Films 341 (1999) 152 – 155.

[202] K. F. Palmer, D. Williams, Optical properties of water in the near infrared, J. Opt. Soc. Am. 64 (1974) 1107 – 1110.

[203] G. M. Hale, M. R. Querry, Optical constants of water in the 200-nm to 200-μm wavelength region, Appl. Opt. 12 (1973) 555.

[204] K. L. Johnson, Contact Mechanics, Cambridge University Press, 1985.

[205] F. P. Incropera, D. P. DeWitt, T. L. Bergman, A. S. Lavine, Fundamentals of heat and mass transfer, 6th ed., Wiley, 2007.

[206] S. Shrestha, Y. Wang, A. C. Overvig, M. Lu, A. Stein, L. D. Negro, N. Yu, Indium tin oxide broadband metasurface absorber, ACS Photonics 5 (2018) 3526 – 3533.

[207] K. Schweikert, A. Sielaff, P. Stephan, Pixel-wise in situ calibration method for high accuracy infrared thermography of moving targets, Infrared Phys. Technol. 118 (2021) 103862.

[208] O. Oikonomidou, S. Evgenidis, C. Argyropoulos, X. Zabulis, P. Karamaoynas, M. Raza, J. Sebilleau, F. Ronshin, M. Chinaud, A. Garivalis, M. Kostoglou, A. Sielaff, M. Schinnerl, P. Stephan, C. Colin, L. Tadrist, O. Kabov, P. D. Marco, T. Karapantsios, Bubble growth analysis during subcooled boiling experiments on-board the international space station: Benchmark image analysis, Adv. Colloid Interfac. 308 (2022) 102751.

[209] C. Tecchio, X. Zhang, B. Cariteau, G. Zalczer, P. Roca i Cabarrocas, P. Bulkin, J. Charliac, S. Vassant, V. Nikolayev, Microlayer dynamics at bubble growth in boiling, in: Proc. 16th Int. Conf. Heat Transfer Fluid Mech. Thermodynamics (HEFAT-ATE 2022), 2022, pp. 624 – 629.

[210] X. Zhang, V. S. Nikolayev, Liquid film dynamics with immobile contact line during meniscus oscillation, J. Fluid Mech. 923 (2021) A4.

[211] L. Bureš, Y. Sato, Direct numerical simulation of evaporation and condensation with the geometric VOF method and a sharp-interface phase-change model, Int. J. Heat Mass Transfer 173 (2021) 121233.

[212] M. Bucci, A theoretical and experimental study of vapor bubble dynamics in separate effect pool boiling conditions, Ph.D. thesis, University of Pisa, Italy, 2020.

[213] H. A. MacLeod, Thin-film optical filters, 3rd ed., CRC Press, 2010.

[214] I. H. Malitson, A redetermination of some optical properties of calcium fluoride, Appl. Optics 2 (1963) 1103 – 1107.

[215] M. J. Dodge, Refractive properties of magnesium fluoride, Appl. Optics 23 (1984) 1980 – 1985.

[216] I. H. Malitson, Refraction and dispersion of synthetic sapphire, J. Opt. Soc. Am. 52 (1962) 1377 – 1379.

[217] A. N. Bashkatov, E. A. Genina, Water refractive index in dependence on temperature and wavelength: A simple approximation, in: Proc. SPIE 5068. Saratov Fall Meeting 2002: Optical Technologies in Biophysics and Medicine IV, 2003.

[218] J.-H. Yoo, M. Matthews, P. Ramsey, A. C. Barrios, A. Carter, A. Lange, J. Bude, S. Elhadj, Thermally ruggedized ITO transparent electrode films for high power optoelectronics, Opt. Express 25 (2017) 25533 – 25545.

[219] D. C. Montgomery, G. C. Runger, Applied statistics and probability for engineers, Wiley, 2013.

[220] A. Savitzky, M. J. E. Golay, Smoothing and differentiation of data by simplified least squares procedures, Anal. Chem. 36 (1964) 1627 – 1639.

[221] C. Shekhar, On simplified application of multidimensional Savitzky-Golay filters and differentiators, in: AIP Conf. Proc., 2016.

[222] J. Luo, K. Ying, J. Bai, Savitzky-Golay smoothing and differentiation filter for even number data, Signal Process. 85 (2005) 1429 – 1434.

[223] M. Browne, N. Mayer, T. R. H. Cutmore, A multiscale polynomial filter for adaptive smoothing, Digit. Signal Process. 17 (2007) 69 – 75.

[224] S. R. Krishnan, C. S. Seelamantula, On the selection of optimum Savitzky-Golay filters, IEEE Trans. Signal Process. 61 (2013) 380 – 391.

APPENDICES

Appendix A

Electromagnetic theory of interference in multilayer stacks

We briefly remind here the electromagnetic theory of interference in multilayer systems [159, 213] that corresponds to the multiple beam interference approach, to evaluate the validity of much simpler two-beam interference theory that will be used for the data treatment in this thesis.

Let us consider first the case of light interference from a single thin film (represented by a spacer layer) as illustrated in the schematics of Fig. 4.3a. The spacer layer of thickness h, deposited on top a porthole with thickness H, represents the ITO in the boiling case. Here, $H \gg h$ and $h < l_{coh}$, where l_{coh} is the coherent length of white light so that the fringe pattern is only due to the interference between the reflected rays from the interfaces a and b of the spacer layer, represented by R_1 and R_2. The effect of ray R_0 is, therefore, introduced apart. Part of the incident light ray traveling from porthole towards the spacer layer will be reflected at A while another part of it will be transmitted and then reflected at B. The light rays reflected from A and B will interfere with other, producing an interference fringe map of intensity I that depends, among other factors, of the film thickness.

The intensity, I, depends on the light source and reflectance in a relationship expressed as

$$I = \mathcal{I} I_s; \tag{A.1}$$

where I_s is the intensity of the light source (incidence light) whereas $\mathcal{I}$ stands for the normalized intensity defined by the reflectance $\mathcal{R}$ created by the interference. The wave reflection from the interface between the media 0 and 1 (bottom of the porthole) R_0 in Fig. 4.3a contributes with the reflectance $\mathcal{R}_0$ and transmittance $\mathcal{T}_0$ given by Eqs. (4.24, 4.27) because the reflected wave is not coherent with the wave coming from the interfaces a and b as mentioned before. In agreement with Eqs. (4.32, 4.33), the full normalized light intensity is thus

$$\mathcal{I} = \mathcal{R}_0 + \mathcal{T}_0^2 \mathcal{R}. \tag{A.2}$$

The main goal is to obtain a solution that expresses $\mathcal{R}$ as a function of h and λ. The classic solution is obtained from the electromagnetic theory derived from Maxwell equations by solving the electric $\vec{E}$ and magnetic $\vec{H}$ vector fields at the interfaces of the film.

We consider the case of normal incidence and denote the waves traveling in the z direction by the superscript $(^+)$ and in the opposite direction as $(^-)$. The positive direction of $\vec{E}$ is defined along the x-axis for incident, transmitted and reflected waves. Since $\vec{E}$ and $\vec{H}$ are orthogonal with the wave propagation direction $\vec{E} \times \vec{H}$ given by the Pointing vector, the direction of $\vec{H}$ is along y-axis (perpendicular to the paper plane), positive for incident and transmitted but negative for reflected. The boundary conditions establish that the tangential components of $\vec{E}$ and $\vec{H}$ (parallel to the interfaces), with amplitudes given by E and H, respectively, must be continuous across the

interfaces. Therefore, at the interface b one writes

$$E_b = E_{2b}^+ + E_{2b}^-, \tag{A.3}$$
$$H_b = \eta_2 E_{2b}^+ - \eta_2 E_{2b}^-, \tag{A.4}$$

where

$$\eta_j = \frac{H_j}{E_j} = \mathcal{N}_j \sqrt{\varepsilon_0/\mu_0}, \tag{A.5}$$

is the characteristic optical admittance of the medium j that involves the complex refraction index

$$\mathcal{N}_j = n_j - i\kappa_j, \tag{A.6}$$

where n_j represents the real part of the refractive index whereas κ_j stands for the extinction coefficient. The subscripts indicate the interface at which the field is defined and the side of the interface (that of the medium 2 in this case) as illustrated in Fig. 4.3a. From Eqs. (A.3–A.5), it can be shown that the amplitudes of the electric and magnetic fields for the incident and reflected waves at the interface b are given as

$$E_{2b}^+ = \frac{1}{2}\left(E_b + \frac{H_b}{\eta_2}\right), \tag{A.7}$$
$$E_{2b}^- = \frac{1}{2}\left(E_b - \frac{H_b}{\eta_2}\right), \tag{A.8}$$
$$H_{2b}^+ = \frac{1}{2}(H_b + \eta_2 E_b), \tag{A.9}$$
$$H_{2b}^- = \frac{1}{2}(H_b - \eta_2 E_b), \tag{A.10}$$

At the interface a, after having passed the medium 2 of thickness h with the index $\mathcal{N}_2$, so the optical path difference is $\Delta = \mathcal{N}_2 h$, the incident wave acquires a phase shift

$$\Omega_2 = \frac{2\pi}{\lambda}\mathcal{N}_2 h. \tag{A.11}$$

For the reflected wave, the phase shift is of opposite sign. Therefore, at the interface a, one writes

$$E_{2a}^+ = \frac{1}{2}\left(E_b + \frac{H_b}{\eta_2}\right)\exp(i\Omega_2), \tag{A.12}$$
$$E_{2a}^- = \frac{1}{2}\left(E_b - \frac{H_b}{\eta_2}\right)\exp(-i\Omega_2), \tag{A.13}$$
$$H_{2a}^+ = \frac{1}{2}(H_b + \eta_2 E_b)\exp(i\Omega_2), \tag{A.14}$$
$$H_{2a}^- = \frac{1}{2}(H_b - \eta_2 E_b)\exp(-i\Omega_2), \tag{A.15}$$

At the interface a, $E_a = E_{2a}^+ + E_{2a}^-$ and $H_a = H_{2a}^+ + H_{2a}^-$. Therefore, using Eqs.(A.12-A.15), one can write, in the matrix format, the two resulting equations as

$$\begin{bmatrix} E_a \\ H_a \end{bmatrix} = \mathbf{M}_2 \begin{bmatrix} E_b \\ H_b \end{bmatrix}, \tag{A.16}$$

where

$$\mathbf{M}_j = \begin{bmatrix} \cos\Omega_j & (i\sin\Omega_j)/\eta_j \\ i\eta_j \sin\Omega_j & \cos\Omega_j \end{bmatrix}, \tag{A.17}$$

is the characteristic matrix of the medium j (in this case, $j = 2$). Normalizing Eq. (A.16) by E_b, one gets

$$\begin{bmatrix} B \\ C \end{bmatrix} = \mathbf{M} \begin{bmatrix} 1 \\ \eta_4 \end{bmatrix}, \tag{A.18}$$

where $\mathbf{M} = \mathbf{M}_2$, $B = E_a/E_b$ and $C = H_a/E_b$. Both E and H fields are continuous at the interface b with the medium 4 so $H_b = \eta_4 E_b$. The reflectance $\mathcal{R}$ of the interface with the medium 1 (the porthole) is just the squared amplitude ratio of the reflected and incident waves that result in the expression

$$\mathcal{R} = \left| \frac{\eta_1 - \Upsilon}{\eta_1 + \Upsilon} \right|^2, \tag{A.19}$$

where

$$\Upsilon_a = \frac{H_a}{E_a} = \frac{C}{B}. \tag{A.20}$$

is the optical admittance of the assembly. For $\mathbf{M} = \mathbf{M}_2$,

$$\Upsilon_a = \frac{\eta_4 \cos\Omega_2 + i\eta_2 \sin\Omega_2}{\cos\Omega_2 + i(\eta_4/\eta_2)\sin\Omega_2}. \tag{A.21}$$

Eq. (A.19) thus gives the reflectance provided by the interference.

We consider now an additional film on the top of the spacer layer as illustrated in Fig. 4.3b. It corresponds to the liquid microlayer that can be formed during the bubble growth in boiling or air in the validation case. This system presents two thin layers thus producing a fringe pattern that is a result of the interference between the reflected rays from the interfaces a, b and c. The aforementioned theory can be applied to this medium 3 where

$$\begin{bmatrix} E_b \\ H_b \end{bmatrix} = \mathbf{M}_3 \begin{bmatrix} E_c \\ H_c \end{bmatrix}. \tag{A.22}$$

The characteristic matrix $\mathbf{M}_3$ of the medium 3 is similar to that of medium 2; the phase shift due to the microlayer is

$$\Omega_3 = \frac{2\pi}{\lambda} n_3 \delta, \tag{A.23}$$

where the absorbtion in water can be neglected. From Eqs. (A.16, A.18), the characteristic matrix $\mathbf{M}$ of the film assembly is

$$\mathbf{M} = \prod_{j=2}^{3} \mathbf{M}_j \tag{A.24}$$

Eqs. (A.18-A.20) hold for 3-layer stack too so one can calculate the intensity thus evaluating the validity of the scalar interference theory (subsection 4.1.2). Under the assumptions that the absorbtion

is important only for the medium 2 (ITO), and $n_4 = 1$ (for vapor), one obtains

$$\begin{aligned}
\mathcal{R} = \{ &- \{ \cosh\Big(2\hat{h}\kappa_2\Big)\{ - 8n_1n_2^2n_3^2 + \kappa_2^4(1+n_3^2) + n_1^2(1+n_3^2)(n_2^2+n_3^2) \\
&+ n_2^2(1+n_3^2)(n_2^2+n_3^2) + \kappa_2^2(1+n_3^2)(n_1^2+2n_2^2+n_3^2) \\
&+ (n_3^2-1)\big[(\kappa_2^2+n_1^2+n_2^2)(\kappa_2^2+n_2^2-n_3^2)\cos(2\Omega_3) + 4\kappa_2 n_1 n_2 n_3 \sin(2\Omega_3)\big]\}\} \\
&+ \cos\Big(2\hat{h}n_2\Big)\{\kappa_2^4(1+n_3^2) - (n_1^2-n_2^2)(n_2^2-n_3^2)(1+n_3^2) - \kappa_2^2(n_1^2-2n_2^2+(1+(n_1-8)n_1-2n_2^2)n_3^2+n_3^4) \\
&+ (n_3^2-1)\big[(\kappa_2^2-n_1^2+n_2^2)(\kappa_2^2+n_2^2+n_3^2)\cos(2\Omega_3) + 4\kappa_2 n_1 n_2 n_3 \sin(2\Omega_3)\big]\} \\
&+ 2\sin\Big(2\hat{h}n_2\Big)\{\kappa_2(2n_1^2n_3^2 - 2n_2^2n_3^2 + n_1(n_2^2-n_3^2)(1+n_3^2) + \kappa_2^2(n_1+(n_1-2)n_3^2)) \\
&+ (n_3^2-1)\big[\kappa_2 n_1(\kappa_2^2+n_2^2+n_3^2)\cos(2\Omega_3) - n_2(\kappa_2^2-n_1^2+n_2^2)n_3\sin(2\Omega_3)\big]\} \\
&+ 2\{n_2\big[n_1(\kappa_2^2+n_2^2) + (\kappa_2^2(n_1-2)+n_1-2n_2^2+n_1(n_2^2-2n_1))n_3^2 + n_1n_3^4\big] \\
&+ (n_3^2-1)\big[n_1n_2(\kappa_2^2+n_2^2-n_3^2)\cos(2\Omega_3) + \kappa_2(\kappa_2^2+n_1^2+n_2^2)n_3\sin(2\Omega_3)\big]\}\sinh\Big(2\hat{h}\kappa_2\Big)\} \\
\Big/ &\{ - \{ \cosh\Big(2\hat{h}\kappa_2\Big)\{8n_1n_2^2n_3^2 + \kappa_2^4(1+n_3^2) + n_1^2(1+n_3^2)(n_2^2+n_3^2) + n_2^2(1+n_3^2)(n_2^2+n_3^2) \\
&+ \kappa_2^2(1+n_3^2)(n_1^2+2n_2^2+n_3^2) + (n_3^2-1)\big[(\kappa_2^2+n_1^2+n_2^2)(\kappa_2^2+n_2^2-n_3^2)\cos(2\Omega_3) - 4\kappa_2 n_1 n_2 n_3\sin(2\Omega_3)\big]\}\} \\
&+ \cos\Big(2\hat{h}n_2\Big)\{\kappa_2^4(1+n_3^2) - (n_1^2-n_2^2)(n_2^2-n_3^2)(1+n_3^2) - \kappa_2^2\{n_1^2-2n_2^2+\big[1+n_1(8+n_1)-2n_2^2\big]n_3^2+n_3^4\} \\
&+ (n_3^2-1)\big[(\kappa_2^2-n_1^2+n_2^2)(\kappa_2^2+n_2^2+n_3^2)\cos(2\Omega_3) - 4\kappa_2 n_1 n_2 n_3\sin(2\Omega_3)\big]\} \\
&- 2\sin\Big(2\hat{h}n_2\Big)\{\kappa_2\big[-2n_1^2n_3^2 + 2n_2^2n_3^2 + n_1(n_2^2-n_3^2)(1+n_3^2) + \kappa_2^2(n_1+(2+n_1)n_3^2)\big] \\
&+ (n_3^2-1)\big[\kappa_2 n_1(\kappa_2^2+n_2^2+n_3^2)\cos(2\Omega_3) + n_2(\kappa_2^2-n_1^2+n_2^2)n_3\sin(2\Omega_3)\big]\} \\
&+ 2\{-n_2\{n_1(\kappa_2^2+n_2^2) + \big[\kappa_2^2(2+n_1) + n_1(1+2n_1) + (2+n_1)n_2^2\big]n_3^2 + n_1n_3^4\} \\
&+ (n_3^2-1)\big[-n_1n_2(\kappa_2^2+n_2^2-n_3^2)\cos(2\Omega_3) + \kappa_2(\kappa_2^2+n_1^2+n_2^2)n_3\sin(2\Omega_3)\big]\}\sinh\Big(2\hat{h}\kappa_2\Big)\}, \quad \text{(A.25)}
\end{aligned}$$

where $\hat{h} = 2\pi h/\lambda$.

Appendix B

Spectral and spatial calibrations

B.1 Spectral calibration

Ten different optical filters have been placed, one at a time, between the white light source and the visible light beam splitter (Fig. 3.1) to select a very narrow bandwidth of the light($\approx$ 10 nm at full width at half maximum for all of them except for $\lambda = 532$ which has ≈ 3 nm) so that its spectrum could be observed. The central wavelengths of the filters are known from the manufacturer. Fig. B.1 shows the images obtained with the filters. They show narrow horizontal bright stripes located in different positions along λ'. Their positioning depends on the filter.

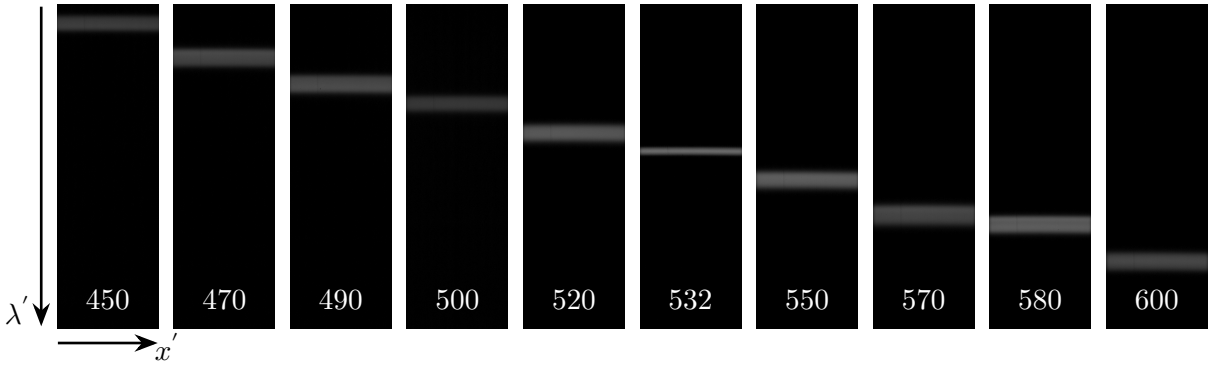

Figure B.1: Spectra of the optical filters with known central wavelengths indicated in nm. The wavelength increases downwards.

In Fig. B.2a, the light intensity along the vertical axis has been taken from vertical line profiles for each one of the ten images shown in Fig. B.1. The raw signals have been filtered out to minimize the effects of noise. The maximum of each filtered signals (central wavelength), represented by red triangles in Fig. B.2a, have been located by a peak analysis algorithm. The location of the central wavelengths is then determined along λ'. In Fig. B.2b, the central wavelengths and their positioning along λ' are plotted. A linear regression in the form of Eq. (4.39) is performed with $1 \leq \lambda' \leq 1280$. The coefficient of determination of 0.999 confirms the linearity of spectrum. Our spectral resolving power, given as λ/a, is roughly 3400 at $\lambda = 550\,\text{nm}$. It is a measure of the optical system's ability to differentiate two wavelengths very close to each other. It is provided by the proper choice of the optical magnification of the visualization system. The uncertainties on a and on λ are $\pm 0.002\,\text{nm/px}$ and $\pm 2.5\,\text{nm}$, respectively, for a confidence interval of 95%, see Appendix E.

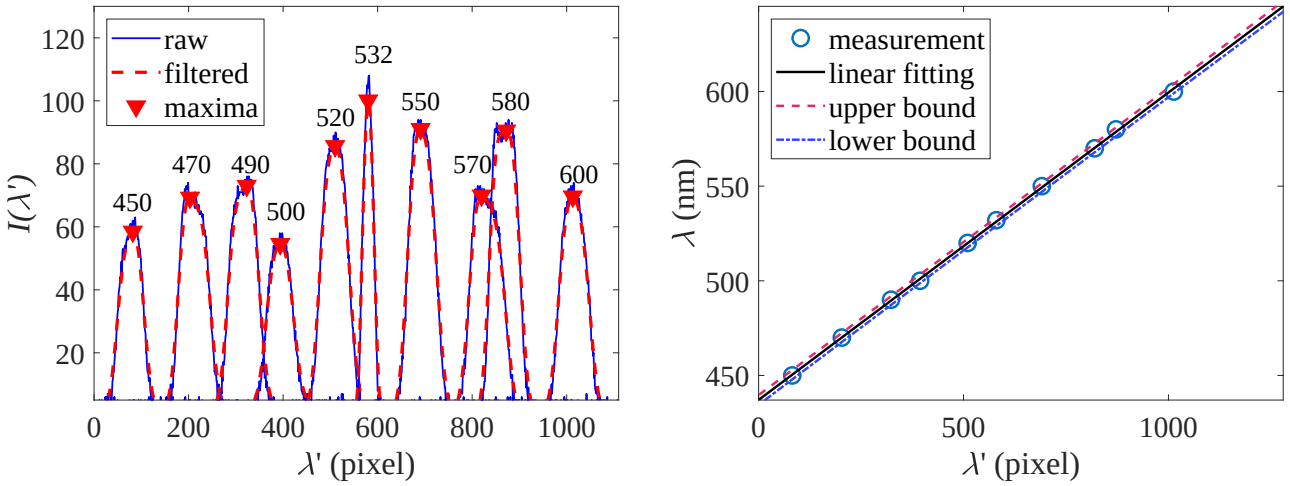

(a) Intensity of the light passing through the bandpass filters over λ'.

(b) Linear regression of the bandpass filters over λ'.

Figure B.2: Calibration of the wavelength axis in WLI.

B.2 Spatial calibration

The horizontal axis is calibrated by imaging the square target with known dimensions shown in Fig. B.3a. To image it in WLI, the turret inside the spectrometer is rotated to insert the mirror into the optical path. Fig. B.3b shows the calibration of the x' axis. x and x' are given in meters and pixels, respectively. The relation is in the form of Eq. (4.40). The slopes of the linear fits give the calibration factors $\mathsf{K}_{\mathsf{WLI}}$ and K_{LI}. The coefficient of determination is 0.999 thus confirming the absence of optical distortions. The uncertainties on K_{WLI} and K_{laser} are $\pm 0.16\,\mu$m/px and $\pm 0.02\,\mu$m/px, respectively, whereas the uncertainty intervals on x_{WLI} and x_{LI} are roughly ± 0.04 mm and ± 0.01 mm, respectively. The confidence interval is 95%, see Appendix E.

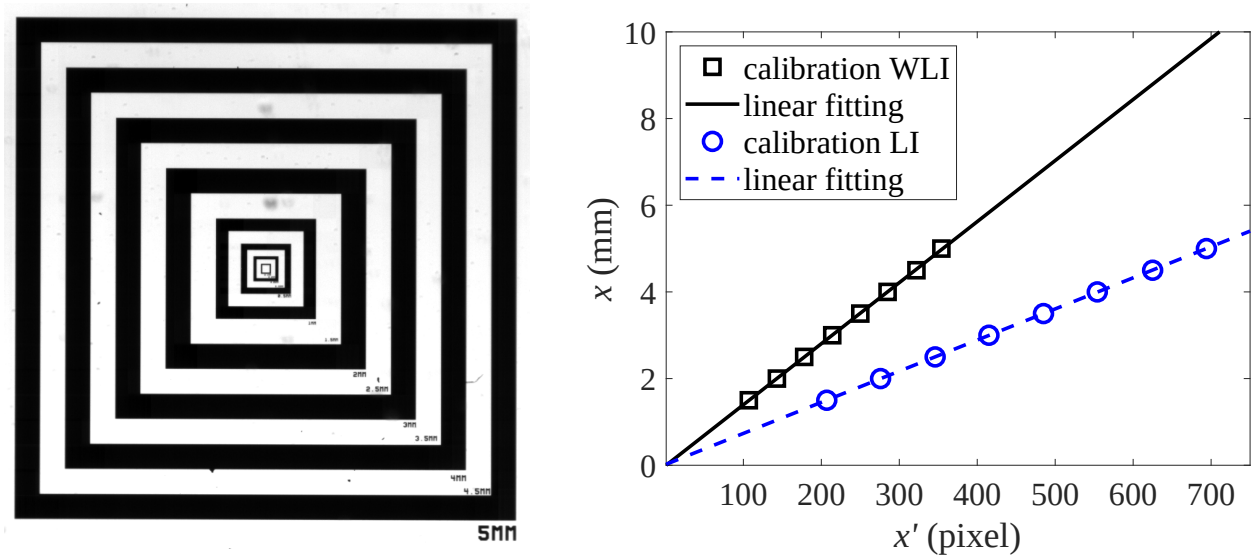

(a) Square resolution test target for calibration of the x and y axes. Its dimensions are shown.

(b) Calibration and linearity of the x' axis in WLI and LI.

Figure B.3: Calibration of the x axis for WLI and LI.

B.3 Optical magnification

Our optical system aims at creating an enlarged image of the actual fringes. This image enlargement is characterized by the system's optical magnification, M, defined as

$$M = \frac{\Delta x^i}{\Delta x}; \tag{B.1}$$

where Δx^i and Δx stand for the size of the fringe's image on the CCD and its actual size, respectively, both expressed in meters. The size of the image on the CCD is given by

$$\Delta x^i = \Delta x' s, \tag{B.2}$$

where s represents the pixel size of the camera's sensor in meters/px and $\Delta x'$ gives the size of the image in px. Substituting Eqs. (B.2,4.40) into Eq. (B.1) one obtains

$$M = \frac{s}{\mathsf{K}}. \tag{B.3}$$

Because of sensibility and frame rate constrains we have used two different cameras for WLI and LI, so that $s_{LI} = 17\,\mu$m and $s_{WLI} = 28\,\mu$m. This yields, $M_{LI} = 2.37$ and $M_{WLI} = 2.0$.

Appendix C

Physical properties

C.1 Optical properties

The knowledge of the indexes of refraction for each material within the optical path is the most important optical property for the analysis of light reflectance in films. Some of them are listed in Table C.1.

Table C.1: Refraction indexes for $\lambda = 550\,\text{nm}$.

Material	refraction index, n
Sapphire	1.7705
Fused silica	1.4599
CaF_2	1.4348
MgF_2	1.3785
ITO	1.9538
Liquid water	1.3330
Water vapor	1.00
Lens KPX124, glass NBK-7	1.5185
Air	1.0003

Since our white light interferometer is a spectral method one needs to know the relationship of n and λ within the visible bandwidth. For the typical optical materials such as sapphire, fused silica, CaF_2, MgF_2 and NBK-7, one can used the dispersion formulas expressed in the form

$$n^2 - 1 = \frac{A\lambda^2}{\lambda^2 - B^2} + \frac{C\lambda^2}{\lambda^2 - D^2} + \frac{E\lambda^2}{\lambda^2 - F^2}, \tag{C.1}$$

Table C.2: Coefficients for the dispersion formula in Eq. (C.1).

	A	B	C	D	E	F
CaF_2, Ref.[214]	0.567589	0.050264	0.471091	0.100391	3.848472	34.649040
MgF_2, Ref.[215]	0.487551	0.043384	0.398750	0.094614	2.312035	23.793604
Sapphire, Ref.[216]	1.431349	0.072663	0.650548	0.119324	5.341402	18.028251
NBK-7, (Schoot catalog)	1.039612	0.077464	0.231792	0.141485	1.010469	10.176475

For liquid water, we use the indexes of refraction reported by Bashkatov and Genina [217] for $T = 100\,°\text{C}$. The refraction on ITO is highly dependent on λ. Also, it depends on the deposition

method and thermal treatment, for instance. Thus, one needs to determine it. To do so, spectroscopy ellipsometry has been performed at LPICM (Ecole Polytechnique) by Pavel Bulkin. It consists of a non-contact, optical, model-based, high-sensitive and precise method used for characterization of semi-transparent thin films. The working principle is as follows: A light beam with a known polarized state is directed to the ITO sample with an oblique incident angle. The reflected light, with a modified polarization with regards to the incident beam, is then captured. The change in light polarization is then captured by a detector. A theoretical model is used to determine the fitting parameters (index of refraction and thickness, for instance) that provide the best fit to the experimental data. The ITO index of refraction n and its extinction coefficient κ are shown in Fig. C.1.

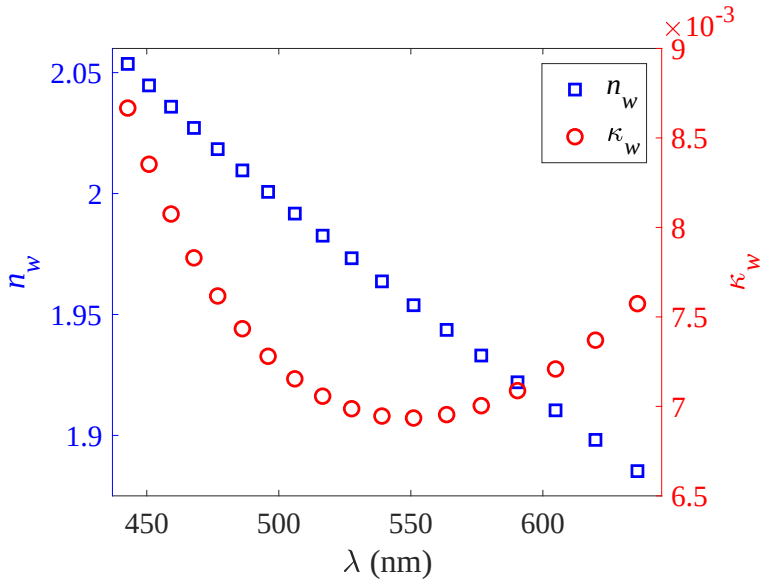

Figure C.1: ITO index of refraction n (blue rectangles) and extinction coefficient, κ (red circles).

C.2 Thermophysical properties

The physical properties for ITO, water at $T = 100\,°\text{C}$ and MgF_2 are presented in table C.3.

Table C.3: Physical properties of ITO, liquid water and MgF_2.

	ITO [218]	Water [205]	MgF_2 [193]
density [kg/m^3]	7140	957.9	3148
thermal conductivity [W/(mK)]	11	0.68	11.6
specific heat [J/(kgK)]	340	4217	955
surface tension [N/m]	-	0.059	-
heat of vaporization [kJ/kg]	-	2257	-
melting point [°C]	1526–1926	-	1255
dynamic viscosity [Ns/m^2]	-	279×10^{-6}	-
effusivity [Ws$^{1/2}$/(m^{2}K)]	5167.5	1657.4	5905.4
diffusivity [m^2/s]	4.5×10^{-6}	1.7×10^{-7}	3.8×10^{-6}

C.3 Mechanical properties

The mechanical properties of ITO, MgF_2, CaF_2, saphhire and N-BK7 are given in table C.4.

Table C.4: Mechanical properties of several optical material.

	ITO	MgF_2	CaF_2	sapphire	N-BK7
Young's modulus [GPa]	116	138	75.8	370	82
Poisson ratio	0.35	0.28	0.26	0.3	0.21
hardness [Knoop]	-	415	158.3	1800-2200	160

Appendix D

Film thickness determination: alternative formulas

Here, we present alternative formulas to determine the film thickness that can be advantageous in some particular cases. They are based on the classical Eq. (4.22) with $h = 0$, which yields

$$\delta = \frac{\lambda}{2n}(N - \phi), \tag{D.1}$$

where the subscripts have been dropped for the sake of simplicity.

D.1 Wavelength and fringe order difference of maxima

The main issue in Eq. (D.1) is that the fringe order is usually unknown. However, this can be solved by rearranging it as

$$N = \frac{1}{\lambda}a + \phi, \tag{D.2}$$

where $a = 2n\delta$ is the slope. For two maxima taking place at λ_1 and λ_2 with fringe order N_1 and N_2, respectively, one can write

$$N_1 = \frac{1}{\lambda_1}a + \phi, \tag{D.3}$$

$$N_2 = \frac{1}{\lambda_2}a + \phi. \tag{D.4}$$

By subtracting Eq. (D.3) from Eq. (D.4) one obtains

$$\Delta N = a\Delta\lambda^{-1}, \tag{D.5}$$

where $\Delta N = N_2 - N_1$ is the difference of fringe order and $\Delta\lambda^{-1} = \lambda_2^{-1} - \lambda_1^{-1}$ is the difference of the inverse wavelength. By plotting ΔN against $\Delta\lambda^{-1}$ one can determine δ based on the slope a of the line given by a linear regression. The advantages of this method are two: one no longer needs to know ϕ (the phase shift at reflection), and second: the absolute fringe order value is not required since $\Delta N = 1$ between two adjacent maxima. In this case, $\Delta\lambda^{-1}$ determines the slope thus the film thickness.

D.2 Wavelength difference of maxima

The next equation is based as follows: Let us say that we have two adjacent maxima taking place at λ_1 and λ_2(with $\lambda_1 > \lambda_2$) with fringe order N_1 and $N_2 = N_1 + 1$, respectively. Since δ is constant for

a fixed x in WLI, we use Eq. (D.1) to write

$$\frac{\lambda_1}{2n}(N_1 - \phi) = \frac{\lambda_2}{2n}(N_1 + 1 - \phi); \tag{D.6}$$

By solving Eq. (D.6) for $(N_1 - \phi)$ one obtains

$$N_1 - \phi = \frac{\lambda_2}{\lambda_1 - \lambda_2}; \tag{D.7}$$

Thus, substituting Eq. (D.7) into Eq. (4.22)(with $h = 0$), we have

$$\delta = \frac{1}{2n}\frac{\lambda_2\lambda_1}{\lambda_1 - \lambda_2}; \tag{D.8}$$

D.3 Film thickness difference

If the film thickness difference $\Delta\delta = \delta(x_2) - \delta(x_1)$ is searched between the points x_2 and x_1, one can obtained it in WLI as follows. Let us consider the schematics shown in Fig.D.1. The two straight lines represent constructive interference in a $x - \lambda$ fringe map for a wedge film profile, such as the one shown in Fig.4.10a. To compute the film thickness we use Eq. (4.22) (with $h = 0$). Using the fringe

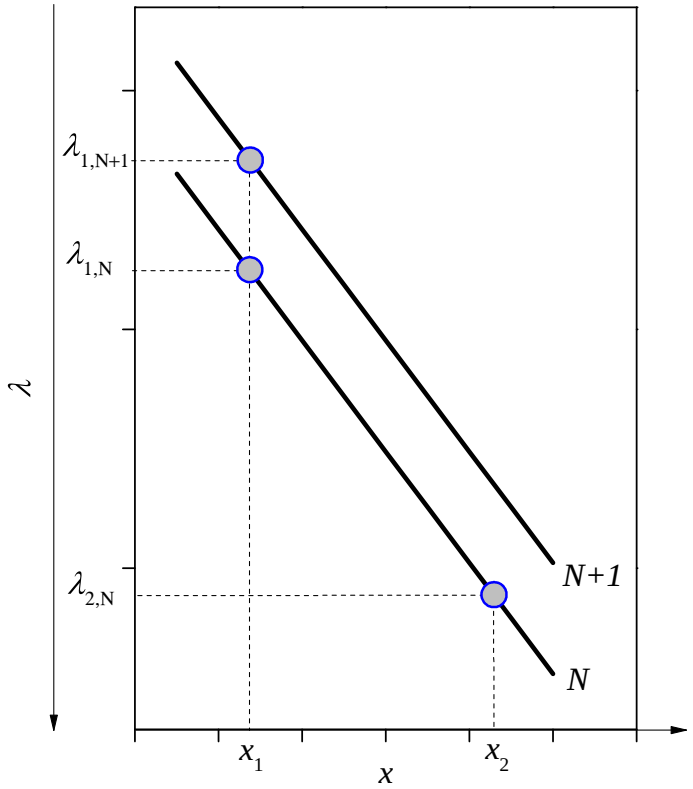

Figure D.1: Schematics of constructive fringes with order N and $N + 1$ in a $x - \lambda$ fringe maps.

with order N, the film thicknesses at x_1 and x_2, are given by

$$\delta(x_1) = \frac{\lambda_{1,N}}{2n}(N - \phi), \tag{D.9}$$

and

$$\delta(x_2) = \frac{\lambda_{2,N}}{2n}(N - \phi), \tag{D.10}$$

respectively. Thus, $\Delta\delta$ can be written as

$$\Delta\delta = \frac{\lambda_{2,N} - \lambda_{1,N}}{2n}(N - \phi). \tag{D.11}$$

At x_1, we can compute δ_1 either by using the fringe N or $N + 1$ so that one can write

$$\frac{\lambda_{1,N+1}}{2n}(N + 1 - \phi) = \frac{\lambda_{1,N}}{2n}(N - \phi) \tag{D.12}$$

By solving Eq. (D.12) for $(N - \phi)$, it yields

$$N - \phi = \frac{\lambda_{1,N+1}}{\lambda_{1,N} - \lambda_{1,N+1}} \tag{D.13}$$

Substituting Eq. (D.13) into Eq. (D.11), one obtains

$$\Delta\delta = \frac{\lambda_{1,N+1}}{2n}\frac{\lambda_{2,N} - \lambda_{1,N}}{\lambda_{1,N} - \lambda_{1,N+1}} \tag{D.14}$$

This is also a formula that is independent of N and ϕ. We used it to determine the inclination angle in Fig. 4.10a, for instance. From Eq. (D.14), the inclination angle of the flat plate α in Figs. 4.10, using the WLI and LI fringe maps, are given by

$$\alpha = \arctan[\Delta\delta/\Delta x]. \tag{D.15}$$

where $\Delta x = x_2 - x_1$.

In LI, $\Delta\delta$ is given by counting the $\mathcal{M}$ maxima existing between x_2 and x_1. One knows that the relative distance between two adjacent maxima is $\lambda_{laser}/(2n)$ thus $\Delta\delta = \mathcal{M}\lambda_{laser}/(2n)$.

Appendix E

Uncertainty and error analysis

E.1 Uncertainty in the linear regression for λ and x determination

The following general procedure is used to determine the uncertainty on λ and x. Given a linear regression in the form $\hat{y} = \hat{b}_0 + \hat{b}_1\hat{x}$ from n experimental data points (x_i, y_i), $i = 1, 2, 3, ..., n$, a new observation of y at x_0 given by $\hat{y}_0 = \hat{b}_0 + \hat{b}_1\hat{x}_0$ has an interval of prediction given by [219]

$$\hat{y}_0 - t_{\alpha/2,n-2}\sqrt{\hat{\sigma}^2\left[1 + \frac{1}{n} + \frac{(x_0 - \bar{x})^2}{S_{xx}}\right]} \leq y_0 \leq \hat{y}_0 + t_{\alpha/2,n-2}\sqrt{\hat{\sigma}^2\left[1 + \frac{1}{n} + \frac{(x_0 - \bar{x})^2}{S_{xx}}\right]}, \tag{E.1}$$

where $t_{\alpha/2,n-2}$ is the Student's distribution for $n-2$ degrees of freedom and $100(1-\alpha)\%$ interval of confidence. $\hat{\sigma}^2$ stands for the unbiased estimator of σ^2 (the variance), given by the error sum of squares as

$$\hat{\sigma}^2 = \frac{\sum_{i=1}^{n}(y_i - \hat{y}_i)^2}{n-2}, \tag{E.2}$$

and $S_{xx} = \sum_{i=1}^{n}(x_i - \bar{x})^2$ where $\bar{x} = (1/n)\sum_{i=1}^{n} x_i$. The uncertainty interval on the slope b_1 is given

$$\hat{b}_1 - t_{\alpha/2,n-2}\sqrt{\hat{\sigma^2}/S_{xx}} \leq b_1 \leq \hat{b}_1 + t_{\alpha/2,n-2}\sqrt{\hat{\sigma^2}/S_{xx}}. \tag{E.3}$$

E.2 Uncertainty on measurements

The uncertainty on the measurement of a quantity $u = f(x_1, ..., x_n)$, *i.e.* that depends on n parameters, is given by the error propagation as [219]

$$\Delta u = \sqrt{\left(\frac{\partial f}{\partial x_1}\Delta x_1\right)^2 + ... + \left(\frac{\partial f}{\partial x_n}\Delta x_n\right)^2} \tag{E.4}$$

where Δx_n is the uncertainty of the n-th parameter.

The uncertainties on r_b, r_m and r_{cl} are linked to the sharpness of the transition zones from bright/dark in Figs. (5.3,4.39). For T_w, the uncertainty is linked to error on the RTD used as reference temperature and on the intensity read by the IR camera. The uncertainty on δ depends mainly on the error on the wavelength axis calibration and on the quality of the fit of $I_{c,theo}$ to $I_{c,exp}$. Table E.1 presents the uncertainties on measurements.

Table E.1: Uncertainties on measurements.

variable	uncertainty
r_{cl}	$\pm 0.07\,\mathrm{mm}$
r_m	$\pm 0.1\,\mathrm{mm}$
r_b	$\pm 0.07\,\mathrm{mm}$
λ	$\pm 2.5\,\mathrm{nm}$
h	$\pm 10\,\mathrm{nm}$
δ	$\pm 15\,\mathrm{nm}$
T	$\pm 0.75\,\mathrm{K}$
q''	$\pm 0.04\,\mathrm{MW/m^2}$
R^i	$\pm 2.5\,\mu\mathrm{Km^2/W}$

E.3 Error on formulas to compute film thickness

Here, we present an error analysis in the computation of δ by using different formulas in WLI.

- **Error on Eq.** (4.22)**:** For the sake of simplicity, here we take $h = 0$ (single film thickness) and drop the subscripts. N, n and ϕ are often known with high precision. Thus, one can state that an error $\Delta\lambda$ from the true value on λ will produce an error $\Delta\delta$ on δ. Eq. (4.22) is then rewritten as

$$\delta + \Delta\delta = \frac{(\lambda + \Delta\lambda)}{2n}(N - \phi), \tag{E.5}$$

  By expanding the RHS of Eq. (E.5), one can write

$$\frac{\Delta\delta}{\Delta\lambda} = \frac{1}{2n}(N - \phi), \tag{E.6}$$

  and using Eq. (4.22) again (with $h = 0$) one gets

$$\frac{\Delta\delta}{\Delta\lambda} = \frac{\delta}{\lambda}, \tag{E.7}$$

  Therefore, we can expect an error on δ of δ/λ for each nano-metric error on λ.

- **Error on Eq.** (4.50)**:** Proceeding similarly as before and considering only the maxima, one writes

$$\bar{\delta} + \Delta\bar{\delta} = \frac{1}{2n}\frac{1}{\mathcal{M}}\sum_{i=1}^{\mathcal{M}}(\lambda_i + \Delta\lambda_i)(N_i - \phi) \tag{E.8}$$

  Considering that $\Delta\lambda_i \approx \Delta\lambda$ and $\lambda_i \approx \lambda$ on can show that

$$\frac{\Delta\bar{\delta}}{\Delta\lambda} \approx \frac{\bar{\delta}}{\lambda} \tag{E.9}$$

  Thus, averaging has no effect on the error. Similarly, one can show that the error remains the same if maxima and minima are considered.

- **Error on Eq.** (D.5) We proceed similarly as previously and assume, for simplicity, $\Delta N = 1$ and $\Delta\lambda_1 \approx \Delta\lambda_2 \approx \Delta\lambda$. Thus, Eq. (D.5) is rewritten as

$$1 = 2n(\delta + \Delta\delta)\left(\frac{1}{\lambda_2 + \Delta\lambda} - \frac{1}{\lambda_1 + \Delta\lambda}\right) \tag{E.10}$$

Considering that $\Delta\lambda \ll \lambda$, one can assume that $(\Delta\lambda/\lambda)^2 \approx 0$ and Eq. (E.10) becomes

$$\frac{1}{2n} = (\delta + \Delta\delta)\left[\frac{1}{\lambda_2}\left(1 - \frac{\Delta\lambda}{\lambda_2}\right) - \frac{1}{\lambda_1}\left(1 - \frac{\Delta\lambda}{\lambda_1}\right)\right] \tag{E.11}$$

By expanding the RHS of Eq. (E.11) and considering that $\Delta\delta \ll \delta$ and $\lambda_1 \approx \lambda_2$ one can rearrange the terms in order to yield

$$\frac{\Delta\delta}{\Delta\lambda} \approx 2\frac{\delta}{\lambda}. \tag{E.12}$$

Thus, despite its advantages this method gives twice the error compared to the first one.

- **Error on Eq.**(D.8) As previously, one writes

$$\delta + \Delta\delta = \frac{1}{2n}\frac{(\lambda_2 + \Delta\lambda_2)(\lambda_1 + \Delta\lambda_1)}{\lambda_1 + \Delta\lambda_1 - \lambda_2 - \Delta\lambda_2} \tag{E.13}$$

By assuming again that $\Delta\lambda_1 \approx \Delta\lambda_2 \approx \Delta\lambda$, $(\Delta\lambda)^2 \approx 0$ and $\lambda_1 \approx \lambda_2$, one can simplify Eq. (E.13) in order to get

$$\frac{\Delta\delta}{\Delta\lambda} \approx 2\frac{\delta}{\lambda}. \tag{E.14}$$

Again, here the error is twice compared to Eq. (4.22). Eqs. (D.5,D.8) actually combine the information of two maxima into a single equation and that is the reason why the error is multiplied by two when compared to the error given by Eq. (D.1). Thus, one rather use Eq. (4.22) (in case of single maximum) or Eq. (4.50) (in case of multiple maxima) to compute the film thickness.

E.4 RTD Temperature verification

An RTD (resistance thermal detector) sensor changes its resistance linearly with the temperature. By knowing its calibration curve one can then make temperature measurements. Our RTD is a 4-wire Pt100 sensor, *i.e* it has a resistance of 100 Ω at 0 °C, which is connected to a NI-cDAQ9178 data acquisition system through a dedicated slot. It is already loaded into the data acquisition calibration curves for standard RTD's, including ours. The user only needs to connect the wires and set the sensor type. Then, the system reads the resistance and converts into temperature in real time. However, our RTD is commercialized without a calibration certificate. This means that its resistance and temperature relationship has not been verified. Thus, we can not ensure if it follows the standard calibration curve used by the acquisition system. One needs to verify it. To do so, we use another certified calibrated platinum RTD to serve as a temperature reference for comparison with our non-calibrated RTD. The measurements are preformed at steady-state conditions in a high-precision thermal bath filled with oil. An aluminum block with holes is immersed into the bath. The RTD's are inserted into the holes in a close proximity to each other.

Table E.2 depicts the temperatures measured at steady-state conditions. T_{bath}, T_{ref} and T_{RTD} stand for the temperatures set at the bath, reference calibrated RTD and our non-certified RTD, respectively. One can observe that the values of T_{ref} fall within the accuracy range of T_{RTD} for all T_{bath}. Thus, we can conclude that our RTD follows its standard calibration curve and it can be used for further measurements.

Table E.2: Temperatures measured at steady-state conditions.

T_{bath}(°C)	T_{ref}(°C)	T_{RTD}(°C)
50	50.0195	49.9955±0.1100
60	60.0317	59.9455±0.1199
70	70.0467	69.9276±0.1299
80	80.0345	79.9111±0.1399
90	90.0063	89.9024±0.1499
100	99.9299	99.8745±0.1599

Appendix F

WLI setup: optical alignment protocol

Due to the presence of several optical elements in the WLI installation, the alignment plays a role on the error associated to the measurements of the microlayer thickness. Considering the schematics depicted in Fig. F.1, first of all, a rough adjustment is performed to find the focus plane of the camera with regards to the output of the spectrometer and the adequate working distance between the lens and the reference mirror. To do so, we replace the reference mirror by a target and move the lens, spectrometer and camera to obtain a clear image of the target. To perform the fine optical alignment we use a laser light source, which provides us more light thus increasing the precision of the alignment. The optical alignment is performed based on reflecting the incident light back to the source to adjust its positioning step-by-step. The procedure is the following:

- 1. The mirrors M_1 and M_2, placed parallel to each other, adjust the direction of the beam R_s so that it passes through two iris diaphragms D_1 and D_2.

- 2. Without the visible light beam splitter in the optical path, the mirror M_3 is adjusted so that it directs the beam upwards to strike the reference mirror M_4 perpendicularly. This is accomplished when the ray R_1, reflected from M_4, passes through D_1 and D_2.

- 3. Next, by inserting a cube visible light beam splitter into the optical path, we then create R_2 and R_3, reflected from the lower surface and the diagonal of the beam splitter, respectively. The diagonal is where the beam is splitted up, which makes an angle of 45° with its surfaces. The beam splitter is ajusted so that R_2 passes through D_1 and D_2. The upper the lower surfaces of the beam splitter are then parallel to the M_4. As a consequence, R_3 is parallel to M_4.

- 4. Now, without the lens in the optical path, we place the mirror M_3 in front of the slit. The spectrometer is then adjusted so that the incident light beam enters it perpendicularly. This is obtained by the reflected beam R_4 similarly as explained for the previous steps.

- 5. We remove M_3 and add the mirror M_4 on the camera. This mirror is screwed on the camera so that CCD and mirror are parallel. The camera has independent 6-degrees of freedom adjustments (three of translation and three of rotation). The ray R_5, reflected from the M_4 is used to adjust the camera pitch and yaw angles with respect to the optical axis so that the incident beam is perperdicular to the plane of the CCD.

- 6. Next, we remove M_4 so that one can adjust the roll angle of the camera. This is performed so that the slit is seen on the CCD as an horizontal line. This is one of the most important steps of the alignment protocol. It ensures that wavelength and spatial axes of the fringe map are parallel to the vertical and horizontal axes of the CCD. If the roll alignment is properly done the bright strips in Fig. B.1 should, therefore, be horizontal lines. To verify this, Fig. F.2 shows the position

of λ' along x' for the bandpass filter at $\lambda = 532\,\text{nm}$. It varies only one pixel which confirms the good alignment of the CCD to the slit.

- 6. Finally, we reinsert M_4 on the camera and install the lens in front of the spectrometer. The lens position is adjusted because of bending due to its size. This is attained similarly as discussed before.
- 7. The mirror M_4 is removed and the camera is set back to its focal plane.
- 8. For white light interferometry, we replace the laser by a white light source but the incident light beam keeps the same optical path passing through D_1 and D_2 by adjusting M_1 and M_2.

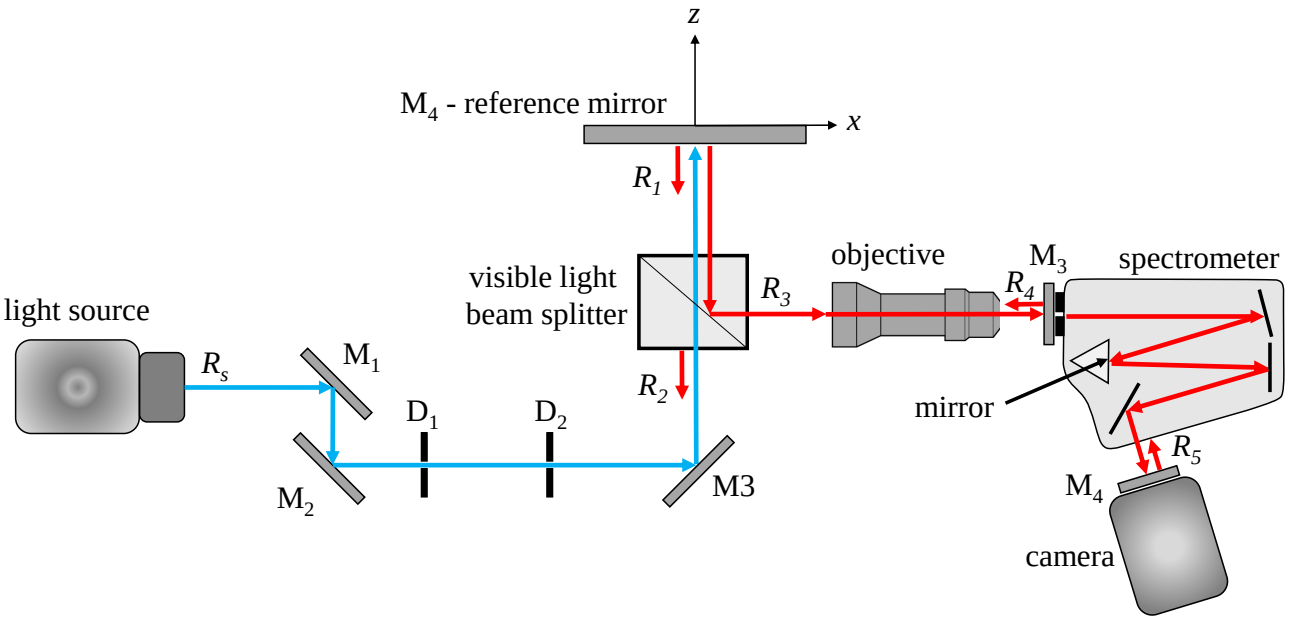

Figure F.1: Optical path during fine alignment. The M_4 reference mirror replaces the MgF_2 porthole.

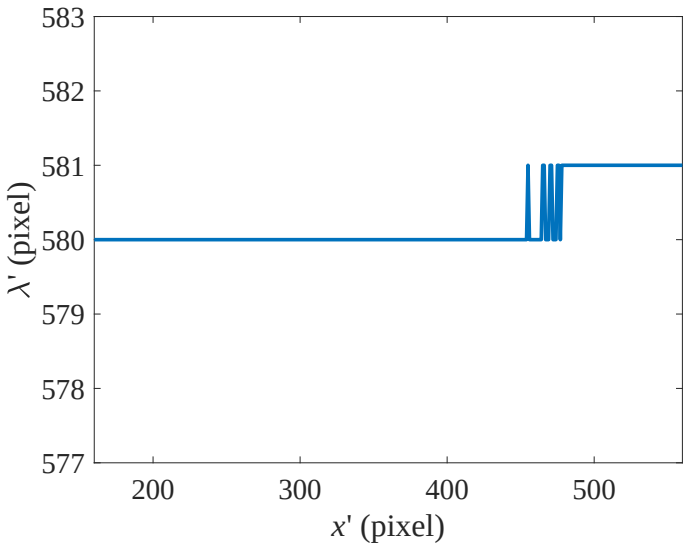

Figure F.2: Position of λ' along x' for the bandpass filter at $\lambda = 532\,\text{nm}$.

Appendix G

Scanning line positioning

G.1 Positioning protocol

During the boiling experiments one of the main challenges is to set the position of the scannning line on the ITO in a such way that it passes at the center of the bubble(in other words, at the bubble nucleation site). The following procedure is adopted to position the scanning line.

- **Centering the laser on the nucleation site**. Once the bubble nucleation has been triggered, We first move the laser head along the ITO film by using micrometric translation stages until one gets a symmetric temperature distribution (given by the IR thermography). This is achieved when the laser beam is on the bubble nucleation site. This ensures the symmetry on the microlayer thickness.
- **Adjusting the image**. First, with the slit open and the spectrometer in mirror mode(so that the 2D distribution of the dry-spot and microlayer extent can be seen on the boiling surface such as in Fig. 4.2) we center the bubble nucleation site on the center of the image.
- **Positioning the scanning line**. Next, still with the spectrometer in mirror mode, we partially close the slit (to its position used in diffraction mode) and the bubble nucleation is recorded. We perform a fine adjustment of the scanning line position so that we get the nucleation point on the line defined by the slit image.

G.2 Positioning verification

We verify the positioning of the scanning line by comparing the dry spot r_{cl} and microlayer r_m radii on the ITO film given by the WLI and the IR thermography. The IR thermography provides a 2D temperature distribution on the ITO film in which one can extract the true values of r_{cl} and r_m and compare to the ones obtained via WLI. These two quantities have been identified from the WLI images as discussed in sections 4.1.1. To obtain r_{cl} from the IR thermography one mentions that it corresponds to the maximum of q_l''(the heat flux at the contact line) whereas r_m is obtained as discussed in section 5.5.

Figures G.1a and G.1b show the r_{cl} and r_m radii given by WLI and IR thermography. The good agreement observed for both r_{cl} and r_m between the two different techniques shows that the scanning line has been correctly positioned at the center of the bubble. If that was not the case, r_{cl} and r_m would both appear shorter in WLI once the scanning line measures an extent inferior than the actual radius. The oscillations that appear in r_{cl} and r_m when $dr_m/dt < 0$ are due to the noise existing in the IR image, specially when depletion of the microlayer approaches at $t = 12.5\,\text{ms}$.

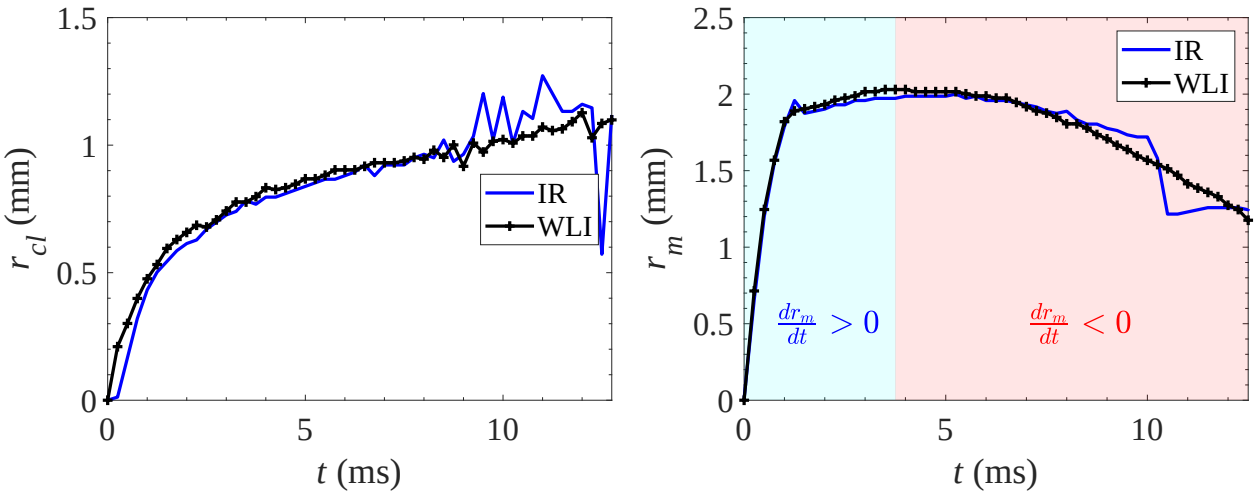

(a) r_{cl} extent over time.

(b) r_m extent over time.

Figure G.1: Comparison between WLI and IR thermography for r_{cl} and r_m radii.

Appendix H

Temperature spatial extrapolation and smoothing

H.1 Temperature extrapolation

The distribution of T_w in the $x-y$ plane is known only on a small area around the growing bubble. This distribution is used further as boundary condition at $z=0$ to compute the wall heat flux towards the microlayer. Its extent is however insufficient to model correctly the T_p distribution in the whole porthole because ΔT does not drop to zero at the edges of the IR image. One only knows that far from the bubble, $T_w = T_{sat}$ independently of time. The T_p distribution far from the bubble can however be approximated by that formed by the point source located at the porthole surface. As T_p is nearly independent of time in this region, the stationary thermal distribution from the point source can be used. It is well known to be proportional to the inverse distance from the source. Therefore, the power law extrapolation

$$T_w(x,y,t) = T_{sat} + C(t)/r, \tag{H.1}$$

where $r = \sqrt{(x-x_m)^2+(y-y_m)^2}$ was used far from the point (x_m, y_m) of T_w maximum, in practice, for $r > 3.75\,\text{mm}$. The constant C, with units of mK, was determined for each t from the $T_w(r)$ fits along different polar angles Θ in the $x-y$ plane as an averaged over the polar angle value. Figure H.1a locates Θ, x_m, y_m and r on the $x-y$ plane, where $x = r\cos\Theta$ and $y = r\sin\Theta$. The axis ζ_r is along r and centered at (x_m, y_m). Therefore, one can take profiles of $T_w = T_w(\zeta_r, \Theta)$.

First, we verify the validity of Eq. (H.1). In Fig. H.1b experimental T_w profiles along ζ_r are taken at $\Theta = 0, \pi/4, \pi/2$ and $3\pi/4$. Because the bubble is nucleated slightly outside the center of the porthole we have more experimental data along $-\zeta$ for $\Theta = 0$, being therefore particularly useful for validation. In Fig. H.1b, the power law is the fit of Eq. (H.1) for $\Theta = 0$ using the data within $-3.75 \leq \zeta_r(\text{mm}) \leq -0.75$. The root mean square error between the power law and the experimental T_w outside the fitting range ($-11.4 \leq \zeta_r(\text{mm}) \leq -3.75$) is 0.4 °C. Changes in T_w with Θ are minor as seen in Fig. H.1b. Therefore, the power law also holds for other values of Θ.

In Fig. H.2 the temperature profile with extrapolation is shown for $\Theta = 0$. For the range $-3.75 < \zeta_r(\text{mm}) < 3.75$, the temperature is kept as the one from experiments as the data within this region is available from the IR thermography measurements. T_w is then extrapolated for $-16.7 \leq \zeta_r(\text{mm}) \leq -3.75$ and $3.75 \leq \zeta_r(\text{mm}) \leq 16.7$. In the inset figure one can observe that the continuity of T_w profile is conserved at $\zeta_r = 3.75$. Therefore, one can use Eq. H.1 to extrapolate the wall temperature.

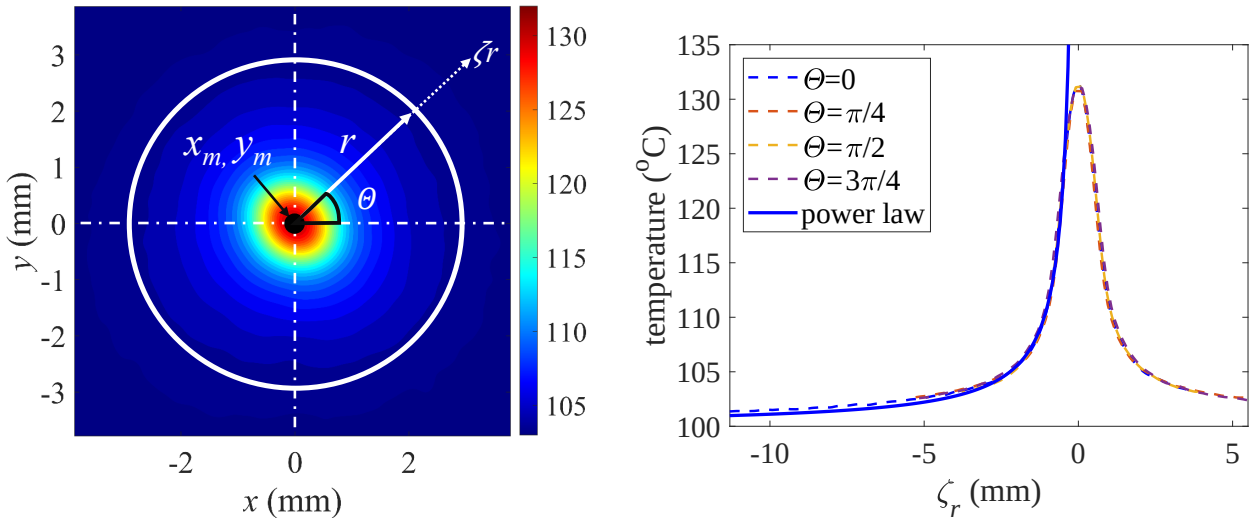

(a) Θ and r on $x-y$ plane. The graduation bar represets the temperature in °C.

(b) T_w profiles at different Θ.

Figure H.1: T_w distribution on the ITO before bubble nucleation for different Θ.

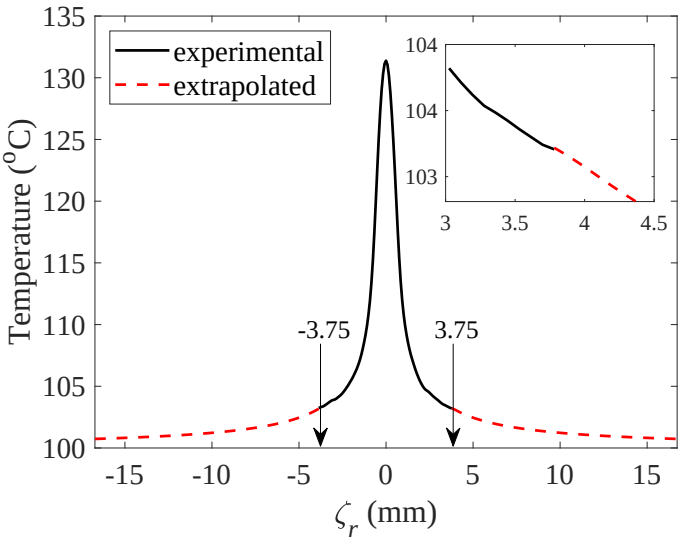

Figure H.2: T_w profile with extrapolation for $\Theta = 0$.

H.2 Temperature smoothing

The temperature distribution (Fig. 5.8) obtained from the IR thermography measurements is not free of noise. The electronic components in the IR camera are the main source of random oscillations in the IR intensity that is recorded, thus introducing a noise in $T_w(x, y)$. This noise is a concern, in particularly, to the wall heat flux computation towards the liquid, q_l'' in Fig. 2.5. In this work, we use Eq. (2.44) to determine q_l''. Therefore, $T_w(x, y, t)$ is used and its noise affect the computation of q_l''.

In order to decrease the noise amplitude and thus its minimize its effect on the heat flux analysis, $T_w(x, y)$ is smoothed by filtering $T_w(x, y)$. We apply a two-dimensional $(x-y)$ spatial Savitzky-Golay filter [220] to the raw $T_w(x, y)$ as described by Shekhar [221]. The least square method is used to fit the best polynomial to the raw $T_w(x, y)$, by using a Lagrangian minimization equation. More details

about the filter are given in section H.2.1.

Figures H.3a and H.3b show the raw and smoothed $T_w(x)$ for $y = 0$ at $t = 0.5\,\text{ms}$ and $0.75\,\text{ms}$, respectively. These profiles represent the two most critical raw temperature distributions to filter due to the abrupt changes in $T_w(x)$ in a very short length scale. Nevertheless, the algorithm is capable of representing well the inflection points of the raw data while reducing the noise from 1 K to 0.1 K.

Figures (H.4a) and (H.4b) show the second order in x and first order in time derivatives, respectively, obtained from the smoothed $T_w(x, y)$. One can observe that the low amplitude of noise compared to the absolute values thanks to the smoothing algorithm.

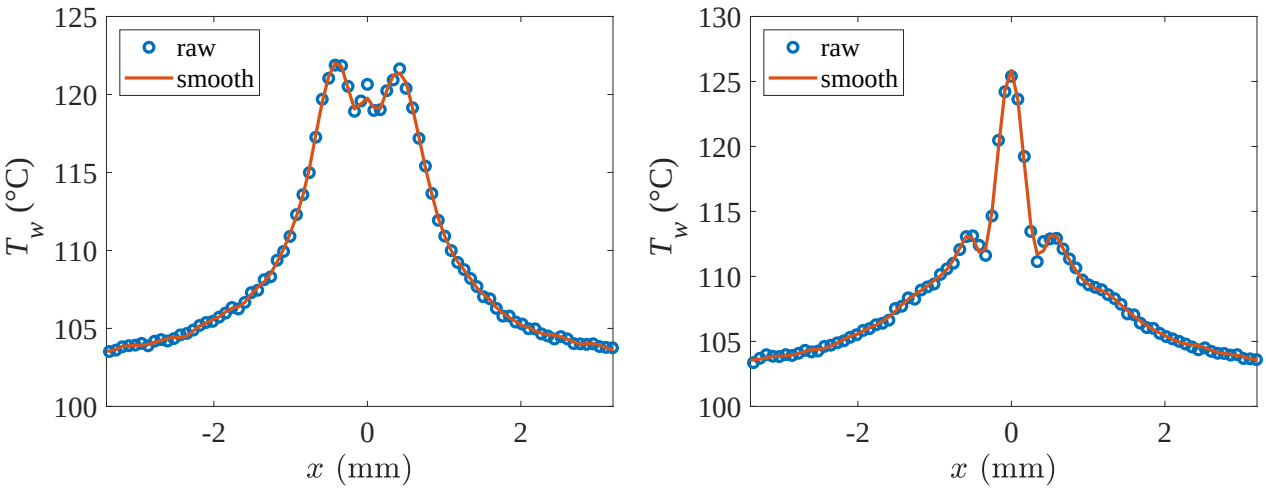

(a) $T_w(x)$ at $t = 0.5\,\text{ms}$.

(b) $T_w(x)$ at $t = 0.75\,\text{ms}$.

Figure H.3: Raw and smoothed $T_w(x)$ at $y = 0$ for $t = 0.5\,\text{ms}$ and $0.75\,\text{ms}$.

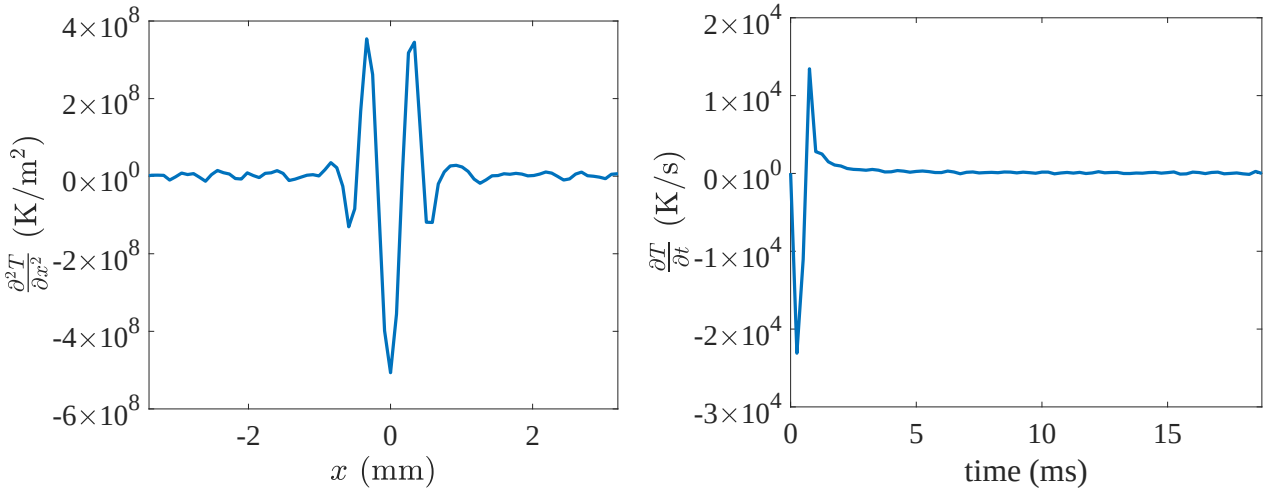

(a) Second order derivative in x for $t = 0.75\,\text{ms}$.

(b) First order derivative in time for $x = 0, y = 0$.

Figure H.4: Spatial and temporal derivatives from the smoothed temperature distribution.

H.2.1 Savitzky-Golay filter

In order to simplify the analysis, we introduce the spaces $\mathcal{P}_k$, $\mathcal{I}_k$ and $\mathcal{K}$. The space $\mathcal{P}_k := \{0, ..., n_k\}$ of the dimension k is indexed by i_k and represents the space of polynomials of the order n_k. The

space $\mathcal{I}_k := \{-m_k, ..., m_k\}$ represents the values of the convolution kernel indexed by j_k. Finally, $\mathcal{K} := \{1, ..., D\}$, where D is the dimension of the data space, is indexed by k. We fix:

$$f(x_1(j_1), ..., x_D(j_D)) = \sum_{i_1 \in \mathcal{I}_1} ... \sum_{i_D \in \mathcal{I}_D} a_{i_1 ... i_D} \prod_{k \in \mathcal{K}} \left(x_k^{i_k}(j_k) \right), \tag{H.2}$$

where $x_k^{i_k}(j_k) = j_k^{i_k}$. After that we introduce the least square method to fit the polynomial with the data, by using the Lagrangian minimization equation. After several developments, we obtain the following expression: $\{a\} = ([\psi]^t[\psi])^{-1}[\psi]^t\{y\}$, where:

$$\{a\} = [a_{i_1 ... i_D}], \tag{H.3}$$

$$\{y\} = [y_{j_1 ... j_D}] \tag{H.4}$$

are vector with dimension given, respectively, as

$$Dim\{a\} = \prod_{k \in \mathcal{K}} Card(\mathcal{P}_k), \tag{H.5}$$

$$Dim\{y\} = \prod_{k \in \mathcal{K}} Card(\mathcal{I}_k) \tag{H.6}$$

and

$$[\psi] = \left[\prod_{k \in \mathcal{K}} x_k^{i_k}(j_k) \right] \tag{H.7}$$

is a matrix of dimensions given by

$$Dim[\psi] = Dim\{a\} \times Dim\{y\} \tag{H.8}$$

Now, with the knowledge of the coefficients $a_{i_1 ... i_D}$ we can estimate the value of the "interrogation point" and the derivatives. To do that, we simply derive the function $f(x_1(j_1), ..., x_D(j_D))$ α_i times and write the space of derivatives $\mathcal{P}_{k/\alpha_k} := \{\alpha_k, ..., n_k\}$, we deduce for the 2D case:

$$\frac{\partial^{\alpha_1 + \alpha_2} (y_{j_1, j_2})}{\partial x_1^{\alpha_1}(j_1) \partial x_2^{\alpha_2}(j_2)} = \sum_{i_1 = \alpha_1}^{n_1} \sum_{i_2 = \alpha_2}^{n_2} a_{i_1, i_2} \prod_{k=1}^{2} \frac{i_k!}{(i_k - \alpha_k)!} x_k^{i_k}(j_k) \tag{H.9}$$

The choice of parameters to smooth the data is the key to save the maximum of information as possible while reducing noise. Luo et al. [222] studied the differentiation properties of this method and recommended polynomials degree 3 or 5 to have a correct representation. Browne et al. [223] and Krishnan and Seelamantula [224] studied the impact of the kernel size on the smoothing quality. They suggested that when the data distribution is characterized by low gradient, large kernels should be suitable. On the other hand, small kernels should be used for high gradients. In our case, we use a set of parameters at $t = 0.5\,\text{ms}$, to faithfully preserve the inflection points, as follows: $n = 4$ and $m = 3$ for all dimensions (x and y coordinates). Concerning the others frames, we have found $n = 4$ and $m = 4$.

Abstract in French (Résumé substantiel)

Introduction

Le transfert de chaleur et de masse par ébullition est impliqué dans un large éventail d'applications scientifiques et industrielles, telles que le refroidissement d'équipements électroniques par des échangeurs de chaleur diphasiques, la production de vapeur dans les usines chimiques et dans les centrales nucléaires. De grandes quantités d'énergie peuvent être transportées au moyen d'un changement de phase sans nécessiter de grandes surfaces ou de gradients de température, ce qui rend les équipements basés sur l'ébullition compacts, moins chers et très efficaces.

L'ébullition est un phénomène multi-échelle. Le rayon de la bulle qui peut être observe à l'œil nu lors de sa croissance sur la paroi est de quelques mm. Cependant, une microcouche liquide de quelques micromètres d'épaisseur peut se former entre la paroi et l'interface liquide-vapeur de la bulle. Les conditions dans lesquelles cette microcouche est formée font actuellement l'objet de recherches [7–9]. Sur la paroi il existe aussi une zone sèche entourée d'une ligne de contact. Cette dernière est une ligne où les trois phases (liquide, vapeur et solide) se rencontrent. La zone sèche est une surface du solide avec laquelle le liquide n'est pas en contact. La microcouche a une épaisseur de quelques μm et s'étend sur quelques mm sur la surface du solide.

Cette thèse se concentre sur les phénomènes physiques se produisant dans la microcouche et la tache sèche appelés phénomènes proches paroi. Plus spécifiquement, nous étudions expérimentalement la dynamique de la microcouche, de la tache sèche et le transfert de chaleur sur la paroi. La première motivation de cette thèse est que le profil de la microcouche peut être très complexe, dont les mécanismes physiques de formation sont toujours débattus dans la communauté scientifique. La deuxième motivation est que des simulations numériques, même directes au niveau d'une seule bulle, nécessitent des modèles microscopiques pour décrire complètement les phénomènes physique. Pour comprendre la physique à l'échelle nano- et micrométrique, des expériences doivent être réalisées à haute résolution spatiale. Par conséquent, cette étude concerne la croissance d'une seule bulle.

L'ébullition proche paroi: Etat de l'art

À proximité de la paroi, les forces visqueuses et de tension superficielle sont prédominantes et la dynamique dans cette région est indépendante des écoulements hydrodynamiques autour de la bulle. La microcouche peut se former, en fonction des propriétés de la surface telles que la mouillabilité, la vitesse d'assèchement et la surchauffe de la paroi. Le profil de la microcouche peut varier. Alors que la plupart des approches expérimentales montrent des formes courbées, les simulations numériques décrivent la présence d'un bourrelet de démouillage près de la ligne de contact. L'évaporation de la microcouche peut contribuer de manière significative à la croissance globale des bulles. Alors que certains résultats indiquent que la disparition de la microcouche est dû à des effets hydrodynamiques, d'autres montrent que son amincissement est dû à l'évaporation. Des flux de transfert de chaleur

élevés se produisent près de la ligne de contact. Le phénomène de proximité de la paroi nécessite encore une compréhension plus fondamentale.

Afin d'avoir un accès optique à travers de la paroi pour mesurer l'épaisseur de la microcouche, les hublots chauffants transparents sont utilisés dans les installations expérimentales les plus avancées. CaF_2 et MgF_2 sont tous deux transparents dans les spectres visible et IR et sont donc considérés comme des hublots dans ce travail. Le film d'ITO (oxyde d'étain et d'indium) a servi de l'élément de chauffage. Il est transparent dans le spectre visible mais opaques dans l'infrarouge (IR). L'ITO est donc adapté à la thermographie IR et à l'interférométrie en lumière visible. Ils peuvent également servir de chauffage, soit par effet Joule, soit par absorption locale d'un laser IR. Dans ce travail, c'est la seconde méthode qui a été exploitée car elle permet de ne produire qu'une seule bulle à la fois sur l'élément chauffant, même pour des flux de chaleur élevés.

Notre revue de littérature montre que les méthodes optiques de mesure sont avantageuses car elles sont non intrusives et des caméras à haute vitesse peuvent être utilisées pour capturer les phénomènes avec une résolution temporelle suffisante. Des publications dans ce domaine montrent que l'interférométrie laser (LI) est la technique la plus utilisée dans les études d'ébullition alors que l'interférométrie en lumière blanche (WLI) n'est pas encore exploitée. Les caractéristiques de LI et WLI sont étudiées dans des conditions statiques en utilisant un nouveau dispositif expérimental totalement développée dans le cadre de cette thèse. Pour mesurer la température de la paroi, l'utilisation d'une caméra IR est la plus appropriée. L'ombroscopie latérale est utilisée pour mesurer le comportement macroscopique de la bulle.

Instrumentation

Cellule d'ébullition: La cellule d'ébullition comprend une chambre d'ébullition en vase contenant l'eau à pression atmosphérique et dont la température est régulée jusqu'à la saturation à l'aide d'un fluide caloporteur circulant dans une double enveloppe. La surface d'ébullition se trouve au fond de la cellule. Les parois extérieures de la cellule sont isolées pour minimiser les pertes de chaleur dans l'environnement. Une sonde de température à résistance est placé à l'intérieur de la chambre d'ébullition pour surveiller la température du bain liquide. Quatre fenêtres optiques latérales transparentes à la lumière visible fournissent un accès optique à la macro dynamique de la bulle. L'eau utilisée a subi un traitement de purification particulier. Elle est osmosé, dé-ionisée et dégazé.

La surface d'ébullition est constituée d'un film d'ITO d'une épaisseur d'environ 950 nm déposé sur un hublot optique en fluorure de magnésium (MgF_2). Le MgF_2 est transparent dans les spectres visible et IR alors que l'ITO est transparent dans le visible mais opaque dans la bande IR. Un laser IR continu déclenche une bulle unique sur l'ITO par chauffage local par le bas grâce à la forte absorbance de l'ITO au rayonnement IR.

Des questions pratiques concernant l'ITO et le hublot ont été abordées et comprises au moyen de tests préliminaires visant à garantir leur stabilité mécanique, thermique et chimique dans des conditions d'ébullition. Ces questions incluent la réduction électrochimique de l'ITO, l'adhésion au hublot, la qualité des dépôts et la dissolution et la fragilité du hublot. Le choix final consiste en un film d'ITO déposé sur toute la surface du hublot de MgF_2. Il permet d'assurer la solidité de l'ensemble dans des conditions d'ébullition sans impacter la physique des phénomènes en proche paroi lors de la croissance d'une bulle. Des expériences ont été réalisées pour mesurer l'absorbance de l'ITO et pour déterminer le profil du faisceau laser. Le flux de chaleur source induit par le chauffage laser de l'ITO est ainsi mesuré.

Les méthodes de mesures: Trois mesures optiques simultanées et synchronisées sont effectuées afin de révéler les caractéristiques micrométriques et la macro-dynamique de la bulle. La WLI, la thermographie IR et l'ombroscopie latérale mesurent respectivement l'épaisseur variable dans l'espace et dans le temps de la microcouche, la distribution temporelle 2D de la température de la paroi et le

diamètre macroscopique de la bulle.

L'appareil optique WLI consiste en une source de lumière blanche collimatée, un séparateur de faisceau en lumière visible, un objectif installé à l'entrée d'un spectromètre et une caméra à sa sortie. Une source de lumière blanche à LED fournit un éclairage par le bas vers la bulle tandis que le séparateur de faisceau achemine vers le spectromètre le motif de franges créé par l'interférence lumineuse aux interfaces entre MgF_2, l'ITO, la microcouche et la vapeur. Les mesures d'épaisseur du film ont été effectuées par l'interférométrie laser (LI) et en lumière blanche (WLI). Un cas d'essai est utilisé pour valider le dispositif expérimental et les méthodes. Il consiste à mesurer le profil d'une couche d'air entre un hublot plat et une lentille plano-convexe à la courbure connue. L'interférence entre les rayons réfléchis par le film crée une image comportant des franges constructives et destructives, qui est utilisée pour déterminer l'épaisseur du film. La méthode WLI est exempte d'interférences indésirables causées par les réflexions d'éléments optiques épais et la carte de franges n'est donc pas contaminée. WLI et LI peuvent tous deux récupérer la forme théorique de la lentille avec des erreurs similaires. Ces tests dans une situation statique ont donc permis de valider la WLI. Nous avons montré qu'en WLI, les franges d'interférence ont la même géométrie que la microcouche. Une inférence qualitative sur le profil de la microcouche est donc possible sans aucun post-traitement de l'image. Plus de données pour calculer l'épaisseur du film sont obtenues en WLI par rapport à LI, ce qui réduit l'erreur aléatoire. La résolution de l'épaisseur par WLI est supérieure à celle de LI. En WLI, l'ITO fonctionne comme une couche d'espacement, ce qui réduit l'épaisseur minimale qui peut être mesurée. Par conséquent, nous avons choisi d'utiliser WLI pour notre expérience d'ébullition.

Un séparateur de faisceau visible-IR transparent au visible et réfléchissant à la largeur de bande d'une caméra IR est utilisé pour réfléchir le rayonnement IR émis par l'ITO vers la caméra IR pendant la croissance de la bulle afin de mesurer la variation temporelle 2D de la température sur la paroi. Le flux thermique de la paroi vers la microcouche est également déterminé par le calcul en utilisant la distribution de température comme condition limite pour résoudre le problème thermique transitoire 3D dans le hublot.

L'observation optique par ombroscopie latéral consiste à envoyer de la lumière d'un côté de la cellule d'ébullition vers la bulle à travers les fenêtres optiques transparentes latérales pour enregistrer la dynamique macroscopique de la bulle avec une caméra à grande vitesse du côté opposé, comme le montre le schéma de la Fig. fig:shadow. En raison de la courbure de la bulle, la lumière qui frappe son interface est déviée et n'atteint pas le CCD. Les rayons lumineux qui ne traversent pas la bulle se déplacent en ligne droite à travers le volume liquide pour atteindre le CCD. Par conséquent, l'ombre de la bulle est projetée vers la caméra et elle apparaît comme une zone noire alors que le liquide environnant est blanc. Une mesure de la forme macroscopique de la bulle est donc possible pour déterminer son diamètre, par exemple.

Résultats

Les résultats expérimentaux montrent une nouvelle caractéristique du profil de la microcouche : une "bosse" dans sa région centrale qui apparaît pendant sa formation. Nous expliquons cette bosse comme le résultat de l'interaction des forces visqueuses et capillaires agissant dans la microcouche pendant la phase de retrait du bord du pied de la bulle. Un très bon accord de ces résultats a été trouvé avec les simulations numériques effectuées dans notre groupe de recherche, confirmant ainsi notre compréhension physique de la formation des microcouches. Nous montrons également que l'amincissement de la microcouche se produit du fait de l'évaporation. En revanche, sa disparition est dû au recul de la ligne de contact.

Les observations par WLI ne montrent pas la présence de frange d'interférence près de la ligne de contact. Ceci indique la présence d'un bourrelet d'assèchement. Son existence pendant la croissance d'une bulle unique a été confirmée par nos simulations numériques et celles d'autres groupes [7, 115,

116]. Nous montrons que l'assèchement est plus rapide sous le mode de chauffage par laser IR par rapport à des études similaires employant le chauffage par effet Joule. La formation rapide de la tache sèche et le mouvement rapide de la ligne de contact balaye le liquide situé dans son environnement, provoquant ainsi une accumulation d'une grande quantité de liquide dans le bourrelet. Sa largeur et son épaisseur augmentent, ce qui entraîne des pentes élevées de l'interface vapeur-liquide au voisinage de la ligne triple. Elles sont beaucoup plus élevées que la limite maximale de pente que le WLI peut mesurer, de sorte que les franges d'interférence ne peuvent être observée.

Une comparaison avec le flux thermique déterminé à partir de l'épaisseur de la microcouche et de la surchauffe de la paroi montre une résistance thermique interfaciale plusieurs fois supérieure à sa valeur théorique. De plus, nous montrons qu'elle augmente dans le temps. Ce résultat indique que malgré le niveau élevé de pureté de l'eau utilisée dans les expériences, des impuretés subsistent et s'accumulent à l'interface liquide-vapeur au fur et à mesure de la croissance de la bulle.

Conclusions

Dans ce travail, nous avons effectué des mesures à micro-échelle durant la croissance d'une bulle dans le régime d'ébullition nucléée. L'accent est mis sur les phénomènes physiques proches de la paroi qui se produisent dans la microcouche d'une épaisseur de quelques μm formée entre la bulle de vapeur et le solide. La formation de la microcouche fait toujours l'objet de débats dans la communauté scientifique qui étudie l'ébullition et seul un nombre limité de résultats expérimentaux précis est disponible. De nouvelles méthodes de diagnostic optique à haute résolution et à haute vitesse ont été développées dans le cadre de ce travail pour comprendre la physique de l'ébullition. L'interférométrie en lumière blanche a été utilisée pour étudier la dynamique de l'épaisseur de la microcouche et l'étendue de la tache sèche et de la microcouche sur la paroi. La thermographie IR donne la distribution de la température de la paroi et la distribution du flux de chaleur transmis dans le liquide. L'ombroscopie donne la forme macroscopique de la bulle.

La première nouveauté de ce travail concerne l'instrumentation utilisée dans cette étude. Nous avons développé, validé et mis en œuvre un nouvel appareil d'interférométrie spectrale en lumière blanche pour mesurer la dynamique de l'épaisseur de la microcouche. Cette méthode a été utilisée pour la première fois dans des études d'ébullition. Elle présente plusieurs avantages notables par rapport à l'interférométrie laser classique utilisée pour les études d'ébullition par plusieurs groupes de recherche. En particulier, cette approche offre une résolution plus élevée de l'épaisseur de la microcouche, fournissant ainsi plus de données pour calculer l'épaisseur, ce qui assure une plus grande précision. Plus important encore, grâce à la dimension de la longueur d'onde, la géométrie des franges montre le profil de la microcouche au moment de l'observation sans aucun post-traitement. Cette information est très utile car elle permet à l'observateur d'évaluer instantanément les propriétés de la surface du foyer à proximité d'un site de nucléation particulier et de décider si un site voisin est plus avantageux pour les observations ou non. Nous avons également optimisé la disposition d'un grand nombre d'éléments optiques sous la cellule d'ébullition afin que les trois mesures susmentionnées puissent être effectuées simultanément et de manière synchrone à 4000 ips avec une haute résolution spatiale.

La deuxième nouveauté de ce travail est une description physique exhaustive de la formation de la microcouche et de sa dynamique en comparant nos données expérimentales à des simulations numériques, un modèle théorique simple et d'autres travaux similaires. Nous décrivons sa formation comme une interaction entre les forces visqueuses et capillaires agissant dans la microcouche pendant la phase de retrait du bord de la bulle. Nous montrons que son amincissement est bien le résultat de son évaporation. Nous montrons également que la croissance de la tache sèche sous la bulle est accéléré par le chauffage local au laser IR, créant ainsi un épais bourrelet près de la ligne de contact. La résistance thermique interfaciale liquide-vapeur a été montrée comme étant importante pour le flux

de chaleur.